III-NITRIDE SELF-ASSEMBLED NANOWIRE LIGHT EMITTING DIODES AND LASERS ON (001) SILICON

by

Shafat Jahangir

A dissertation submitted in partial fulfillment
of the requirements for the degree of
Doctor of Philosophy
(Electrical Engineering)
in The University of Michigan
2015

Doctoral Committee:

Professor Pallab K. Bhattacharya, Chair
Professor Joanna Mirecki-Millunchick
Professor Jamie D. Phillips
Associate Professor Zhaohui Zhong

© Shafat Jahangir 2015
All Rights Reserved

To my parents,

SIKDER JAHANGIR RASHID

and

SAYEDA SULTANA

ACKNOWLEDGMENT

I would like to express my sincere gratitude and deepest appreciation to my advisor Prof. Pallab Bhattacharya who remained a constant source of inspiration throughout my work. He was always there with an open door for all the problems that I faced. His constant encouragements have kept me going and have helped me to keep focus without losing sight during the times of failure. His excellent mentorship, guidance and personality will remain a cherished memory for the rest of my life. It has truly been an honor to work with him. I am grateful to my committee members, Prof. Joanna Mirecki-Millunchick, Prof. Jamie D. Phillips and Prof. Zhaohui Zhong, for devoting their time to review this dissertation and providing valuable suggestions and comments to improve the quality of this work.

I would like to thank Dr. Debashish Basu, Dr. Hyun Kum, Dr. Sishir Bhowmick and Dr. Animesh Banerjee for their help in getting me acquainted with epitaxial growth, device fabrication and characterization. Special thanks to Dr. Sishir Bhowmick, my roommate for three long years after I came to Ann Arbor, whom I could always rely upon. I am thankful to Prof. Wei Guo, Dr. Meng Zhang, Dr. Chi-sen Lee, Prof. Junseok Heo and Dr. Ayan Das for their constant support and technical inputs. I would like to thank Thomas Frost, Saniya Deshpande and Jimmy Chen for their countless hours of technical discussion, their advice and cooperation. I would like to extend my gratitude to Md Zunaid Baten, Arnab Hazari, Alan Teran, Bo Xiao, Ethan Stark, Trevor LaMountain

and Aniruddha Bhattacharya for their cooperation and wish them all the success in the years to follow.

I would like to acknowledge my collaborators who contributed to this thesis. I express special thanks to Prof. Joanna Mirecki-Millunchick and her students Dr. Kevin Grossklaus and Lifan Yan at University of Michigan for their insights and contributions to the structural characterizations of the nanowires. My gratitude is extended to Dr. Martin Strassburg, Martin Mandl and Tilman Schimpke at OSRAM Opto Semiconductors GmbH, Germany for their suggestions and guidance on the processing and characterizations of nanowire LEDs and wavelength converter white QD LEDs.

I greatly appreciate all the Lurie Nanofabrication Facility staff for their constant support in and out of the cleanroom. I express my gratitude to Dennis Schweiger whose generous help and cheerful demeanor have helped me come out of seemingly hopeless situations. I would also like to thank Dennis Grimard, Pilar Herrera-Fierro, Gregory Allion, David Sebastian, Anthony Sebastian, Russ Clifford, Matthew Oonk, Terre Briggs, Steven Sostrom, James Kulman, Katharine Beach, Robert Hower, Brian Armstrong, Brian VanDerElzen, Sandrine Martin, Nadine Wang, Kevin Owen and Shawn Wright for their mentorship and help in device fabrication and characterization.

I thank Lisa Vogel, Melanie Caughey, Laura Jarels, Deb Swartz, Karen Liska, Anne Rhodes, Beth Stalnaker and Steven Pejuan for excellent administrative support throughout my graduate career. I wish to acknowledge the University of Michigan Rackham Graduate School for providing partial fellowships to support my education, OSRAM Opto Semiconductors GmbH, Germany, the National Science Foundation (NSF) and King Abdullah University of Science and Technology (KAUST), Saudi

Arabia for funding this research. Finally, I could not have completed this work without the constant inspiration and support from my friends and family. I am grateful for the unconditional love and encouragement from my parents, Sikder Jahangir Rashid and Sayeda Sultana, and my brother, Ifat Jahangir. I am truly indebted to my wife, Fariha Nowshin Jahan, who has always been there for me at all times.

TABLE OF CONTENTS

DEDICATION ii

ACKNOWLEDGMENT iii

LIST OF FIGURES x

LIST OF TABLES xxii

LIST OF APPENDICES xxiv

ABSTRACT xxv

CHAPTER

I. INTRODUCTION 1

1.1 Solid State Lighting 1
1.2 Brief History of III-Nitride Research 8
1.3 Challenges in III-Nitride Research 10
1.3.1 Large Polarization Field and Related Effects 10
1.3.2 Availability of Substrates 13
1.3.3 Green Gap and Efficiency Droop 14
1.3.4 Problems with p-doping 16
1.3.5 Issues with Lasing Threshold and Emission Wavelength in Ga(In)N Lasers 17
1.4 Use of InGaN/GaN Disk-in-Nanowires as Gain Media 18
1.5 Dissertation Overview 21

II. GROWTH AND CHARACTERIZATION OF SELF-ASSEMBLED INGAN/GAN DISK-IN-NANOWIRES ON (001) SILICON BY PLASMA-ASSISTED MOLECULAR BEAM EPITAXY (MBE) 25

2.1 Introduction 25
2.2 Growth and Characterization of Self-Assembled GaN Nanowires on (001) Silicon 28
2.3 Growth and Characterization of Self-Organized Blue, Green and Red-emitting InGaN/GaN Disk-in-nanowires on (001) Silicon 39
2.3.1 Optimization of Radiative Efficiency of InGaN/GaN Disk-in-Nanowires by Temperature Dependent Photoluminescence Measurements 39

2.3.2 Temperature Dependent Photoluminescence Peak Shift : Absence of S-shaped Behavior 44
2.3.3 Surface Passivation of Optimized Ga(In)N Nanowires 46
2.3.4 Study of Carrier lifetimes in Ga(In)N Disk-in-Nanowires by Time Resolved Photoluminescence Measurements 49
2.4 Structural and Compositional Characterization of Ga(In)N Nanowires 52
2.4.1 Scanning Electron Microscopy (SEM) Imaging of Ga(In)N Nanowires 52
2.4.2 Transmission Electron Microscopy (TEM) Imaging of InGaN Disks in GaN Nanowires 54
2.4.3 Energy-Dispersive X-Ray (EDX) Measurements 54
2.5 Summary 56

III. INGAN/GAN DISK-IN-NANOWIRE ARRAY LIGHT EMITTING DIODES 57

3.1 Introduction 57
3.2 Growth of Blue, Green and Red InGaN/GaN Disk-in-Nanowire Light Emitting Diode (LED) Heterostructures on (001) Silicon 59
3.3 Fabrication of InGaN/GaN Disk-in-Nanowire LEDs 62
3.3.1 Fabrication of Nanowire LEDs on (001) Silicon 62
3.3.2 Fabrication of Flip-Chip Nanowire LEDs on Metal Reflector 63
3.4 Output Characteristics of Nanowire LEDs 67
3.4.1 Current-Voltage Characteristics 67
3.4.2 Electroluminescence of Nanowire LEDs 69
3.4.3 Efficiency of Nanowire LEDs 73
3.5 Summary 75

IV. EFFECT OF COALESCENCE ON THE OPTICAL PROPERTIES OF SELF-ASSEMBLED GA(IN)N NANOWIRES GROWN ON (001) SILICON 77

4.1 Introduction 77
4.2 Optical and Structural Characterization of GaN Nanowires with Different Areal Densities 79
4.2.1 Transmission Electron Microscopy (TEM) Imaging of Nanowires 79
4.2.2 Temperature Dependent Photoluminescence Measurements : Radiative Efficiency 82
4.3 Effect of Nanowire Coalescnece on the Output of Nanowire LEDs 84
4.3.1 Electroluminescnece of LEDs with Different Nanowire Areal Densities 84
4.3.2 Efficiency Analysis of Nanowire LEDs with Different Areal Densities 89
4.4 Transient Capacitance Measurements 91

4.4.1 Growth and Fabrication of n^+p GaN Nanowire diodes 91
4.4.2 Electron and Hole Traps in GaN Nanowires 94
4.4.3 Comparison of Deep Level Electron and Hole Traps in GaN Nanowires and Bulk GaN 100
4.5 Summary 102

V. PHOSPHOR-FREE MONOLITHIC INGAN/GAN DISK-IN-NANOWIRE TUNABLE WHITE LIGHT EMITTING DIODES ON (001) SILICON 104

5.1 Introduction 104
5.2 Different Schemes for White Light Emitting Diodes (LEDs) 106
5.3 Problems with Phosphor-Converted White LEDs 109
5.4 Growth of All-Nitride Monolithic InGaN/GaN Disk-in-Nanowire White LED Heterostructures on (001) Silicon 110
5.5 Fabrication of Nanowire White LEDs 112
5.6 Output Characteristics of Nanowire White LEDs 114
5.6.1 Current-Voltage Characteristics and Electroluminescence of White LEDs 114
5.6.2 Correlated Color Temperatures (CCT) of White Emission...... 118
5.6.3 Tunability of White Emission 121
5.7 Phosphor-Free Monolithic InGaN/GaN Quantum Dot (QD) Wavelength Converter White LEDs 123
5.7.1 Growth and Fabrication of QD White LED Heterostructures 123
5.7.2 Output Characteristics 130
5.8 Summary 133

VI. ELECTRICALLY INJECTED MONOLITHIC INGAN/GAN DISK-IN-NANOWIRE ARRAY EDGE-EMITTING LASERS ON (001) SILICON 136

6.1 Introduction 136
6.2 Different Schemes for Electrically Injected Lasers on (001) Silicon...... 137
6.3 Previous Reports of Ga(In)N Nanowire Lasers 141
6.4 Design and Growth of Green (λ=533nm) and Red (λ=610nm) Edge-Emitting Nanowire Laser Heterostructures on (001) Silicon 144
6.5 Fabrication of Ridge Waveguide InGaN/GaN Disk-in-Nanowire Lasers 152
6.5.1 Processing of Ridge Geometry Waveguide Laser Heterostructures 152
6.5.2 Highly Reflective Facets for Edge-Emitting Nanowire Lasers 154
6.6 Light Propagation in Nanowire Waveguide 155
6.7 DC Characteristics of Electrically Injected Monolithic Green-Emitting (λ=533nm) InGaN/GaN Disk-in-Nanowire Lasers on (001) Silicon 159

6.7.1 Light-Current and Spectral Characteristics 159
6.7.2 Measurement of Modal Gain 164
6.7.3 Output Polarization and Near-Field Characteristics 166
6.7.4 Far-Field Pattern and Long-Term Reliability Measurements .. 166
6.8 Dynamic Characteristics of Green-emitting (λ=533nm) InGaN/GaN Disk-in-Nanowire Lasers on (001) Silicon 168
6.9 Characteristics of Electrically Injected Monolithic Red-Emitting (λ=610nm) InGaN/GaN Disk-in-nanowire Lasers on (001) Silicon 171
6.10 Summary 178

VII. CONCLUSION AND SUGGESTION FOR FUTURE WORK 181

7.1 Summary of Present Work 181
7.2 Suggestions for the Future Work 186
7.2.1 Selective Area Growth of Ga(In)N Nanowires by MBE for Monolithic Tunable White LEDs 186
7.2.2 High Power Near-Infrared Electrically Injected Monolithic Nanowire Lasers on (001) Silicon 188
7.2.3 Room Temperature Nanowire Visible Spin-Polarized LEDs .. 190

APPENDICES 193

BIBLIOGRAPHY 206

LIST OF FIGURES

Figure

1.1: (a) Illustration of illuminated gas-light at night in 1880s with a thorium oxide–soaked mantle, (b) replica of Edison's incandescent lamp, (c) compact fluorescent lamp (CFL), (d) high-pressure sodium lamp [2]. 2

1.2: Electromagnetic spectrum depicting visible regime spanning from 380 to 750 nm. Human eye sensitivity is the highest at ~ 550nm [3]. 3

1.3: Applications of nitride-based LEDs and lasers 4

1.4: Life-cycle energy consumption for incandescent, CFL and LED lamps. The "use" phase of all three types of lamps accounted for almost 90% of the total life-cycle energy consumption, followed by manufacturing and transport. 5

1.5: Light emitting diode (LED)-based and LED-plus-phosphor–based schemes for white light sources. Highest luminous efficiency and best color rendering index are obtained with dichromatic and tetrachromatic approaches, respectively. Trichromatic schemes can provide good color rendering and luminous efficiency [2]. 6

1.6: Illustration of (a) on-chip optical interconnect for data communication [11], (b) coupling of processed optical data from a chip with optical fibers for off-chip communication [12]. 7

1.7: Wurtzite GaN crystal lattice structure illustrating c-plane {0001}(polar), m-plane {1-100}(non-polar), a-plane {11-20}(non-polar), and {11-22} semipolar planes [23] 10

1.8: Simulated band diagram of InGaN/GaN multi quantum well LEDs (a) with (solid line) and (b) without (dashed line) polarization fields [24] 11

1.9: Measured external quantum efficiency (EQE) of high performance LEDs emitting in the visible spectrum [31] 15

2.1: Cross-sectional Transmission electron micrograph (XTEM) showing the bending of threading dislocations towards the nanowire sidewall [47].. 26

2.2: RF plasma assisted (a) Veeco Gen II and (b) Veeco Gen 930 molecular beam epitaxy (MBE) systems in our lab.. 29

2.3: High resolution transmission electron microscopy (HRTEM) image of GaN nanowire/Si substrate interface showing the formation of thin Si_xN_y layer between GaN and Si [54].. 30

2.4: Illustration of growth mechanism of self-assembled GaN nanowires on (001) Si showing various adatom paths that contribute to nanowire growth along with their desorption.. 30

2.5: 45° tilted SEM images of 250 nm long GaN nanowires grown with Ga fluxes of (a) $3x10^{-8}$, (b) $7.8x10^{-8}$, and (c) $9x10^{-8}$ Torr keeping the same nitrogen flux and otherwise identical growth conditions demonstrating different nanowire areal densities as a function of Ga flux [90].. 31

2.6: Phase diagram for GaN nanowire growth at fixed N_2 plasma conditions [92]....32

2.7: Growth rate of GaN columnar and compact layers as a function of the Ga flux [93].. 32

2.8: Morphology of GaN layers, grown on (111) Si, as a function of the III–V ratio (decreasing the Ga flux) grown at 690°C: a) compact flat layer, b) compact rough layer, c) coalesced nanowires, and d) isolated nanowires [94]..34

2.9: 45° tilted SEM image of GaN nanowires on (001) silicon grown at a high substrate temperature of 870^oC and a low Ga flux of $5.6x10^{-8}$ Torr, resulting in non-uniform nanowires. 34

2.10: Diameter dependence of the axial growth rate of the GaN nanowires grown for long deposition time of 6 hours [93]. 35

2.11: Photoluminescence (PL) spectra of growth-optimized as-grown GaN nanowires measured at 10K and 300K with 325 nm excitation..........................36

2.12: Schematic representation of InGaN/GaN disks-in-nanowire heterostructures grown on (001) silicon for the calibration of emission wavelength and optimization of radiative efficiency of the disks. 37

2.13: PL intensities of as-grown red disks at 10K and 300K grown at (a) 515^oC, (b) 580^oC and (c) 545^oC; (d) variation of PL peak intensity of the optimized as-grown red DNW sample with excitation power density at 10K and 300K.....38

2.14: PL intensities of optimized as-grown (a) blue- and (b) green-emitting InGaN disks in GaN nanowires at 10K and 300K grown on (001) silicon. 40

2.15: Measured variation of PL peak energy with temperature at three different points in an as-grown red-emitting DNW sample. The solid line is the calculated InGaN bandgap shift with temperature according to the Varshni equation using $\alpha = 9.39 \times 10^{-4} eVK^{-1}$ and $\beta = 772K$.. 41

2.16: PL intensities of growth-optimized as-grown and surface passivated (with Si_3N_4 and parylene) (a) blue-, (b) green-, and (c) red-emitting InGaN disks in GaN nanowires at 10K and 300K grown on (001) silicon.............................42

2.17: PL spectra of growth-optimized as-grown and parylene passivated red-emitting InGaN/GaN disk-in-nanowires measured at 10K and 300K with 267 nm excitation.. 43

2.18: (a) Time resolved PL of as-grown DNW samples at room temperature. Solid lines show the calculated carrier lifetime in accordance with the stretched exponential model. Variation of carrier lifetimes with temperature in (b) as-grown and (b) parylene passivated red-emitting DNWs samples... 45

2.19: Arrhenius plot, derived from temperature dependent PL measurements on passivated green-emitting InGaN disks, yields two activation energies (E_{a1} =58meV and E_{a2} =1.34eV). The origins of these activation energies are however unknown and need to be further investigated... 47

2.20: (a) 45° tilted SEM image of the ensemble of InGaN/GaN disk-in-nanowires grown on (001) silicon with an optimized areal density of 2×10^{10} cm^{-2}, (b) top-view of nanowires from SEM image demonstrates almost near-perfect hexagonal cross-sections...51

2.21: Illustration of Ga and N atoms in GaN nanowires, grown in wurtzite crystalline form with Ga-face polarity on the top surface [98]..........................51

2.22: (a) High resolution transmission electron microscopy (HRTEM) image of InGaN nanowire showing almost defect-free crystalline structure along the growth direction of nanowires [65]. The inset shows the selective area diffraction (SAD) pattern; (b) HRTEM image of a single nanowire showing multiple InGaN disks separated by GaN barriers..53

2.23: Estimation of In compositions in (a) blue, (b) green and (c) red-emitting InGaN nanowires by energy dispersive x-ray (EDX) measurements. 55

3.1: 45° tilted scanning electron microscopy (SEM) image of as-grown nanowire LED heterostructure on (001) silicon substrate... 60

3.2: Normalized photoluminescence of the optimized blue (λ=430nm), green (λ=540nm) and red-emitting (λ=610nm) InGaN/GaN DNWs at 300K, used as active regions in the LED heterostructure. 60

3.3: (a) Schematic representation of the fabricated nanowire LED on (001) silicon showing n-GaN, p-GaN, DNWs active region and p-$Al_{0.15}Ga_{0.85}N$ electron blocking layers separately; (b) SEM image of the fabricated nanowire LED on silicon illustrating p- and n-contacts of the device.. 61

3.4: Reflectance of Ag, Au and Al as a function of emission wavelength [103]. Ag was used as metal reflector in flip-chip nanowire LEDs. It has a reflectance of higher than 90% for the emission wavelengths of our working LEDs... 62

3.5: (a) Schematic representation of nanowire LED heterostructure waferbonded with a silicon carrier on the top before removing the silicon growth substrate, (b) schematic illustration of flip-chip nanowire LED on Ag reflector after removing the entire silicon growth substrate.. 64

3.6: Room temperature current voltage characteristics: (a) blue, (b) green, and (c) red-emitting nanowire LEDs with Ni/Au/ITO contact (device A), (d) red-emitting nanowire LEDs with only ITO contact (device B) on (001) silicon. Insets of Figs. 3.6(a)-(c) show corresponding illuminated fabricated devices; (e) I-V characteristics of flip-chip red-emitting nanowire LED on Ag reflector at 300K. Inset shows optical micrograph of the fabricated flip-chip red LED wafer-bonded on a Si carrier.. 66

3.7: (a) Normalized room temperature electroluminescence (EL) of the LEDs on silicon under cw operation. L-I characteristics of (b) blue and (c) green-emitting LEDs on silicon at 300K under cw bias; (d) output characteristics of devices A and B on silicon and red-LEDs on Ag reflector under the same conditions. Solid lines are guide to the eye.. 68

3.8: Shift in electroluminescence (EL) peak at room temperature with increasing injection current density for (a) blue, (b) green and (c) red-emitting (device A) nanowire LEDs on (001) silicon. Solid lines are guide to the eye. 69

3.9: (a) Optical image of the red-emitting nanowire LED on silicon under 5x optical microscope, (b) near field image of the same device with 100x optical microscope reveals that around 38% of the total device area is illuminated at a current bias of 20 A/cm^2. 70

3.10: External quantum efficiency (EQE) vs injection current density under cw bias at 300K for (a) blue, (b) green and (c) red-emitting (device B) parylene passivated nanowire LEDs on (001) silicon. Fig. 3.10(c) also depicts the EQE

of the unoptimized flip-chip red-LED on metal reflector. The EQE curves have been analyzed by ABC recombination model (solid line). 72

4.1: High resolution Transmission electron microscope (HRTEM) image of coalescence-free single GaN nanowire collected from the ensemble of GaN nanowires with areal density of $2x10^{10}cm^{-2}$, showing no defects in the crystal structure along the growth direction. Inset shows selective area diffraction (SAD) pattern of the nanowire. 80

4.2: High resolution Transmission electron microscope (HRTEM) images of coalesced GaN nanowires with areal density of $\sim 3x10^{11}cm^{-2}$: (a) an example of chain of stacking fault defects near the boundary of coalescing nanowires at low and high magnification (inset); (b) a pair of nanowires that coalesced and a high resolution image of the defects (inset) in the vicinity of the juncture. 81

4.3: (a) Schematic representation of the red-emitting (λ=610 nm) $In_{0.51}Ga_{0.49}N$/GaN disks-in-nanowire heterostructure on (001) silicon. Photoluminesces of the as-grown red-emitting DNWs with areal densities of (b) $3.5x10^{11}cm^{-2}$, (c) $5.2x10^{10}cm^{-2}$ and (d) $2x10^{10}cm^{-2}$, at room temperature and 10K. 83

4.4: (a) Schematic illustration of red-emitting (λ=610nm) nanowire LEDs on silicon; (b) room temperature current-voltage characteristics of the LED under continuous wave operation. Inset shows the electroluminescence data of the device. 85

4.5: Room temperature electroluminescences of nanowire LEDs with areal densities of $3x10^{10}$, $6x10^{10}$ and $2x10^{11}$ cm^{-2} at the same injection current density of $40A/cm^2$, showing suppression of light output from the higher density devices. 86

4.6: Near field image of EL from the red nanowire LEDs with 100x magnification and 5V bias having (a) $2x10^{11}$, (b) $6x10^{10}$, (c) $3x10^{10}$, and (d) $2x10^{10}$ cm^{-2} nanowire areal density. Only 3%, 20%, 33% and 38% of the device area produce luminescence for (a), (b), (c) and (d), respectively. 87

4.7: Measured external quantum efficiencies of the red LEDs with different nanowire areal densities under CW mode of operation. Solid curves represent the calculated internal quantum efficiency (IQE) of the LEDs based on the A-B-C recombination model. 89

4.8: 45° tilted scanning electron microscopy (SEM) images of GaN n^+p nanowire diodes grown on (001) Si substrates with areal densities (a) $10^{11}cm^{-2}$, (b) $7.4x10^{10}cm^{-2}$, and (c) $3.6x10^{10}cm^{-2}$. 90

4.9: Measured room temperature I-V characteristics of the three nanowire n^+p diodes 1, 2 and 3. Inset shows the schematic representation of the fabricated nanowire diode on (001) n-silicon.. 93

4.10: Measured $1/C^2$ vs V plots of the nanowire diodes at room temperature. Electrically active doping concentration on the p-side, N_A is derived from the slope of the $1/C^2$ vs V curves to be ~ $3x10^{17}cm^{-3}$ for all three diodes. 93

4.11: Arrhenius plots (with measured data points) for electron traps (a) and hole traps (b) in p-GaN nanowires. The solid lines (red) without data points are Arrhenius plots of deep level traps identified in bulk GaN. 95

4.12: Measured external quantum efficiencies of the LEDs with different nanowire areal densities under CW mode of operation. Solid curves represent the calculated internal quantum efficiency (IQE) of the LEDs based on the A-B-C recombination model using non-radiative recombination coefficient A_2 (Table 4.3) which does not consider recombination at deep levels................99

5.1: (a) Normalized room temperature photoluminescence (PL) intensities of the optimized blue, green and red-emitting InGaN disks those have been used in LED A, (b) Normalized PL intensities of the optimized blue, green and red-emitting InGaN disks at 300K those have been used in LEDs B, C and D...111

5.2: Schematic representation of InGaN/GaN disk-in-nanowire white LED heterostructures grown on (001) silicon. The number of blue- and red-emitting InGaN disks and the emission wavelengths of the disks were varied to investigate the tunability of white emission…...113

5.3: (a) Room temperature current-voltage characteristics of the fabricated LEDs (A to D), (b) optical micrograph of LED B at an injection current density of $60A/cm^2$... 114

5.4: Room temperature electroluminescence (EL) intensities of (a) LED A and (b) LED C as a function of injection current density......................................115

5.5: Room temperature light-current characteristics and external quantum efficiencies (EQE) of (a) LED A and (b) LED C as a function of injection current density... 116

5.6: XY Chromaticity coordinates of white light emission from (a) LED A, and (b) LED C with variation of injection current density from $30A/cm^2$ to 110 A/cm^2... 117

5.7: Variation of correlated color temperatures of the white emission for different white nanowire LEDs as a function of injection current density from 30A/cm^2 to 110 A/cm^2.. 118

5.8: Variation of chromaticity coordinates of the white emission changing the emission wavelengths of the blue, green and red-emitting InGaN disks in LEDs A and B. The numbers of blue, green and red-emitting InGaN disks were kept same in both the devices.... 119

5.9: Variation of chromaticity coordinates of the white emission changing the number of blue and red-emitting InGaN disks in LEDs B, C and D. Emission wavelengths of the blue, green and red-emitting InGaN disks were kept same in all the devices.... 120

5.10: (a) Schematic representation of InGaN/GaN quantum dot wavelength converter white LED heterostructure; atomic force microscopy images of self-organized (b) $In_{0.24}Ga_{0.76}N$/GaN dots with peak emission at λ = 450 nm and (c) $In_{0.37}Ga_{0.63}N$/GaN dots with peak emission at λ = 600 nm.... 124

5.11: Room temperature photoluminescence of (a) blue-emitting pump dots and (b) red-emitting converter dots incorporated in the QD wavelength converter white LED heterostructure... 125

5.12: (a) Measured current-voltage characteristics of QD wavelength converter white LEDs at room temperature; optical micrographs of the devices biased at an injection current density of 45A/cm^2: (b) device C′ (c) and device E′... 126

5.13: (a) Electroluminescence of device C′ under CW operation as a function of injection current density, (b) light-current characteristics and external quantum efficiency of device C′ under CW biasing.. 127

5.14: (a) Trend of chromaticity coordinates of white light emission from device C′ with variation of injection current density, (b) variation of correlated color temperature (CCT) of white light emission with injection current density for different LEDs. Solid lines are guides to the eye............................ 129

5.15: Chromaticity coordinates of white emission for different wavelength converter quantum dot white LEDs at a constant injection current density of 45A/cm^2...... 132

6.1: (a) Room temperature light-current characteristics of GaAs/AlGaAs lasers [153] on silicon, (b) L-I characteristics of $In_{0.5}Ga_{0.5}As$ QD laser at 300K along with the emission spectrum above threshold [154], (c) room

temperature light output from high performance InAs QD laser (λ=1.3µm) grown on misoriented (001) silicon [155].. 138

6.2: (a) Schematic illustration of Ge-on-Si p-n-n laser heterostructure along with the L-I characteristics [156], (b) schematic representation of III-V heterostructure bonded on (001) silicon, where optical mode is guided by the silicon waveguide via evanescent mode coupling [157]............................ 139

6.3: (a) SEM image of single GaN nanowire laser dispersed on sapphire substrate. The color indicates laser emission at the two ends of the nanowire, (b) power dependence of the lasing near threshold (blue) and that of the photoluminescence emission from a non-lasing region (black) [165].. 141

6.4: (a) Schematic representation of the fabricated nanowire laser consisting of a single GaN nanowire and a 2D photonic crystal microcavity, (b) an oblique view SEM image of the fabricated device, (c) variation of peak output intensity with pump power (the L-L curve). The change in slope of the L-L curve near threshold ~120 kW/cm^2 is clearly observed [166].............. 142

6.5: (a) CCD image of a single-mode GaN nanowire laser optically pumped above lasing threshold, The nanowire laser emits a highly divergent beam from the facets, some of which is collected by the objective lens. The objective lens also collects radiation emitted from the facets that is scattered by the SiN substrate surface, as well as spontaneous emission exiting perpendicular to the nanowire axis. Scale bars are 2 µm, (b) nanowire laser intensity versus pump laser intensity with cavity length of 4.7 µm. In set shows SEM image of a single GaN nanowire dispersed on SiN substrate [167]... 143

6.6: (a) Schematic representation of the green-emitting (λ = 533 nm) nanowire array laser heterostructure showing the active region, In0.6Ga0.94N waveguide and asymmetric Al0.11Ga0.89N cladding. The calculated mode profile is shown alongside, assuming that the space between the nanowires is filled with parylene; (b) 45o tilted scanning electron microscope (SEM) image of green-emitting (λ = 533 nm) In0.34Ga0.66N/GaN disk-in-nanowire array laser heterostructures grown by molecular beam epitaxy on (001) silicon substrate. Inset shows the high resolution transmission electron microscope (HRTEM) image of a ~2 nm thick In0.34Ga0.66N disk in a single GaN nanowire.. 145

6.7: Room temperature photoluminescence of (a) Al0.15Ga0.85N nanowire and (b) In0.06Ga0.94N nanowire, which were used as p-doped electron blocking layer (EBL) and waveguide layer, respectively, for both the green and red-emitting nanowire lasers, (c) Energy-dispersive X-ray (EDX)

measurement of the elemental composition along the c-axis of an InGaN disk used in the green-emitting (λ=533nm) nanowire laser heterostructure, which yields a maximum In composition of 34% in the disk. Inset shows EDX scan direction across a single InGaN disk... 147

6.8: (a) Enhancement in 300K photoluminescence of the green-emitting disk-in-nanowire sample by surface passivation with parylene,
(b) Photoluminescence of GaN nanowires at 300K, before and after treatment with ammonium sulfide $(NH_4)_2S_x$... 149

6.9: Energy-dispersive X-ray (EDX) measurement along the c-axis of an InGaN disk used in the red-emitting (λ=610nm) nanowire laser heterostructure, which yields a maximum In composition of 51% in the disk. Inset shows EDX scan direction across a single InGaN disk... 150

6.10: (a) XRD data of $In_{0.18}Al_{0.82}N$ nanowire grown on GaN. This $In_{0.18}Ga_{0.82}N$ nanowire lattice matched to GaN was used as cladding layer in red-emitting nanowire laser, (b) High resolution transmission electron microscope image (HRTEM) of $In_{0.18}Al_{0.82}N$ nanowire showing defect-free crystal structure along the growth direction. Inset shows the selective area diffraction (SAD) pattern of the nanowire, (c) Energy-dispersive X-ray (EDX) measurement of the elemental composition along the c-axis of $In_{0.18}Al_{0.82}N$ nanowire... 151

6.11: Schematic illustration of the red-emitting (λ=610nm) nanowire array laser heterostructure showing the active region, $In_{0.6}Ga_{0.94}N$waveguide and $In_{0.18}Al_{0.82}N$ cladding. The calculated mode profile is shown alongside, assuming that the space between the nanowires is filled with parylene............ 152

6.12: Schematic representation of the fabricated ridge waveguide InGaN/GaN disk-in-nanowire array (a) green and (b) red laser heterostructures on (001) silicon.. 153

6.13: (a) Schematic representation of nanowire array waveguide heterostructures similar to green-emitting nanowire laser heterostructures except the disks and without Si and Mg doping used in transmission measurements. x is the direction of the nanowire waveguide/cavity made up of nanowire-parylene composite and z is the nanowire growth direction, (b) output intensity from the nanowire-array ridge waveguides of (a), measured with a charged coupled device (CCD) detector, as a function of waveguide length. The input excitation was focused light from a 532 nm laser. The propagation loss was obtained for ridge nanowire waveguides of different length and having a fixed width of 10μm. The inset shows a CCD image from the output facet of the nanowire waveguide... 155

6.14: Optical field distribution in the (a) x-y and (b) x-z planes, respectively of the nanowire waveguide, used for the green-emitting laser, (with reference to the schematic in Fig. 6.13(a) in response to a y-polarized plane wave modulated by a Gaussian distribution approximating the calculated mode in Fig. 6.6(b). Light can propagate freely in the in-plane direction as the field is continuous over the nanowires.. 157

6.15: (a) Light-current (L-I) characteristics of a broad area (1 mm x 50 μm) green nanowire laser at 300K. The threshold current density, J_{th} is 1.76 kA/cm^2 and 1.72 kA/cm^2, respectively, under continuous wave and pulsed biasing; (b) the electroluminescence (EL) spectrum of the 1.5 mm x 10 μm ridge waveguide laser biased cw above and below threshold. The smallest recorded linewidth is 8Å, (c) the variation of the emission linewidth and the blueshift of the peak emission with increasing injection current density for the ridge waveguide laser. The total blueshift of the peak emission is 8 nm which corresponds to a polarization field of 618 kV/cm................................. 160

6.16: (a) Temperature dependence of the threshold current density in a ridge waveguide green nanowire laser under cw biasing. The inset shows the measured L-I characteristics at different temperatures; (b) the variation of the inverse differential quantum efficiency with cavity length for ridge waveguide lasers with 10μm width. From the analysis of these data, an internal quantum efficiency of η_i= 0.55 was derived, (c) the variation of threshold current density, J_{th} with inverse cavity length. A value of differential gain dg/dn = 2.8x10^{-17} cm^2 and a transparency current density of 454 A/cm^2 are derived from this plot using a total carrier lifetime τ of ~395 ps... 161

6.17: (a) Emission spectra of green-emitting nanowire laser near threshold, characterized by a succession of peaks and valleys, (b) modal gain spectrum at threshold obtained from Hakki-Paoli measurement. The peak net modal gain at threshold is 24cm^{-1}.. 163

6.18: (a) Polarization dependent output from single facet of green nanowire array laser, which shows that TE polarized component increases significantly with a threshold of 1.82 kA/cm^2, (b) near field mode intensity profiles from the low reflectivity facet along the growth (transverse) and lateral directions of the green nanowire laser cavity.. 165

6.19: (a) Far field pattern from the low reflectivity facet of a ridge waveguide green-emitting nanowire array laser, (b) the output power from the green nanowire laser versus time with an extrapolated lifetime for the output power to be reduced to half the maximum value of 7000hrs............................ 167

6.20: (a) Measured small-signal modulation response of a 400μm x 4μm ridge waveguide green nanowire laser at 300K for varying dc injection current

values. The data is analyzed to derive the response frequency fr and damping factor γ_d, (b) plot of f_r versus square root of injection current. The differential gain is derived from the slope of this plot, (c) Plot of γ_d versus square of resonance frequency. The gain compression factor ϵ is derived from the slope of this plot....... 169

6.21: (a) Light-current (L-I) characteristics of a ridge waveguide nanowire red nanowire laser at 300K. The threshold current density, J_{th} is 2.88 kA/cm^2 under continuous wave operation; (b) the electroluminescence (EL) spectrum of the 1.5 mm x 10 μm ridge waveguide laser biased cw above and below threshold. The smallest recorded linewidth is 9Å, (c) the variation of the emission linewidth and the blueshift of the peak emission with increasing injection current density for the ridge waveguide laser. The total blueshift of the peak emission is 14.8 nm which corresponds to a polarization field of 1098 kV/cm.. 172

6.22: (a) Modal gain spectrum at threshold obtained from Hakki-Paoli measurement. The peak net modal gain at threshold is 27cm^{-1}, (b) Temperature dependence of the threshold current density in a ridge waveguide red nanowire laser under cw biasing. The inset shows the measured L-I characteristics at different temperatures, (c) Polarization dependent output from single facet of red nanowire array laser....... 173

6.23: (a) The variation of the inverse differential quantum efficiency with cavity length for ridge waveguide lasers with 10μm width. From the analysis of these data, an internal quantum efficiency of η_i= 0.58 was derived, (b) the variation of threshold current density, Jth with inverse cavity length. A value of differential gain dg/dn = 3x10^{-17} cm^2 and a transparency current density of 312 A/cm^2 are derived from this plot using a total carrier lifetime τ of ~482 ps....... 174

6.24: (a) Measured small-signal modulation response of a 400μm x 4μm ridge waveguide red nanowire laser at 300K for varying dc injection current values; (b) measured chirp of nanowire laser as a function of small-signal modulation frequency; (c) measured α-parameter as a function of emission wavelength.. 176

7.1: Scanning electron microscopy (SEM) imaging of (a) 45° tilted and (b) top surface views for selective area growth (SAG) of GaN nanocolumn array [1]... 186

7.2: Schematic illustration of the proposed edge-emitting near-IR monolithic InGaN/GaN disk-in-nanowire laser heterostructure on (001) silicon............... 188

7.3: Refractive indices of wurtzite GaN (square), InN (empty triangle), AlN (circle) and $Al_{0.1}Ga_{0.9}N$ (solid triangle) [190]....... 189

7.4: Schematic representation of the proposed flip-chip spin-polarized LED heterostructure........ 191

LIST OF TABLES

Table

1.1: Substrates used for the growth of III-nitride LEDs and lasers. 13

2.1: Growth conditions for the optimized InGaN disks with the highest radiative efficiency..40

2.2: Radiative efficiencies of as-grown and passivated optimized InGaN disks. 46

2.3: Carrier lifetimes in as-grown and passivated InGaN/GaN disks-in-nanowires at T=300K. The measurements were carried out with 405 nm excitation.. 48

2.4: Carrier lifetimes in as-grown and passivated GaN region of the nanowire at T=300K with 267 nm excitation.. 48

4.1: Radiative and non-radiative recombination coefficients derived from red-LED efficiency measurements...89

4.2: Characteristics of deep levels in GaN nanowires obtained from transient capacitance measurements...97

4.3: Non-radiative recombination coefficients derived from LED efficiency measurements and trap densities...98

4.4: Characteristics of deep levels in bulk GaN obtained from transient capacitance measurements...100

5.1: Chromaticity coordinates and color temperatures of white emission for LEDs A and B, where emission wavelengths of InGaN disks were varied.. 119

5.2: Chromaticity coordinates and color temperatures of white emission for LEDs B, C and D where number of InGaN disks were varied...........................120

5.3: Growth parameters and radiative efficiencies of blue- and red-emitting InGaN/GaN self-organized quantum dots...128

5.4: CIE chromaticity coordinates and correlated color temperatures of wavelength converter white LEDs at an injection current density of $45A/cm^2$ 130

LIST OF APPENDICES

Appendix

A: Silicon Substrate Preparation for MBE Growth 194

B: InGaN/GaN Disks-in-nanowire Ridge Waveguide Laser Processing 195

ABSTRACT

Substantial research is being devoted to the development of III-nitride light emitting diodes (LEDs) and lasers, which have numerous applications in solid state lighting. In particular, white LEDs play an increasingly important role in our daily lives. Current commercially available white LEDs are nearly all phosphor-converted, but these have some serious disadvantages. Planar quantum well (QW) devices on foreign substrates exhibit large threading dislocation densities, strong strain induced polarization field, and In-rich nanoclusters. These result in poor electron-hole wavefunction overlap, large emission peak shift with injection, and substantial efficiency reduction at high injection currents in QW based LEDs and large threshold current densities in lasers. The objective of this doctoral research is to investigate the prospects of self-assembled InGaN/GaN disks-in-nanowire (DNW) LEDs and lasers for solid state lighting. The research described here embodies a detailed study of the optical and structural characteristics of the nanowire heterostructures by varying the growth conditions and by surface passivation, and using the disks as the active region in high performance nanowire LEDs and gain medium in nanowire lasers on (001) silicon.

Self-assembled InGaN/GaN DNWs are grown in a plasma-assisted molecular beam epitaxy (PA-MBE) system. Due to their large surface to volume ratio, the growth optimized and surface passivated DNWs on (001) silicon are relatively free of extended defects and have smaller polarization field resulting in higher radiative efficiencies. The

growth conditions for the DNWs are optimized to obtain high radiative efficiencies (48%, 43% and 41% for as-grown blue (λ=430nm), green (λ=540nm) and red (λ=650nm) DNWs, respectively). Upon surface passivation by parylene, radiative efficiency of the disks is enhanced by 10-12%. Blue-, green- and red-emitting DNW LEDs, with optimized nanowire densities, are demonstrated with substantially reduced efficiency droop (< 15%) and small peak shift with injection currents. With very large nanowire density, we might have more non-radiative recombination of carriers in the coalesced nanowires instead of having higher light output from LED or higher modal gain in laser. As a trade off, self-assembled nanowire density has been optimized to a moderate value of $2x10^{10}$ cm^{-2} for making nanowire LEDs and lasers.

Phosphor-free tunable electrically injected white nanowire LEDs are realized by incorporating InGaN/GaN disks with different color emissions in the active region. Unlike QW based white LEDs, they demonstrate excellent stability of color temperature with injection currents and low color temperature required for true cool and warm white lights. The first ever monolithic edge-emitting electrically pumped green (λ=533nm) and red (λ=610nm) nanowire lasers on (001) silicon are demonstrated using DNWs as the gain media. The lasers are characterized by low threshold current densities of 1.76-2.88 kA/cm^2, small peak shifts of 11-14.8 nm, significantly large T_0 of 234 K and relatively high differential gain of $3x10^{-17}$ cm^{-2}. Dynamic measurements performed on these lasers yield a maximum small signal modulation bandwidth of 5.8 GHz. Extremely low value of chirp (0.8 Å) and a near-zero linewidth enhancement factor at the peak emission wavelength are also obtained from these measurements, which are encouraging for optical communication in plastic fibers.

Chapter I

Introduction

1.1 Solid State Lighting

Visual perception, by which humans assimilate information from their surroundings to perform day-to-day activities, is not possible without light. Other than by direct sunlight during daytime, we depend on artificial light to continue our productivity from the day into the non-sunlit hours of the night. The role of artificial light is inseparable in every sphere of our life so much so that we consumed an estimated 6.5% of total global primary energy in 2005 [1] just to fuel these artificial light sources. The history of lighting has seen quite a number of drastic twists and turns. The first commercially available lighting technology that served numerous homes, streets and offices near the end of 19th century was fueled by natural gas. Edison's invention of the incandescent light bulb gave tremendous competition to these gas-based light sources for their existence and eventually they were replaced by these incandescent light bulbs which were first demonstrated in 1879. An incandescent lamp works by flowing a current through a filament to heat it up to a high temperature until it glows (mostly infrared emission), and therefore has poor radiative efficiency. Only the visible light that comes out of it is useful. Compared with incandescent lamps, fluorescent tubes and compact fluorescent Lamps (CFL)

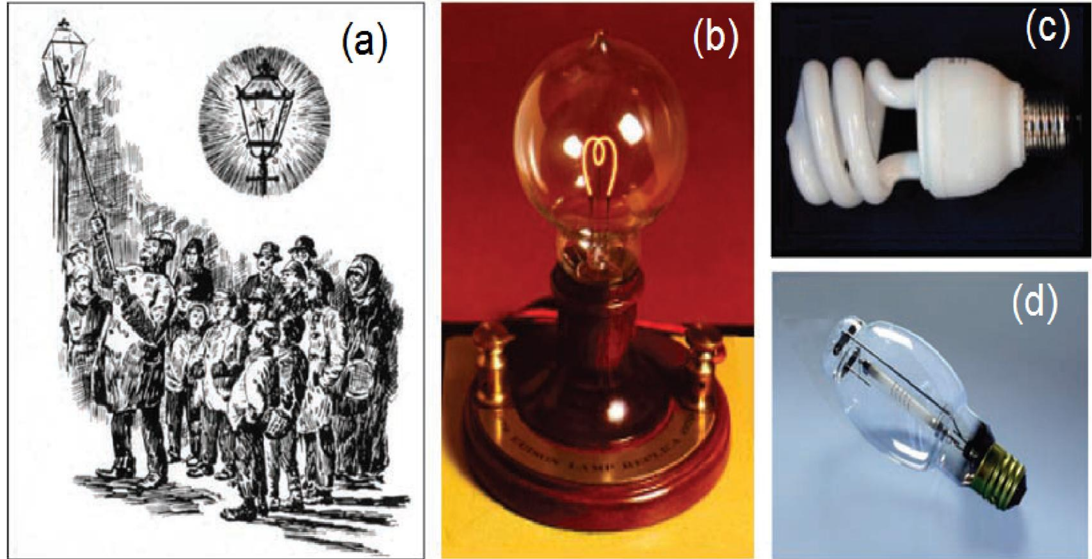

Figure 1.1 (a) Illustration of illuminated gas-light at night in 1880s with a thorium oxide–soaked mantle, (b) replica of Edison's incandescent lamp, (c) compact fluorescent lamp (CFL), (d) high-pressure sodium lamp [2].

reduce the amount of electric energy that is converted to wasteful infrared emission to some extent and became a mainstream lighting technology after the 1950s. However, fluorescent light sources, which produce light from mercury discharge, suffer from parasitic energy losses and the left-over mercury from burned out lamps is harmful to environment. The advent of solid state lighting, in terms of light emitting diodes and lasers, has revolutionized the lighting industry in many applications. In solid state light sources, electrons radiatively recombine with holes to emit visible light. Thus, unlike incandescent bulbs and fluorescent lamps, electricity is directly converted into light into the visible spectrum, therefore bringing down the parasitic energy losses significantly. Hence, solid state lighting has become the most energy-efficient and environment-friendly lighting technology over the last decade. Progress in solid state lighting primarily depends on the research and development of visible nitride-based

light emitting diodes (LEDs) and lasers. III-nitride based light sources, constituting of direct and wide band-gap semiconductors, emit in the visible spectrum needed in daily applications. In addition to the energy-saving and its positive effect on the environment, nitride based solid state lighting offers what is inconceivable with conventional light sources : tunability of spectral and polarization properties as well as the color temperature. Currently emerging solid state lighting technologies

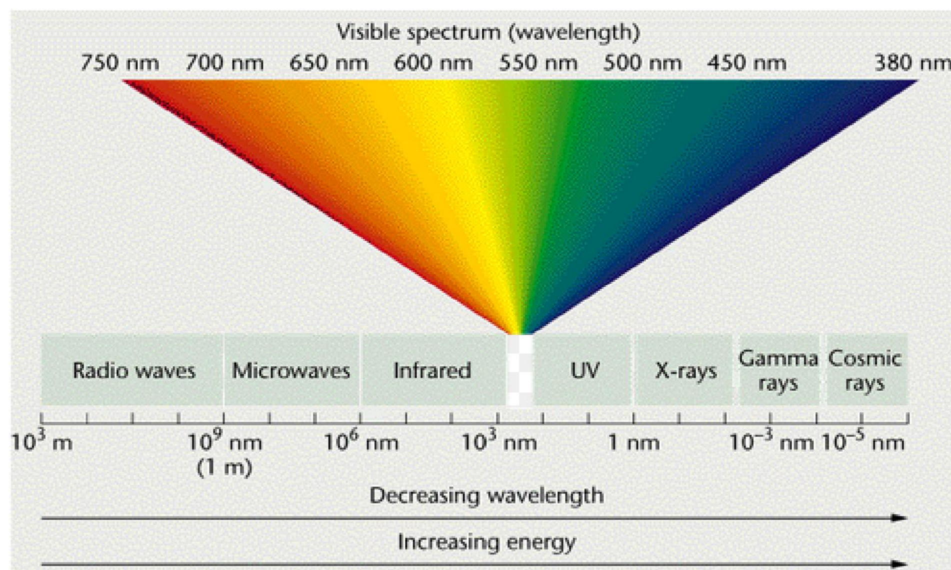

Figure 1.2 Electromagnetic spectrum depicting visible regime spanning from 380 to 750 nm. Human eye sensitivity is the highest at ~ 550nm [3].

are expected to have applications in indoor-, outdoor- and colored-lighting, portable lights, displays, automobiles, transportation, communication, imaging, agriculture and medicine. Some of the applications of solid state LEDs and lasers are depicted in Fig. 1.3.

In 2012, the United States Department of Energy (DOE) conducted a study on the lifecycle-energy consumption of different lighting technologies [4]. It was found that the average life-cycle energy consumption of LED lamps and CFLs were similar,

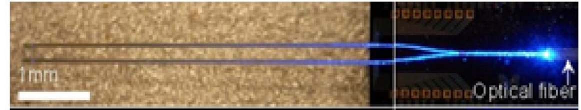

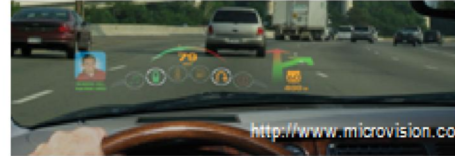

Figure 1.3 Applications of nitride-based LEDs and lasers.

and was around one-fourth the consumption of incandescent lamps. It was predicted that if LED lamps can keep on improving to meet industry performance targets by 2015, their life-cycle energy consumption is expected to reduce by approximately one-half, whereas the performance of CFLs is not likely to improve by nearly as much. As derived from that study, Fig. 1.4 illustrates the energy consumption for incandescent, CFL and LED lamps up to the year 2015. As we proceed toward 2015, from incandescent to LED lamps, the significant drop in energy consumption (Joule/lumen-hour) is clearly visible.

LEDs play a very important role in the generation of white light. The latter can be achieved in two ways : (i) We have a fairly proportionate mixture of blue,

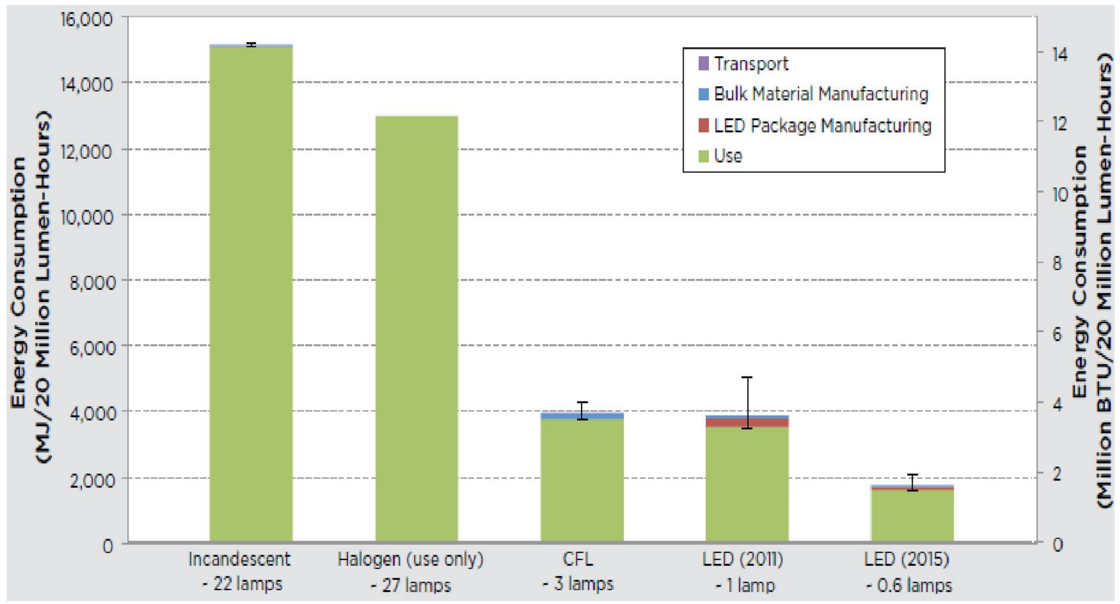

Figure 1.4 Life-cycle energy consumption for incandescent, CFL and LED lamps. The "use" phase of all three types of lamps accounted for almost 90% of the total life-cycle energy consumption, followed by manufacturing and transport.

green and red (RGB) emission to generate true white light, or ii) we can use phosphor coating to convert a relatively short-wavelength emission to a longer one with the combination giving white light. At present, most commonly used "white" LEDs use phosphors [5], dichromatic blue/green LEDs [6], CdSe/ZnS nanocrystals for conversion into red light [7], prestrained growth of InGaN wells [8], and structure-controlled GaN microfacets [9] etc. In absence of high-efficiency red light sources, they mostly convert lower wavelength visible light into amber or red emission and thus the light generated from these devices has poor color chromaticity with bluish white emission. Moreover, these devices also have low overall efficiency due to the significant conversion losses as blue or ultraviolet (UV) light is used to pump phosphor to obtain white emission. Highly efficient InAlGaP red LEDs are available in the market, but we cannot monolithically integrate it with the existing high

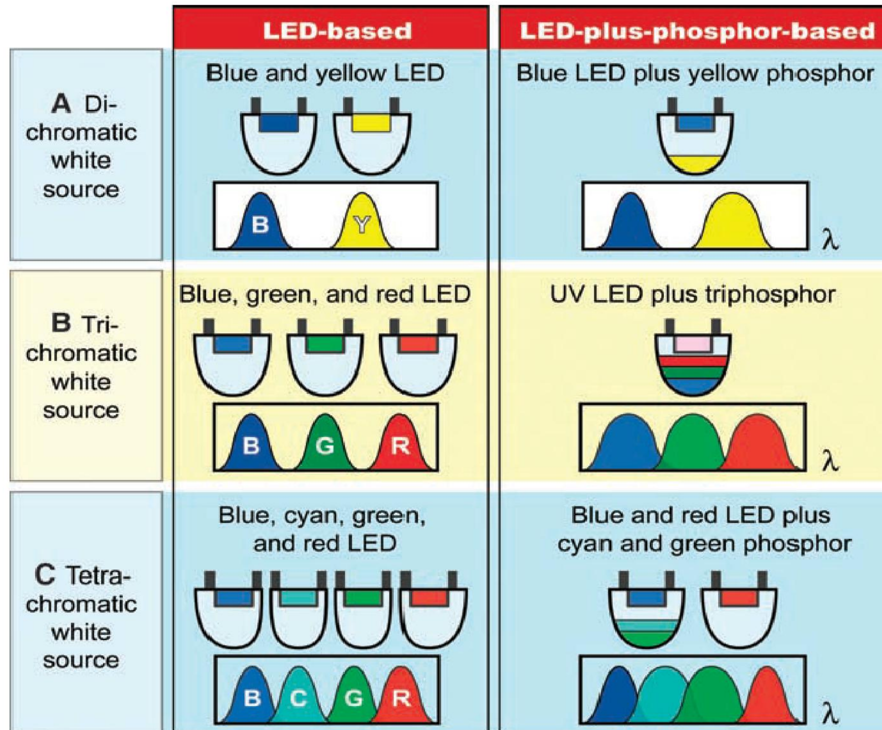

Figure 1.5 Light emitting diode (LED)-based and LED-plus-phosphor–based schemes for white light sources. Highest luminous efficiency and best color rendering index are obtained with dichromatic and tetrachromatic approaches, respectively. Trichromatic schemes can provide good color rendering and luminous efficiency [2].

efficiency blue-green nitride LED technology to collect white light from the same chip. One alternative can be to replace the phosphor coating in wavelength converter white LEDs with some other nitride structure that is capable of generating bright red light when excited with short-wavelength emission. Further, if such highly efficient nitride based red light sources can be made available, then by incorporating blue-green-red light sources in the active region, monolithic phosphor-free tunable white light sources could be realized.

Apart from nitride LEDs in solid state lighting, nitride based lasers can be used in a host of applications such as in heads up display and front lights in

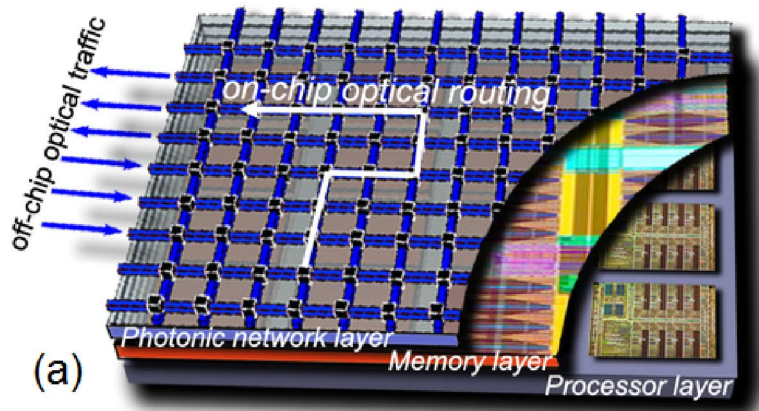

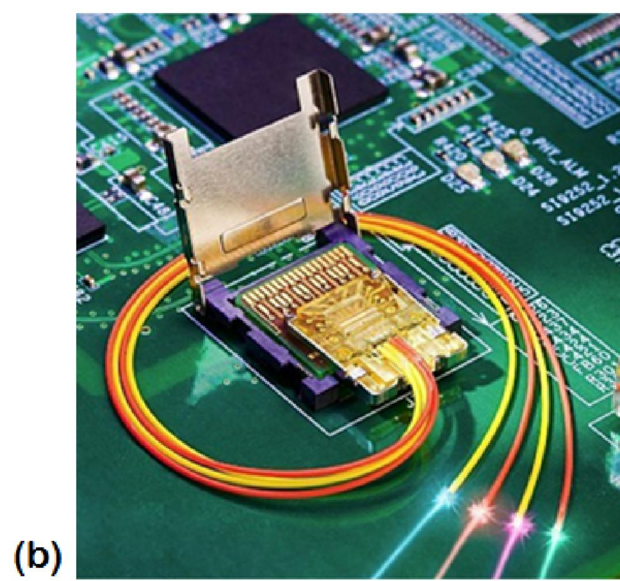

Figure 1.6 Illustration of (a) on-chip optical interconnect for data communication [11], (b) coupling of processed optical data from a chip with optical fibers for off-chip communication [12].

automobiles, pico-projectors, surgery, laser dazzlers, etc [5-9]. In the future, a potential application of monolithic nitride-based lasers on silicon substrate could be on-chip and chip-to-chip optical communications replacing present-day metal interconnects. In order to maintain the aggressive scaling of computing chips to follow Moore's law which predicts that the number of components on a chip doubles approximately every two years [10], manufacturers now focus on multi-core design

along with increasing clock speed. Due to the associated time delay and cross-talk, metal interconnect is causing a problem in this regard. A combination of electronic and photonic components on the same chip could be a promising solution where electronic components can process the data and optical elements can deal with data communication. Moreover, with such a combination, the processed data from a chip can also be coupled in to an optical fiber for various applications. Having these ambitious goals in mind, substantial research is going on in the field of silicon photonics, which could be enhanced by III-nitride based lasers on silicon.

1.2 Brief History of III-Nitride Research

The first visible LEDs were demonstrated with Gallium Arsenide Phosphide (GaAsP) on a GaAs substrate in the 1960s [13]. With further development, green-emitting gallium phosphide (GaP) LEDs and yellow-emitting silicon carbide (SiC) LEDs were realized, although they were very inefficient. In 1990s, high efficiency gallium aluminum arsenide phosphide (GaAlAsP) and aluminum indium gallium phosphide (AlInGaP) LEDs were demonstrated with yellow and red emissions. While blue-emitting LEDs are an absolute necessity to make white light sources, GaAs and InP based materials cannot emit at such short wavelengths. GaN based materials, on the other hand, are suitable candidates for visible light sources. Though the research on the III-nitride based materials started in the 1970s, the inability to grow a single crystal GaN epitaxial layer and the problems with p-doping of GaN due to high residual background doping and large effective hole mass were two major obstacles for the development of nitride based solid state lighting. In late 1980s, the first single

crystal GaN was grown on lattice mismatched sapphire and SiC substrates using low temperature AlN buffer layers grown by chemical vapor deposition (CVD) [14, 15]. After that, p-type doping of GaN through Mg incorporation was demonstrated [16, 17]. *The ability to grow single crystal GaN on mismatched sapphire substrates and achieving p-doping of GaN eventually laid the foundation for the first realization of InGaN/GaN blue LEDs, which recently earned Isamu Akasaki, Hiroshi Amano and Shuji Nakamura the 2014 Nobel Prize in physics.* The first high-efficiency indium gallium nitride (InGaN) based blue-emitting LED was demonstrated by Shuji Nakamura at Nichia Corporation in 1995 [18]. Apart from a high brightness blue light source, this also opened up a window of possibility for realizing longer wavelength visible emissions in the green, amber and red wavelengths by using a higher In composition in the InGaN active region. In current commercial devices, blue LEDs are used to excite yellow phosphors to produce white light sources in solid state lighting [19]. Over the course of time, an AlGaN electron blocking layer (EBL) was introduced followed by the incorporation of InGaN quantum well active region instead of the double heterostructure which facilitated the realization of blue LEDs with high output power (1.5 mW) [20]. OSRAM, Phillips and Nichia have mastered the use of GaN-on-sapphire for their LED technology, whereas Cree has developed GaN-on-SiC technology and Soraa has recently started growing GaN-on-GaN i.e. free standing GaN substrates for their commercial LEDs. Nakamura et. al. demonstrated the first successful blue-emitting InGaN-based lasers in 1996 [21]. Achieving lasing at longer wavelengths became difficult due to the problems associated with higher In incorporation in the InGaN active region required for obtaining longer wavelength

emissions such as high defect density, In inhomogeneity and large strain induced polarization field. The first InGaN/GaN quantum well (QW) based green-emitting laser was reported in March, 2009 [22].

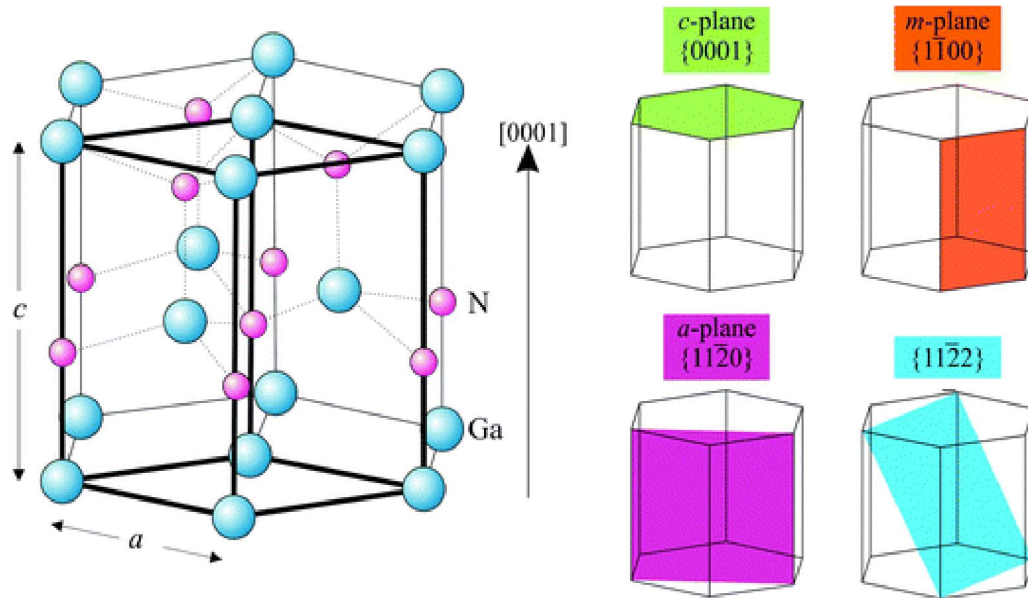

Figure 1.7 Wurtzite GaN crystal lattice structure illustrating c-plane {0001}(polar), m-plane {1-100}(non-polar), a-plane {11-20}(non-polar), and {11-22} semipolar planes [23].

1.3 Challenges in III-Nitride Research

1.3.1 Large Polarization Field and Related Effects

Figure 1.7 shows the wurtzite crystal structure of GaN having alternating planes of Ga and N atoms and illustrates the polar c-plane and other non-polar and semi-polar growth planes for nitride epitaxy. Compared with other conventional semiconductors, the spontaneous polarization field in nitride semiconductors is much stronger due to the high electronegativity of the nitrogen atoms in the crystal lattice. During heteroepitaxy, polarization charges accumulate at the interface between layers

resulting in a spontaneous field as high as 2MV/cm in AlGaN/GaN heterointerfaces [24]. However, this strong polarization field has applications in high performance devices such as high electron mobility transistors for creating a high mobility two dimensional electron gas. The other kind of polarization observed in nitride heterostructure is piezoelectric polarization. This field is formed during the epitaxy of lattice mismatched layers resulting in large strain at the heterointerface which causes the displacement of anion sub-lattice with respect to the cation sub-lattice. In particular, in visible Ga(In)N LEDs and lasers, piezoelectric polarization field, being stronger than the spontaneous polarization field, plays a more significant role on the device performances. Figure 1.8 shows the band bending associated with the large polarization fields in planar InGaN quantum well (QW) LEDs with AlGaN electron

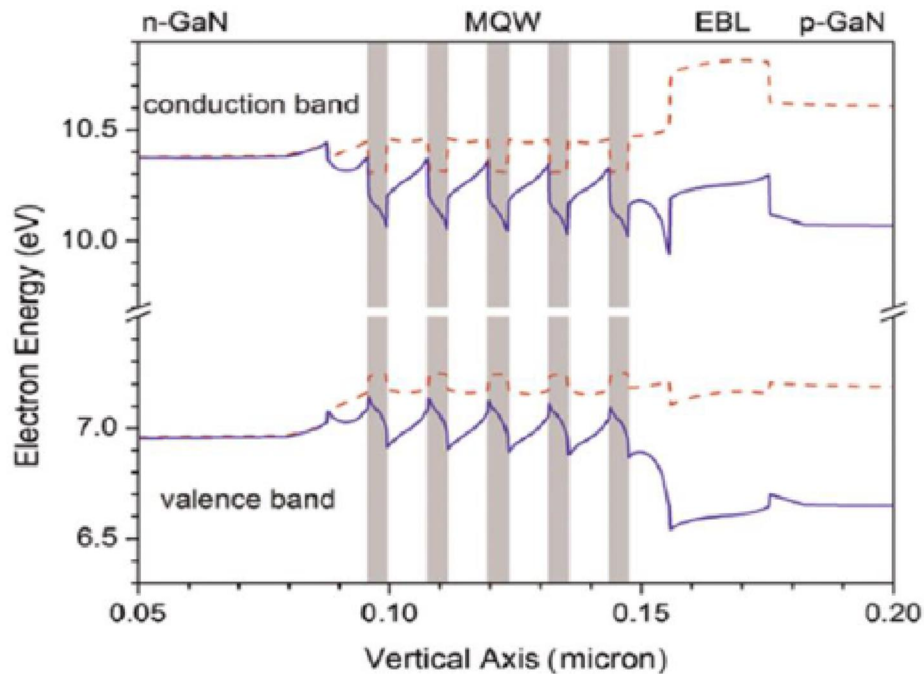

Figure 1.8 Simulated band diagram of InGaN/GaN multi quantum well LEDs (a) with (solid line) and (b) without (dashed line) polarization fields [24].

blocking layer (EBL) that causes the reduction of potential barrier to electrons on the p-GaN side and pulls down the AlGaN EBL making it less efficient for blocking electrons. As a result, carrier leakage from the active region increases a potential source of efficiency droop. Additionally, due to the band bending, triangular potential wells are formed in conduction and valence bands resulting in poor electron-hole wavefunction overlap in the active region and thereby low radiative efficiency. This becomes a severe problem, especially in InGaN QWs with high In composition, one reason why growing red-emitting LEDs with planar InGaN QWs with high radiative efficiency is still found difficult. With increasing injection currents in InGaN LEDs and lasers, these polarization fields are screened by the injected carriers, leading to flat-bands with an associated blue-shift in the emission peak. This phenomena, known as the quantum confined Stark effect (QCSE), is responsible for the large shift in peak wavelengths for visible InGaN LEDs and lasers. Another adverse effect of the band bending resulting from large polarization fields in the nitrides is a non-uniform hole distribution across the multiple InGaN QWs with the first few QWs close to the p-GaN getting filled with holes first before holes can reach the subsequent QW layers. Due to the detrimental effects of the large polarization field and the related effects on device performance, efforts have been made to grow blue- and green-emitting LEDs and lasers on non-polar and semi-polar GaN substrates, from which were demonstrated reduced efficiency droop in LEDs and longer emission wavelengths in lasers. However, the LEDs grown on non-polar or semi-polar planes have poor peak radiative efficiency and the lasers grown on those planes have very large threshold current densities [25-27]. Other schemes that have been adopted to reduce the

polarization fields include a double heterostructure design replacing strained InGaN/GaN QWs [28], epitaxy of lattice matched InGaN/InAlGaN QWs [29] and the application of external tensile strain on the substrates [30], etc. Our group has extensively used InGaN/GaN disks-in-nanowires as gain media in LEDs and lasers to reduce the polarization fields in the nitride-based devices, which will be discussed in subsequent chapters in detail.

1.3.2 Availability of Substrates

GaN based LEDs need to be improved further in terms of luminous efficacy and they need to be grown on large wafers with high yield in order to reduce the per unit cost to make this alternative solid state lighting technology affordable for everyday applications. To achieve this goal, large-size single crystal GaN wafers or foreign wafers lattice matched to the GaN crystal, need to be made readily available. Ideally, nitride-based LEDs should be grown on GaN substrates. While GaN melts above 2500°C and at a pressure higher than 4.5GPa, at low pressure, it decomposes

Table 1.1 Substrates used for the growth of III-nitride LEDs and lasers.

Substrate	Lattice constant (Å)	Lattice mismatch to GaN (%)	Thermal conductivity ($Wm^{-1}K^{-1}$)
GaN	3.189	0	130
Silicon	5.43	17	3.59
Sapphire	2.747	13	7.5
6H SiC	3.081	3.4	490

into Ga and N_2 before melting. Therefore, traditional crystal growth techniques such

as the floating zone technique, which are used for Si and GaAs, are not applicable for GaN crystal growth. Substrates, currently used for GaN growth, including sapphire, SiC, GaN and Si, are listed in Table 1.1. Because of the uniqueness and difficulty of single crystal GaN growth technology, it is not readily available in large-size wafers, and even though it is available in small-size wafers, it is very expensive compared to large-size Si and GaAs substrates. Hence, large GaN crystals are usually grown on lattice mismatched foreign substrates such as sapphire, SiC and Si, which leads to the formation of threading dislocation defects with a typical areal density of 10^7-10^{10} cm^{-2} at GaN/substrate interface. These dislocation defects propagate through the epitaxial layers in the growth direction and act as nonradiative recombination centers for the carriers causing heating of the device and subsequently carrier leakage resulting in the degradation of nitride based LED and laser efficiency.

1.3.3 Green Gap and Efficiency Droop

(Ga,Al)InP-based LEDs emit in the red wavelengths, but it is not possible to cover the entire visible spectrum (blue-green-red) with this material as can be seen in Fig. 1.9. On the other hand, by varying the In composition in Ga(In)N LEDs, any emission wavelength across the visible spectrum can be achieved. The very well-known problem in solid state visible spectrum lighting is the so-called “green gap” (Fig. 1.9) which results from the fact that the radiative efficiency of planar InGaN active region decreases abruptly with higher In composition as the nitride LEDs proceed towards green emission wavelengths and other than the nitrides, there is no other material that can provide high efficiency blue and green emissions. One of the

major problems of planar nitride based LEDs with emission wavelengths λ > 520 nm at high injection currents is the large drop in device efficiency, which is known as

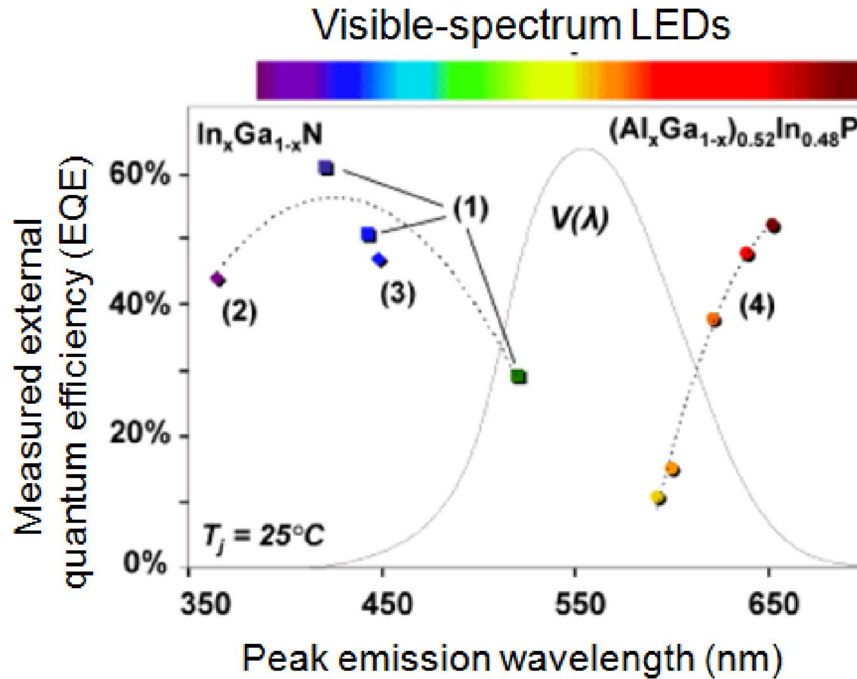

Figure 1.9 Measured external quantum efficiency (EQE) of high performance LEDs emitting in the visible spectrum [31].

"efficiency droop". Significant research has been devoted to understanding the origin of this problem and to find out a way how to solve it. Nonradiative Auger recombination [32], self-heating of device [33] and carrier leakage from the quantum wells [34] can contribute to the drop in efficiency at high injection levels. The large polarization fields in wurtzite c-plane polar Ga(In)N materials may also be responsible for the observed efficiency droop. Phillips Lumileds first proposed that Auger recombination is the root cause behind the large efficiency droop in nitride LEDs [35], which was later backed by other groups [36] including ours [37] through varying experimentation. Carrier leakage from the active region is held accountable

for this efficiency droop by some other groups [38, 39]. Self-heating of the device on the other hand could not be responsible as a possible reason, since efficiency droop was found to be independent of device surrounding temperature [40].

1.3.4 Problems with p-doping

One of the major drawbacks in the early days of research into visible solid state lighting was the p-doping of GaN, which was a major roadblock for achieving high performance visible LEDs and lasers. In both molecular beam epitaxy (MBE) and metal organic chemical vapor deposition (MOCVD) grown techniques, as-grown GaN epitaxial layers were found to be unintentionally n-doped due to the presence of oxygen impurities and nitrogen vacancies in the epilayers that act as compensating donors. Though initially tremendous progress in GaN crystal growth was achieved by the MOCVD techniques, incorporation of hydrogen atoms as interstitial defects in the crystal during growth impeded the activation of Mg acceptors by forming a Mg-H complex. A post-growth annealing step demonstrated by Nakamura *et al.* [41] solved the problem of MOCVD growth of p-GaN. Based on this discovery, he eventually succeeded to demonstrate the first GaN based LEDs and lasers. Still the p-doping level in most MOCVD grown GaN epi-layers is poor (~ $10^{17}cm^{-3}$) due to the high activation energy of Mg acceptor levels (~200 meV). In the hydrogen-free environment of plasma assisted molecular beam epitaxy (PA-MBE), highly p-doped GaN epi-layers ($2x10^{18}cm^{-3}$) was demonstrated by our group [42] in 2010 under nitrogen rich conditions at low substrate temperatures. In MBE growth, electrically active hole concentrations in GaN have been limited to low 10^{18} cm^{-3} range with a

doping efficiency of ~5% due to the high activation energy of Mg acceptor level, lower solubility, and compensation from defects present in the structure. Recently there is report of enhanced doping efficiency as high as ~10% in GaN by metal modulation epitaxy, where the hole concentration was obtained to be ~1.5×10^{19} cm^{-3} by periodically modulating Ga atoms and Mg dopants [43]. There is scope for further investigation and to increase the doping levels of p-GaN epilayers.

1.3.5 Issues with Lasing Threshold and Emission Wavelength in Ga(In)N Lasers

Since the demonstration of first blue-emitting nitride-based laser in 1995, substantial research has been going on to increase the lasing wavelength to green and beyond. In 2009, the first green-emitting InGaN QW lasers were reported, though with very large threshold current densities [44]. Several factors contribute to the high lasing threshold of nitride-based lasers with increasing emission wavelengths. First, in order to increase the lasing emission wavelength, higher In composition is required in the InGaN QW active region. With higher In incorporation, large strain induced polarization fields, In inhomogeneities (clustering) [45] and other related defects are observed in the active region reducing the radiative efficiency of the gain medium. Increasing the indium composition in the InGaN QWs to obtain longer emission wavelengths lead to large piezoelectric polarization fields that cause poor electron-hole wavefunction overlap, i.e. low optical gain, and carrier leakage from the active region. Moreover, to incorporate such high indium in the wells, the substrate temperature during QW growth is reduced substantially, resulting in rough

morphology [46] and In alloy fluctuations in the wells due to poor growth kinetics. These effects lead to broadening of the spontaneous emission spectrum which subsequently decreases the peak modal gain needed to surmount the losses and reach the lasing condition.

1.4 Use of InGaN/GaN Disk-in-Nanowires as Gain Media

A major challenge faced by the nitride research community is the unavailability of large-area GaN substrates for the epitaxy of nitride heterostructures at reasonable costs, as mentioned in section 1.3.2. As an alternative, nitride epitaxy is being performed on lattice mismatched SiC and sapphire templates to avoid using the expensive free standing GaN substrates, which results in the formation of threading dislocation defects at the GaN/template interface with an areal density of ~10^7-10^{10}cm^{-2} that can propagate into the active region. These defects can act as nonradiative recombination centers for carriers, therefore decreasing the radiative efficiency of nitride-based LEDs and lasers. Self-assembled Ga(In)N nanowires can be grown on substantially less expensive (001) Si substrates along the c-axis by molecular beam epitaxy (MBE). While growing the GaN nanowires, thin regions of InGaN (~2-3 nm), sandwiched between GaN barriers on both sides, can be incorporated along the c-axis. These are commonly called as InGaN disks-in-GaN-nanowires (DNW) due to their shape and behave as quantum wells in GaN nanowires by providing spatial confinement of carriers along the growth direction. In this dissertation, our approach revolves around these InGaN/GaN disks-in-nanowires (DNW) as the active medium for making LEDs and lasers on silicon. Typically, the

nanowires have an average diameter of ~60-80 nm and they can be as long as several micrometers. There is almost no epitaxial constraint in the growth of wurtzite GaN nanowires on silicon substrates unlike the heteroepitaxy of planar GaN on sapphire or SiC substrates, which will be discussed in detail in chapter II. This reduces the number of threading dislocations at GaN/silicon interface to a great extent. The fewer threading dislocations that generate at GaN/silicon boundary usually bend towards the sidewall of the nanowires and therefore do not propagate into the active region [47]. From detailed structural characterization by our and other research groups, it is found that these nanowires are nearly defect-free, compared to planar GaN grown on lattice mismatched substrates [48-53]. To estimate the extent of defects in the Ga(In)N nanowires, we have performed some measurements on them. Measured Auger coefficient C_0, at low excitation, is 4.1×10^{-33} cm^6s^{-1} in the DNW samples (λ=500nm), which is in reasonably good agreement with theoretical predictions for InGaN alloy semiconductors [54]. These values are much smaller than the earlier measured values of ~10^{-30}-10^{-31} cm^6s^{-1} in InGaN/GaN quantum wells and bulk InGaN samples that have a defect density of 10^7-10^{10} cm^{-2}. Thus, a defect-assisted Auger recombination process might be operative in planar Ga(In)N materials grown on lattice mismatched substrates which account for the large value of C_0. We have also measured the Schottky barrier height of a Pt contact on InGaN nanowires (Pt–$In_xGa_{1-x}N$ ($0 \leq x \leq 0.5$)) with different In compositions, which varies from 1.4eV (GaN) to 0.44eV ($In_{0.5}Ga_{0.5}N$) and this data agrees well with the ideal barrier heights in the Schottky limit [55]. Unlike planar Ga(In)N grown on lattice mismatched substrates, the consistency of these measured values with theoretical calculations obtained from

Ga(In)N nanowires on silicon implies that the nanowires are relatively free of extended defects such as threading dislocations, stacking faults, etc. as compared to epitaxial GaN on SiC or sapphire substrates.

In addition to the defect-free nitride material useful for making visible LEDs and lasers, InGaN nanowires or InGaN/GaN disk-in-nanowires on silicon also provide the advantage of emission wavelength tunability. By varying the indium composition in the InGaN disks, nanowire LEDs and lasers on silicon with any emission color over the entire visible spectrum and even in the near-infrared should be possible. Achieving emission at longer wavelength ($\lambda > 600$ nm) with high radiative efficiency by planar InGaN quantum wells grown on polar GaN substrates poses some serious challenges including In inhomogeneity or clustering, high defect density due to large strain at the heterointerface, strong strain-induced polarization field, etc [56, 57]. The large polarization field also results in poor electron-hole wavefunction overlap in the active region, thereby reducing the radiative efficiency of the devices [58]. In case of InGaN QW lasers on non-polar or semi-polar GaN substrates, this polarization field is minimized, but there are problems with limited In incorporation and stacking fault formation in the QWs for emission wavelengths higher than 500 nm [59]. On the other hand, due to their large surface-to-volume ratio (SVR) and radial strain relaxation during epitaxy, the strain induced polarization fields in the nanowires and InGaN disks are significantly smaller than those in planar InGaN quantum wells. Hence, defect-free Ga(In)N/GaN disk-in-nanowires with reduced strain induced polarization field are promising as the gain medium for making LEDs and lasers with high radiative efficiency.

1.5 Dissertation Overview

This dissertation focuses on the optimization of the self-assembled growth and improving the radiative efficiency of InGaN/GaN disks-in-nanowire by MBE. The optimized disks were used as the active medium for making monolithic visible nanowire array LEDs and lasers on (001) silicon substrates. Additionally, coalescence of the nanowires during their self-organized epitaxy is discussed in the context of an optimum range of areal densities for high performance nanowire based devices.

Chapter II discusses the growth of self-assembled blue, green and red-emitting InGaN/GaN disks-in-nanowires on (001) silicon by molecular beam epitaxy (MBE). By varying the growth conditions and by passivating the nanowire surface, the radiative efficiency of the InGaN disks have been optimized. Temperature dependent and time-resolved photoluminescence measurements were performed on as-grown and passivated disks-in-nanowires to study carrier lifetimes in them. Detailed structural characterizations and elemental analysis were performed on the nanowires to investigate the crystal quality of the material and alloy compositions in the disks.

Growth, fabrication and characteristics of nanowire array visible LEDs on (001) silicon are reported in chapter III. External quantum efficiency (EQE) (in arbitrary units) at room temperature was measured as a function of injection current density to determine the peak efficiency of the device and the efficiency drop at high injection current compared to the peak efficiency. Shift in the electroluminescence (EL) peak with increasing injection current density was investigated, from which the polarization field in the InGaN disks, was estimated and compared with that in planar InGaN quantum wells. To increase light output from the device, nanowire LEDs,

grown on a silicon substrate, were transferred to a metal reflector, since silicon absorbs the light emitting from the disks.

In the self-assembled growth of nanowires with high areal density, coalescence can take place between two or more misaligned nanowires or nanowires with increasing diameter during epitaxy. The degree of nanowire coalescence with increasing areal density and its effect on the optical properties of the nanowires is discussed in chapter IV. Structural characterization of the nanowires, grown with high areal density, was performed using high resolution transmission electron microscopy (HRTEM) imaging to investigate the nature of the defects formed near the coalescing boundaries. The effects of coalescence on the optical properties of the InGaN disk active region was studied by measuring their radiative efficiency as a function of nanowire densities. To understand how this coalescence affects the performance of nanowire LEDs, devices were fabricated with different areal densities keeping other growth conditions the same. The peak efficiency and near-field images of the electroluminescence from the LEDs were compared. Transient capacitance measurements were performed on planar GaN and GaN nanowire n^+p diodes to compare and characterize the deep level traps in these structures. Nanowire n^+p diodes were grown with similar set of areal densities as those of the LEDs.

White LEDs, which are at the center of solid state lighting, are mostly phosphor-converted. Due to some major disadvantages of the phosphor-converted white LEDs, a white nanowire LED, based on direct electrical injection, or a monolithic semiconductor-based wavelength converter quantum dot (QD) white LED can be a desirable alternative. In chapter V, we demonstrate and characterize

electrically injected tunable InGaN/GaN disk-in-nanowire white LEDs on (001) silicon introducing blue, green and red-emitting InGaN disks in the active region. We have also reported the characteristics of phosphor-free self-organized InGaN/GaN QD wavelength converter white LEDs on c-plane GaN-on-sapphire substrates. The exciting quantum dots were blue-emitting, in which electrically injected carriers recombine, and the converter dots were red-emitting. Stability of correlated color temperatures of white emission with injection currents was studied for these LEDs. Tunability of white emission was investigated by changing the number and emission wavelengths of the disks in the nanowire LEDs and those of the exciting and converter dots in the wavelength converter QD devices.

A suitable monolithic electrically injected nitride laser on (001) silicon can have a host of applications as visible lasers on less expensive silicon substrates and in silicon photonics when emitting in the near-IR wavelengths. The first monolithic electrically injected edge-emitting nanowire array lasers (green (λ=533nm) and red (λ=610nm)) on (001) silicon are demonstrated in chapter VI. Finite difference time domain (FDTD) simulation and transmission measurements were done on the nanowire waveguides to study the propagation of light in them. DC and dynamic characteristics of the green and red-emitting nanowire lasers have been investigated in detail. Nanowire lasers on silicon have demonstrated potential for superior performance in terms of threshold current density, differential gain, temperature coefficient and small signal modulation bandwidth compared with planar QW-based devices. Characteristics of the green and red-emitting Ga(In)N nanowire lasers are compared with those of planar green InGaN quantum well lasers and conventional

InAlGaP based red lasers.

Finally, a brief summary on the work done in this dissertation is presented in chapter VII and suggestions for future work are outlined.

Chapter II

Growth and Characterization of Self-Assembled InGaN/GaN Disk-in-Nanowires on (001) Silicon by Plasma-Assisted Molecular Beam Epitaxy (MBE)

2.1 Introduction

III-nitride based nanowires and quantum-confined heterostructures have emerged as a promising technology base for the development of visible light emitting diodes (LEDs) and lasers [60-62]. Ga(In)N nanowires grown on (001) silicon by molecular beam epitaxy (MBE) are relatively free of extended defects compared to planar GaN grown on foreign substrates [48-53]. The nanowire geometry prevents the propagation of threading dislocations into the active region of the heterostructure because the free surface at the nanowire sidewalls allows for the elastic relaxation of the strain [63]. Therefore, threading dislocations generated at nanowire/silicon interface are expected to bend toward the sidewalls near the bottom of the nanowires (NWs) [47]. Auger coefficients measured in InGaN/GaN disks-in-nanowires are ~2-3 orders of magnitude smaller than those measured in heteroepitaxial bulk materials [54]. This is important in the context of LED and laser efficiency at high injection currents. Achieving emission at longer wavelengths (green and beyond) with planar InGaN quantum wells (QWs) with high radiative efficiency is difficult. This is due to

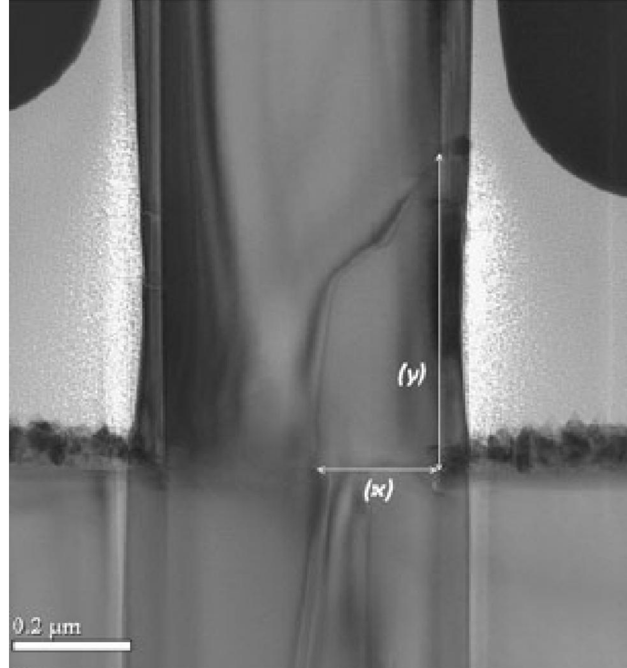

Figure 2.1 Cross-sectional transmission electron micrograph (XTEM) showing the bending of threading dislocations towards the nanowire sidewall [47].

the strong polarization field and associated quantum-confined Stark effect (QCSE) [58], the presence of compositional inhomogeneities in the ternary alloys with high In composition [56, 57] and an increasing rate of non-radiative recombination due to the lack of confinement of carriers in the in-plane direction in the wells. It has been reported that the internal quantum efficiency (IQE), η_{IQE}, of planar quantum wells decreases with an increase of emission wavelength at a rate of ~ 0.6-0.7% per nanometer [64]. In contrast, Ga(In)N nanowires and InGaN/GaN disks-in-nanowires (DNW) have reduced strain-induced polarization field even with high In compositions. This is due to the radial strain relaxation during their epitaxy resulting from their large surface-to-volume ratio. As a consequence, electron-hole wavefunction overlap is better and radiative lifetimes are smaller in the disks [65]. Accessibility to the longer wavelengths, such as 600 nm and beyond, could then very

well emerge as the most useful attribute of nanowire heterostructures in the context of solid state lighting.

Current white light sources in solid state lighting require the use of rare-earth doped phosphors, e.g. for the conversion of blue light to the yellow-red spectral range [19, 66-69]. Such conversion is inevitably accompanied by a variety of losses and is limited by long-term reliability [64, 70-72]. Combining multiple colors with the same material system, either as direct emitters (R-G-Y-B) or as a combination of internal converter and emitter, is an attractive alternative. InGaN ternary alloys with different In compositions cover the entire visible range in bandgap from blue to red emission. Therefore, they could in principle, provide a white light source with any desired color coordinates and color temperature [18, 61, 73, 74]. Increasing the In composition in the InGaN disks in GaN nanowires further can even result in near-infrared (near-IR) emission which is important for silicon photonics. However, before these important applications can be realized, the epitaxy and optical properties of the nanowire heterostructures need to be characterized and optimized. While it has been reported that the surface recombination velocity of GaN nanowires is smaller than that of GaAs by 2 orders of magnitude [75], the injected carriers would encounter a large area of nanowire surface with a detrimental effect on the radiative efficiency [76, 77]. Due to their large surface-to-volume ratio and the presence of surface states on the nanowires, there can be substantial nonradiative recombination of carriers through these states—leading to reduced radiative efficiency. Hence, surface passivation of nanowires is likely to play a significant role in the improvement of the radiative efficiency of the Ga(In)N disks and nanowires. This chapter focuses on the growth

study of the InGaN/GaN disks-in-nanowires by MBE that can be used as active medium for making visible light sources. It also discusses their detailed optical and structural characterization required for the improvement of LED and laser performances.

2.2 Growth and Characterization of Self-Assembled GaN Nanowires on (001) Silicon

Self-assembled III-nitride nanowires were grown on (001) silicon without any foreign catalyst or self-catalyst Ga droplets by Veeco Gen II and Veeco Gen 930 plasma-assisted molecular beam epitaxy (MBE) systems (Fig. 2.2). Both MBE systems are equipped with Ga, In Al, Si and Mg effusion cells and a uni-bulb nitrogen plasma source. At the initial stage of nanowire growth, Si-N bonding is more energetically favorable than Ga-N bonding and hence Si_xN_y grows on Si. During this stage, Ga incorporation rate is very low. From the high resolution transmission electron microscope (HRTEM) imaging of the Si/GaN interface, as shown in Fig. 2.3, usually a thin (~2nm) amorphous non-uniform Si_xN_y layer was observed by us and other groups [47, 78-80] between GaN nanowire and Si substrate. The formation of this thin amorphous Si_xN_y layer mainly removes the epitaxial requirement from the growth of wurtzite GaN nanowires on (001) Si substrates. The stress field generated on the Si_xN_y layer helps in the formation of the initial GaN clusters and nanowire growth then proceeds with large Ga incorporation at a substrate temperature of 800^oC under nitrogen rich condition. The Ga flux is maintained at $1.65x10^{-7}$ Torr, and the nitrogen flux is typically 1 sccm. As depicted in Fig. 2.4, there are three adatom paths

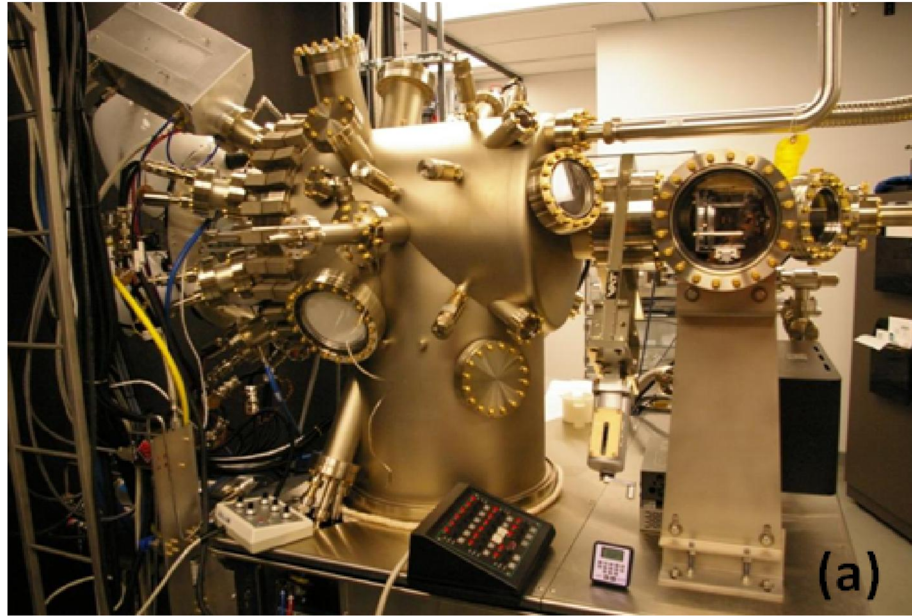

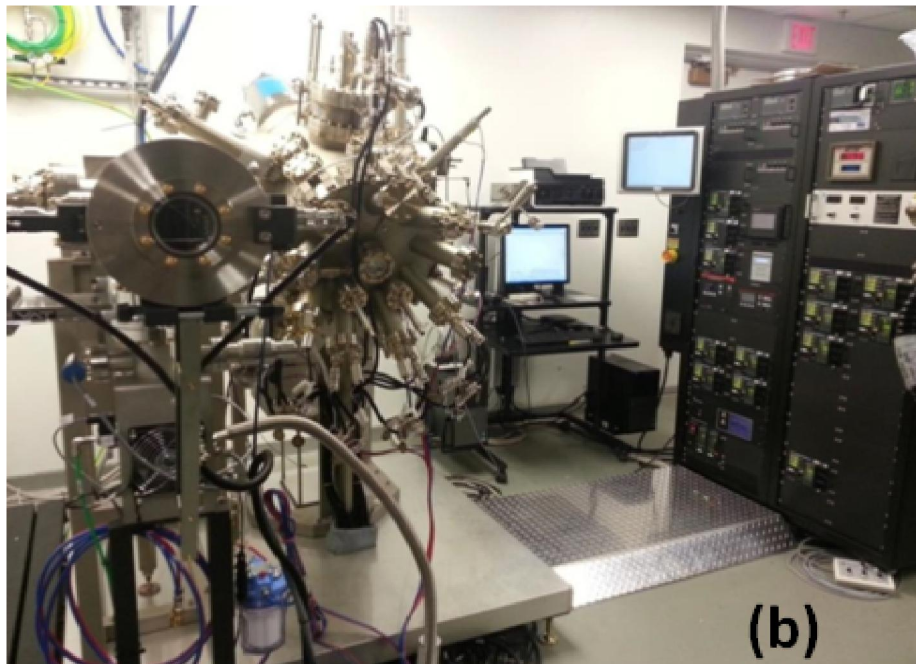

Figure 2.2 RF plasma assisted (a) Veeco Gen II and (b) Veeco Gen 930 molecular beam epitaxy (MBE) systems in our lab.

that contribute to nanowire growth, together with their desorption : i) adatoms impinge on the top surface of NWs, ii) adatoms that impinge on the silicon diffuse towards the foot of nanowires and cross the energy-barrier between Si and GaN and

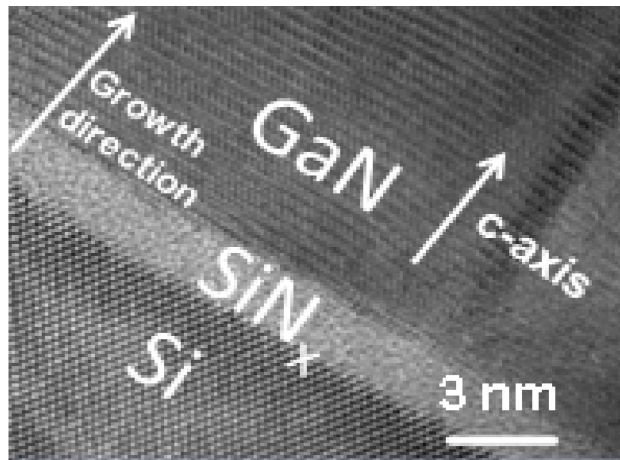

Figure 2.3 High resolution transmission electron microscopy (HRTEM) image of GaN nanowire/Si substrate interface showing the formation of thin Si_xN_y layer between GaN and Si [54].

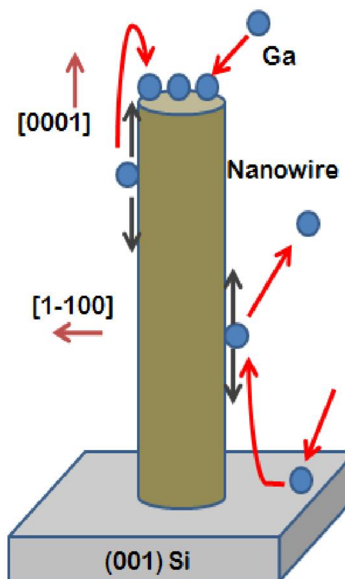

Figure 2.4 Illustration of growth mechanism of self-assembled GaN nanowires on (001) Si showing various adatom paths that contribute to nanowire growth along with their desorption.

iii) adatoms that impinge on the nanowire sidewalls. In the latter two cases, adatoms diffuse on the nanowire sidewall. Fastest growth occurs on lower energy (0001) GaN facet. Nanowire growth is carried out under nitrogen rich condition. Nitrogen rich

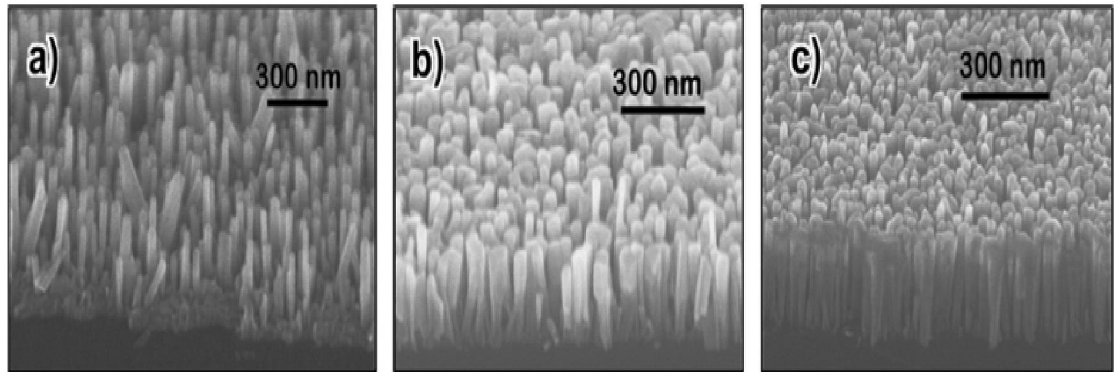

Figure 2.5 45° tilted SEM images of 250 nm long GaN nanowires grown with Ga fluxes of (a) $3x10^{-8}$, (b) $7.8x10^{-8}$, and (c) $9x10^{-8}$ Torr keeping the same nitrogen flux and otherwise identical growth conditions demonstrating different nanowire areal densities as a function of Ga flux [81].

condition slows down random movement of the adatoms on silicon initially and helps to accumulate adatoms at the nucleation centers. Top surface of nanowire (NW) acts as an efficient collector of adatoms that are driven towards it due to the lower chemical potential at the top. While diffusing on the silicon and nanowire sidewalls, desorption of adatom might take place. Most semiconductor nanowires are grown via catalyst based vapor–liquid–solid (VLS) mechanism as mentioned in literature. However, in molecular beam epitaxy (MBE), the self-assembled GaN nanowires grow due to the thermodynamically driven higher surface sticking coefficients of the group III adatoms on the c-plane nanowire tip relative to the m-plane nanowire sidewalls under certain growth conditions [82]. Therefore, group III atoms that impinge on the growing nanowire at the very tip or within a surface diffusion length of the tip will likely to incorporate there. Adatoms that impinge farther down the nanowire sidewall will mostly desorb and will not contribute to nanowire growth. The sticking coefficients on tip and sidewalls and surface diffusion length of adatoms

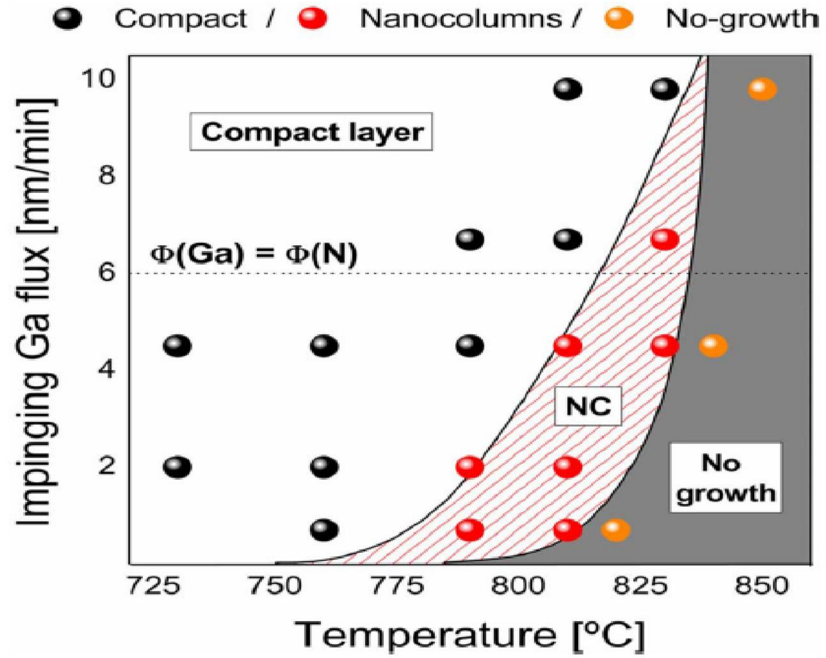

Figure 2.6 Phase diagram for GaN nanowire growth at fixed N_2 plasma conditions [83].

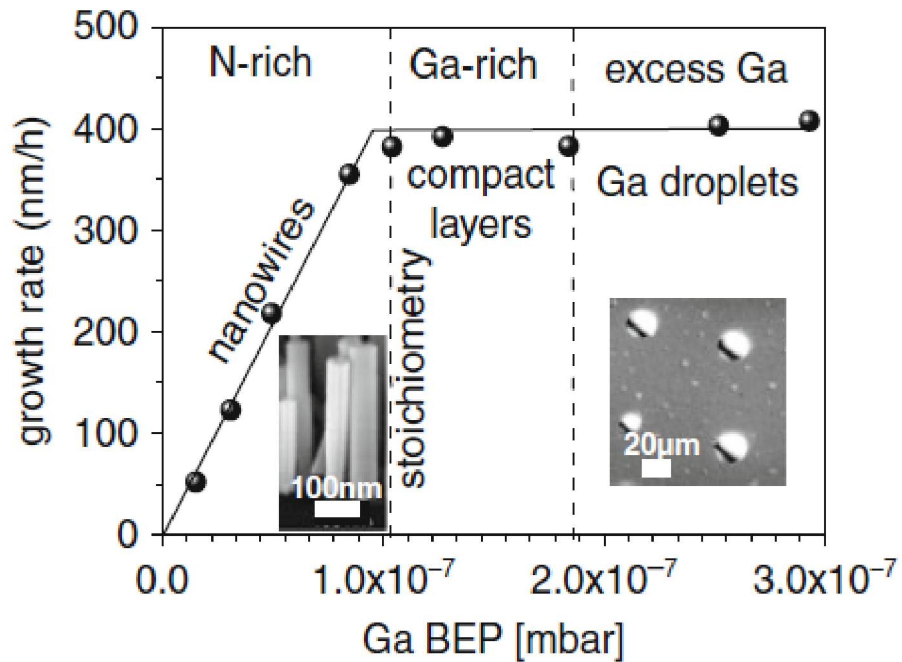

Figure 2.7 Growth rate of GaN columnar and compact layers as a function of the Ga flux [84].

depend on the growth conditions such as substrate temperature and V/III flux ratio.

Nanowires nucleate spontaneously on random places of silicon. Then they keep on growing vertically because the sticking coefficient on the polar [0001] c-plane is higher than that on the non-polar [1-100] m-plane under high substrate temperature (800–830°C) and high N_2 overpressure. We may shower Ga droplets initially on the silicon substrate before starting the nanowire growth. But they cannot act as catalytic sites since these Ga droplets are unstable under these growth conditions and undergo strong desorption and/or a quick transformation into GaN [82]. In fact, alternative means of growth using Ga self-catalyst is disproved by the absence of Ga droplets on the sample surface. This has been observed by SEM imaging even after cooling the substrate in Ga flux inside the growth chamber [82].

The lateral growth of a nanowire cannot be completely suppressed in this growth mechanism. If the nanowires are grown long enough, then there will be a temperature gradient along the growth axis with the top surface being at a lower temperature compared to the substrate temperature. This can contribute to the increasing diameter during epitaxy. Figure 2.5 shows the 45° tilted scanning electron microscope (SEM) images of self-organized GaN nanowires grown on (001) silicon substrates. The SEM image demonstrates the variation of nanowire areal density as a function of Ga flux keeping the nitrogen flux and other growth conditions constant. SEM images show that GaN NWs do not grow on preferential nucleation sites. Instead, they grow at random sites and the diameter of these nucleation sites might be different—giving rise to NWs with different diameters. By varying V/III ratio, NW diameter and areal density can be controlled as depicted in Fig. 2.5. Figure 2.6 shows the effect of substrate temperature on the growth of GaN nanowires, as investigated

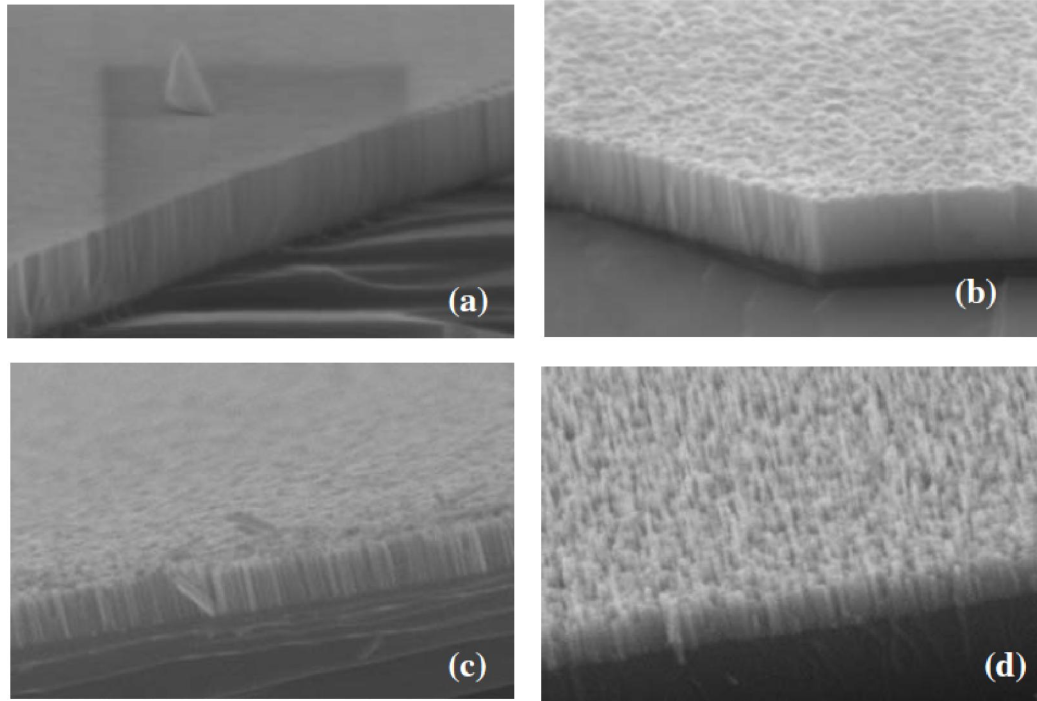

Figure 2.8 Morphology of GaN layers, grown on (111) Si, as a function of the III–V ratio (decreasing the Ga flux) grown at 690°C: a) compact flat layer, b) compact rough layer, c) coalesced nanowires, and d) isolated nanowires [85].

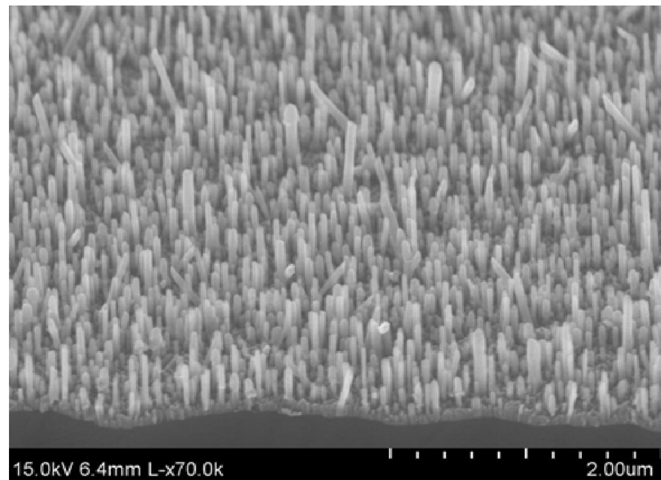

Figure 2.9 45° tilted SEM image of GaN nanowires on (001) silicon grown at a high substrate temperature of 870°C and a relatively low Ga flux of $5.6x10^{-8}$ Torr, resulting in non-uniform nanowires.

by Bertness et *al.* [83]. Only within the nanowire growth window, the density and diameter of the self-assembled nanowires can be influenced by changing the Ga flux, substrate temperature and N_2 plasma conditions. Figure 2.7 demonstrates the variation

of growth rate of GaN nanowire and GaN compact layer with Ga flux as observed by Stoica *et al.* [84]. For high Ga flux, compact layers are formed, and the excess Ga is accumulated as droplets on the substrate surface. With a gradual decrease in Ga flux

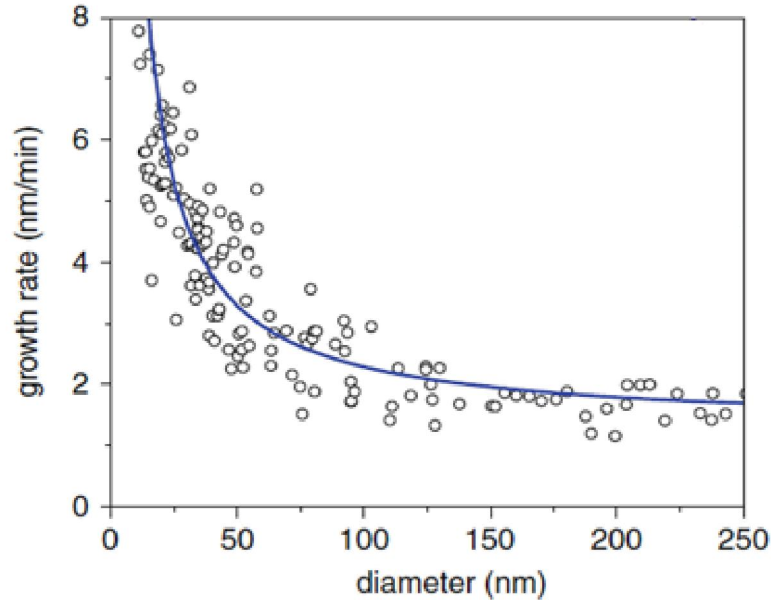

Figure 2.10 Diameter dependence of the axial growth rate of the GaN nanowires grown for long deposition time of 6 hours [84].

compact layers are still formed, but without massive Ga accumulation on the sample surface. At low Ga flux i.e. under the N-rich condition, the growth is limited by the group III flux and the nanowire growth is observed. Calleja et *al.* [85] reported similar observations for the growth of GaN nanowires under nitrogen-rich conditions, as demonstrated by the SEM images in Fig. 2.8. The nanowire growth requires optimized III–V ratio and substrate temperature. Starting from stoichiometric conditions at a given substrate temperature and a fixed nitrogen flux, Ga flux is gradually decreased until a nanocolumnar structure is obtained. Figures 2.8 (a)-(d) show the formation of a flat compact GaN layer, a compact rough GaN layer, coalesced nanowires and finally isolated nanowires, respectively, with gradual

increase in V/III ratio. Figure 2.9 shows the SEM image of GaN nanowires on (001) silicon grown at a high substrate temperature (870°C) and a low Ga flux (5.6x10^{-8} Torr). Too low III/V flux ratio and high growth temperature result in non-uniform (in height) ensemble of nanowires, which is not suitable for making planar LEDs and lasers. The correlation between the length and diameter of NWs for a long growth time of 6 hours is also reported in Ref. [84]. The vertical growth rate (length/time) estimated for individual NW using SEM images is demonstrated as a function of the nanowire diameter in Fig. 2.10. It is found that for growth times longer than 60 min, the formation of GaN clusters on Si_xN_y terminates due to the lack of space between the nanowires.

Ga(In)N nanowires can be grown on Si in two ways – as a regular array by

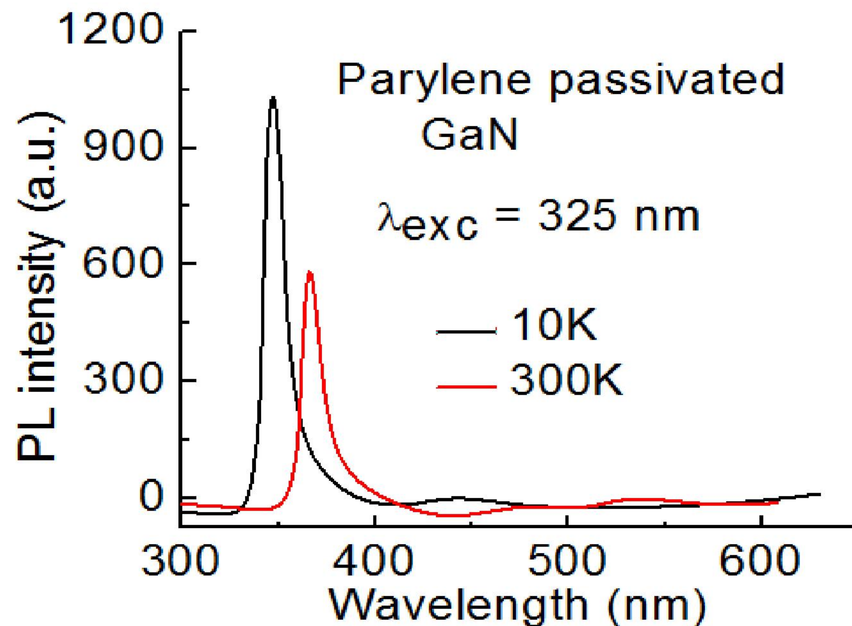

Figure 2.11 Photoluminescence (PL) spectra of growth-optimized as-grown GaN nanowires measured at 10K and 300K with 325 nm excitation.

patterning [86, 87], or as a random array by the formation of initial nucleation centers

followed by nanowire growth along the c-axis [61, 73, 74]. The latter is simpler from a technological point of view, and the nanowire density can be increased to ~(5-8)x10^{11}cm^{-2} to maximize light output. The present research concentrates entirely on self-assembled Ga(In)N nanowires for making nanowire LEDs and lasers on (001) Si. Due to the non-uniformity of Si_xN_y layer, some nanowires grow tilted—which can lead to the coalescence of nanowires. Also, as will be discussed in Chapter IV, large areal densities can lead to coalescing of the nanowires and the formation of dislocations and stacking faults [81, 88-90], which can give rise to deep level traps in the structure. This, in effect, would reduce the radiative efficiency (IQE) of the nanowires and disk-in-nanowires. We have grown GaN nanowires with an optimized areal density of 2x10^{10} cm^{-2}. Room temperature photoluminescence (PL) from the ensemble of GaN nanowires grown on (001) silicon is shown in Fig. 2.11.

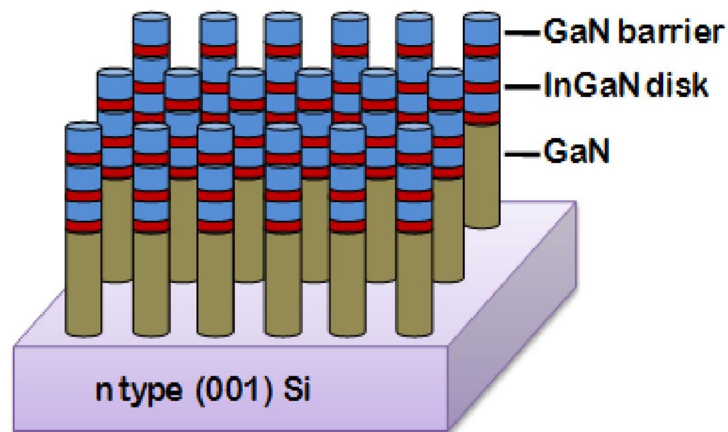

Figure 2.12 Schematic representation of InGaN/GaN disks-in-nanowire heterostructures grown on (001) silicon for the calibration of emission wavelength and optimization of the radiative efficiency of the disks.

Temperature dependent photoluminescence measurements were made at 10K and 300K with excitation at 325 nm by mounting the samples in a liquid He cryostat. This is to determine the radiative efficiency (or internal quantum efficiency-- IQE) of GaN

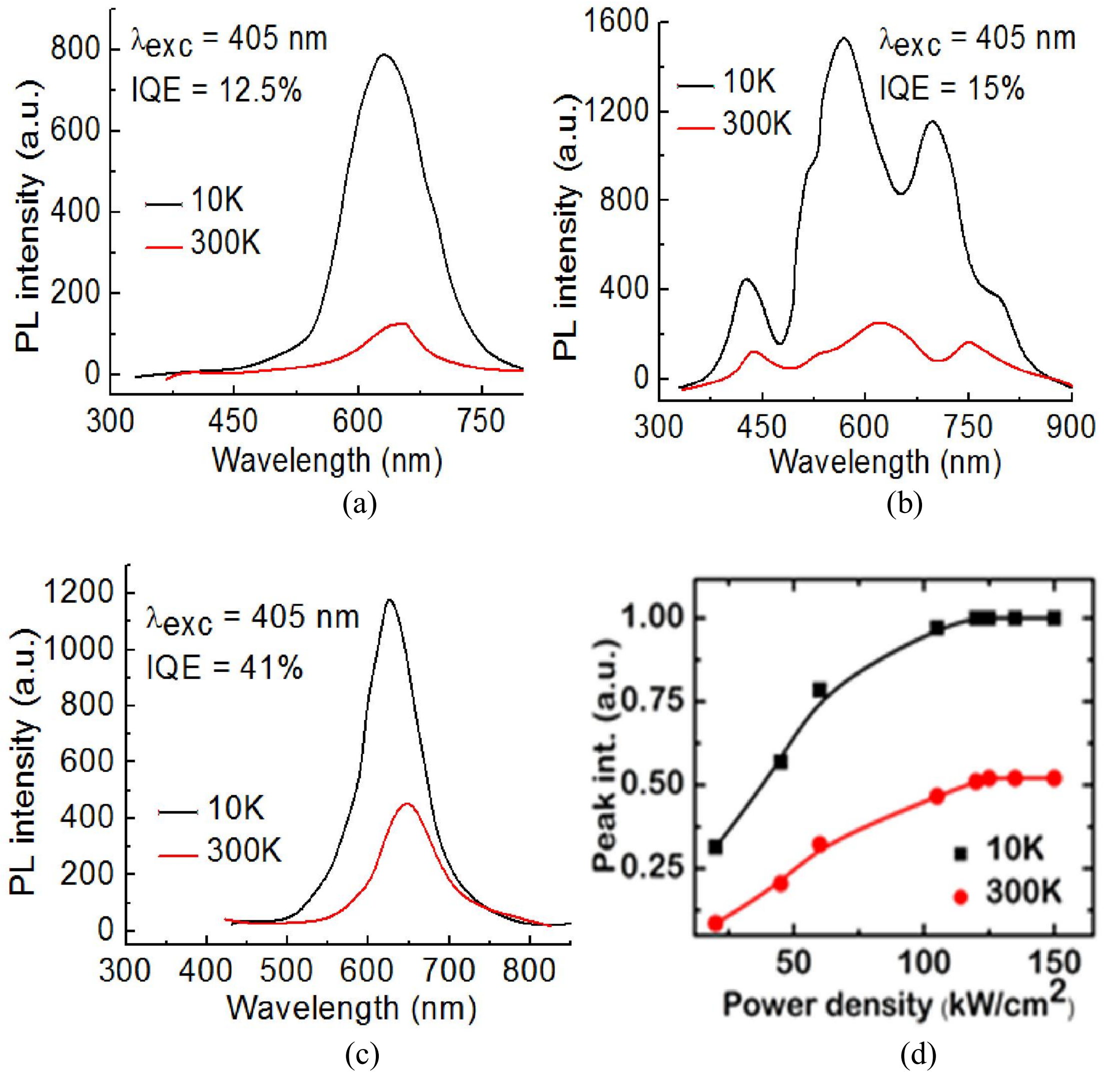

Figure 2.13 PL intensities of as-grown red disks at 10K and 300K grown at (a) 515°C, (b) 580°C and (c) 545°C; (d) variation of PL peak intensity of the optimized as-grown red DNW sample with excitation power density at 10K and 300K.

nanowires. The photoluminescence was analyzed with a high resolution Acton SpectraPro 2750 monochromator (resolution ~0.03 nm) and was detected with lock-in amplification during steady-state PL measurements. The IQE is calculated as the ratio of the maximum intensities at 300 and 10K, assuming that non-radiative recombination centers are frozen at 10K, and the quantum efficiency is approximately unity at this temperature. By optimizing the growth conditions in MBE (Ga flux =

$1.65x10^{-7}$ Torr, nitrogen plasma = 1sccm, substrate temperature = 800°C), a maximum radiative efficiency of 68% was measured for the as-grown GaN nanowires.

2.3 Growth and Characterization of Self-Organized Blue, Green and Red-Emitting InGaN/GaN Disk-in-Nanowires on (001) Silicon

InGaN/GaN disks-in-nanowires (DNW) were used as gain media for making visible LEDs and lasers with high radiative efficiency. For that, emission wavelengths (blue-green-red) of the disks were calibrated, and the growth conditions of DNW samples were optimized inside MBE to maximize their radiative efficiency.

2.3.1 Optimization of Radiative Efficiency of InGaN/GaN Disk-in-Nanowires by Temperature Dependent Photoluminescence Measurements

To optimize the growth conditions of the InGaN disks for high radiative efficiency, we have grown 300 nm GaN nanowire on (001) silicon followed by 6 InGaN disks (~2nm) separated by GaN barriers (~12 nm). Schematic illustration of such a heterostructure is shown in Fig. 2.12. After growing the GaN region at 800°C, substrate temperature is lowered to grow the InGaN/GaN DNW regions. Both substrate temperature and In-to-total group III flux ratio were varied to optimize the radiative efficiency of the InGaN disks and to extend the peak emissions to the range of 600-650 nm. Table 2.1 shows the growth conditions for the optimized InGaN disks with the highest radiative efficiency we have obtained so far. In order to go from blue

to red emission, substrate temperature needs to be reduced substantially from 630°C to 545°C. At the same time, indium flux was increased from 3.4×10^{-8} Torr to 1.3×10^{-7} Torr, and Ga flux was decreased to some extent from 1.57×10^{-7} Torr to 1.45×10^{-7} Torr, respectively. For the optimized as-grown blue, green and red-emitting InGaN disks, In-to-total group III flux ratios were 17.8%, 30.5% and 45.3%, respectively. In this section, we have reported the optimized radiative efficiency for blue (λ=430nm),

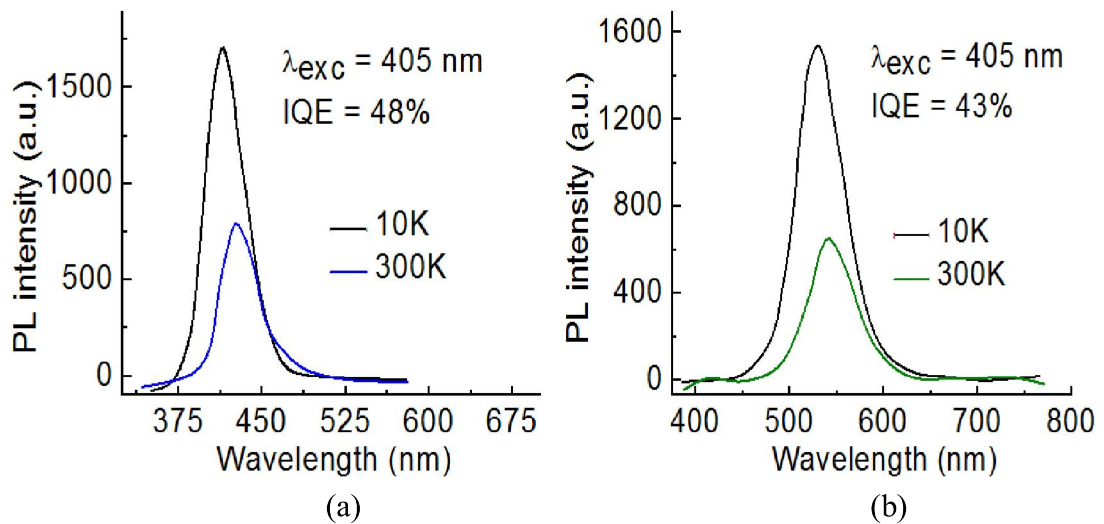

Figure 2.14 PL intensities of optimized as-grown (a) blue- and (b) green-emitting InGaN disks in GaN nanowires at 10K and 300K grown on (001) silicon.

Table 2.1 Growth conditions for the optimized InGaN disks with the highest radiative efficiency.

Growth parameters	Blue disks (λ=430 nm)	Green disks (λ=540 nm)	Red disks (λ=650 nm)
Substrate T (°C)	630	590	545
In flux (Torr)	3.4×10^{-8}	6.5×10^{-8}	1.2×10^{-7}
Ga flux (Torr)	1.57×10^{-7}	1.48×10^{-7}	1.45×10^{-7}

green (λ=540nm) and red emitting (λ= 600-650 nm) DNWs samples. Optimizing the

radiative efficiency at the longer wavelengths (i.e. red) was the most challenging of all. At first, both substrate temperature and In-to-total group III flux ratios were varied to calibrate the emission wavelength. Once we obtained the desired emission wavelength, both substrate temperature and In-to-total group III flux ratio were reduced to maximize the radiative efficiency with minimum In composition in the disks keeping the emission wavelength almost constant. But if the substrate temperature is reduced too much (~515°C), then photoluminescence (PL) intensity at room temperature becomes very weak, possibly due to the presence of growth defects

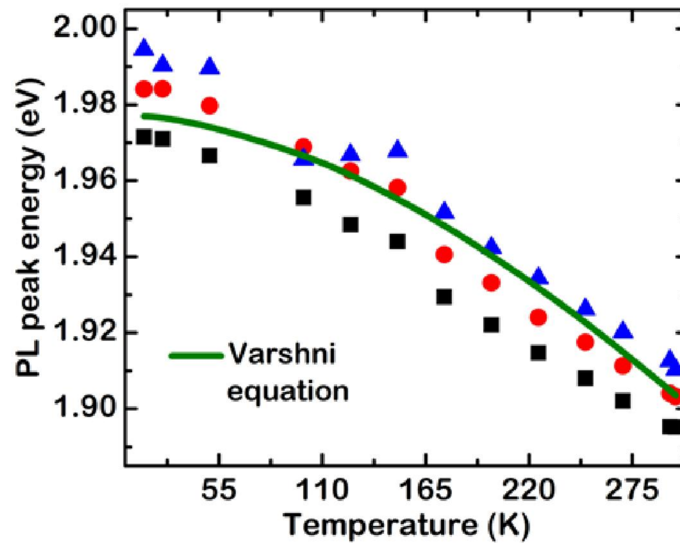

Figure 2.15 Measured variation of PL peak energy with temperature at three different points in an as-grown red-emitting DNW sample. The solid line is the calculated InGaN bandgap shift with temperature according to the Varshni equation using $\alpha = 9.39\text{x}10^{-4}\text{eVK}^{-1}$ and $\beta = 772\text{K}$.

resulting from limited adatom diffusion, as shown in Fig. 2.13(a) and radiative efficiency of the red-emitting InGaN disks drops down to 12.5%. Another way of calibration is to increase both the substrate temperature and In-to-total group III flux

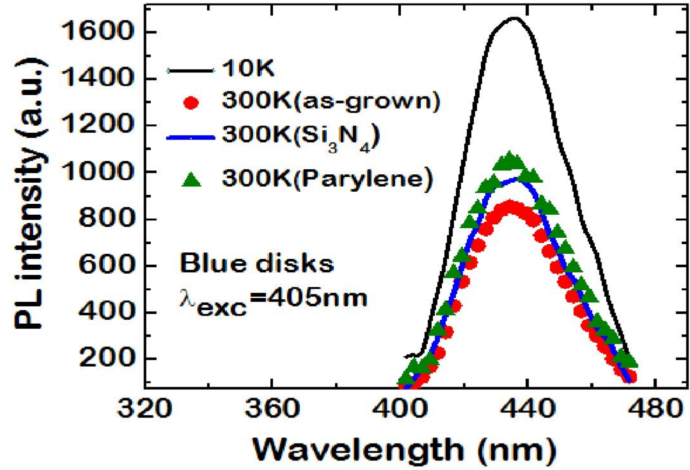

(a)

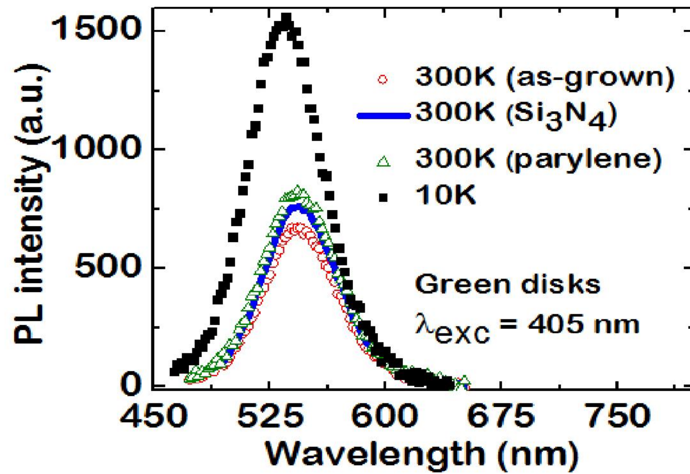

(b)

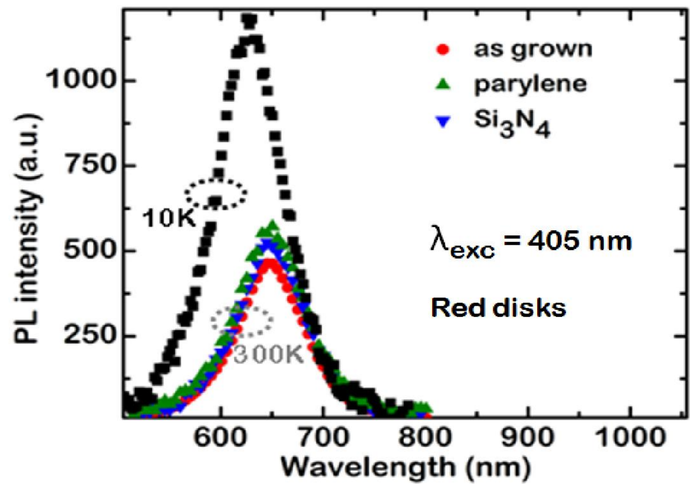

(c)

Figure 2.16 PL intensities of growth-optimized as-grown and surface passivated (with Si_3N_4 and parylene) (a) blue-, (b) green-, and (c) red-emitting InGaN disks in GaN nanowires at 10K and 300K grown on (001) silicon.

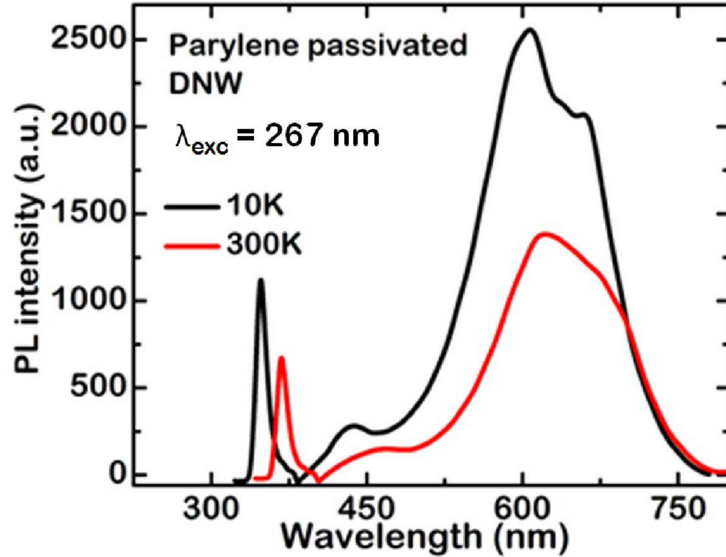

Figure 2.17 PL spectra of growth-optimized as-grown and parylene passivated red-emitting InGaN/GaN disk-in-nanowires measured at 10K and 300K with 267 nm excitation.

ratio to maximize the radiative efficiency with good crystalline quality and without changing the emission wavelength. If the substrate temperature is increased too much (~580°C), a broad PL emission having multiple peaks with low intensity is observed due to the indium phase segregation in the disks as demonstrated in Fig. 2.13(b) and the IQE is again reduced to 15%. Following these calibration methods, the highest radiative efficiency of 41% was obtained for the as-grown red disks as shown in Fig. 2.13(c) with an In-to-total group III flux ratio of ~45.3% and a substrate temperature of 545°C. Photoluminescence measurements were made with a wide range of excitation intensities to determine the radiative efficiency. Excitation of variable intensity was provided with a frequency-doubled Ti: sapphire laser (λ = 405 nm, pulse width 130 fs, repetition rate 80 MHz) focused to a ~10 μm^2 spot. The excitation is, therefore, confined within the InGaN disks for all the DNW samples (blue-green-red) and does not produce carriers in the GaN nanowire region. Data for the as-grown

red DNW sample is shown in Fig. 2.13(d), where the peak intensities measured at 10K and 300K are plotted as a function of excitation power density. At both temperatures, the peak intensity increases with excitation and then saturates due to the screening of the polarization field in the red InGaN disk with the optically excited carriers. The IQE is calculated as the ratio of the maximum intensities at 300K and 10K. For blue and green DNWs, similar methods as mentioned above have been followed to optimize the radiative efficiency and maximum radiative efficiencies of 48% and 43% have been measured for the as-grown blue- and green-emitting disks, respectively. Figures 2.14(a) and (b) depict the photoluminescence of growth-optimized as-grown blue and green-emitting disks, respectively at 10K and 300K.

2.3.2 Temperature Dependent Photoluminescence Peak Shift : Absence of S-shaped behavior

Since we had to increase the In composition in the disks to a great extent to have red emission from them, In-rich nanoclusters might have formed in the disks. The peak energy of the luminescence from the red InGaN disks measured at three different locations on a DNW sample (Fig. 2.15) exhibits a red-shift with increasing temperature. This is due to the temperature induced bandgap shrinkage and the measured data agree extremely well with bandgap energies calculated according to the Varshni relation (Eq. (2.1)) [91] with the bandgap at 10K assumed from the results of Fig. 2.13(c).

$$E_g(T) = E_g(0) - \frac{\alpha T^2}{T+\beta'} \quad (2.1)$$

Where, $E_g(0)$ is the bandgap at 10K, and α and β' are material constants. The data do

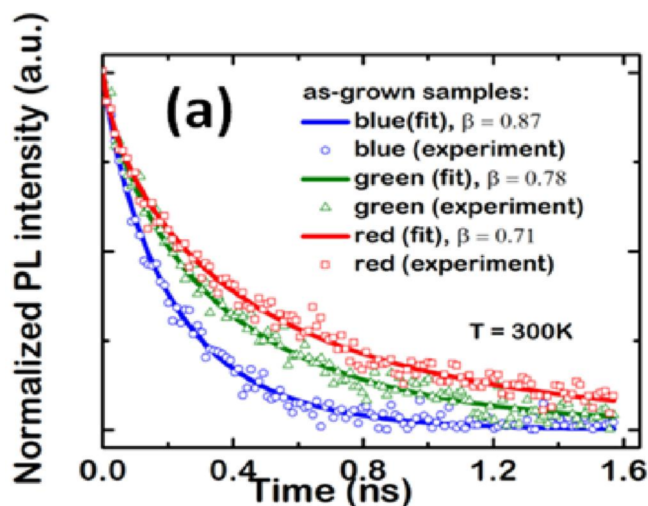

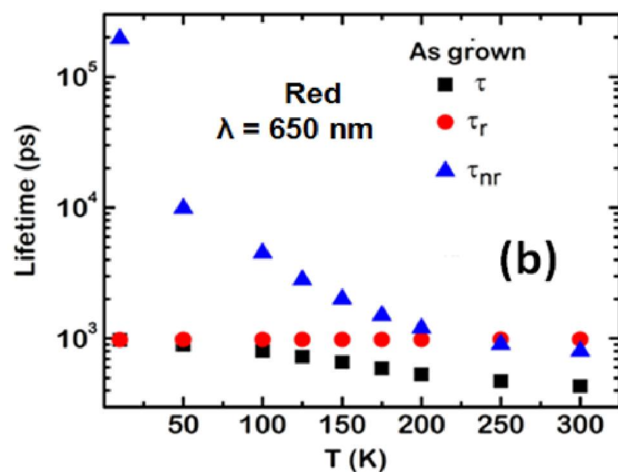

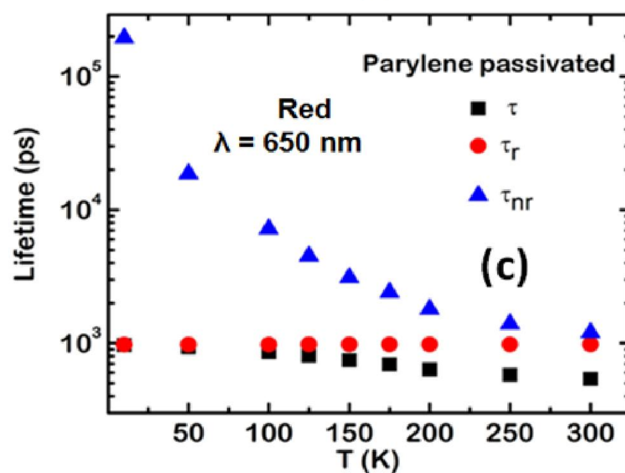

Figure 2.18 (a) Time resolved PL of as-grown DNW samples at room temperature. Solid lines show the calculated carrier lifetime in accordance with the stretched exponential model. Variation of carrier lifetimes with temperature in (b) as-grown and (b) parylene passivated red-emitting DNWs samples.

not exhibit the S-shaped variation of bandgap with temperature commonly attributed to In-rich nanoclusters formed by In phase segregation [92, 93] during the growth of the nanowires.

2.3.3 Surface Passivation of Optimized Ga(In)N Nanowires

As mentioned earlier, due to their large surface-to-volume ratio and the presence of surface states on the nanowires, non-radiative recombination of carriers through these states can have a detrimental effect on device performance reducing the radiative efficiency of the disks. Hence, by passivating these surface states on the nanowires, radiative efficiency of the growth-optimized as-grown InGaN disks can be improved further. We have passivated the nanowires with Si_3N_4 and parylene. Parylene is a transparent insulator with a dielectric constant of ~3 and we

Table 2.2 Radiative efficiencies of as-grown and passivated optimized InGaN disks.

Samples	as-grown	Si_3N_4 passivated	parylene passivated
Blue disks (λ=430 nm)	48%	52%	55%
Green disks (λ=540 nm)	43%	49%	53%
Red disks (λ=650 nm)	41%	48%	52%

have deposited parylene conformally on the nanowire surface by physical vapor deposition at room temperature. Si_3N_4 was deposited at 300°C by plasma enhanced chemical vapor deposition (PECVD). Maximum improvement in radiative efficiency was obtained with parylene and upon parylene passivation, an increase in radiative

efficiency of ~10-12% was measured in all the passivated DNW samples irrespective of sample emission wavelength. The radiative efficiencies of Si_3N_4-passivated and parylene-passivated blue-emitting DNW samples are 52% and 55%, respectively, whereas for green they are 49% and 53%, respectively and for red disks they are 48% and 52%, respectively [Figs. 2.16(a)-(c)]. Radiative efficiencies of as-grown and passivated optimized InGaN disks are listed in Table 2.2. Surface recombination velocities have been estimated to be 2.3×10^3 cm s^{-1}, and 1.44×10^3 cm s^{-1} in the as-grown and parylene passivated $In_{0.51}Ga_{0.49}N$/GaN disks-in-nanowires (DNW), respectively with an areal density of 2×10^{10} cm^{-2} [75].

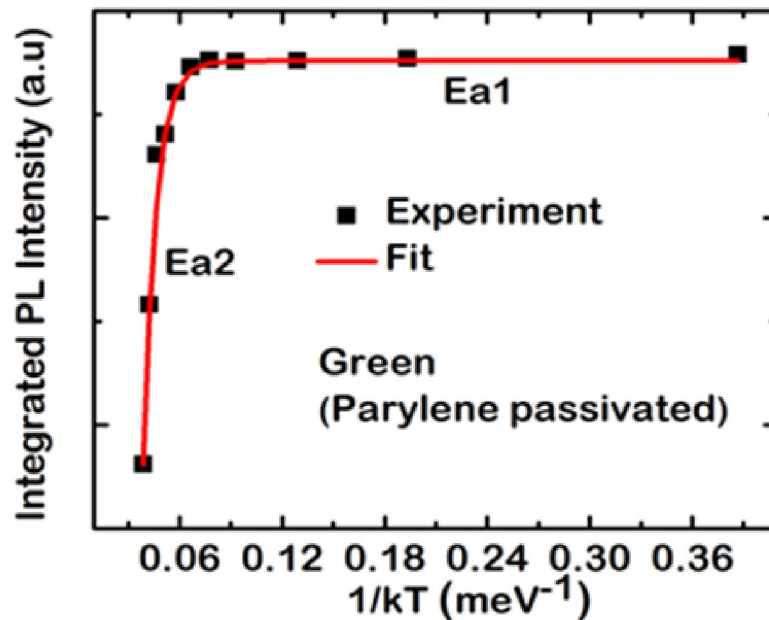

Figure 2.19 Arrhenius plot, derived from temperature dependent PL measurements on passivated green-emitting InGaN disks, yields two activation energies (Ea_1 =58meV and Ea_2 =1.34eV). The origins of these activation energies are however unknown and need to be further investigated.

To understand the significance of the surface passivation in thin InGaN disks region along the growth direction, we repeated the temperature dependent PL

measurements on the red emitting as-grown and passivated DNW samples with excitation at 267 nm. This is provided by a frequency-tripled Ti:sapphire laser, such that electron-hole pairs were generated in the GaN nanowire sections also [Fig. 2.17]. The improvement in efficiency upon parylene passivation obtained from these data is ~10% for both the GaN nanowire and red InGaN disk regions. Since this value is almost identical to the improvement in efficiency of the luminescence from the disk

Table 2.3 Carrier lifetimes in as-grown and passivated InGaN/GaN disks-in-nanowires at T=300K. The measurements were carried out with 405 nm excitation.

Sample	Passivation	τ	τ_r (ps)	τ_{nr} (ps)
Blue (λ = 430 nm)	As-grown	209	409	397
	Si_3N_4	236	408	562
	Parylene	253	408	687
Green (λ = 540 nm)	As-grown	338	750	632
	Si_3N_4	404	748	725
	Parylene	434	748	1058
Red (λ = 650 nm)	As-grown	404	985	685
	Si_3N_4	471	982	905
	Parylene	510	981	1062

Table 2.4 Carrier lifetimes in as-grown and passivated GaN region of the nanowire at T=300K with 267 nm excitation.

GaN region of nanowire	τ (ps)	τ_r (ps)	τ_{nr} (ps)
As-grown	940	1843	1918
Parylene passivation	1160	1840	3138

regions obtained by 405 nm excitation and since the surface-to-volume (SVR) ratio remains constant in the nanowire and the disk regions ($SVR=(2\pi rh/\pi r^2h) = 2/r >> 1$, where r is the average nanowire diameter and h is the thickness of the region along the growth direction), it may be concluded that passivation by Si_3N_4 and parylene

reduces non-radiative recombination via surface states. Additionally, band bending on the lateral surfaces of nanowires due to space charge related surface depletion can enhance surface recombination [94, 95]. With passivation, the extent of the depletion is reduced in both the nanowire and disk regions [55]. The reduction of surface state density will also improve the transport of electrically injected carriers from the contact regions to the InGaN disks gain media in LEDs and lasers.

2.3.4 Study of Carrier Lifetimes in Ga(In)N Disk-in-Nanowires by Time Resolved Photoluminescence Measurements (TRPL)

To confirm the improvement of IQE values of the InGaN/GaN DNW samples measured by the temperature dependence of the PL intensities, TRPL measurements were performed on the as-grown and passivated DNW samples with excitation at both 405 nm and 267 nm. The luminescence was detected by a Picoquant single photon avalanche diode having a resolution time of 40 ps. Typical transient data with 405 nm excitation at room temperature are shown in Fig. 2.18(a). Similar measurements were made at several temperatures in the range 10-300K. The transient response was analyzed with the stretched exponential model: $I(t)=I_0\exp[-(t/\tau)^{\beta}]$, where τ is the photoexcited carrier lifetime and β is the stretching parameter. The value of β obtained from analysis of TRPL data varied in the range ~0.7-0.9 which suggests that the polarization field in the disks is small. This is expected because of the radial relaxation of strain during the growth of nanowires. The values of carrier lifetime τ obtained from analysis of data recorded at room temperature from the different samples are listed in Table 2.3. Total carrier lifetime, τ increases with the emission

wavelength. A clear trend is observed: τ increases significantly upon passivation, being the largest in the parylene passivated DNW samples.

The radiative and non-radiative lifetimes, τ_r and τ_{nr} can be derived from the measured IQE (η) and τ using the relations : $\eta = (1+ \tau_r/\tau_{nr})^{-1}$ and $\tau^{-1} = \tau_r^{-1} + \tau_{nr}^{-1}$. The values of carrier lifetimes so derived at room temperature are also listed in Table 2.3. The lifetimes for red DNW samples are plotted as a function of temperature together with the measured values of τ for as-grown and parylene passivated samples in Figs. 2.18(a) and (b), respectively. Similar trends for the radiative and nonradiative carrier lifetimes in as-grown and parylene passivated blue- and green-emitting DNW samples have been observed. A few relevant observations can be made from the lifetime data. For example, if we consider the red emitting DNW samples, the values of τ in the InGaN/GaN disks are ~2 orders of magnitude smaller than those reported for planar InGaN quantum wells with lower In composition [96, 97]. The disks are 2 nm thick and 60 nm in average diameter and in the context of quantum confinement they are quite similar to wells. It is therefore apparent that the significantly smaller lifetimes in the DNW are due to a smaller polarization field resulting from a near absence of strain, and a weak confinement in the lateral direction [65]. Also, the radiative lifetime remains almost constant with variation of temperature, as expected, and the non-radiative lifetime attains very large values at low temperatures due to the freeze-out of non-radiative recombination centers. Finally, it is evident that for the samples passivated with parylene, $\tau_r < \tau_{nr}$ and hence the IQE is larger than 50%. This is significant since quantum wells emitting in the red cannot easily be grown due to effects related to excess indium. Therefore, the InGaN/GaN quantum disks in

nanowires may emerge as a viable active region for red-emitting light emitting diodes and lasers on silicon.

We next describe and discuss the results of TRPL measurements made on red-emitting as-grown and parylene passivated samples at 300K with 267 nm excitation, which excites the GaN nanowire region also. Again, the values of τ_r and τ_{nr} are derived from the measured time constant τ by using the measured IQE values, and the lifetimes are listed in Table 2.4. The values of τ are comparable to those reported earlier for GaN nanowires [75]. More significantly, the value of τ_{nr} in the GaN region of the nanowire increases by a factor of 1.64 upon passivation. This value is nearly identical to the increase in τ_{nr} in the InGaN disk region which is 1.55 (Table 2.3). This result corroborates the identical (~10%) increase in IQE in both regions (with equal surface-to-volume ratio) and strongly suggests that the improvement in efficiency is a result of the passivation of surface states. From Table 2.3, it is seen that τ_r is increasing as a function of emission wavelength. According to the Fermi-Golden rule, radiative recombination rate is proportional to the joint density of states. With increase in emission wavelength, two-dimensional joint density of states (DOS) decreases from 6.92×10^{13} eV^{-1} cm^{-2} in the blue disks to 5.63×10^{13} eV^{-1} cm^{-2} in the red InGaN disks. Hence, radiative recombination rate decreases, i.e. radiative lifetime increases. According to Table 2.3, nonradiative lifetimes also increase with emission wavelengths. Figure 2.19 shows Arrhenius plot, derived from temperature dependent PL measurements on passivated green-emitting InGaN disks, which yields two activation energies (Ea_1 =58meV and Ea_2 =1.34eV). The origins of these activation energies are however unknown and need to be further investigated.

2.4 Structural and Compositional Characterization of Ga(In)N Nanowires

2.4.1 Scanning Electron Microscopy (SEM) Imaging of Ga(In)N Nanowires

In this work, self-assembled InGaN/GaN disk-in-nanowires were grown by MBE on (001) silicon substrate with an areal density ranging from ~10^{10} to 10^{11} cm^{-2} and an average diameter ranging from 60-80 nm, as observed by 45° tilted scanning

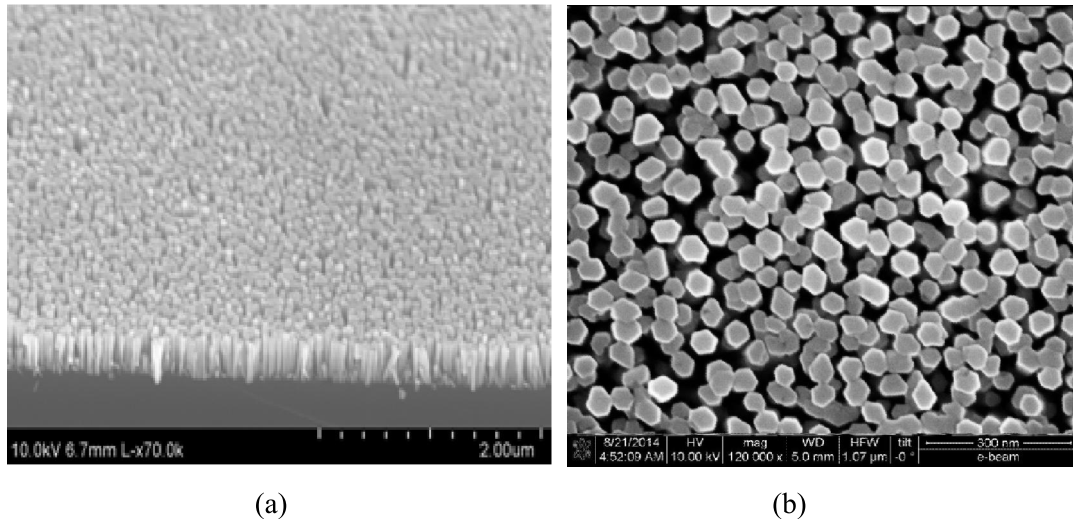

Figure 2.20 (a) 45° tilted SEM image of the ensemble of InGaN/GaN disk-in-nanowires grown on (001) silicon with an optimized areal density of $2x10^{10}$ cm^{-2}, (b) top-view of nanowires from SEM image demonstrates almost near-perfect hexagonal cross-sections.

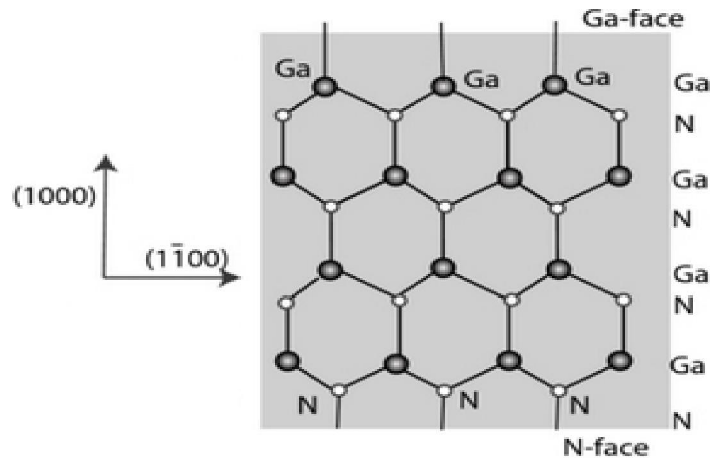

Figure 2.21 Illustration of Ga and N atoms in GaN nanowires, grown in wurtzite crystalline form with Ga-face polarity on the top surface [98].

electron microscopy (SEM) imaging shown in Fig. 2.20(a). It is seen that the nanowires are vertically aligned on silicon and separated at the top. Ga(In)N nanowires are grown exclusively in the wurtzite (or hexagonal) crystal structure with the growth axis parallel to the [0001] crystal direction, also called the c-axis. The

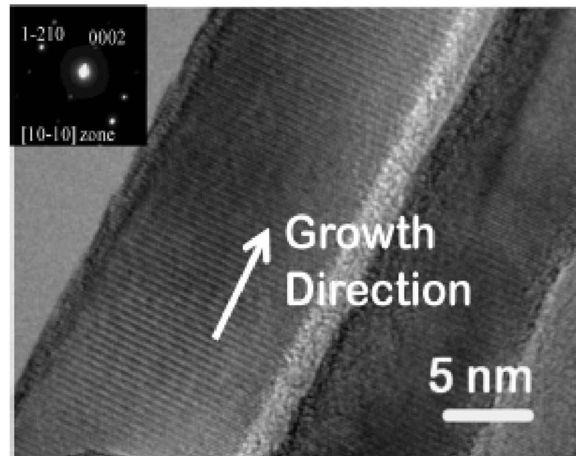

(a)

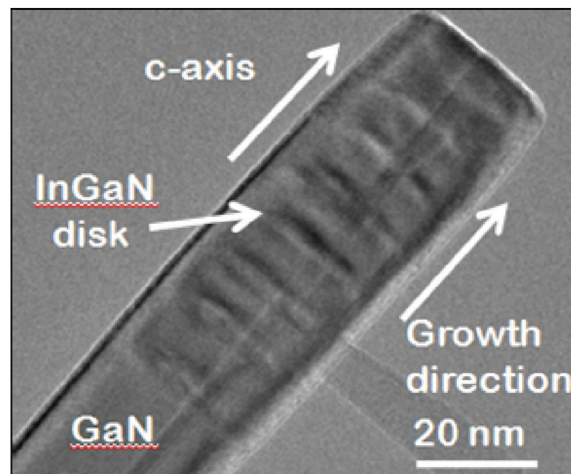

(b)

Figure 2.22 (a) High-resolution transmission electron microscopy (HRTEM) image of InGaN nanowire showing almost defect-free crystalline structure along the growth direction of nanowires [65]. The inset shows the selective area diffraction (SAD) pattern; (b) HRTEM image of a single nanowire showing multiple InGaN disks separated by GaN barriers.

sidewalls of the nanowires conform to the non-polar [1-100] m-planes. From SEM imaging, the top view of the ensemble of nanowires, as depicted in Fig. 2.20(b),

reveals that the nanowires, when well separated, have near perfect hexagonal cross sections. Ga(In)N nanowires grown on silicon by MBE generally have Ga-face polarity [79], [99], although one study found mixed polarity [100].

2.4.2 Transmission Electron Microscopy (TEM) Imaging of InGaN Disks in GaN Nanowires

The structural properties of the nanowires were investigated by high-resolution TEM (HRTEM) imaging. Figure 2.22(a) shows HRTEM image of InGaN nanowire depicting defect-free uniform crystalline structure along the growth direction of nanowires i.e. c-axis [65]. The inset to Fig. 2.22(a) demonstrates the selective area diffraction (SAD) pattern which indicates that the entire nanowire is single crystal with wurtzite structure and the c-plane is normal to the growth direction. It is derived from the SAD pattern that the lattice constant of this nanowire is 5.4 Å that corresponds to an In composition of ~25%. Figure 2.22(b) depicts HRTEM image of a single nanowire having multiple ~2nm thick InGaN disks separated by ~12 nm GaN barriers. Due to the relatively large diameter of the base of the InGaN disks in GaN nanowires, the quantum confinement in the InGaN disks is primarily provided along the growth direction. The size of the InGaN quantum wells (shaped as disks), buried in between GaN barriers, is almost identical to that of self-assembled InGaN/GaN quantum dots [101].

2.4.3 Energy-Dispersive X-ray (EDX) Measurements

Indium composition in the InGaN disks was varied to have emissions from

blue (λ=430nm) to red (λ=650nm) wavelengths. From energy-dispersive x-ray spectroscopy (EDS), as shown in Fig. 2.23, In composition in the InGaN nanowires, sandwiched between two GaN nanowire regions, was estimated to be ~20%, 38% and 54% for blue (λ=430nm), green (λ=540nm) and red emitting (λ=650nm) DNW

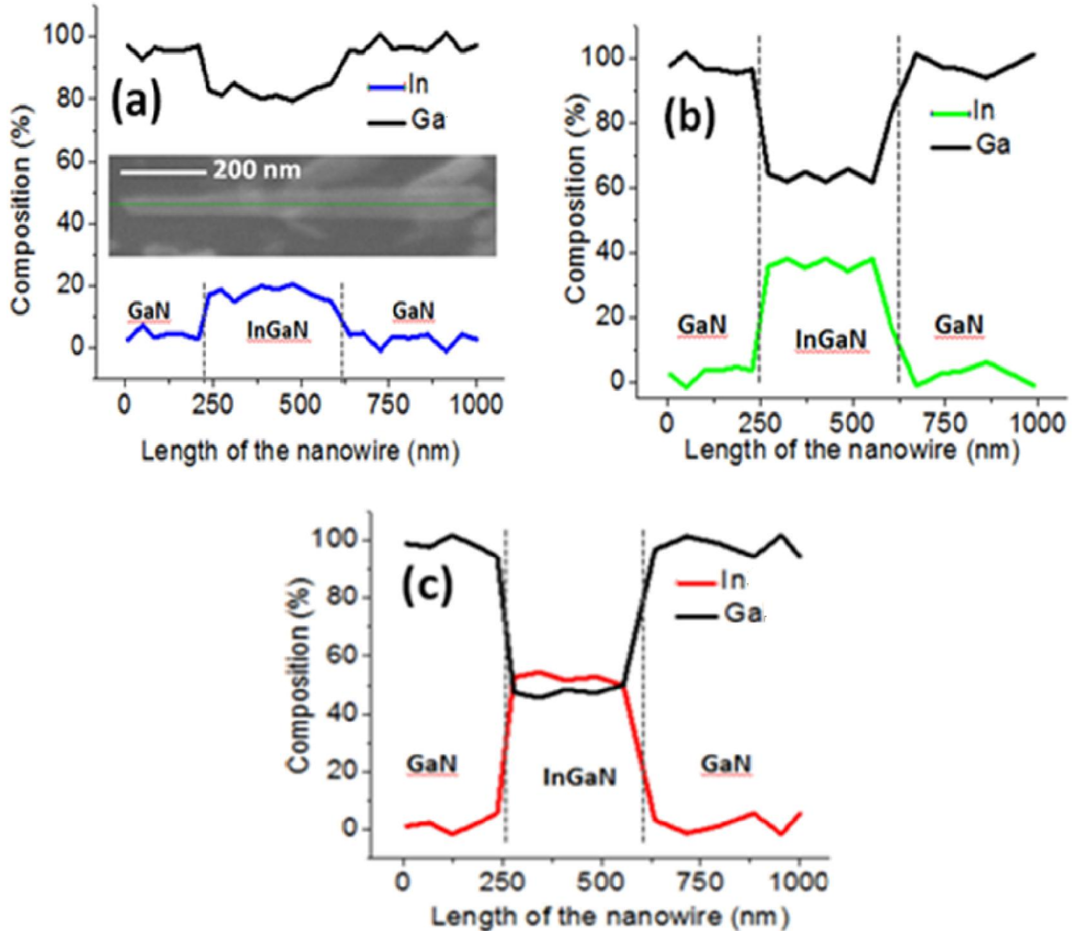

Figure 2.23 Estimation of In compositions in (a) blue, (b) green and (c) red-emitting InGaN nanowires by energy dispersive x-ray (EDX) measurements.

samples, respectively. For the EDX measurement, GaN (250nm) / InGaN (400nm) / GaN (350nm) nanowire heterostructure was grown, and line scan was performed along the c-axis of the nanowire for elemental analysis. Similar growth conditions as those for the optimized InGaN disks were used to grow the InGaN regions. In

compositions estimated from EDX measurements, hence indicates the elemental compositions of the corresponding InGaN disks.

2.6 Summary

In summary, we have grown self-assembled blue (λ=430nm), green (λ=540nm) and red (λ=650nm) InGaN/GaN DNWs on (001) silicon by MBE. Radiative efficiency of the InGaN disks has been optimized by varying the growth conditions inside MBE and passivating the surface states with Si_3N_4 and parylene. IQE of as-grown blue, green and red DNW samples was measured to be as high as 48% 43% and 41%, respectively. Parylene provided better surface passivation, compared to Si_3N_4, increasing the radiative efficiency by ~ 10-12% for all emission wavelengths. Upon parylene passivation, we obtained maximum IQEs of 54%, 52% and 51% for the passivated blue, green and red disks, respectively. Temperature dependent and time-resolved PL measurements were performed on as-grown and surface passivated DNW samples to investigate the total, radiative, and non-radiative carrier lifetimes in the disks. The trend in the lifetimes corroborate the improvement in radiative efficiency of InGaN disks after parylene passivation. Detailed structural characterizations were performed on InGaN nanowires and InGaN/GaN DNWs by SEM, HRTEM, and EDX measurements to investigate the crystal quality of the material and to estimate the elemental compositions of the disks. Optimization of the radiative efficiency and detailed structural characterization of InGaN/GaN DNWs will facilitate their use as gain media in high-performance visible LEDs and lasers, which will be discussed in Chapters III and VI.

Chapter III

InGaN/GaN Disk-in-Nanowire Array Light-Emitting Diodes

3.1 Introduction

Nitride-based light emitting diodes (LEDs) with emission in the visible spectrum play an important role in solid state lighting, A great deal of research is being devoted to the development of state-of-the-art nitride LEDs. Some of the major challenges that the current nitride planar quantum well (QW) LED industry is facing are low radiative efficiency, large shift of peak emission wavelength due to quantum-confined Stark effect (QCSE) [58] and efficiency drop at high injection currents [103], etc. These problems become even more severe when long wavelength emission (green and beyond) with high radiative efficiency is desired with planar quantum wells. White LEDs are at the center of solid state lighting, and high efficiency monolithic blue-green-red-emitting QW LEDs are required to realize white light sources with optimum color coordinates and correlated color temperatures. For the planar InGaN QWs having high indium composition to obtain green and red emissions, large strain induced polarization field is observed. This leads to poor electron-hole wavefunction overlap resulting in low radiative efficiency and large shift in emission peak (~20-30 nm) when bias is increased across the device [58, 103]. Self-assembled InGaN/GaN disks-in-nanowires (DNWs) on (001) silicon, on

the other hand, demonstrate significantly smaller polarization field due to the radial strain relaxation during their epitaxy resulting from their large surface-to-volume ratio (SVR). This, in turn, provides much better electron-hole wavefunction overlap in the active region leading to high radiative efficiency even at longer emission wavelengths and a small blueshift in emission peak as injection current is increased.

Efficiency drop in planar QWs at high injection currents mostly results from nonradiative Auger recombination of carriers [32, 36, 37] and carrier leakage from the quantum wells [34]. This is again facilitated by the presence of large polarization field associated with planar QWs with high In composition to achieve long emission wavelengths. Our measurements on nonradiative Auger recombination in InGaN nanowires and disks reveal that the Auger recombination rate is ~2-3 orders of magnitude smaller in them compared to those in planar InGaN QWs grown on lattice mismatched substrates [54]. Therefore, at high injection currents, Auger recombination driven efficiency drop is likely to be much smaller in InGaN/GaN DNWs gain media irrespective of the In composition. Also, due to the smaller strain-induced polarization field in the nanowires, carrier leakage from the disks is small at high injection. As presented and explained in Chapter II, structural characterizations of self-organized InGaN/GaN DNWs grown on (001) silicon with optimized areal density show that the nanowires are almost free of any extended defects. S-shaped behavior is not observed from the temperature dependence of PL peak emission indicating that the disks (even with high In) do not have significant In-rich clustering. Moreover, the InGaN disks are characterized by stretched monoexponential carrier decay times and low radiative lifetimes resulting in high radiative efficiency for blue-

green-red emissions. Hence, InGaN disks in GaN nanowires are promising candidate as gain media for making visible LEDs and lasers. This chapter focuses on the growth and fabrication of visible InGaN/GaN disk-in-nanowire LEDs on (001) silicon. Light-current (L-I) characteristics, electroluminescence (EL) and LED efficiencies are investigated. Additionally, to extract more light from the LEDs, the nanowire device heterostructures have been transferred to a metal reflector from the silicon substrate. Fabrication process, detailed characterization and the challenges with the nanowire LEDs on metal mirrors are discussed.

3.2 Growth of Blue, Green and Red InGaN/GaN Disk-in-Nanowire Light Emitting Diode (LED) Heterostructures on (001) Silicon

Monolithic InGaN/GaN disks-in-nanowires p-i-n LED heterostructures were grown with good uniformity in height on n-type (001) Si by plasma-assisted molecular beam epitaxy (PA-MBE). 300 nm of Si-doped n-type GaN nanowire was first grown, followed by 8 pairs of InGaN (2nm) disks/ GaN (12 nm) barrier as the active region, 15 nm p-doped $Al_{0.15}Ga_{0.85}N$ electron blocking layer (EBL) and 150 nm Mg-doped p-type GaN. Figure 3.1 demonstrates 45° tilted SEM image of the as-grown nanowire LED on (001) silicon substrate with an average diameter of ~ 60nm and optimized areal density of ~2x10^{10}cm^{-2}. High density of nanowires is needed to increase the light output, but the areal density cannot be too large such that the nanowires coalesce with each other and form defects at the coalesced boundary. We will address this issue of nanowire coalescence with high areal density in Chapter IV. N-doped GaN region was grown at a substrate temperature of 800°C under nitrogen

rich condition with a Ga flux of $1.62x10^{-7}$ Torr. P-GaN region of the LED was grown at a substrate temperature of 680°C. To grow blue (λ=430nm), green (λ=540nm) and

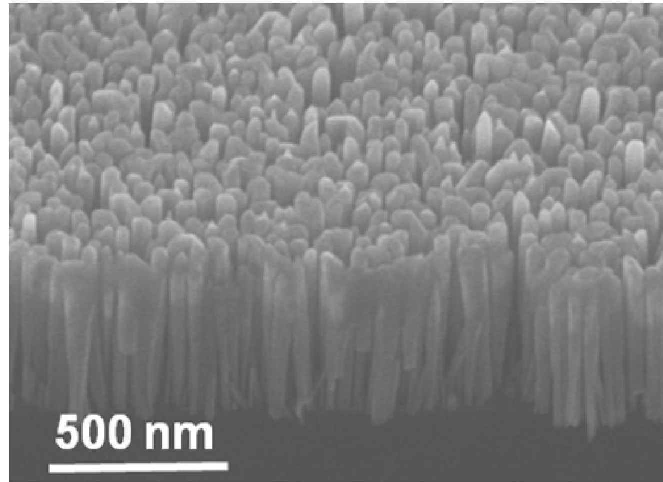

Figure 3.1 45° tilted scanning electron microscopy (SEM) image of as-grown nanowire LED heterostructure on (001) silicon substrate.

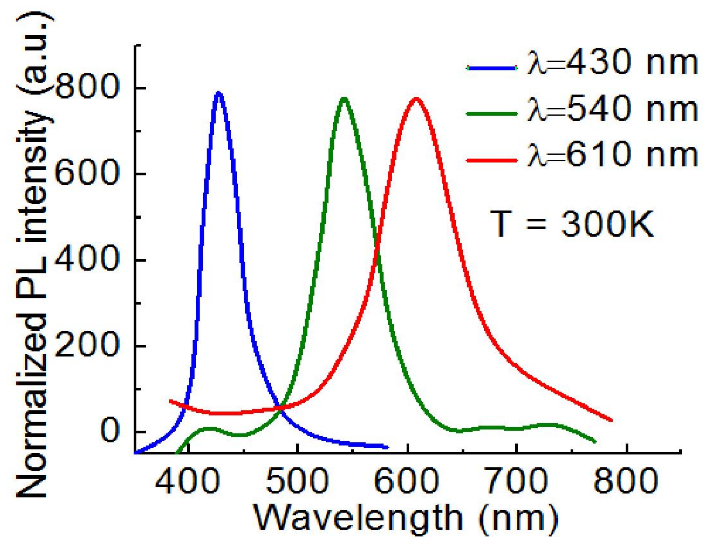

Figure 3.2 Normalized photoluminescence of the optimized blue (λ=430nm), green (λ=540nm) and red-emitting (λ=610nm) InGaN/GaN DNWs at 300K, used as active regions in the LED heterostructure.

red-emitting (λ=610nm) nanowire LED heterostructures, indium composition in the disks was changed along with the growth temperature for the InGaN disks. A detailed

discussion on the In compositions and growth temperatures for the optimized InGaN disks with the highest radiative efficiency we have obtained so far was presented in Chapter II. Growth temperatures for the optimized blue, green and red-emitting

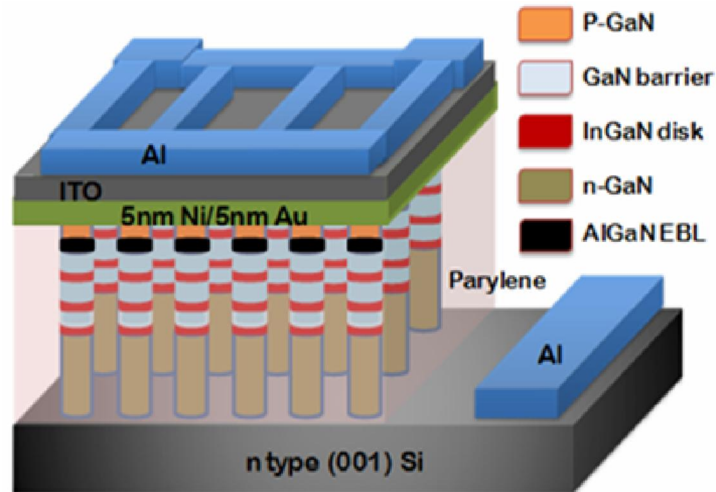

(a)

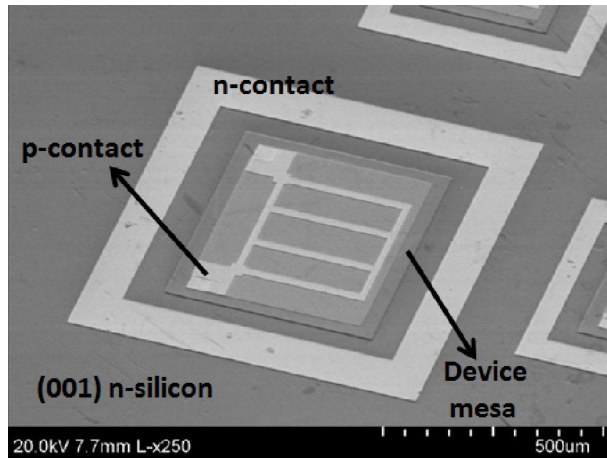

(b)

Figure 3.3 (a) Schematic representation of the fabricated nanowire LED on (001) silicon showing n-GaN, p-GaN, DNWs active region and p-$Al_{0.15}Ga_{0.85}N$ electron blocking layers separately; (b) SEM image of the fabricated nanowire LED on silicon illustrating p- and n-contacts of the device.

InGaN disks were 630, 590 and 558°C, respectively, where In-to-total group III flux ratios were 17.8%, 30.5% and 42.1%, respectively. Figure 3.2 shows the room

temperature photoluminescence of the optimized blue, green and red-emitting InGaN/GaN DNWs that have been used as active regions in the LED heterostructure. The electrically active doping level of the p-GaN layer was estimated to be (6-7) x 10^{17} cm^{-3} from C-V measurements on $n^{+}p$ GaN nanowire diodes. Doping level of the n-GaN layer was estimated to be ~$5x10^{18}$ cm^{-3} from C-V measurements on Pt Schottky contact deposited on GaN nanowires. To optimize the Ohmic contact on p-GaN, the final 20nm of p-GaN was grown with a higher Mg flux increasing the p-doping level to $8.7x10^{17}cm^{-3}$.

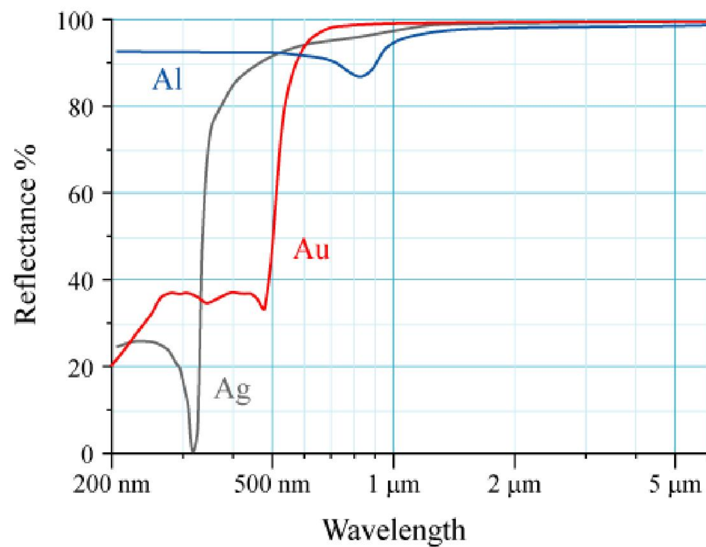

Figure 3.4 Reflectance of Ag, Au and Al as a function of emission wavelength [103]. Ag was used as metal reflector in flip-chip nanowire LEDs. It has a reflectance of higher than 90% for the emission wavelengths of our working LEDs.

3.3 Fabrication of InGaN/GaN Disk-in-Nanowire LEDs

3.3.1 Fabrication of Nanowire LEDs on (001) Silicon

At first, as-grown nanowire LED heterostructures were dry etched to make 600 µm x 600 µm device mesa. Then the ensemble of nanowires were planarized and passivated with parylene. This step of planarization is extremely critical while

processing the nanowire LEDs. The nanowires should have good uniformity in terms of their height, which was assured by optimizing substrate temperature and V/III flux ratio during growth. After its deposition on the nanowires, excess parylene was etched up to the average height of the ensemble of nanowires to expose most of the nanowire tips. The parylene etch calibration for a particular LED heterostructure was achieved by step-by-step etching along with SEM imaging of the etched heterostructure. Once the device was planarized, thin semitransparent Ni/Au (5nm/5nm) layer was deposited by e-beam evaporation on p-GaN. The contact was then annealed at 550^oC for 2 min under 4:1 N_2:O_2 ambient to minimize the contact resistance. 250nm transparent indium tin oxide (ITO) current spreading layer was deposited by sputtering. The ITO layer was annealed at 500^oC for 1 min under Ar environment to increase the transparency and reduce the resistance of the layer. The thickness of the ITO layer was chosen such a way as to avoid the formation of standing waves within the ITO layer for the emission wavelength. Finally, Al/Au (100nm/200nm) layer was deposited on n-type (001) silicon to form the n-contact of the device. Figures 3.3(a) and (b) show the schematic illustration of the fabricated LED on silicon depicting each layer and SEM image of the fabricated nanowire LED on silicon demonstrating the p-and n-contacts of the device, respectively.

3.3.2 Fabrication of Flip-chip Nanowire LEDs on Metal Reflector

With LEDs on (001) silicon substrates, we can collect the light that is going upward and finally coming out of the top surface. Most of the emitted light from the disks that is traveling downward is absorbed by the silicon substrate and thus wasted.

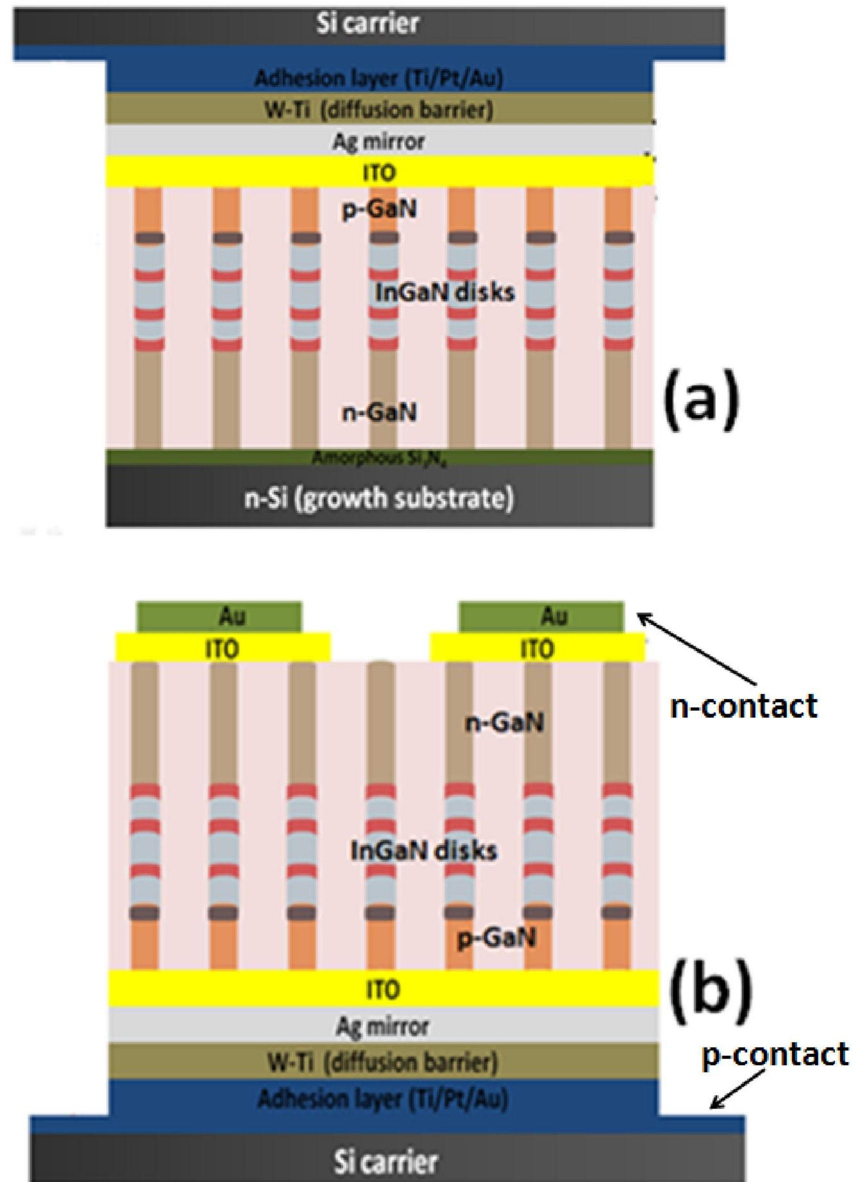

Figure 3.5 (a) Schematic representation of nanowire LED heterostructure wafer bonded with a silicon carrier on the top before removing the silicon growth substrate, (b) schematic illustration of flip-chip nanowire LED on Ag reflector after removing the entire silicon growth substrate.

Hence, LED heterostructure was transferred from the silicon substrate to a metal reflector so that the downward-propagating light is reflected by the mirror at the bottom and can be collected from the top. This should in turn increase the light output

for the same injection current, therefore increasing the device efficiency. As shown in Fig. 3.4, Ag metal has a reflectance of higher than 90% for the blue (λ=430 nm), green (λ=540 nm) and red (λ=600-650 nm) emission wavelengths. For flip-chip LED on a metal reflector, at first p-i-n LED heterostructure, as discussed in the previous section, was grown on (001) n-type silicon. 230 nm ITO was deposited by sputtering on the p-GaN side and annealed to form the p-contact. It will be discussed later in this chapter that ITO itself can make both n- and p-contacts on n- and p-GaN, respectively, and we used ITO directly on p-GaN without using Ni/Au layer. Because, though thin, Ni/Au (5nm/5nm) layer was found to absorb a significant fraction of the light output. Continuing with the flip-chip LED fabrication, after ITO deposition, 600 nm Ag mirror was deposited by sputtering. A metal diffusion barrier (W-Ti (100nm)) was then deposited by sputtering on top of Ag so that bonding metal cannot diffuse into Ag mirror and cause its deterioration especially at high injection currents. The bonding metal stack consisting of Ti(20nm) /Pt(30nm) /Au(400nm) was then deposited on the device heterostructure at the p-GaN side and also on a silicon carrier wafer simultaneously. The device was wafer bonded to the carrier at an elevated temperature of ~350°C and high pressure (400N). Figure 3.5(a) shows the schematic representation of nanowire LED heterostructure wafer bonded with a silicon carrier on the top before removing the silicon growth substrate. The whole structure was then flipped and the silicon growth substrate was removed in two steps. Most of the silicon substrate was removed by reactive ion etching (DRIE) using SF_6+C_4F_8 and the remaining silicon layer was isotropically dry-etched by XeF_2. The thin amorphous Si_3N_4 layer was removed by dry-etching. Using standard lithography

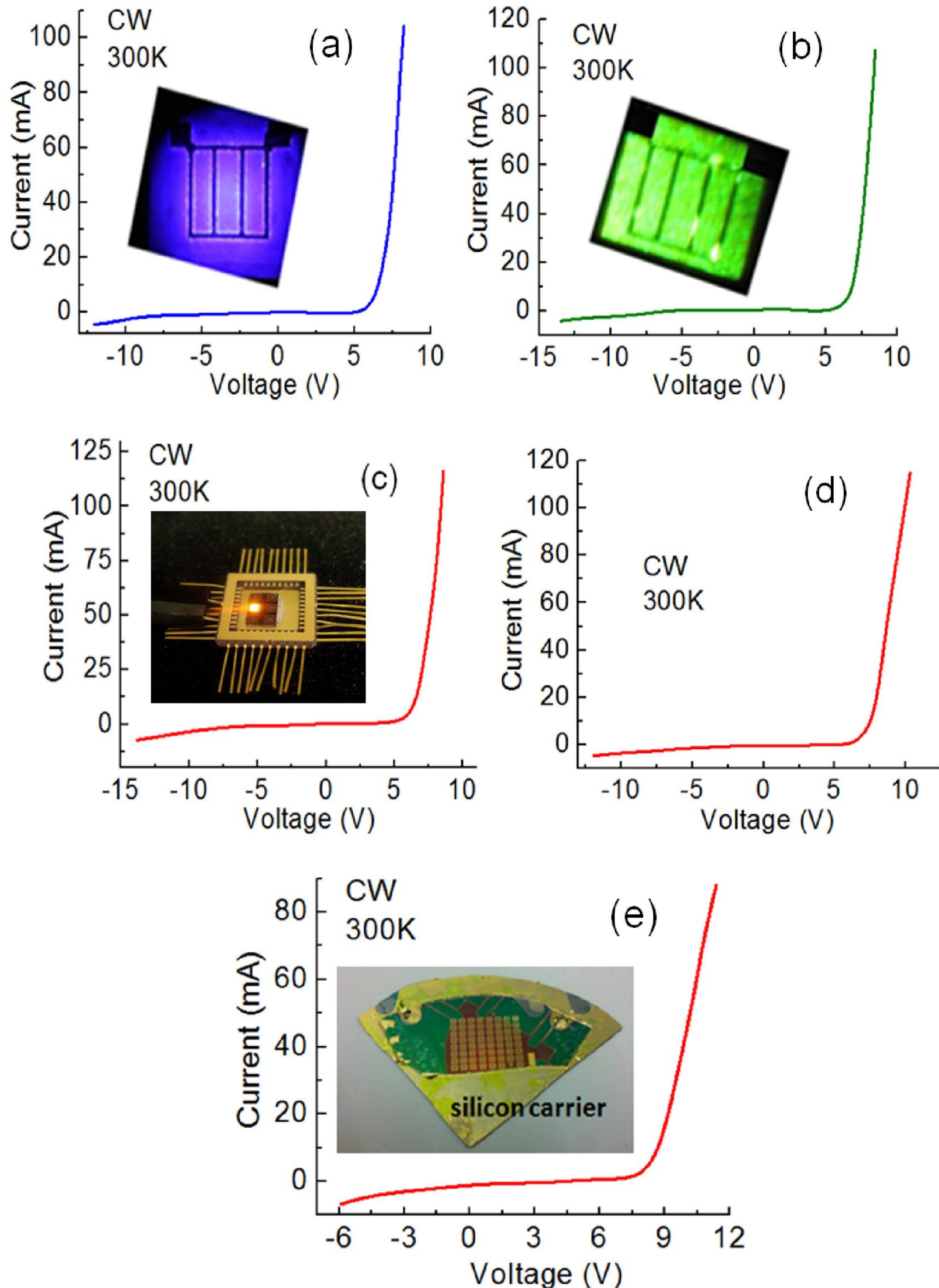

Figure 3.6 Room temperature current-voltage characteristics: (a) blue, (b) green, and (c) red-emitting nanowire LEDs with Ni/Au/ITO contact (device A), (d) red-emitting nanowire LEDs with only ITO contact (device B) on (001) silicon. Insets of Figs. 3.6(a)-(c) show corresponding illuminated fabricated devices; (e) I-V characteristics of flip-chip red-emitting nanowire LED on Ag reflector at 300K. Inset shows the optical micrograph of the fabricated flip-chip red LED wafer bonded on a Si carrier.

and metallization processes, 230 nm ITO and 200 nm Au were deposited to make the n-contact of the device.

3.4 Output Characteristics of Nanowire LEDs

3.4.1 Current-Voltage Characteristics

Figures 3.6(a) and (b) depict room temperature current-voltage characteristics of the blue- and green-emitting nanowire LEDs on silicon under continuous wave (cw) operation. The light emission area is 3.6×10^{-3} cm^{-2} and the fill factor of the nanowires is estimated to be 28% from SEM images. The blue-emitting diodes show a turn on voltage of ~6.5V and a series resistance of 15Ω, whereas the green-emitting device has a turn-on voltage of 6.8V and a series resistance of ~18Ω. As mentioned earlier, deposition and annealing of ITO layer form Ohmic contact on both n- and p-GaN. We compared the I-V characteristics of the red-emitting nanowire LEDs with and without Ni/Au contact. For some red-emitting LEDs, both Ni/Au and ITO were deposited on p-GaN region of the device heterostructure and annealed to form the p-contact (device A). For others only ITO was sputtered and annealed (device B). From the I-V characteristics of red-emitting LEDs, shown in Figs. 3.6(c) and (d), it was found that the device with only ITO contact (device B) exhibits higher series resistance and turn-on voltage compared to those with Ni/Au + ITO contact (device A). Device A and B show turn-on voltages of ~6.8V and 7.6V, respectively and series resistances of 22Ω and 28Ω, respectively. Insets of Figs. 3.6 (a)-(c) show optical micrographs of the corresponding fabricated devices. I-V characteristics between nanowire LEDs on silicon and LEDs on metal mirrors were compared for the red

emission wavelength. Fig. 3.6(e) depicts the I-V characteristics of the flip-chip red-emitting nanowire LED on Ag reflector at 300K. The diode shows poor I-V characteristics compared to those of red-LEDs on silicon. One possible reason behind the worse I-V performance of the flip-chip device is that we could not anneal the ITO contact on the n-GaN side at the optimum high temperature (~500°C) to reduce the

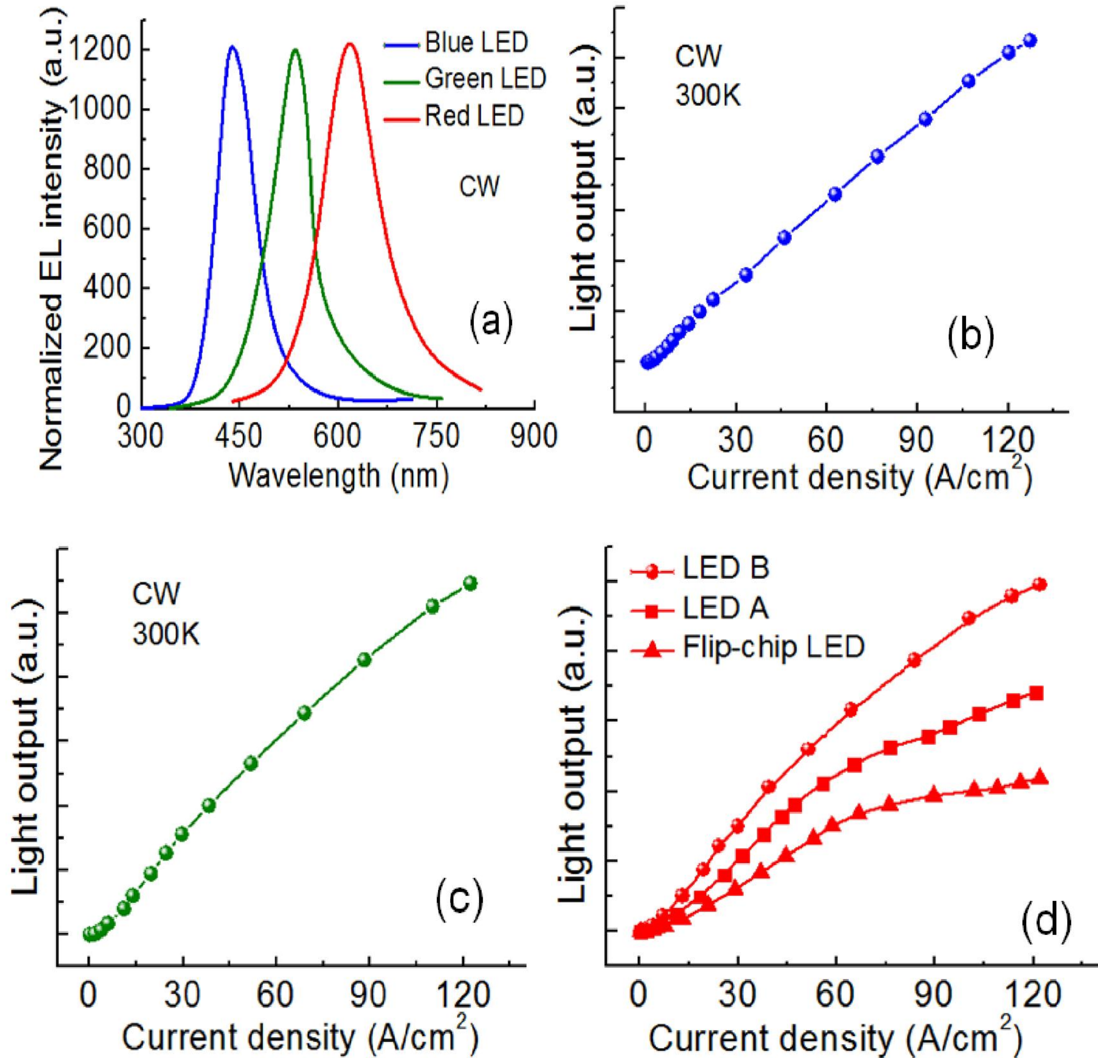

Figure 3.7 (a) Room temperature electroluminescence (EL) of the LEDs on silicon under cw operation. L-I characteristics of (b) blue and (c) green-emitting LEDs on silicon at 300K under cw bias; (d) output characteristics of devices A and B on silicon and red-LEDs on Ag reflector under the same conditions. Solid lines are guide to the eye.

contact resistance. This is because of the fact that Au-Au bond was formed at ~350°C previously during the wafer bonding of the LED heterostructure with the silicon carrier (Fig. 3.5(a)). Hence, it cannot withstand the elevated annealing temperature. Further work needs to be done to overcome this annealing issue and to optimize the flip-chip device processing steps.

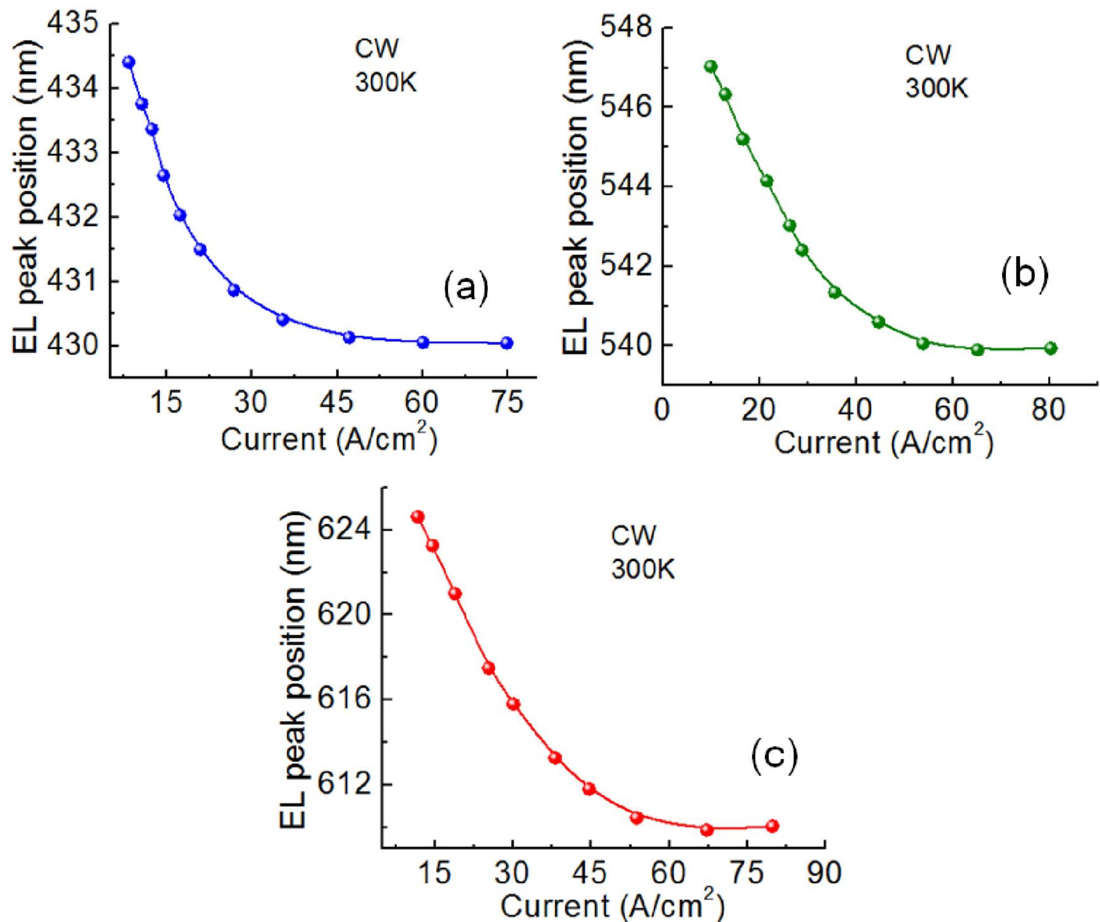

Figure 3.8 Shift in electroluminescence (EL) peak at room temperature with increasing injection current density for (a) blue, (b) green and (c) red-emitting (device A) nanowire LEDs on (001) silicon. Solid lines are guide to the eye.

3.4.2 Electroluminescence of Nanowire LEDs

Light-current (L-I) characteristics of the devices were measured at room

temperature. Figure 3.7(a) demonstrates the normalized electroluminescence (EL) of the nanowire LEDs on silicon with different emission wavelengths at 300K under cw operation. Blue and green LEDs have a half power linewidth of ~80 nm, where red LED has a half power linewidth of ~110 nm. Figures 3.7(b)-(d) depict the L-I

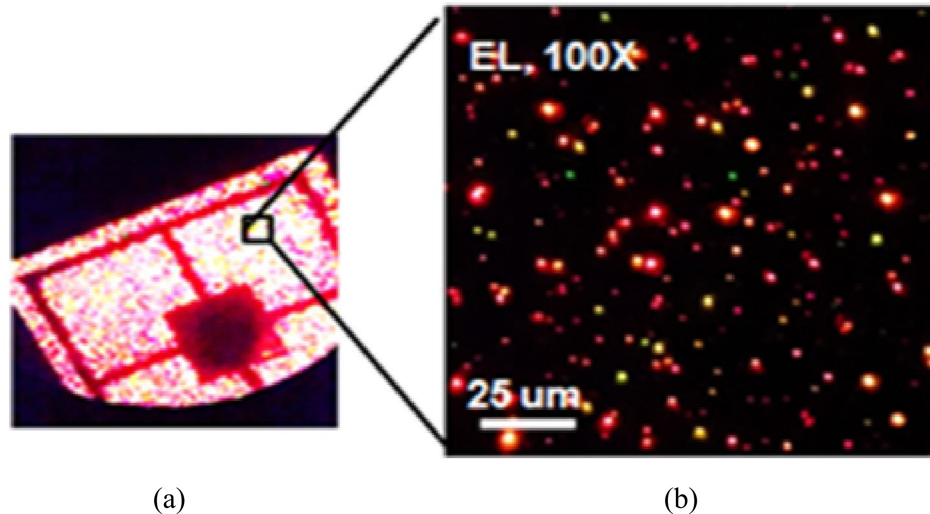

(a) (b)

Figure 3.9 (a) Optical image of the red-emitting nanowire LED on silicon under 5x optical microscope, (b) near field image of the same device with 100x optical microscope reveals that around 38% of the total device area is illuminated at a current bias of 20 A/cm^2.

characteristics of the devices under cw bias. The injection current density is calculated using the effective area (A_{eff}) of the nanowire LEDs, where A_{eff} is the total area of the device times the nanowire fill factor (FF). Since Ni/Au was absorbing a large fraction of the emitted light from the disks, light output from device A (red-LED with Ni/Au/ITO contact) is much lower compared to that from device B (red-LED with only ITO contact) for the same injection current as shown by Fig. 3.7(d). The light output from the flip-chip red-LED on the metal reflector with only ITO contact was also smaller compared to that from device B on silicon. As mentioned

earlier, since we could not anneal the ITO contact on the n-GaN side due to the temperature constraint of the wafer bonding, the transparency of the ITO layer was not optimized. A blueshift in EL peak wavelength with increasing injection current density was observed for all the devices on silicon (Figs. 3.8 (a)-(c)) due to the screening of the polarization fields in the InGaN/GaN DNWs by the injected carriers. Total blue shifts in EL peaks were measured to be ~4.5 nm, 7 nm and 14.5 nm for the blue, green and red-emitting LEDs on silicon, respectively which correspond to calculated polarization fields of 396kV/cm, 605kV/cm and 1260 kV/cm, respectively. These values are significantly smaller than those reported for equivalent planar green-emitting InGaN quantum wells (~2 MV/cm) grown on c-plane sapphire substrate [104]. The field would be much higher in planar red-emitting quantum wells if such heterostructures could be grown reproducibly. The small polarization field in the disks is a result of the radial strain relaxation during their epitaxy.

Under 5x optical microscope, as illustrated by Fig. 3.9(a), EL of the red-emitting nanowire LED seems uniform across the device. As shown in Fig. 3.9(b), near-field image of the electroluminescence from the same device under 100x optical microscope reveals that around 38% of the total device area (~125μm x 100μm) produces luminescence at a current bias of 20 A/cm^2. The remaining area of the device appeared dark under the microscope. In the self-assembled growth of nanowires on silicon, not all nanowires are of the same height. During planarization, excess parylene is etched up to the average height of the nanowire forest so that the maximum number of nanowires get connected to the top p-metal contact. The nanowires that are longer than the average height might get shorted since metal

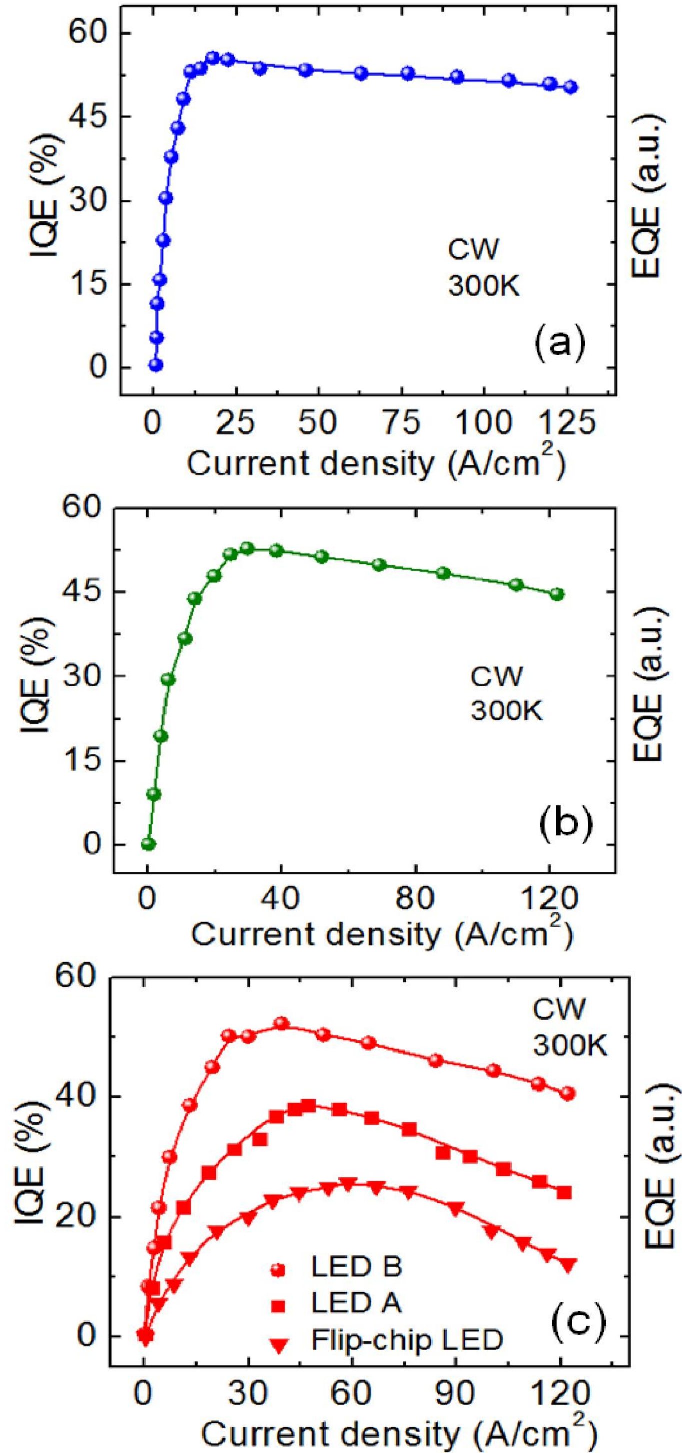

Figure 3.10 External quantum efficiency (EQE) vs injection current density under cw bias at 300K for (a) blue, (b) green and (c) red-emitting (devices A and B) parylene passivated nanowire LEDs on (001) silicon. Fig. 3.10(c) also depicts the EQE of the unoptimized flip-chip red-LED on the metal reflector. The EQE curves have been analyzed by ABC recombination model (solid line).

contact is in direct contact of their active region. The ones shorter than the average height are not even exposed above the parylene layer. In both cases, these nanowires cannot emit any light and appear dark when observed (Fig. 3.9(b)). With the same V/III flux ratio for a DNW sample with a particular emission color, In incorporation in the InGaN disks varies between nanowires to some extent due to the difference in the nanowire diameter. Hence, as seen in Fig. 3.9(b), some of the nanowires are emitting light at different wavelengths other than the desired red. To increase the light output from nanowire LEDs, we need high density of nanowires on silicon. If the areal density becomes too large such that the nanowires coalesce with each other and form defects at the coalesced boundary, then these defects can act as nonradiative recombination centers for carriers. Hence, the coalesced nanowires appear dark or have reduced light intensity. We will discuss this issue of nanowire coalescence with high areal density in Chapter IV. More disks in the active region will result in higher light output. However, increasing the number of disks will cause a non-uniform injection of holes amongst the disk layers due to the heterostructure band line-up. Thickness of GaN barriers and number of disks used in the heterostructure have been optimized by the I-V characteristics of the device. We have included six disk layers in our heterostructures based on our optimization. The thickness of the disks affects the electron-hole wavefunction overlap and hence the emitted light intensity. We have used the optimum value of ~2 nm.

3.4.3 Efficiency of Nanowire LEDs

Figures 3.10(a)-(c) show the external quantum efficiency (EQE) of blue, green

and red-emitting nanowire LEDs on silicon at 300K under cw mode as a function of injection current density. Fig. 3.10(c) also depicts the EQE of the unoptimized flip-chip red-LED on the metal reflector. As discussed in section 3.4.2, light output from the flip-chip device is lower than that from red-LED on silicon (device B) since unannealed ITO contact had poor transparency. Similar observations were made from the EQEs of these devices with the flip-chip device on reflector having smaller EQE values through the entire range of injection currents. EQE reaches its peak value at low injection current densities of ~18 A/cm^2, 27 A/cm^2 and 38A/cm^2 for blue, green and red-emitting LEDs, respectively. The efficiency drops at an injection level of ~120 A/cm^2 were measured to be 10%, 13% and 16%, respectively compared to the peak efficiency of the corresponding device. These values of efficiency drop are smaller than those in planar InGaN QW LEDs [54, 55, 65, 105]. Nonradiative Auger recombination and carrier leakage from the active regions are two major reasons behind the drop of device efficiency at high injection currents. Compared to those in planar InGaN QWs, Auger recombination coefficients in InGaN/GaN DNWs are ~2-3 orders of magnitude smaller [54]. Also, an optimized p-doped $Al_{0.15}Ga_{0.85}N$ EBL was used just after the active region in all these LED heterostructures to reduce the carrier leakage from the disks. The EQE curves can be analyzed with the A-B-C recombination model [106, 107]. By using the relations: $\eta = Bn^2/(An+Bn^2+Cn^3)$ and $J=qd(An+Bn^2+Cn^3)$, the values of A, B and C were estimated to be $2.88x10^8 s^{-1}$, $8.34x10^{-11} cm^3 s^{-1}$, and $4.3x10^{-33} cm^6 s^{-1}$, respectively for the red-LED on silicon. Here, n is the injected carrier density and A, B, and C are the non-radiative, radiative and Auger recombination coefficients, respectively. It is considered that the effective

recombination thickness for each disk is ~2 nm. It is, of course, assumed here that the maximum IQE of 52% for this device, as determined from the temperature dependent PL measurements on the parylene passivated red DNW samples described earlier, is valid under electrical injection. Other factors to note are that the IQE at 10K may not be 100%, and carrier injection and transport may be temperature dependent. Most notable here is the fact that the values of the Auger coefficient in the InGaN/GaN disks are consistently ~ 10^{-34}-10^{-33} $cm^6\ s^{-1}$, which agree well with calculated values [108, 109]. Similar values for Auger recombination coefficients were derived from the ABC model analysis for other LEDs with different emission colors. We did not measure the electroluminescence of the LEDs inside integrating spheres. No post-processing was done to encapsulate the LEDs to improve light extraction. The extraction efficiency of these devices is not accurately known and hence, the external quantum efficiency (EQE) is reported in arbitrary units (a.u). Nevertheless, the measured EQEs (in a.u.) (Figs. 3.10) clearly show the current density at which the device efficiency becomes maximum and the subsequent reduction in efficiency at higher injection currents.

3.5 Summary

In conclusion, we have fabricated self-assembled nanowire array blue, green and red-emitting LEDs on (001) silicon and characterized them. The diodes have demonstrated a turn-on voltage in the range of ~6-7.5 V and an overall series resistance in the range of ~17-28 Ω. Room temperature EQE reaches its peak at a low injection current density of ~ 18-38 A/cm^2. The LEDs suffer from efficiency

reductions of ~ 10-15% at 120A/cm^2 compared to peak efficiency of the corresponding device. These values of efficiency droop are much smaller than those reported in planar InGaN QW LEDs due to the low Auger coefficients in the DNWs and presence of an EBL in the nanowire LED heterostructures. From the analysis of the EQE curves by ABC recombination model, Auger coefficients in the InGaN/GaN disks were consistently derived to be ~ 10^{-34}-10^{-33} cm^6 s^{-1} for all emission colors. This agrees well with theoretical calculations. From the blueshift of the electroluminescence peak with increasing injection current density, polarization fields of 396kV/cm, 605kV/cm and 1260 kV/cm, were derived for the blue, green and red-emitting LEDs on silicon, respectively. These values are significantly smaller than those derived for equivalent planar green-emitting InGaN quantum wells (~2 MV/cm) grown on c-plane sapphire substrate due to the radial strain relaxation of the nanowire heterostructure during epitaxy. In order to increase light output from the device, nanowire LEDs were transferred from the silicon substrate to Ag reflector. However, superior performance in light output, as desired from the flip-chip LEDs on metal mirror, could not be obtained due to the poor transparency and high resistivity of the unannealed ITO contact resulting from the temperature limitation of the existing Au-Au bonding in the flip-chip LED heterostructure.

Chapter IV

Effect of Coalescence on the Optical Properties of Self-Assembled Ga(In)N Nanowires Grown on (001) Silicon

4.1 Introduction

As discussed in previous chapters, InGaN disks in GaN nanowires (DNWs) have advantages over planar InGaN quantum wells (QWs) as the gain media for realizing visible LEDs and lasers. In particular, even at long emission wavelengths, polarization field is smaller in DNWs compared with planar QWs giving rise to their high radiative efficiency. Other advantages of DNWs include small peak shift with injection, reduced efficiency drop at high injections, etc. Moreover, as investigated by detailed structural characterizations by us and others [48-53, 85, 88, 110-113], InGaN/GaN DNWs grown on (001) silicon are relatively free of extended defects compared to planar QWs grown on lattice mismatched substrates. Heteroepitaxy of planar GaN on lattice mismatched substrates is performed due to the unavailability of large free-standing GaN substrates and the very high prices even for the smaller ones. The presence of a thin amorphous Si_3N_4 layer at the GaN/Si interface mostly removes the epitaxial requirement from the growth of wurtzite GaN nanowires on (001) Si. Due to their large surface-to-volume (SVR) ratio, strain relaxes in the radial direction during the epitaxy of InGaN disks in GaN nanowires even for high In compositions

leading to nearly defect-free InGaN/GaN interfaces. The few dislocation defects that generate at the GaN/Si boundary, usually bend toward nanowire sidewall if the nanowires are grown long enough, and therefore do not propagate into the active region. However, in the self-assembled growth of nanowires on silicon, the nanowire areal density plays a crucial role on the optical properties of nanowire LEDs and lasers. The extent of nanowire coalescence can be controlled by the density of the nanowires. The density of self-organized nanowires is difficult to control and depends on growth parameters such as V/III ratio and substrate temperature, etc. A high density of nanowires is usually desired to obtain high light output. However, for high nanowire density, where the nanowires are in close proximity, coalescence can take place between two or more misaligned nanowires or adjacent nanowires with increasing diameter during epitaxy [88-90, 110, 112-114]. Coalescence between adjacent nanowires can result in the formation of defects near the coalesced boundaries that can behave electronically as deep level traps in the structure, therefore having detrimental effect on the radiative efficiency of the devices. Whereas in-depth research is being done on the growth of Ga(In)N nanowires and device fabrication with these materials, the study of the role of nanowire coalescence on the defects needs to be further examined. This chapter discusses the nature of these defects at the coalesced nanowire boundaries through structural characterizations. To understand the effects of nanowire coalescence on the optical properties of DNWs, radiative efficiency of InGaN disks in GaN NWs with different areal density are studied. Transient capacitance measurements are performed on planar GaN and GaN nanowire n^+p diodes to investigate the electron and hole trap characteristics in these

structures. Deep level traps in these structures are compared, and the dependence of trap density in nanowires on their areal density i.e. the degree of nanowire coalescence is presented and explained. Nanowire LEDs made with the similar set of areal densities as that of the nanowire diodes were characterized, and the effect of nanowire coalescence on the device performance was discussed.

4.2 Optical and Structural Characterization of GaN Nanowires with Different Areal Densities

4.2.1 Transmission Electron Microscopy (TEM) Imaging of Nanowires

TEM imaging of GaN nanowires was done to examine the crystalline quality of individual and coalesced nanowires. All TEM imaging on the nanowires was done in Prof. Joanna M. Millunchick's group. It is known that coalescence can occur between two or more slightly misaligned nanowires or two adjacent nanowires very near to each other if the diameter increases during epitaxy. Both kinds of coalescence will be enhanced if the nanowire areal density is large. It has been observed that this coalescence between adjacent nanowires can occur at an early stage of the growth up to several hundred nanometers from the Si substrate [81]. From SEM images it has been found that the majority of the nanowires grew normal to the Si substrate while few of them grew at some angle to the substrate. Coalescence of both parallel and tilted nanowires was observed. Beside the tilted nanowires, the coalescence of the parallel nanowires indicates that the removal of nanowire surface area by coalescence is energetically favored [81]. Hence, coalescence is likely to occur whenever the nanowires come in proximity to each other. GaN nanowire samples for TEM

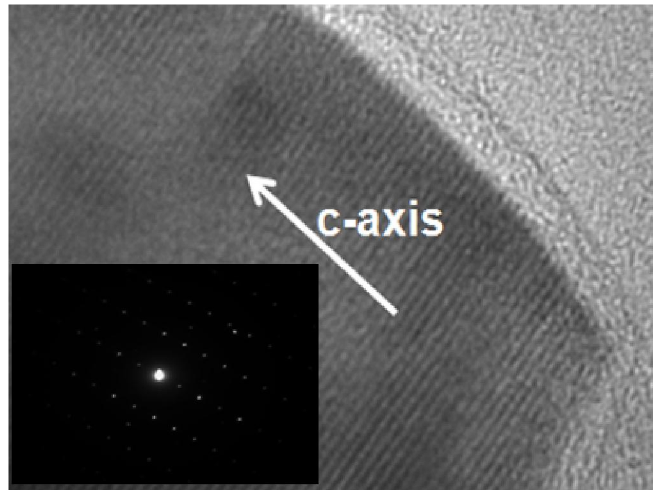

Figure 4.1 High resolution Transmission electron microscope (HRTEM) image of coalescence-free single GaN nanowire collected from the ensemble of GaN nanowires with areal density of $2x10^{10}cm^{-2}$, showing no defects in the crystal structure along the growth direction. Inset shows selective area diffraction (SAD) pattern of the nanowire.

measurements were grown on (001) Si substrates with areal densities ranging from ~ $2x10^{10}cm^{-2}$ - $3x10^{11}cm^{-2}$. Samples for high-resolution TEM analysis were prepared by dispersing individual and coalesced nanowires on carbon coated copper TEM grids. High resolution TEM image of coalescence-free single GaN nanowire collected from the ensemble of nanowires with areal density of $2x10^{10}cm^{-2}$ is shown in Fig.4.1 and HRTEM images of coalesced nanowires from the nanowire forest on silicon with nanowire density $3x10^{11}cm^{-2}$ are shown in Fig. 4.2. As nanowires coalesce, the crystallographic (c-axis) misorientation between impinging nanowires is accommodated by the formation of zipper-like arrays of dislocations and basal plane stacking faults near the boundary of the coalescing nanowires. These defects, once originated, mostly propagate all the way to the top. These threading dislocations and stacking faults at the coalesced boundary are known to give rise to dark lines and dark

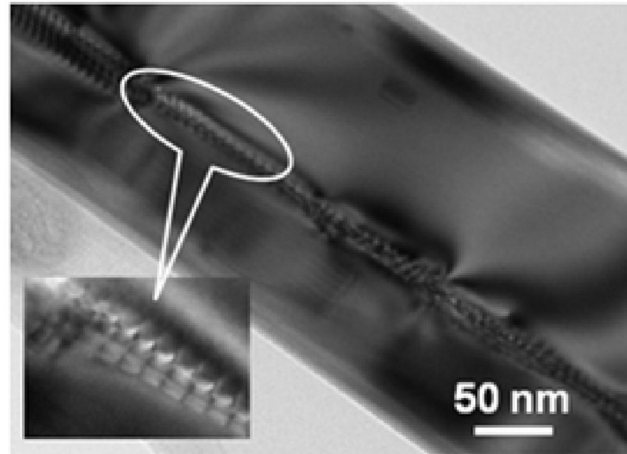

(a)

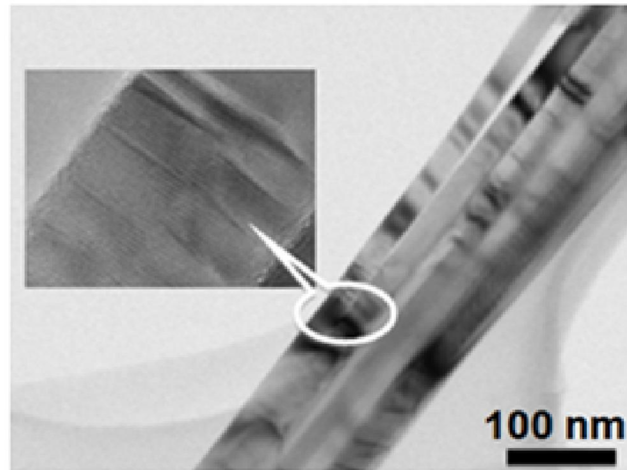

(b)

Figure 4.2 High resolution Transmission electron microscope (HRTEM) images of coalesced GaN nanowires with areal density of ~$3x10^{11}cm^{-2}$: (a) an example of chain of stacking fault defects near the boundary of coalescing nanowires at low and high magnification (inset); (b) a pair of nanowires that coalesced and a high resolution image of the defects (inset) in the vicinity of the juncture.

spots in the near-field image of planar LEDs. These defects can also electronically behave as non-radiative carrier trapping centers. It may then be assumed that as the degree of coalescing increases, with increasing nanowire density, the density of such non-radiative deep levels would increase. Consequently, the radiative efficiency of the nanowires and nanowire based devices such as LEDs and lasers would decrease.

Several other groups [88-90, 110, 112-114] beside us have investigated the coalescence of GaN nanowires. It has been observed that coalescence and resulting defects detrimentally affect optical output, which will be discussed in subsequent sections. In the self-organized scheme of nanowire growth, we can control the proximity of the nanowires by varying the nanowire areal density changing the Ga flux used for the nanowire growth. With smaller areal density, we can reduce the number of coalesced nanowires that is likely to lower the defect density in them resulting from the coalescence.

4.2.2 Temperature Dependent Photoluminescence Measurements : Radiative Efficiency

To investigate the effect of nanowire coalescence on the radiative efficiency i.e. internal quantum efficiency (IQE) of the ensemble of DNWs, we have performed temperature dependent photoluminescence (TDPL) measurements on as-grown red-emitting (λ=610nm) $In_{0.51}Ga_{0.49}N$/GaN disks-in-nanowires (DNW) on (001) silicon with different areal densities in the range of ~ $2x10^{10}$ – $3.5x10^{11}cm^{-2}$. For this study, 300nm GaN was grown on (001) n-type silicon substrate followed by six ~2nm thick $In_{0.51}Ga_{0.49}N$ disks separated by ~12 nm GaN barriers. GaN nanowires were grown on silicon at a substrate temperature of 800^oC under nitrogen rich condition. During growth, Ga flux was kept at $1.62x10^{-7}$ Torr and nitrogen plasma was constant at 1 sccm. To grow the optimized red-emitting $In_{0.51}Ga_{0.49}N$/GaN disks-in-nanowires, substrate temperature was lowered to 553^oC and In-to-total-group III flux ratio of 42% was used. Schematic illustration of the nanowire heterostructure, used in the

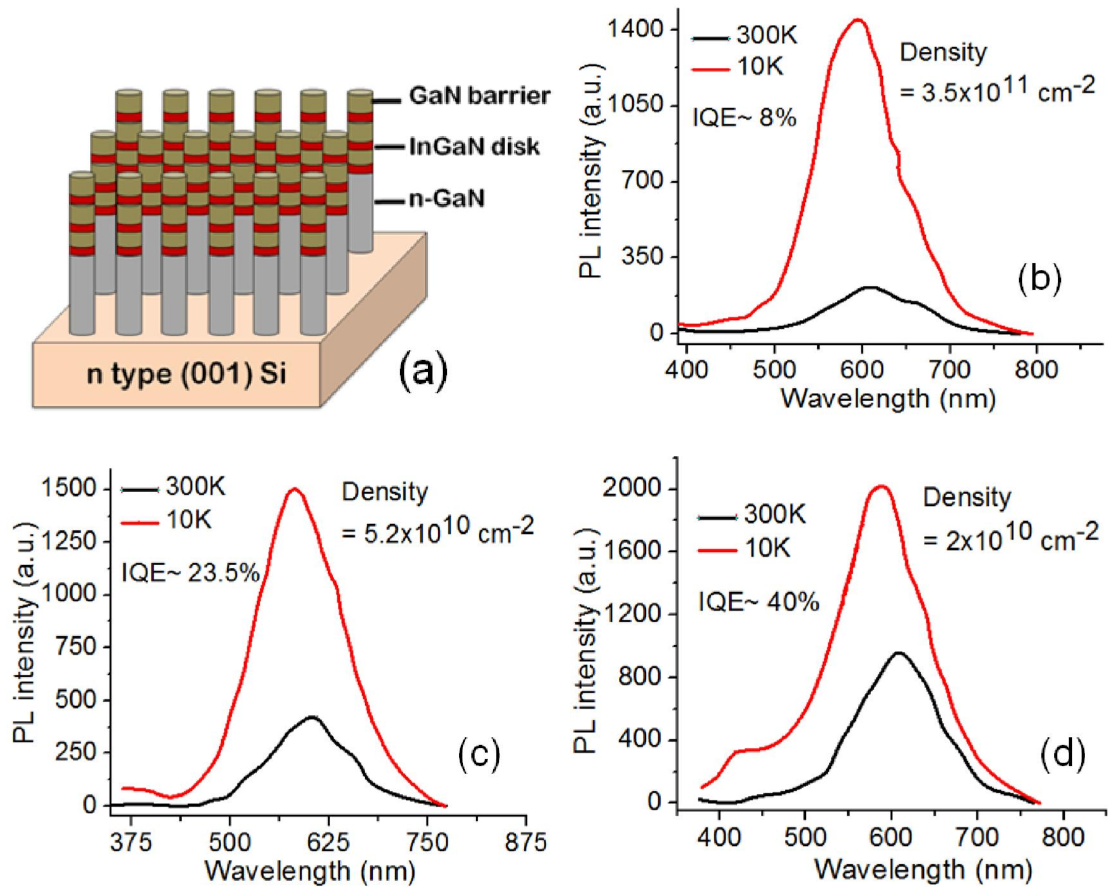

Figure 4.3 (a) Schematic representation (change color) of the red-emitting (λ=610 nm) $In_{0.51}Ga_{0.49}N$/GaN disks-in-nanowire heterostructure on (001) silicon. Photoluminesces of the as-grown red-emitting DNWs with areal densities of (b) $3.5x10^{11}cm^{-2}$, (c) $5.2x10^{10}cm^{-2}$ and (d) $2x10^{10}cm^{-2}$, at room temperature and 10K.

experiment is shown in Fig. 4.3(a). Radiative efficiency or internal quantum efficiency (IQE) of the DNW sample is derived as the ratio of the measured maximum PL intensities at 300K and 10K. It is assumed that non-radiative recombination centers are frozen at 10K and the quantum efficiency is approximately unity at this temperature. The radiative efficiency of the red-emitting as-grown InGaN disks in GaN nanowires increases from 8% to 43% with a reduction in nanowire areal density from $3.5x10^{11}cm^{-2}$ to $2x10^{10}$ cm^{-2}, respectively, as demonstrated in Figs.

4.3(b)-(d). As mentioned in section 4.2.1, the degree of nanowire coalescence increases with areal density that leads to the formation of defects near the coalescing boundary. These defects can electronically behave as electron and hole deep level traps through which carriers can recombine non-radiatively, therefore reducing the radiative efficiency of DNW samples.

4.3 Effect of Nanowire Coalescence on the Output of Nanowire LEDs

4.3.1 Electroluminescence of LEDs with Different Nanowire Areal Densities

We investigated the effect of nanowire coalescence on the light output of disks-in-nanowires (DNWs) array red-emitting LEDs, grown with different areal densities. Red-emitting (λ=610nm) nanowire LED heterostructure having optimized InGaN/GaN disks in the active region was grown on (001) Si substrate as discussed in Chapter III and depicted in Fig. 4.4(a). 300 nm of Si-doped n-type GaN nanowire was first grown, followed by 6 pairs of $In_{0.51}Ga_{0.49}N$ (2 nm)/ GaN (12 nm) barrier as the active region, 15 nm p-$Al_{0.15}Ga_{0.85}N$ electron blocking layer (EBL), and 150 nm Mg-doped p-type GaN. The electrically active doping levels of the p-GaN and n-GaN layers were estimated to be ~$6x10^{17}cm^{-3}$ and $5x10^{18}$ cm^{-3} from C-V measurements. The devices were fabricated with passivation of the nanowires by parylene, which also served to planarize the structure for subsequent p-contact formation with 230 nm indium tin oxide (ITO). Aluminum was deposited on the n-type Si substrate to form the bottom electrode. Four devices were made with nanowire areal density equal to $2x10^{10}$, $3x10^{10}$, $6x10^{10}$ and $2x10^{11}$ cm^{-2}. The InGaN disk alloy composition and emission wavelength (610 nm) and all the other layers and their parameters were

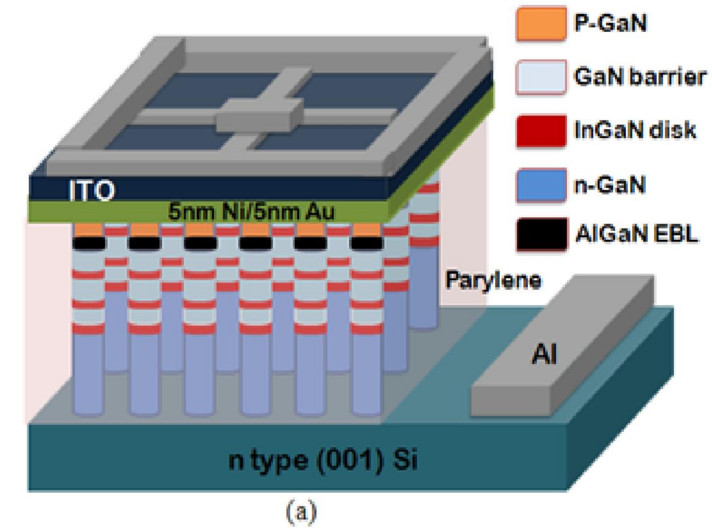

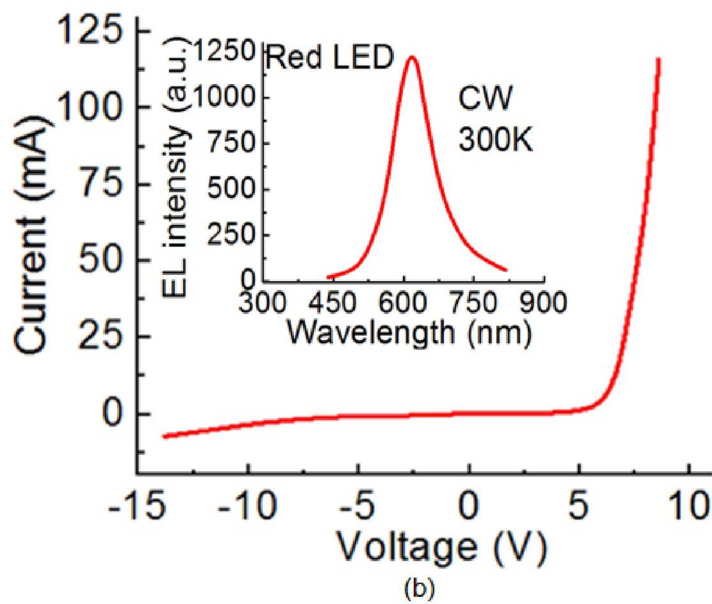

Figure 4.4 (a) Schematic illustration of red-emitting (λ=610nm) nanowire LEDs on silicon; (b) room temperature current-voltage characteristics of the LED under continuous wave operation. Inset shows the electroluminescence data of the device.

maintained constant in the four devices. Typical current-voltage characteristics of a nanowire LED measured with a cw bias is shown in Fig. 4.4(b). A series resistance of 28Ω is measured for the diode. The inset to this figure shows the electroluminescence measured with CW bias, exhibiting a peak at 610 nm. The measured

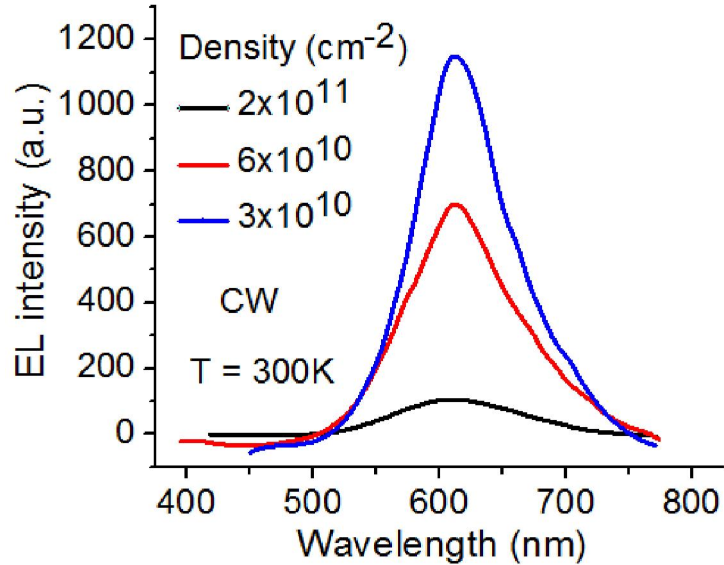

Figure 4.5 Room temperature electroluminescence of nanowire LEDs with areal densities of $3x10^{10}$, $6x10^{10}$ and $2x10^{11}$ cm^{-2} at the same injection current density of $40A/cm^2$, showing suppression of light output from the higher density devices.

electroluminescence (EL) of nanowire LEDs with areal densities of $3x10^{10}$, $6x10^{10}$ and $2x10^{11}$ cm^{-2} at 300K at the same injection current density of $40A/cm^2$ is shown in Fig. 4.5. It is evident from the EL data that light output from the highest density device is significantly smaller than that of the lowest density LEDs at the same injection level. Electrically injected carriers undergo more nonradiative recombination in the higher density nanowire LEDs in presence of a large number of defects near the coalesced interface both in the active region and also while they travel from contacts to active regions. Under 5x optical microscope, electroluminescence from the LED looks uniform across the device (Fig. 4.6(a)). Upon examining the near-field image of the electroluminescence (under 100x optical microscope), it is observed that only a certain percentage of the device area produce luminescence. Figures 4.6(a)-(d) show the same amount of device area (~125µm x 100µm) for all four parylene-passivated red-LEDs, where we have compared the

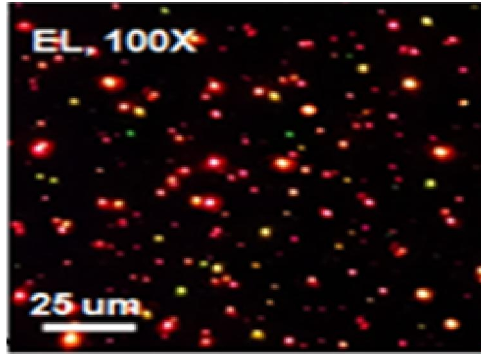

(a)

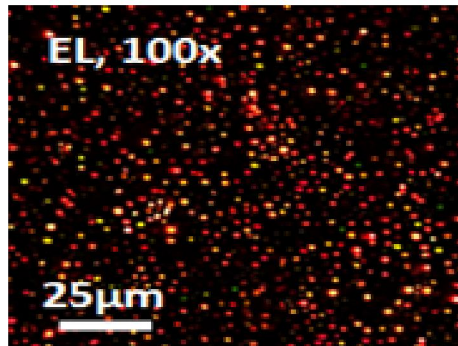

(b)

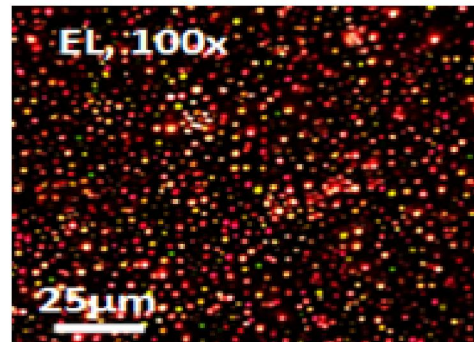

(c)

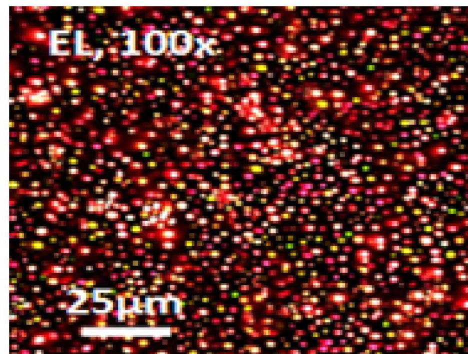

(d)

Figure 4.6 Near field image of EL from the red nanowire LEDs with 100x magnification and 5V bias having (a) $2x10^{11}$, (b) $6x10^{10}$, (c) $3x10^{10}$, and (d) $2x10^{10}$ cm^{-2} nanowire areal density. Only 3%, 20%, 33% and 38% of the device area produce luminescence for (a), (b), (c) and (d), respectively.

percentage of the device area that is lighting up. The injection current is not distributed evenly among all the nanowires since they have different individual series resistances due to the variation in their heights and diameters. As shown in

Figs. 4.6(a)-(d), the percentage of device area being illuminated varies from 3% in the device with $2x10^{11}cm^{-2}$ nanowire density to 38% in the device with $2x10^{10}cm^{-2}$ nanowire density. As mentioned in section 4.2.2, a similar trend was observed in photoluminescence data in terms of the radiative efficiency obtained from red InGaN disk-in-nanowire samples without parylene passivation with similar nanowire density variation. The IQE varies from 8% in the sample with $3.5x10^{11}$ cm^{-2} nanowire density to 43% in the sample with $2x10^{10}$ cm^{-2} nanowire density. IQE is not measured from the percentage of device area or nanowires that is lighting up. Rather it is measured by taking the ratio of the maximum intensities of the ensemble of nanowires at 300K and 10K at a very high excitation level. Careful observation of Fig. 4.6 reveals that the intensity of the light-emitting nanowires is not the same. Nanowires might not emit at all, or they might have weak emission depending on the extent of defects generated at the coalesced boundary. To estimate the percentage of device area that is lighting up, we have assumed a threshold intensity below which a point is considered dark. On the other hand, IQE is calculated from the maximum intensity of the ensemble of nanowires, where all the light-emitting nanowires with varying intensities contribute. The purpose of these near-field images (Fig. 4.6) is to show the significant increment in the percentage of the device area that is lighting up due to the lower coalescence with reduced areal density. Of course, it will improve the IQE. So, they will follow the same incremental trend, but they might not very well be the same. Due to coalescence of nanowires with high areal density, defects are produced at the coalescing boundaries. We believe, therefore, that deep level traps originating from nanowire coalescence account for the large difference in IQE and eventually the

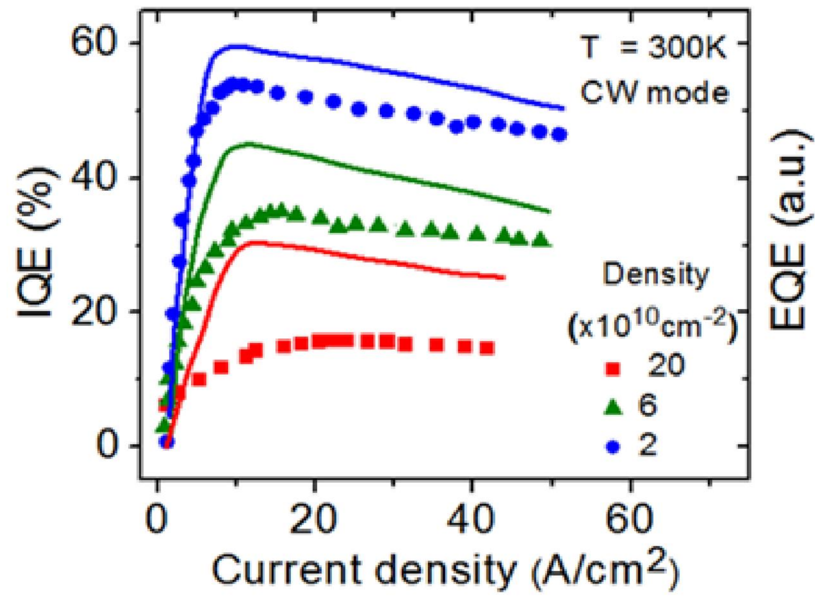

Figure 4.7 Measured external quantum efficiencies of the red LEDs with different nanowire areal densities under CW mode of operation. Solid curves represent the calculated internal quantum efficiency (IQE) of the LEDs based on the A-B-C recombination model.

Table 4.1 Radiative and non-radiative recombination coefficients derived from red-LED efficiency measurements.

Nanowire density (cm^{-2})	A (s^{-1})	B (cm^{3}s^{-1})	C (cm^{6}s^{-1})
2x10^{10}	2.92x10^8	6.38x10^{-11}	3.48x10^{-33}
3x10^{10}	2.98x10^8	6.32x10^{-11}	3.5x10^{-33}
6x10^{10}	4.85x10^8	4.75x10^{-11}	4.7x10^{-33}
2x10^{11}	8.46x10^8	2.85x10^{-11}	4.91x10^{-33}

large variation in the percentage of device area being illuminated (3 to 38%).

4.3.2 Efficiency Analysis of Nanowire LEDs with Different Areal Densities

The measured external quantum efficiency (EQE) of the four LEDs with varying nanowire densities is plotted in Fig. 4.7 as a function of injection current

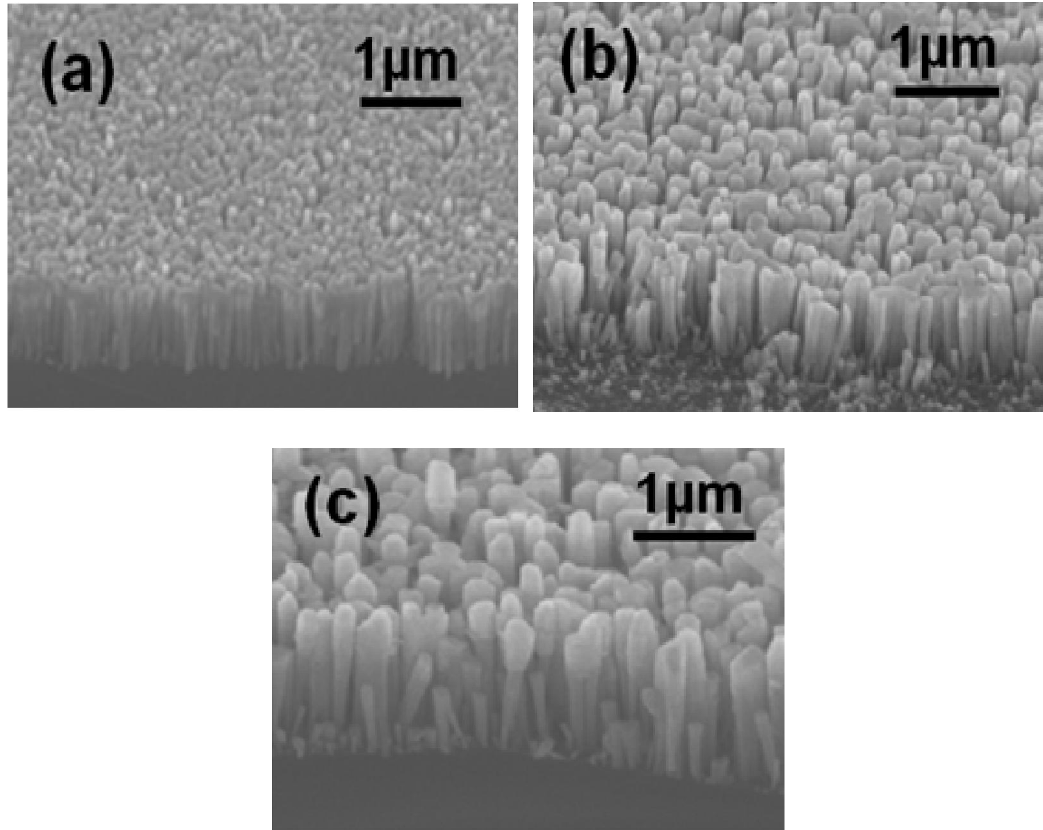

Figure 4.8 45° tilted scanning electron microscopy (SEM) images of GaN $n^{+}p$ nanowire diodes grown on (001) Si substrates with areal densities (a) $10^{11}cm^{-2}$, (b) $7.4x10^{10}cm^{-2}$, and (c) $3.6x10^{10}cm^{-2}$.

density. The injection current density is calculated using the effective area (A_{eff}) of the nanowire LEDs, where A_{eff} is the total area of the device times the nanowire fill factor (FF). The estimated fill factors for the nanowire LEDs, grown with areal densities equal to $2x10^{10}$, $3x10^{10}$, $6x10^{10}$ and $2x10^{11}$ cm^{-2}, are 0.28, 0.32, 0.55, and 0.75, respectively. The best results are obtained with the lowest nanowire density of $2x10^{10}cm^{-2}$. Two features are immediately noticeable. The highest efficiency is achieved in the device with the lowest nanowire density and the current density to reach peak efficiency in this device is also extremely low (~10A/cm^2). The efficiency reduction in this device is ~15% at an injection level of 50 A/cm^2, compared to the

measured maximum efficiency. The data of Fig. 4.7 (dots) have been analyzed with the A-B-C recombination model [106, 107] using the maximum IQEs obtained from temperature dependent PL (TDPL) measurements on the parylene passivated red-emitting (λ=610nm) disk-in-nanowire samples with similar set of areal densities. The values of A, B, and C parameters obtained from the fits to the data (shown alongside with the solid curves) are listed in Table 4.1. Here A, B, and C are, the non-radiative, radiative and Auger recombination coefficients, respectively. It is important to note that the values of C obtained from the analysis for all the samples are ~ $10^{-33} cm^6 s^{-1}$, as predicted from theoretical calculations [108, 109].

4.4 Transient Capacitance Measurements

It is clear from the results presented above that the LED efficiency degrades with increasing nanowire density. We attribute this degradation to the defects generated near the coalescing boundary of nanowires with high areal density. In order to understand quantitatively how nanowire areal density affects the defects density resulting from the coalescence in the self-assembled growth of nanowires, we have performed additional measurements, and the results are described and discussed in the following.

4.4.1 Growth and Fabrication of n^+p GaN Nanowire Diodes

Deep level traps in GaN nanowires were characterized by transient capacitance measurements performed on n^+p GaN nanowire diodes grown on (001) n-type Si. The epitaxy of GaN nanowires was initiated at 800°C under N-rich

conditions. Ga flux was varied from 7.5×10^{-8} to 1.74×10^{-7} Torr to obtain different areal densities of nanowires, and the N flow rate was held constant at 1 sccm. For all three samples, 600 nm of Si-doped n-GaN with a doping concentration of n $\sim1.5\text{x}10^{19}\text{cm}^{-3}$ is grown on an n-type Si substrate, followed by 400 nm of Mg-doped p-GaN with a doping level of p $\sim3\text{x}10^{17}\text{cm}^{-3}$. The nanowire diodes were planarized and passivated with parylene. Using standard optical lithography and metallization techniques, Ni/Au (5 nm/5 nm) and 200 nm indium tin oxide (ITO) were deposited on p-GaN to form ohmic p-contact. Aluminum was deposited on the n-type Si substrate to form the bottom n-contact. The three diodes have nanowire densities of 10^{11}cm^{-2} (Device 1), $7.4\text{x}10^{10}\text{cm}^{-2}$ (Device 2) and $3.6\text{x}10^{10}\text{cm}^{-2}$ (Device 3). The $n^{+}p$ nanowire diodes were grown with similar set of areal densities as those of the fabricated nanowire LEDs to quantitatively investigate the deep level traps characteristics in GaN nanowire. These traps are subjected to nanowire coalescence and responsible for decrease in LED efficiency with higher areal densities. Figures 4.8(a)-(c) show the 45° tilted scanning electron microscopy (SEM) images of the diodes 1, 2, and 3, respectively. Figure 4.9 shows the measured I-V characteristics of all three devices at room temperature along with the schematic representation of the $n^{+}p$ nanowire diode on silicon on the inset. Device 1, grown with the highest nanowire areal density ($\sim10^{11}\text{cm}^{-2}$), has a very high leakage current below the turn-on voltage. Device 3 with the lowest areal density ($\sim3.6\text{x}10^{10}\text{cm}^{-2}$) has the smallest leakage current due to the presence of low defect density in the structure. Additionally, device 3 exhibits a sharp increase in forward current beyond the turn-on voltage, which results in higher currents at low forward voltages compared to those in devices 1 and 2 with relatively

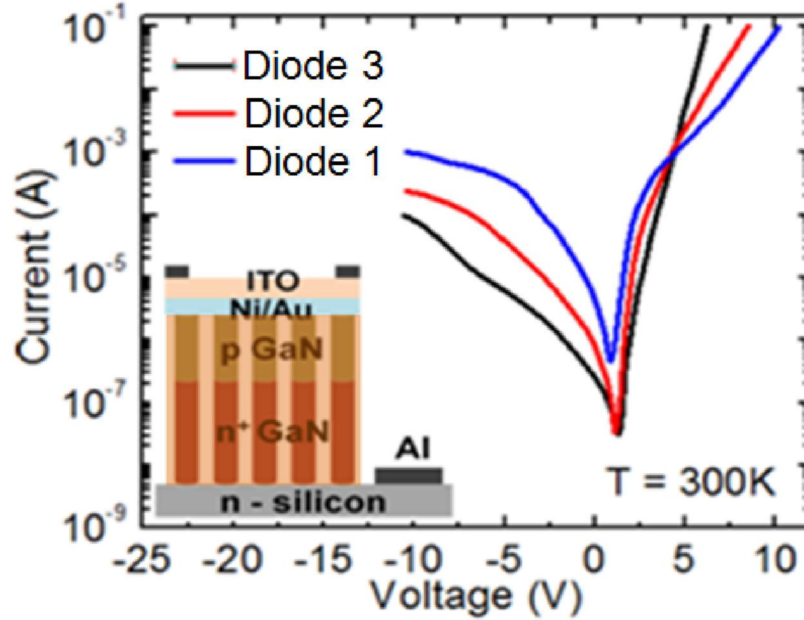

Figure 4.9 Measured room temperature I-V characteristics of the three nanowire n^+p diodes 1, 2 and 3. Inset shows the schematic representation of the fabricated nanowire diode on (001) n-silicon.

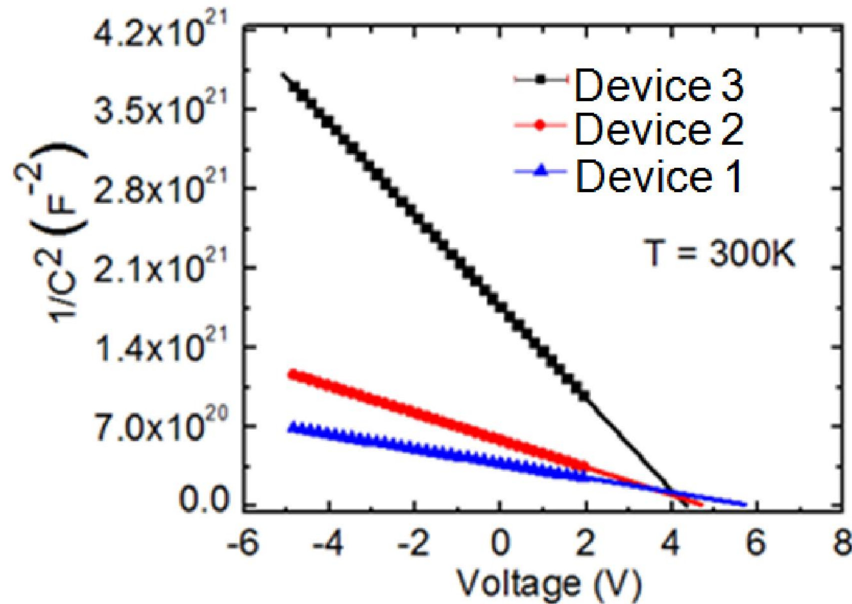

Figure 4.10 Measured $1/C^2$ vs V plots of the nanowire diodes at room temperature. Electrically active doping concentration on the p-side, N_A is derived from the slope of the $1/C^2$ vs V curves to be ~ $3x10^{17}cm^{-3}$ for all three diodes.

higher areal densities. When many defect states are present in the depletion region of

the diode, significant recombination of carriers by trapping in the defect states can occur. This dramatically increases the voltage required to achieve a given level of injection current, therefore increasing the diode forward resistance. The turn-on voltages are ~6V, 5V, 4.5V for devices 1, 2, and 3 respectively with series resistances of ~70Ω, 52Ω and 18Ω, respectively. Figure 4.10 shows the room temperature capacitance-voltage (C-V) characteristics of the n^+p GaN nanowire homojunctions. The dependence of junction capacitance (C) on the bias voltage (V_A) in an n^+p single-sided junction is given by the following relation:

$$1/C^2 = [2/(q\varepsilon_o\varepsilon_s A^2 N_A)](V_{bi}-V_A) , \tag{4.1}$$

where N_A is the carrier concentration on the p-side, ε_s (=8.9) is the static dielectric constant of GaN, A is the effective area of the diode (A= FFx1.5×10^{-3}cm^2, where FF is the nanowire fill factor of the corresponding diode), V_{bi} is the built-in voltage and V_A is the applied bias voltage. V_{bi} is estimated from the intercept of the $1/C^2$ vs V_A curves on the x-axis and the electrically active doping concentration on the p-side, N_A is derived from the slope of the $1/C^2$ vs V_A curves using Eq. (4.1) to be ~ 3×10^{17}cm^{-3} for all three diodes. The doping of the n^+ region is estimated to be 1.5×10^{19}cm^{-3} from Hall measurements on equivalently doped bulk samples.

4.4.2 Electron and Hole Traps in GaN Nanowires

The nanowire diodes were mounted in a closed-loop He cryostat and capacitance transients due to deep level emission were measured by a Boonton 1 MHz capacitance meter for the temperature range of 50K-475K [115]. Both minority

carrier (electron) and majority carrier (hole) traps have been characterized with suitable biasing sequences. Initially, the n^+p nanowire diodes were reverse biased to

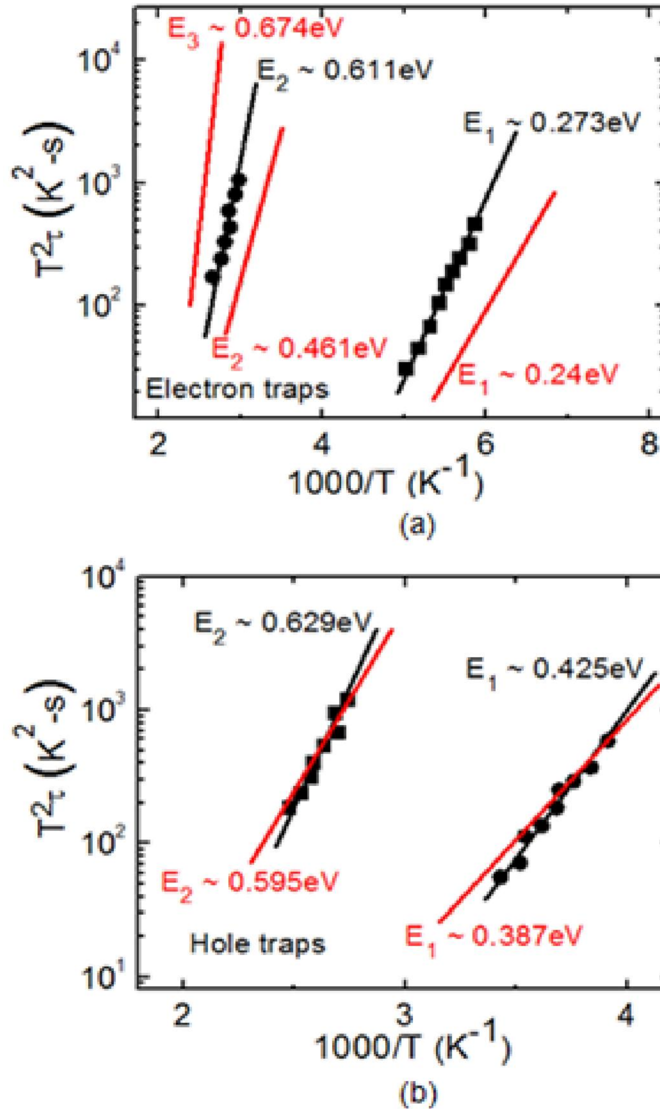

Figure 4.11 Arrhenius plots (with measured data points) for electron traps (a) and hole traps (b) in p-GaN nanowires. The solid lines (red) without data points are Arrhenius plots of deep level traps identified in bulk GaN.

-4V. In order to trace the majority carrier traps (i.e. hole traps) in the depletion region, 0V pulses were applied for 20ms in 200ms cycles across all diodes. The transient data were analyzed to determine the trap activation energy and capture cross-section in

accordance with the equation:

$$1/\tau = \sigma v_{th} N_{c(v)} \exp\left(-\frac{\Delta E}{kT}\right) \qquad (4.2)$$

where τ is the trap emission time constant, v_{th} is the thermal velocity, $N_{c(v)}$ is the density of states in the conduction (valence) band, g is the degeneracy of the trap level, and ΔE and σ are the trap activation energy and capture cross-section, respectively. It is being assumed that ΔE and σ are temperature-independent. Considering the temperature dependence of υ_{th}, and $N_{c(v)}$, Eq. (4.2) can be re-arranged as:

$$\log(T^2\tau) = \Delta E/kT + \gamma \qquad (4.3)$$

where γ is the temperature-independent term. $\mathrm{Log}(T^2\tau)$ is plotted as a function of 1000/T (Arrhenius plots), and the slopes of the resulting straight lines give the activation energies. The Arrhenius plots of the dominant electron and hole traps identified in the nanowire diodes are shown in Figs. 4.11(a) and (b), respectively by the dotted lines (black). The dominant hole traps, observed in all three nanowire diodes, have activation energies $\Delta E_1\sim$ 0.425eV and $\Delta E_2\sim$ 0.629eV. In bulk p-GaN, Gotz *et al.* [116] observed the deep levels at 0.21, 0.39 and 0.41eV and Nagai *et al.* [117] have reported the deep levels at ~0.41, 0.49 and 0.59eV for holes above the valence band. By varying the pulse duration, it has been confirmed that majority (minority) carrier pulses of 20 ms are long enough to completely fill the traps required for deep-level trap concentration measurements. To examine the electron traps in the system, the diodes 1, 2, and 3 were forward biased to 6.5, 5.3 and 4.2V, respectively. The dominant electron traps in samples 1 and 2 were characterized by the activation energies $\Delta E_1\sim$ 0.273eV, and $\Delta E_2\sim$ 0.611eV. Deep levels at energies ~

0.26, 0.4, and 0.62eV [118] and at 0.264, 0.58, and 0.665eV [119] below the conduction band have been previously reported for electrons in GaN epitaxial film. The trap concentration N_T was estimated from the change ΔC in the n^+-p diode

Table 4.2 Characteristics of deep levels in GaN nanowires obtained from transient capacitance measurements.

Nanowire density (cm^{-2})	Electron Traps			Hole Traps		
	ΔE(eV)	σ(cm^2)	N_T(cm^{-3})	ΔE(eV)	σ(cm^2)	N_T(cm^{-3})
Device 1 ($10^{11}cm^{-2}$)	0.273	$6.63x10^{-16}$	$8.32x10^{14}$	0.425	$2.615x10^{-16}$	$4.92x10^{16}$
	0.611	$3.44x10^{-15}$	$4.84x10^{15}$	0.629	$2.198x10^{-16}$	$3.05x10^{16}$
Device 2 ($7.4x10^{10}cm^{-2}$)	0.27	$6.615x10^{-16}$	$1.2x10^{14}$	0.421	$2.61x10^{-16}$	$7.21x10^{15}$
	0.617	$3.33x10^{-15}$	$6.05x10^{14}$	0.625	$2.132x10^{-16}$	$4.195x10^{15}$
Device 3 ($3.6x10^{10}cm^{-2}$)				0.431	$3.38x10^{-16}$	$3.01x10^{15}$
	0.607	$2.824x10^{-15}$	$2.42x10^{14}$	0.632	$3.075x10^{-16}$	$8.34x10^{14}$

capacitance during the trap filling cycle of the applied bias using the equation:

$$N_T = 2(\Delta C/C)N_A \tag{4.4}$$

where C is the capacitance of the diode under quiescent reverse-biased condition, and N_A is the doping concentration on the p side of the junction derived from the C-V measurement. Due to the doping asymmetry of the grown junctions, the deep levels in the lightly doped p-GaN layer are being probed by the capacitance measurements. The background doping in this layer was accurately determined by capacitance-voltage measurements. Both minority carrier (electron) and majority carrier (hole) traps have been characterized with suitable biasing sequences. The activation energy, capture cross-section and density of the traps in devices 1-3 are listed in Table 4.2. It

is immediately apparent that the density of all the identified traps decreases with the decrease of nanowire areal density i.e. with the extent of nanowire coalescence in the sample.

Under high injection conditions ($n = p >> n_i$), the non-radiative recombination coefficient A is related to trap density N_T by the approximate relation: $A \equiv \sigma v_{th} N_T/2$. In Table 4.3, we have listed the values of A (as A_1) for the three LEDs with varying density of nanowires. This is done with the knowledge that the nanowire densities in the three nanowire GaN diodes for trap measurements are very similar to

Table 4.3 Non-radiative recombination coefficients derived from LED efficiency measurements and trap densities.

Nanowire density in LEDs (cm^{-2})	A^a (s^{-1})	Density in GaN diodes (cm^{-2})	A_1^b (s^{-1})	A_2^c (s^{-1})
$3x10^{10}$	$2.98x10^8$	$3.6x10^{10}$	$0.172x10^8$	$2.81x10^8$
$6x10^{10}$	$4.85x10^8$	$7.4x10^{10}$	$0.454x10^8$	$4.4x10^8$
$2x10^{11}$	$8.46x10^8$	10^{11}	$3.515x10^8$	$4.94x10^8$

[a]Derived from LED efficiency measurements [b]Measured from trap concentrations in GaN nanowires
[c]A_2= A-A_1

the nanowire densities in the three LEDs. Also listed in Table 4.3 are the values of A for the three LEDs from Table 4.1, which were derived from the analysis of LED efficiency data (Fig. 4.7). Listed in the last column of Table 4.3 are the difference A_2=(A-A_1) for each device. It is seen that the value of A_1 obtained from the trap concentrations decreases by a factor of 20. We believe, therefore, that the deep level traps originating from the nanowire coalescence account for the large difference in IQE and eventually the large variation in the percentage of the device area being illuminated (3 to 38%). The value of A_2, on the other hand, remains fairly constant

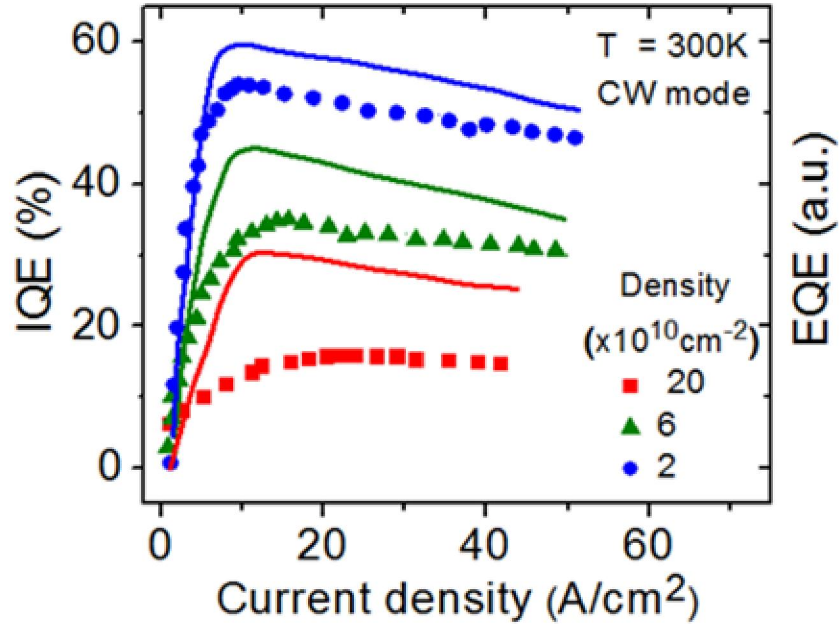

Figure 4.12 Measured external quantum efficiencies of the LEDs with different nanowire areal densities under CW mode of operation. Solid curves represent the calculated internal quantum efficiency (IQE) of the LEDs based on the A-B-C recombination model using non-radiative recombination coefficient A_2 (Table 4.3) which does not consider recombination at deep levels.

and decreases only by a factor of 1.8 as the nanowire density in the LEDs decrease. We believe that this component of the non-radiative recombination results from surface states and other growth related phenomena (such as incorporation of ubiquitous impurities that behave as non-radiative centers). Taking the values of A_2 for the three devices of Table 4.3 and the values of B and C for those devices from Table 4.1, we have calculated the variations of IQE with injection current density. These are depicted in Fig. 4.12 along with measured profiles. The improvement in efficiencies is a result of the absence of deep level traps which, in turn, implies the reduction or absence of nanowire coalescence. The calculated efficiencies also imply that a peak IQE of ~60% could be obtained in the nanowire LEDs for red emission if

the deep traps were absent in the nanowires. This value of IQE is better than that measured for green LEDs with InGaN/GaN quantum wells.

4.4.3 Comparison of Deep Level Electron and Hole Traps in GaN Nanowires and Bulk GaN

To compare the characteristics of the deep levels in GaN nanowires with those in bulk GaN, n^+p bulk GaN diode structures were grown by MBE under optimized growth conditions. These diodes were grown on c-plane n-GaN-on-sapphire templates with a typical dislocation density of $\sim 10^7$ cm^{-2} and having similar thickness and doping concentration in n^+ and p-GaN films as those in the nanowire diodes. Temperature dependent transient capacitance measurements were made on these diodes to investigate the electron and hole traps in the lightly doped p-GaN layer of the device. The background doping in this layer was

Table 4.4 Characteristics of deep levels in bulk GaN obtained from transient capacitance measurements.

Electron traps			Hole traps		
ΔE (eV)	σ (cm^2)	N_T (cm^{-3})	ΔE (eV)	σ (cm^2)	N_T (cm^{-3})
0.24	$5.154\text{x}10^{-16}$	$2.11\text{x}10^{15}$	0.387	$5.08\text{x}10^{-17}$	$3.62\text{x}10^{16}$
0.461	$2.242\text{x}10^{-16}$	$5.12\text{x}10^{15}$	0.595	$1.136\text{x}10^{-16}$	$6.25\text{x}10^{16}$
0.674	$1.22\text{x}10^{-15}$	$4.63\text{x}10^{15}$			

accurately determined by the capacitance-voltage measurements and hall measurements. The dominant electron traps have activation energies $\Delta E \sim 0.24$, 0.461, and 0.674 eV and the hole traps were characterized by $\Delta E \sim 0.387$ and 0.595

eV. The Arrhenius plots of the dominant electron and hole traps identified in the bulk n^+p GaN diodes are shown in Figs. 4.11(a) and (b), respectively by the solid lines (red). The findings, previously reported for electron and hole traps in bulk GaN, are consistent with our observations [116-119]. The activation energy, capture cross-section and density of the traps in bulk GaN diode are listed in Table 4.4. Line and point defects form the core structures of threading dislocation defects in bulk GaN [120-123]. These structural defects which directly or indirectly lead to the dominant traps in the material are located near the edge and screw dislocation lines indicating that trap density can be minimized by reducing these dislocation defects [121]. It is imperative to note that the trap concentrations for carriers (for both electrons and holes) in the nanowire diode 3, which was grown with the lowest areal density to minimize the coalescence in the structure, are more than one order of magnitude smaller than those estimated in bulk GaN diode. It has already been discussed in Chapter II that nanowires grown on Si substrates have relatively low defect density compared to epitaxial GaN film grown on lattice mismatched sapphire or SiC substrates. This is because of the removal of epitaxial requirement at the GaN/Si interface by the growth of thin amorphous Si_3N_4 layer and radial strain relaxation during nanowire epitaxy due to their large surface to volume ratio. Moreover, nanowire areal density was reduced to impede the formation of deep level traps resulting from the coalescing nanowires. It may be noted that the activation energies of the electron and hole deep level traps in bulk GaN are very similar to those for the traps in the nanowire devices. In fact, for the hole traps, the Arrhenius plots are almost coincident [Fig. 4.11(b)]. The origin of the traps may, therefore, be very

similar, i.e., misfit dislocations and stacking faults due to coalescing of impinging nanowires in the nanowire GaN diodes.

4.5 Summary

In conclusion, we have examined the effect of nanowire coalescence that occurs when the nanowire areal density is increased above a certain range. High-resolution transmission electron microscopy reveals that such coalescing leads to zipper-like arrays of threading dislocations and stacking faults near the coalescing nanowire boundaries. To investigate the effects of nanowire coalescence on the optical properties of disks-in-nanowires (DNWs), radiative efficiency of InGaN disks in GaN NWs with different areal densities have been measured. It is observed that radiative efficiency is the lowest for the highest density DNW sample. Red-emitting nanowire LEDs were fabricated with different areal densities, and the LEDs with the lowest optimum density demonstrated the highest peak efficiency. Near-field images of the electroluminescence of these LEDs reveal that only a small percentage of the device area (~3%) is lighting up when the areal density was increased to as high as $2x10^{11}cm^{-2}$. We have characterized deep level electron and hole traps in GaN nanowires and bulk GaN. Transient capacitance measurements were performed on planar GaN and GaN nanowire $n^{+}p$ diodes, grown with the similar set of areal densities as that of the nanowire LEDs, to investigate the trap characteristics in these structures. Deep level traps are compared which reveal that the activation energies for the electron and hole traps in them are similar. This observation leads to the fact that the origin of these trap levels in these structures are similar, including stacking faults,

dislocations, etc. The dependence of the trap density in nanowires on their areal density i.e. the degree of nanowire coalescence is studied. It is found that the density of these traps, which act as non-radiative recombination centers for carriers, increases steadily with increase of nanowire density. It is believed that the traps ultimately originate from the defects arising from nanowire coalescence and account for a relatively low IQE and a significant fraction of the nanowires not being illuminated with injection in LEDs. Injected electrons and holes in the LEDs with high nanowire density can recombine non-radiatively in these traps in the GaN region before reaching the InGaN disks. They can also do that in the InGaN active region after reaching there and therefore reducing the external quantum efficiency of the device. The absence of the traps would result in a peak IQE of ~60% in the red nanowire LEDs. Therefore, in the self-assembled growth of nanowires areal density plays a significant role on the device performance. An optimized areal density of 2×10^{10} cm^{-2} was determined experimentally at which red nanowire LEDs have demonstrated the best performance in terms of peak efficiency. Similar nanowire density was chosen when the nanowire LEDs with optimized performances were presented and characterized in chapter III. It is important to note that too low an areal density will result in a significantly reduced light output from the devices. This study on optimized areal density for reduced nanowire coalescence will be beneficial for the growth of nanowire laser heterostructure on silicon in Chapter VI.

Chapter V

Phosphor-Free Monolithic InGaN/GaN Disk-in-Nanowire Tunable Light Emitting Diodes on (001) Silicon

5.1 Introduction

White light emitting diodes (LEDs) are systematically replacing incandescent bulbs and fluorescent lighting for a host of outdoor and indoor lighting applications due to the advantages of low power consumption and long lifetime [2, 124]. Monolithic planar white LEDs consisting of InGaN/GaN quantum wells, based on both direct electrical injection [8, 125-128] as well as optical pumping in a converter scheme [129], have been reported. Since long wavelength LEDs (λ > 600nm) incorporating III-nitride quantum well (QW) active regions with high radiative efficiency are still in a developmental stage, the most common approach for realizing a solid state white LED is to have a blue-emitting LED optically pump a yellow phosphor [130, 131], or have an ultraviolet (UV) LED excite rare earth doped blue-, green-, and red-emitting phosphors [131]. However, phosphor-converted white LEDs have distinct disadvantages. The conversion is inevitably accompanied by losses due to Stokes shift and non-radiative internal losses [132]. Backscattering of both pump and converted light by the phosphor gives rise to additional optical loss. Heating-related effects and the long-term reliability of the phosphors are additional

detrimental factors [133-136]. As discussed earlier, InGaN/GaN disks-in-nanowires (DNWs) have advantages over planar InGaN quantum wells (QWs) as the active medium in visible LEDs and lasers. Red emission with high radiative efficiency is still lacking in InGaN QWs. This is a major bottleneck for the realization of a direct injection or wavelength conversion device for emitting warm (soft) white light with low correlated color temperatures. A white nanowire LED, based on direct electrical injection, having optimized blue, green and red-emitting InGaN disks-in-nanowires in the heterostructure or a monolithic semiconductor-based wavelength converter white LED are, therefore, desirable alternatives. Additionally, InGaN/GaN self-organized quantum dots (QDs), grown in the Stranski-Krastanow mode by strain relaxation [137], have significantly smaller piezoelectric polarization field and associated quantum-confined Stark effect (QCSE) than those in comparable planar QWs [107, 138]. Therefore, radiative carrier lifetimes in the dots are 10-100 times smaller than those in the wells [97, 107, 139]. Moreover, the quasi-three dimensional confinement of carriers in the InGaN/GaN QDs can reduce the rate of non-radiative recombination of carriers at dislocations and related defects. We have demonstrated red-emitting (λ = 630nm) $In_{0.4}Ga_{0.6}N$/GaN self-organized quantum dot lasers, including a detailed characterization of their DC and small- and large-signal modulation properties [139-141]. We have also reported the characteristics of green-emitting (λ = 524nm) QD light emitting diodes [107] and lasers [37].

This chapter describes all-nitride electrically injected tunable InGaN/GaN disk-in-nanowire white light emitting diodes incorporating blue-, green- and red-emitting InGaN disks in the active region. The shift in correlated color temperature of

white emission with the variation of injection current density is investigated. Tunability of chromaticity coordinates and correlated color temperature (CCT) of the white emission from the nanowire LEDs have been studied by varying the number of blue and red-emitting InGaN disks and the peak emission wavelengths of blue-, green- and red-emitting InGaN disks. The chapter also describes the growth and characteristics of phosphor-free self-organized InGaN/GaN quantum dot wavelength converter white LEDs on c-plane GaN-on-sapphire templates and compared the white emission from them with that from the nanowire white LEDs. Blue-emitting pump quantum dots, in which carriers are injected electrically, are used to optically excite red-emitting converter dots to make the appearance of a white light. Tunability of color temperatures of the white emission from these wavelength converter LEDs is examined by changing the number and emission wavelengths of pump/converter dot layers. Stability of color temperatures with injection currents into the pump dots is also discussed.

5.2 Different Schemes for White Light Emitting Diodes (LEDs)

White LED can be made in two ways. The first approach involves monolithic integration of different color-emitting active regions in the device heterostructure based on direct electrical injection. The other method is by wavelength conversion where a short wavelength light, emitted from a region in which carriers are injected electrically, optically excites a longer wavelength-emitting layer to create white emission. Phosphor-free monolithic planar white LEDs consisting of different color-emitting InGaN/GaN quantum wells, based on direct electrical injection, have been

reported in the literature. Damilano *et al.* [125] have demonstrated white LEDs based on $In_xGa_{1-x}N$ (x = 0.15–0.2)/GaN multiple-quantum wells (MQWs) on sapphire substrates, where wavelength emission from the wells can be tuned from blue to orange by increasing the QW thickness. White emission from the LEDs has been obtained by combining several QWs of various thicknesses. In this scheme, the color coordinates for the white emission in the (blue + yellow) dual color LEDs are x = 0.29, y = 0.31, which correspond to a color temperature of 8000 K. Yamada *et al.* [126] have shown two types of white LEDs composed of InGaN multi-quantum wells in the active region. One type of white LEDs emits light of two colors (blue and yellow) from the MQW active region, while the other type emits light of three colors (blue, green and red). The first type of LEDs has a white emission with CCT of 7600 K, whereas the second type has a lower CCT of 5060 K due to the presence of the red emission. Huang *et al.* [8] have reported phosphor-free white LEDs with blue and yellow-emitting InGaN/GaN multi-QWs with a color temperature of 5600K for the white emission. Park *et al.* [127] have demonstrated white LEDs fabricated with laterally distributed blue and green InGaN/GaN MQWs grown by a selective area growth method. Parallel carrier injection into both the MQWs regions provided the stability of the white emission with injection currents. Lee *et al.* [128] have shown monolithic white LEDs by incorporating five blue-emitting InGaN/GaN QWs and a single InGaN/GaN QW with In-phase separated green/amber emissions in the active region. Electrically injected white nanowire LEDs having different color-emitting InGaN disks/dots within GaN barriers with correlated color temperatures (CCT) of 5500-6500K [55] and ~5000K [62] for white emission have been reported by us and

other groups. Tunability of white emission of such nanowire white LEDs by varying the number and the peak emission wavelengths of the InGaN disks was absent in the literature and is presented in this chapter. Planar InGaN/GaN QWs white LEDs with wavelength conversion technique is also investigated. Damilano *et al.* [129] demonstrated a blue-emitting LED grown on top of InGaN/GaN multiple QWs acting as a light converter from blue to green-yellow wavelength. The blue light, produced by the electrical injection of carriers in the wells, optically pumped the green-yellow emitting QWs. The white emission is characterized with a CCT of 5683K. Though red-emitting QWs were incorporated in the active region of some of the InGaN QW white LEDs mentioned above, growth of planar red QWs with high radiative efficiency is still in a development stage which affects the efficiency of these white LEDs in an adverse way. Besides, due to the substantial blue shift in peak emission because of the large strain induced polarization field in the planar InGaN QWs especially with high indium content, significant change in CCT with injection current is usually observed, both in direct electrical injection and wavelength conversion schemes. To overcome these issues with wavelength converter QW white LEDs, the most common approach is to use short wavelength nitride LED to optically pump different color phosphors. Sheu *et al.* [131] have reported phosphor-converted white LEDs fabricated by precoating blue/green/red phosphors on near-UV LEDs. The color temperature of the white emission was around 5900K. Carriers are electrically injected into UV LED, which then optically excites blue-green-red phosphors to create white emission. No changes in color temperature were observed with the increase in injection currents. Phosphor-converted white light emitters with blue

LEDs optically pumping yellow phosphors have also been reported [130, 131]. However, phosphor-converted white LEDs have some disadvantages, which will be discussed in the subsequent section.

5.3 Problems with Phosphor-Converted White LEDs

In phosphor-converted white LEDs, heat is generated by the phosphor layer due to Stokes shift and light absorption, which can increase the chip junction temperature as well as the temperature of the phosphor itself [8]. It has been shown that depending on CCTs of white emission, ~25% to 45% of radiant power emitting from the LED is converted into heat by phosphor. Heat produced by the phosphor layer needs to be dissipated efficiently to improve the lifetime and efficiency of the device. Heat generated in the phosphor layer can lead to an order of magnitude reduction in the phosphor emission due to the thermal quenching effect [127], along with other detrimental effects including lifetime reduction [128], emission wavelength shift [129], silicone yellowing [131] and silicone carbonization [132]. On the whole, high temperature causes rapid degradation of phosphors and lowers the overall efficiency of the LEDs. It is also found that high humidity can result in a significant reduction in the conversion efficiency of phosphors [142].

5.4 Growth of All-Nitride Monolithic InGaN/GaN Disk-in-Nanowire White LED Heterostructures on (001) Silicon

To grow phosphor-free monolithic InGaN/GaN disk-in-nanowire (DNW) white LEDs, we incorporated blue-, green-, and red-emitting InGaN disks in the same heterostructures. In order to investigate the tunability of white emission, we have

grown four white LED heterostructures-- A, B, C and D. In LED A, the blue, green and red-emitting InGaN disks have emission wavelengths of 430nm, 525nm, and 610nm, respectively, whereas they are 460nm, 550nm, and 650nm, respectively for LEDs B to D. Before incorporating the InGaN disks in the LED heterostructure, their radiative efficiency have been optimized by varying the growth parameters in the MBE system (such as substrate temperature and In-to-total group III flux ratio, etc.) using temperature dependent photoluminescence measurements (TDPL). The radiative efficiency of the InGaN disks was further improved by 10-12% upon parylene surface passivation as mentioned in Chapter II. A detailed description on how the radiative efficiency of the InGaN nanowires have been improved by growth optimization and surface passivation can be found in the same chapter. After growth optimization inside MBE and parylene passivation of surface states on the nanowires, the optimized radiative efficiencies of the blue, green and red-emitting InGaN disks were measured to be ~ 56%, 54% and 52%, respectively. The normalized room temperature photoluminescence (PL) intensities of the optimized blue, green and red-emitting InGaN disks, which were used in LED A, have been depicted in Fig. 5.1(a) and those from the InGaN disks used in the rest of the LEDs (B, C, D) have been shown in Fig. 5.1(b). From energy-dispersive X-ray (EDX) measurements, indium compositions in the blue (λ=430nm), green (λ=525nm) and red-emitting (λ=610nm) InGaN disks, used in LED A, were estimated to be ~22%, 38% and 51%, respectively. In LEDs B, C and D they were ~28%, 42%, and 55% for the blue (λ=460nm), green (λ=550nm) and red-emitting (λ=650nm) InGaN disks, respectively. Monolithic InGaN/GaN disk-in-nanowire LED heterostructures, as

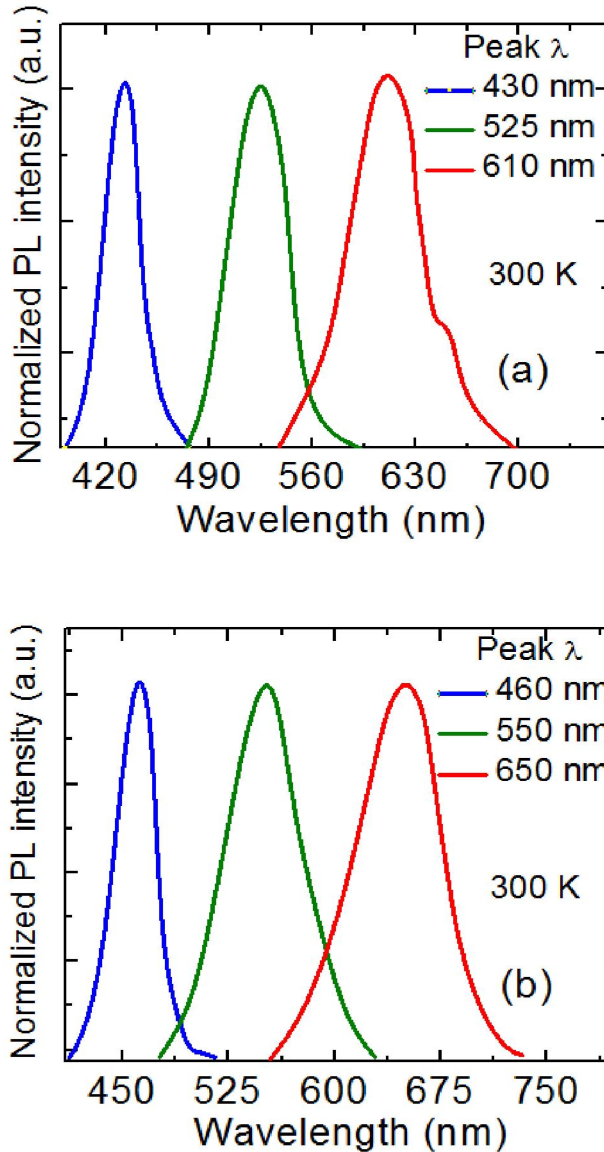

Figure 5.1 (a) Normalized room temperature photoluminescence (PL) intensities of the optimized blue, green and red-emitting InGaN disks those have been used in LED A, (b) Normalized PL intensities of the optimized blue, green and red-emitting InGaN disks at 300K those have been used in LEDs B, C and D.

shown schematically in Fig. 5.2, were grown on (001) n-type silicon substrates by plasma assisted molecular beam epitaxy (PA-MBE) system equipped with standard Ga, In, Al, Mg and Si effusion cells and a UNI-bulb nitrogen plasma source. The nanowire heterostructures have an areal density of $\sim 2 \times 10^{10}$ cm^{-2} and average diameter of ~45 nm. The growth temperatures were monitored by an infrared pyrometer,

calibrated by (1x1) to (7x7) reflection high energy electron diffraction (RHEED) pattern transition on silicon. An n-doped ($5x10^{18}cm^{-3}$) 300 nm GaN region was first grown at a substrate temperature of 800°C on (001) n-silicon. Then three groups of InGaN disks (~2 nm)/GaN barriers (~12 nm), each having four InGaN disks, were grown for LEDs A and B. To study the tunability of white emission further, the number of blue and red-emitting InGaN disks was varied in LEDs C and D, which will be discussed later. At first, optimized red-emitting InGaN disks were grown at a substrate temperature of ~540-555°C, followed by the growth of green, and blue-emitting InGaN disks at substrate temperatures of ~570-580°C and ~610-620°C, respectively. Indium-to-total group III flux ratio was varied to obtain different emission wavelengths. Next, 15 nm p-doped $Al_{0.15}Ga_{0.85}N$ electron blocking layer (EBL) was grown to reduce the leakage of electrons from the active region. Finally, 150 nm thick p-GaN region (p~ $7x10^{17}$ cm^{-3}) was grown at a substrate temperature of 700°C. The Mg flux was increased during the growth of the final 20 nm of p^{+}GaN to achieve a better ohmic contact.

5.5 Fabrication of Nanowire White LEDs

Four LEDs (A, B, C and D) were fabricated varying the number of blue- and red-emitting InGaN disks and the emission wavelengths of the disks to study the tunability of white emission. At first, as-grown nanowire device heterostructures were dry-etched by reactive ion etching (RIE) to have mesa shapes with dimensions of 600µm x 600µm. Then the nanowires were planarized and passivated with parylene, which was deposited by thermal evaporation at room temperature. Using standard

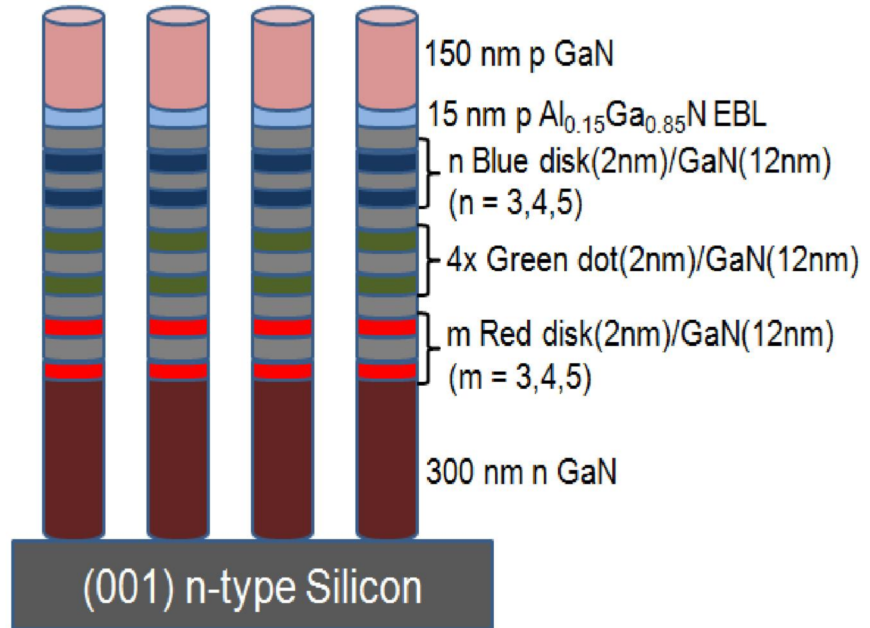

Figure 5.2 Schematic representation of InGaN/GaN disk-in-nanowire white LED heterostructures grown on (001) silicon. The number of blue- and red-emitting InGaN disks and the emission wavelengths of the disks were varied to investigate the tunability of white emission.

photolithography and metallization techniques, transparent indium tin oxide (ITO) current spreading layer was deposited on top of p-GaN and the ITO layer was annealed at 500°C for 1 min under Ar environment to form the p-contact. Finally, Al/Au (100nm/150nm) was deposited by e-beam evaporation on top of the n-silicon region to form the n-contact of the device. Carriers are electrically injected from the p- and n-contacts of the device that recombine in the InGaN/GaN disks-in-nanowire active regions emitting blue, green and red lights- together they create the appearance of white emission. Flip-chip processing, as mentioned in Chapter III, was not tried in the fabrication of these white nanowire LEDs. If the flip-chip processing can be optimized and used in the fabrication of these devices, more light is likely to come out which should increase the overall efficiency of the white LEDs.

5.6 Output Characteristics of Nanowire White LEDs

5.6.1 Current-Voltage Characteristics and Electroluminescence of White LEDs

Figure 5.3(a) shows room temperature current-voltage characteristics of the fabricated nanowire LEDs. The diodes have a series resistance of ~33Ω and a turn on

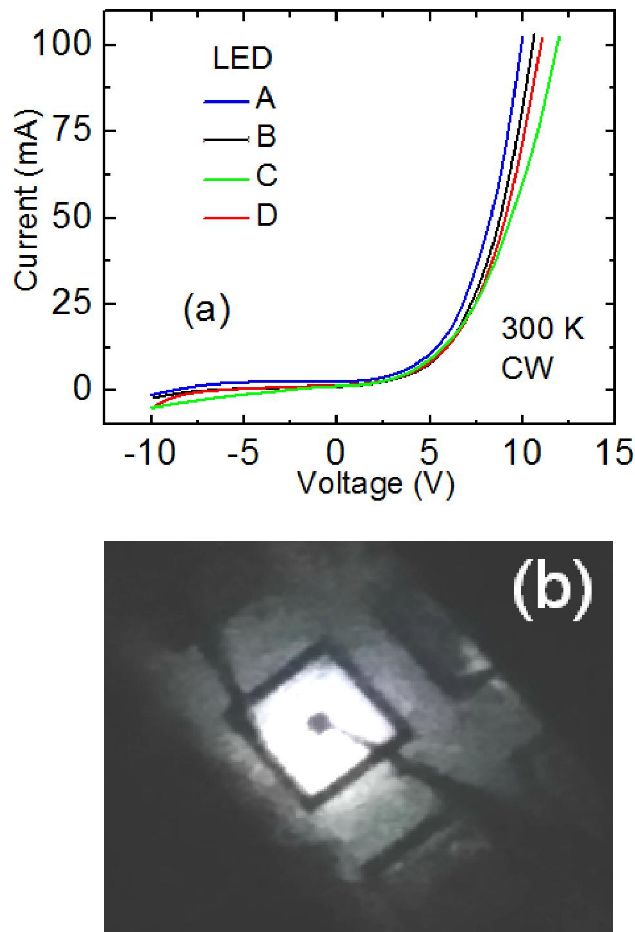

Figure 5.3 (a) Room temperature current-voltage characteristics of the fabricated LEDs (A to D), (b) optical micrograph of LED B at an injection current density of 60A/cm^2.

voltage of ~6-7 V. Figure 5.3(b) depicts an optical micrograph of LED B at injection current density of 60A/cm^2. Room temperature electroluminescence (EL) of the

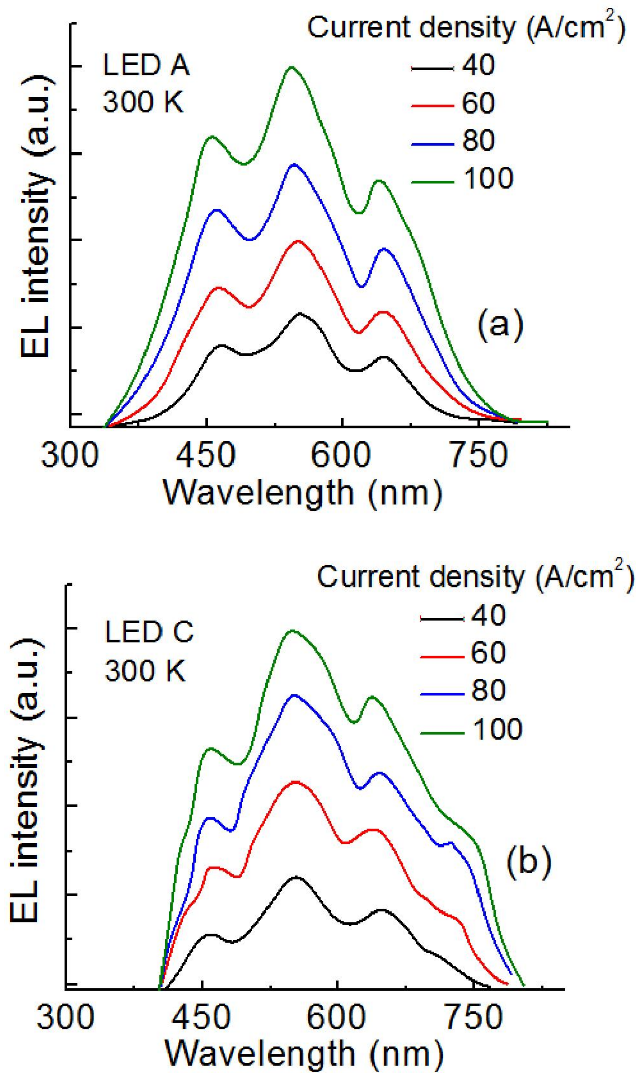

Figure 5.4 Room temperature electroluminescence (EL) intensities of (a) LED A and (b) LED C as a function of injection current density.

LEDs A and C as a function of injection current density are shown in Figs. 5.4(a) and 5.4(b), respectively. In Fig. 5.4(a), for LED A, three peaks corresponding to blue (λ=430nm), green (λ=525nm) and red-emitting (λ=610nm) InGaN disks are visible, whereas in Fig. 5.4(b), for LED C, these three peaks were observed at λ=460nm, 550nm and 650nm, respectively. With increase in injection current density from 40A/cm^2 to 100A/cm^2, a small blueshift of EL peak was observed for all emission

wavelengths. This results from the screening of the polarization fields in the InGaN disks. In LED A, these blueshifts were ~4.5, 7 and 13.2 nm, for blue, green and red

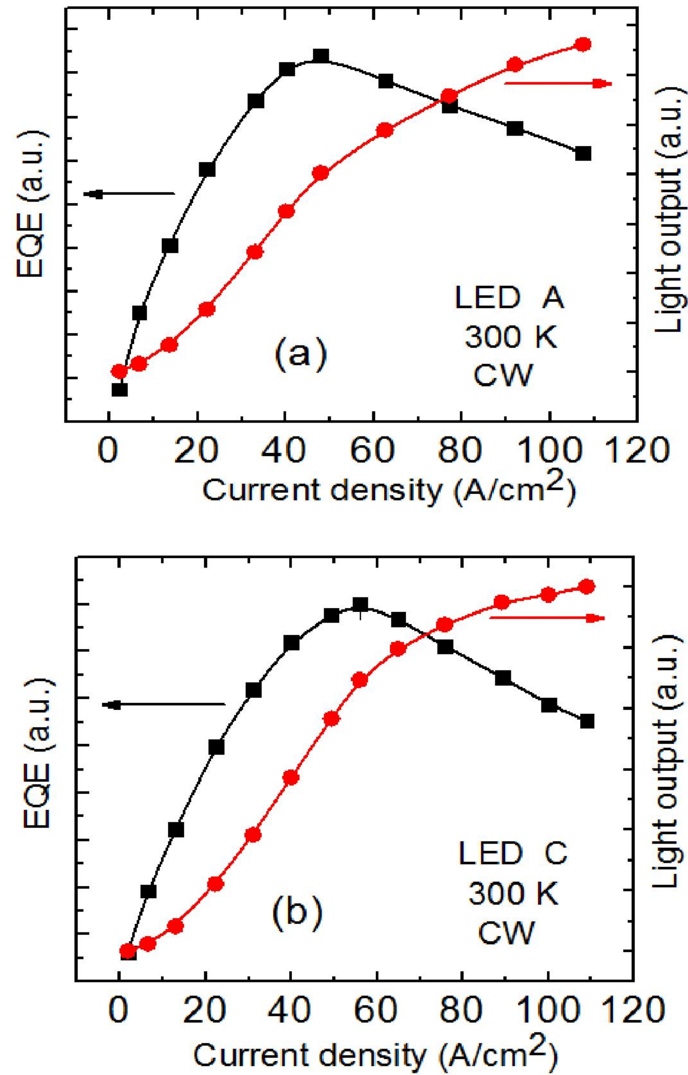

Figure 5.5 Room temperature light-current characteristics and external quantum efficiencies (EQE) of (a) LED A and (b) LED C as a function of injection current density.

EL peaks, respectively which correspond to calculated polarization fields of 396

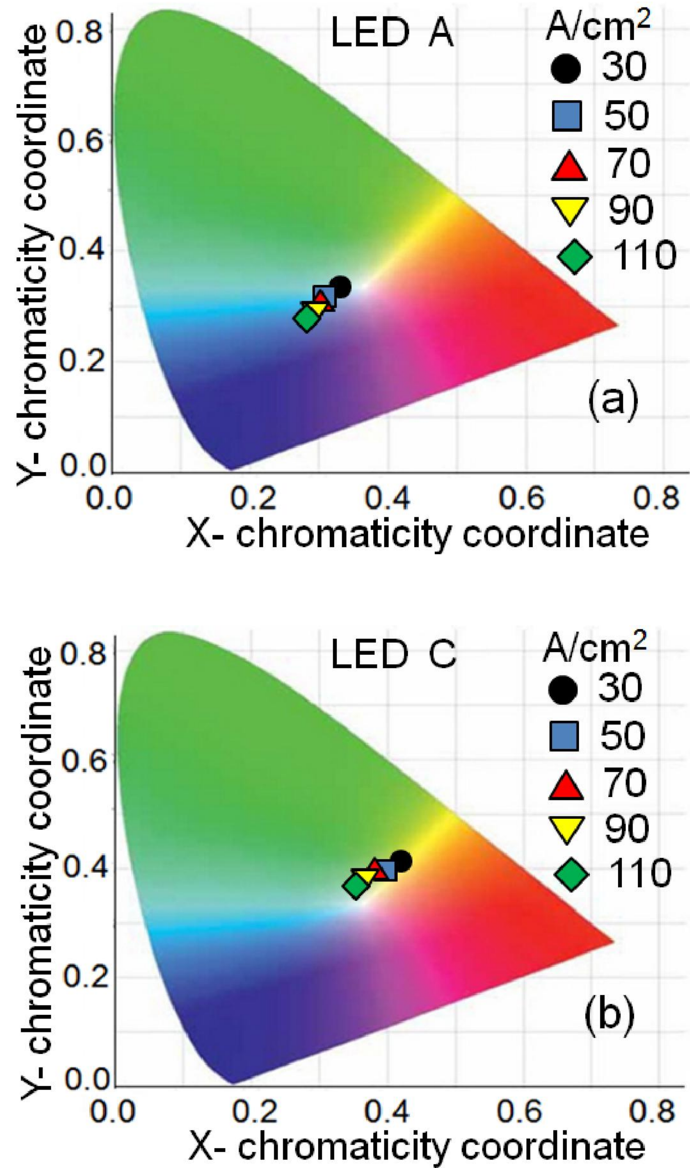

Figure 5.6 XY Chromaticity coordinates of white light emission from (a) LED A, and (b) LED C with variation of injection current density from 30A/cm^2 to 110 A/cm^2.

kV/cm, 588 kV/cm and 1050 kV/cm, respectively. Blueshifts for blue, green and red EL peaks were measured to be ~5, 7.5 and 15 nm, respectively in LED C. These correspond to calculated polarization fields of 427 kV/cm, 610 kV/cm and 1260 kV/cm, respectively. All these blueshifts in EL peaks with increasing injection current density are significantly smaller than those reported for comparable planar

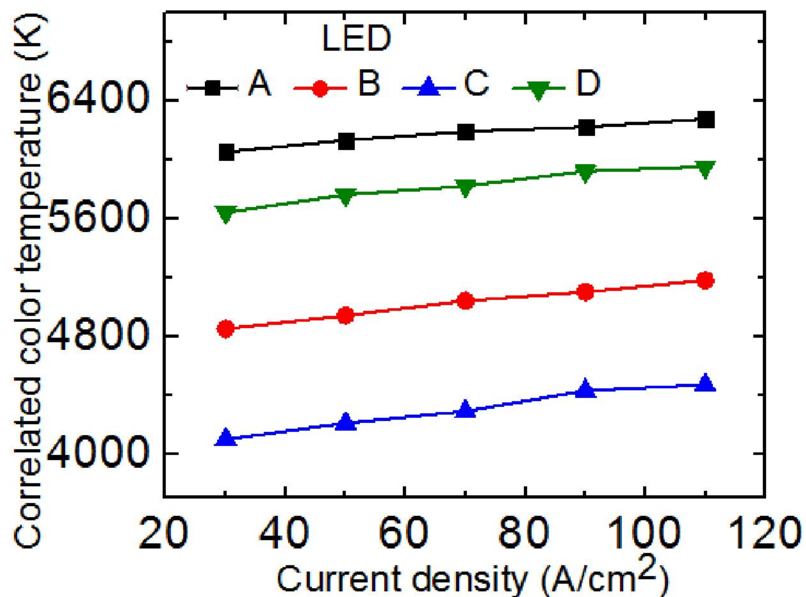

Figure 5.7 Variation of correlated color temperatures of the white emission for different white nanowire LEDs as a function of injection current density from 30A/cm^2 to 110 A/cm^2.

InGaN quantum wells [104, 143]. The smaller polarization field in the InGaN disks in GaN nanowires is a consequence of their large surface-to-volume ratio and radial strain relaxation during epitaxy. The measured light-current (L-I) characteristics and the corresponding external quantum efficiency (EQE) of LEDs A and C are depicted in Fig. 5.5(a) and 5.5(b), respectively. The efficiency reaches its peak value at injection current densities of 47A/cm^2 and 55A/cm^2 in devices A and C, respectively. A reduction of 14% in efficiency at an injection level of 100A/cm^2 was observed in LED A, where it was 22% at 100A/cm^2 for LED C.

5.6.2 Correlated Color Temperatures (CCT) of White Emission

Electroluminescence (EL) intensities of the white nanowire LEDs were recorded with Ocean Optics USB2000+ optical spectrum analyzer (with an optical

Table 5.1 Chromaticity coordinates and color temperatures of white emission for LEDs A and B, where emission wavelengths of InGaN disks were varied.

*LEDs	Blue disks λ (nm)	Green disks λ (nm)	Red disks λ (nm)	Chromaticity coordinates X	Chromaticity coordinates Y	CCT (K)
A	430	525	610	0.31	0.31	6130
B	460	550	650	0.35	0.37	4940

*Each LED has 4 blue, 4 green and 4 red-emitting InGaN disks.

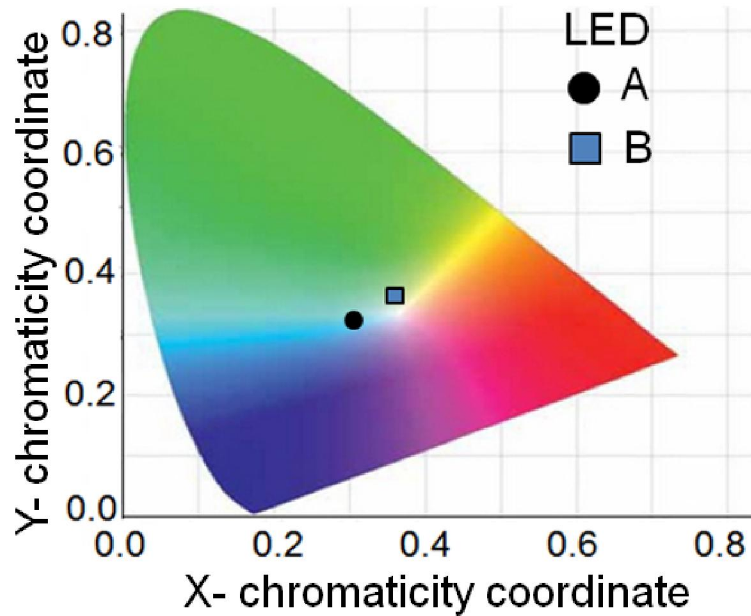

Figure 5.8 Variation of chromaticity coordinates of the white emission changing the emission wavelengths of the blue, green and red-emitting InGaN disks in LEDs A and B. The numbers of blue, green and red-emitting InGaN disks were kept same in both the devices.

resolution of 0.3 nm) to derive the Commission Internationale de I'Eclairage (CIE) chromaticity coordinates and correlated color temperatures (CCT) of white light emission. As shown in Figs. 5.6(a) and 5.6(b), respectively, with increase in injection current density from $30A/cm^2$ to $110A/cm^2$ the CCT of device A changes by 220K, from 6050K to 6275K, and the CCT of device C changes by 370K, from 4100K to

Table 5.2 Chromaticity coordinates and color temperatures of white emission for LEDs B, C and D where number of InGaN disks were varied.

*LEDs	Number of blue disks	Number of green disks	Number of red disks	Chromaticity coordinates X	Chromaticity coordinates Y	CCT (K)
B	4	4	4	0.35	0.37	4940
C	3	4	5	0.4	0.39	4210
D	5	4	3	0.32	0.33	5760

*Blue, green and red-emitting InGaN disks have emission wavelengths of 460nm, 550nm and 650nm, respectively.

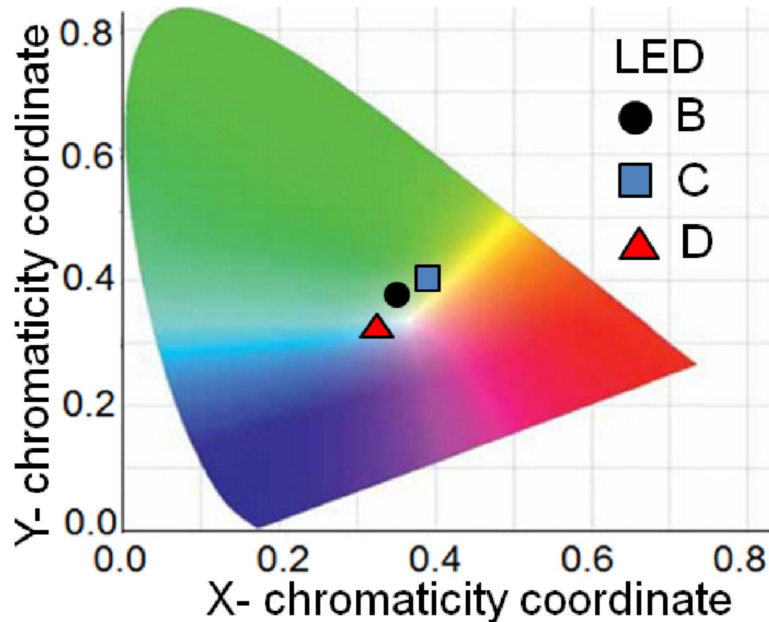

Figure 5.9 Variation of chromaticity coordinates of the white emission changing the number of blue and red-emitting InGaN disks in LEDs B, C and D. Emission wavelengths of the blue, green and red-emitting InGaN disks were kept same in all the devices.

4470K. These results indicate better temperature stability of white light emission with injection current than that reported for planar InGaN/GaN multi-quantum well wavelength converter white LEDs [129]. Small blueshifts in the EL peak emissions

from the blue, green and red-emitting InGaN disks in the LED heterostructure with increasing injection current contribute to the small increase in color temperature. The dependence of the correlated color temperature (CCT) on injection current density for devices A-D is illustrated in Fig. 5.7.

5.6.3 Tunability of White Emission

In our study, we have used the number of blue and red-emitting InGaN disks and the peak emission wavelengths of blue-, green and red-emitting InGaN disks, as tuning parameters for the chromaticity coordinates and correlated color temperature (CCT) of the emitted white light. We first varied the emission wavelengths of the InGaN disks in LEDs A and B to tune the CCT of white light. The chromaticity coordinates and CCT for devices A and B at an injection current density of $50A/cm^2$ are listed in Table 5.1 and illustrated in Fig. 5.8. By increasing the emission wavelengths of the InGaN disks from LED A (blue (λ=430nm), green (λ=525nm), red (λ=610nm)) to LED B (blue (λ=460nm), green (λ=550nm), red (λ=650nm)), the CCT for white light emission decreases by 1190K, with values of 6130K and 4940K for devices A and B, respectively, at a current density of 50 A/cm^2. To observe the dependence of tunability of white emission on the combination of InGaN disks, we then varied the number of blue and red-emitting InGaN disks in the structures keeping the same emission wavelengths as those in LED B. Where LED B has four blue, four green and four red-emitting disks, device C and D have the same number of green disks as that of device B, but LED C has three blue and five red, and LED D has five blue and three red disks. The chromaticity coordinates and CCT for devices

B-D at an injection current density of 50A/cm^2 are listed in Table 5.2 and illustrated in Fig. 5.9. By increasing the number of red disks (five) over blue ones (three) in device C, keeping the same emission wavelengths as those of LED B, the CCT has been reduced by 730K to a value of 4210K at a current density of 50A/cm^2. By increasing the number of blue disks (five) over red ones (three) in device D, the CCT has been increased by 820K to a value of 5760K at a current density of 50A/cm^2. By increasing the emission wavelengths of the InGaN disks further in the nanowire white LEDs, CCT of less than 4210K can be achieved. Correlated color temperatures (CCT) of white emission with values of 5500-6500K [55] and ~5000K [62] for electrically injected InGaN disks/dots in GaN nanowire LEDs have been reported by us and other groups before. In this work, for the first time, we have demonstrated the tunability of white emission of such nanowire white LEDs by varying the number of blue- and red-emitting InGaN disks and the peak emission wavelengths of blue-, green- and red-emitting InGaN disks. The desirable values of CCT for high efficiency cool white and warm (soft) white light are ~ 4500K and ~ 3000K, respectively. These values of CCT would be difficult to achieve with planar all InGaN quantum well electrically injected or wavelength converter white LEDs. Because, long wavelength (λ > 600nm) emission with high radiative efficiency is difficult to achieve with such planar InGaN/GaN quantum wells due to increasing material inhomogeneities [56, 57] and a strong polarization field [58]. Due to the low radiative efficiency of the red-emitting planar InGaN quantum wells, red light component of the white light remains low in the QW based devices—increasing the CCT of white emission from LEDs. Therefore, electrically injected monolithic phosphor-free InGaN/GaN disk-in-

nanowire white LEDs may play a significant role in the realization of tunable white light sources.

5.7 Phosphor-Free Monolithic InGaN/GaN Quantum Dot (QD) Wavelength Converter White LEDs

5.7.1 Growth and Fabrication of QD White LED Heterostructures

Phosphor-free InGaN/GaN QD wavelength converter white LEDs, as shown schematically in Fig. 5.10(a), were grown on c-plane GaN-on-sapphire templates in a Veeco Gen 930 plasma assisted molecular beam epitaxy (PA-MBE) system. An n-doped ($5x10^{18}cm^{-3}$) 300nm GaN buffer layer was first grown at a substrate temperature of 720^oC on c-plane n-GaN-on-sapphire templates for all samples. Multiple layers of self-organized InGaN/GaN QDs with 12nm GaN barrier layers were grown as the long-wavelength converter over the n-GaN buffer layer under nitrogen rich condition at $541\text{-}550^oC$. This was followed by the growth of 150nm n-GaN layer ($n\sim7.5x10^{18}cm^{-3}$) at 720^oC, multiple InGaN/GaN QD layers with 16nm GaN barrier layers for blue emission grown at $T=585\text{-}592^oC$, 15nm p-$Al_{0.15}Ga_{0.85}N$ electron blocking layer (EBL) and finally a 120nm p-GaN ($p\sim7x10^{17}cm^{-3}$) layer grown at 680^oC. The Mg flux was increased during the growth of the final 20 nm of p^+GaN to achieve a better ohmic contact. The number of exciting and converter dot layers was carefully optimized to obtain true white emission. Also, the InGaN thickness to form the dots, the GaN barrier thickness and an interruption period under nitrogen flux were all optimized to maximize the dot radiative efficiency. Five device heterostructures were grown to investigate the tunability of white light emission from

the LEDs by varying the number of exciting and converter $In_xGa_{1-x}N$ quantum dots

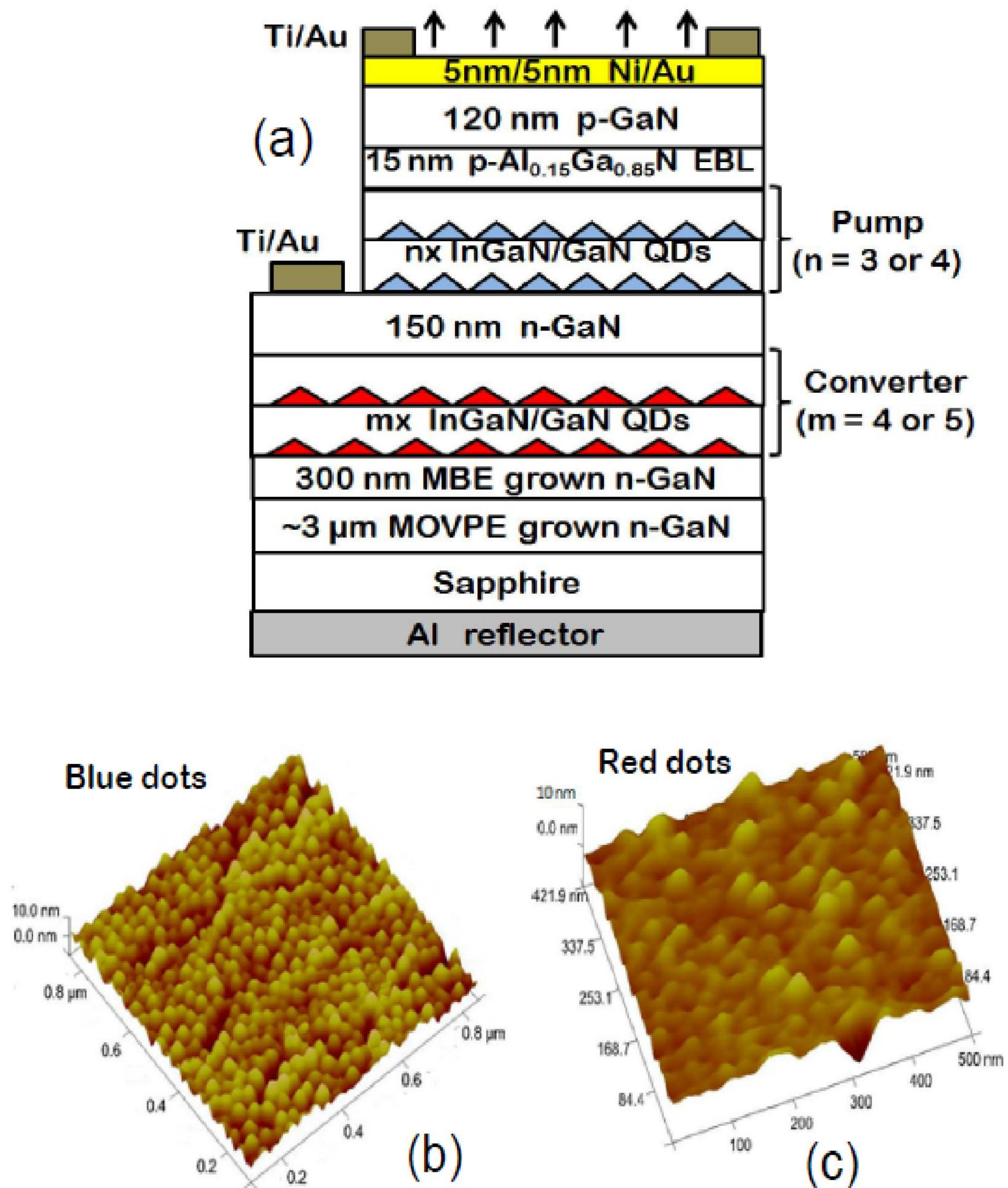

Figure 5.10 (a) Schematic representation of InGaN/GaN quantum dot wavelength converter white LED heterostructure; atomic force microscopy images of self-organized (b) $In_{0.24}Ga_{0.76}N$/GaN dots with peak emission at $\lambda = 450$ nm and (c) $In_{0.37}Ga_{0.63}N$/GaN dots with peak emission at $\lambda = 600$ nm.

and their alloy composition. Devices A′-D′ have three excitation dot layers and five converter dot layers. In devices A′, B′ and C′, the exciting quantum dot indium

content x was kept fixed at 0.24 for blue emission at λ = 450nm and the converter dot

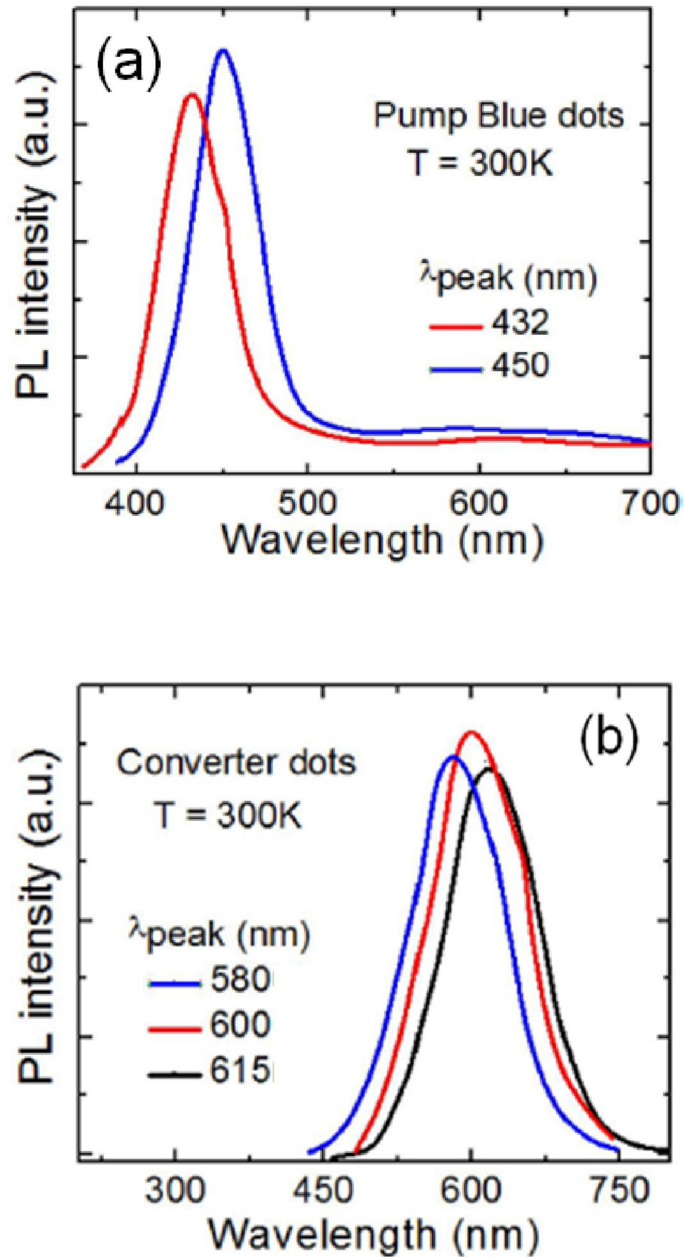

Figure 5.11 Room temperature photoluminescence of (a) blue-emitting pump dots and (b) red-emitting converter dots incorporated in the QD wavelength converter white LED heterostructure.

Emission wavelengths are 580, 600 and 615nm, respectively (x = 0.35, 0.37, and 0.38). In device D′, the exciting and converter dot emissions are at 432nm (x = 0.22)

and 580nm, respectively. Device E′ contains four excitation dot layers (λ = 432nm)

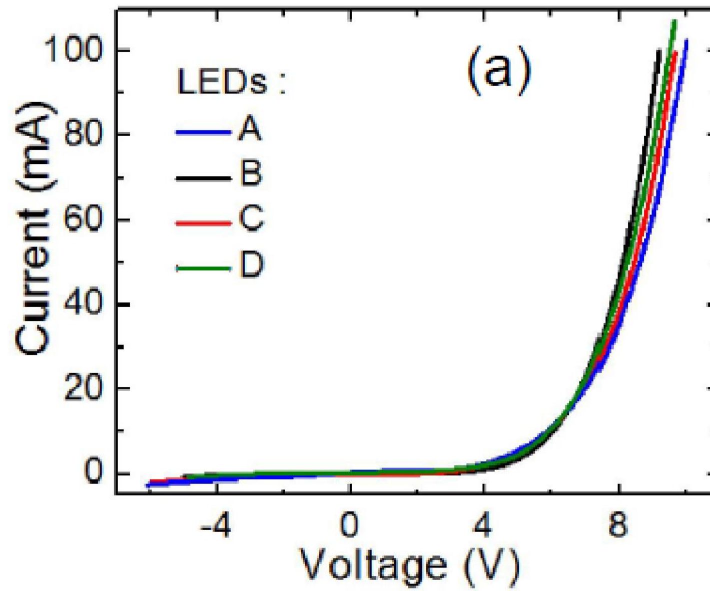

Figure 5.12 (a) Measured current-voltage characteristics of QD wavelength converter white LEDs at room temperature; optical micrographs of the devices biased at an injection current density of $45A/cm^2$: (b) device C′ (c) and device E′.

and four converter dot layers (λ = 580nm). Atomic force microscope (AFM) imaging was done on control QD samples grown under identical conditions to determine the structural characteristics of the dots. Figures 5.10(b) and (c) show AFM images of blue (λ = 450nm) and red (λ = 600nm) emitting QD layers. The blue dots have average height, base width and areal density of 3 nm, 30 nm, and $\sim 4 \times 10^{10}$ cm^{-2},

respectively. The values of these parameters for the red converter dots are 4 nm, 40

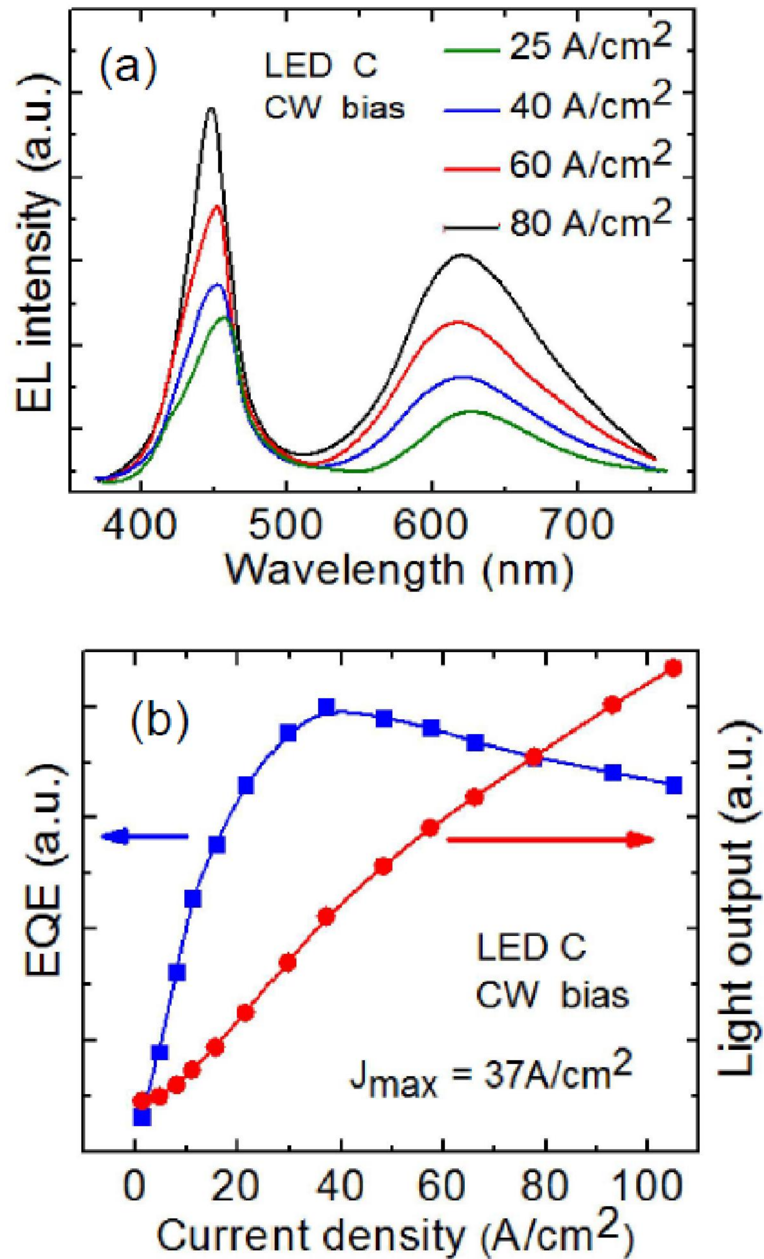

Figure 5.13 (a) Electroluminescence of device C′ under CW operation as a function of injection current density, (b) light-current characteristics and external quantum efficiency of device C′ under CW biasing.

nm, and ~3.5×10^{10} cm^{-2}, respectively. It was observed from theoretical calculations and the measurements performed on the self-assembled InGaN QDs that due to [144]

the quantum confinement and localization of carriers, along with weak polarization field, they provide strong electron-hole wavefunction overlap and superior optical properties [97, 107, 138]. Figures 5.11(a) and (b) show measured room temperature photoluminescence (PL) spectra from blue- and red-emitting QD layers, respectively. The radiative efficiency η_r of the QDs was estimated from room- and low-temperature (10K) PL intensities under saturation excitation, assuming that all non-

Table 5.3 Growth parameters and radiative efficiencies of blue- and red-emitting InGaN/GaN self-organized quantum dots.

	Peak emission (nm)	Substrate T (°C)	In flux (Torr)	Ga flux (Torr)	In/III flux ratio	QD composition (%)	Radiative efficiency (%)
Exciting dots	432	592	$3.4x10^{-8}$	$8.1x10^{-8}$	0.3	22	54
	450	585	$3.7x10^{-8}$	$7.8x10^{-8}$	0.32	24	52
Converter dots	580	550	$1.1x10^{-7}$	$1.04x10^{-7}$	0.51	35	40
	600	545	$1.12x10^{-7}$	$1x10^{-7}$	0.53	37	44
	615	541	$1.18x10^{-7}$	$9.94x10^{-8}$	0.54	38	42

radiative recombination channels are frozen at the lower temperature. The growth parameters of the blue- and red-emitting dots and their radiative efficiencies are listed in Table 5.3. The emission wavelengths of exciting and converter dots in devices A′-E′ and the device characteristics, to be described in the following, are listed in Table 5.4.

Mesa-shaped LEDs of dimension 600μm x 600μm were fabricated using standard photolithography, reactive ion etching (RIE) and metallization techniques. Ti/Au (20nm/200nm) was deposited on top of the n-GaN region below the blue QD

layers to form the n-contact and a thin semi-transparent Ni/Au (5nm/5nm) layer was

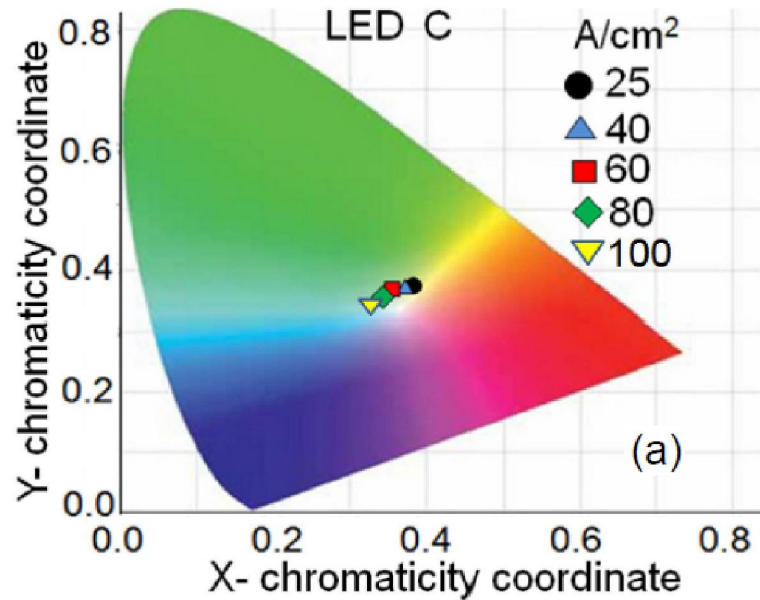

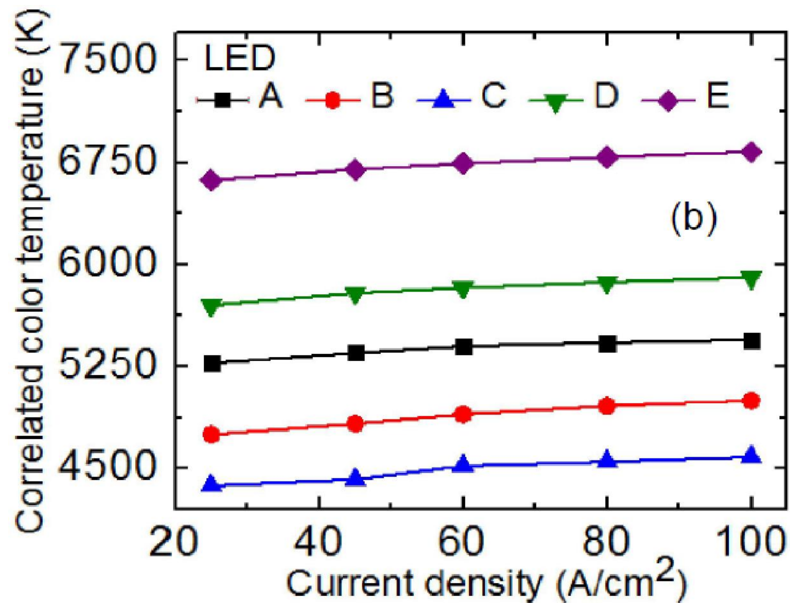

Figure 5.14 (a) Trend of chromaticity coordinates of white light emission from device C′ with variation of injection current density, (b) variation of correlated color temperature (CCT) of white light emission with injection current density for different LEDs. Solid lines are guides to the eye.

evaporated and annealed (at 450°C in 4:1 N_2:O_2) to form the p-contact on top of the

p-GaN layer. Carriers are injected electrically into the blue-emitting InGaN/GaN QD

Table 5.4 CIE chromaticity coordinates and correlated color temperatures of wavelength converter white LEDs at an injection current density of 45A/cm^2.

LEDs*	Pump dot emission λ (nm)	Converter dot emission λ (nm)	Chromaticity coordinates X	Chromaticity coordinates Y	CCT (K)
A	450	580	0.34	0.38	5350
B	450	600	0.35	0.37	4830
C	450	615	0.37	0.35	4420
D	432	580	0.33	0.36	5790
E	432	580	0.32	0.32	6700

*Devices A-D have three exciting dot and five converter dot layers. Device E has four exciting dot and four converter dot layers.

layers and the emission from these dot layers optically excites the red-emitting converter dots to produce white light. An Al reflector layer is deposited on the backside sapphire surface.

5.7.2 Output Characteristics

Figure 5.12(a) shows room temperature current-voltage characteristics of the LEDs. Turn-on voltages of ~5.5-6V and series resistances of ~20-24Ω are measured. White light emission of the phosphor-free LEDs can be tuned by using different combinations of pump and converter dot layers in the LED heterostructure. Figure 5.12(b) shows the optical micrograph of device B′ at an injection current density of 45A/cm^2. Figure 5.12(c) illustrates device E′ emitting bluish white light at the same injection level. Figure 5.13(a) illustrates electroluminescence from device C′ as a function of injection current density. The two peaks at λ = 450nm and 615nm correspond to the exciting and converter QDs, respectively. Small blueshifts in peak

emission of ~ 4nm and 7nm, due to screening of the polarization field by injected carriers, are observed for the peaks at λ = 450nm and 615nm, respectively. The corresponding calculated polarization fields are 82kV/cm and 170kV/cm, respectively, which are significantly smaller than those reported for comparable planar InGaN quantum wells. The smaller polarization field is a consequence of the strain relaxation during the formation of self-assembled QDs. The measured light-current characteristics and the corresponding external quantum efficiency (EQE) of device C′ are depicted in Fig. 5.13(b). The efficiency reaches its peak value at an injection current density of 37A/cm^2 in this device and at 45, 40, 42 and 44 A/cm^2 in devices A′, B′, D′ and E′, respectively. A reduction of 14-17% in efficiency at an injection level of 100A/cm^2 is observed in all the devices. Like before, EL intensities of the white LEDs have been recorded with an Ocean Optics USB2000+ optical spectrum analyzer (with an optical resolution of 0.3 nm) to derive the Commission Internationale de I'Eclairage (CIE) chromaticity coordinates and correlated color temperatures (CCT) of white light emission. As shown in Fig. 5.14(a), with increase in injection from 25A/cm^2 to 100A/cm^2, the CCT of device C′ changes by 210K, from 4375K to 4585K. This reflects better temperature stability of white light emission with injection current than that obtained for InGaN/GaN QWs wavelength converter white LEDs. Small blueshifts in peak emission of exciting and converter dots with increasing injection current contribute to the small increase in color temperature. The dependence of the correlated color temperature on injection current for devices A′-E′ is illustrated in Fig. 5.14(b).

In this study we have used the number of dot layers and their peak emission

wavelength, for both exciting and converter QDs, as tuning parameters for the chromaticity coordinates and CCT of the emitted white light. The chromaticity coordinates and CCT for devices A′-E′ at an injection current density of $45A/cm^2$ are listed in Table 5.4 and illustrated in Fig. 5.15. We found that the optimum number of dot layers were three for the exciting (blue) dots and five for the converter (red) dots. These were held constant for the devices A′ to D′. Devices A′, B′ and C′ have the

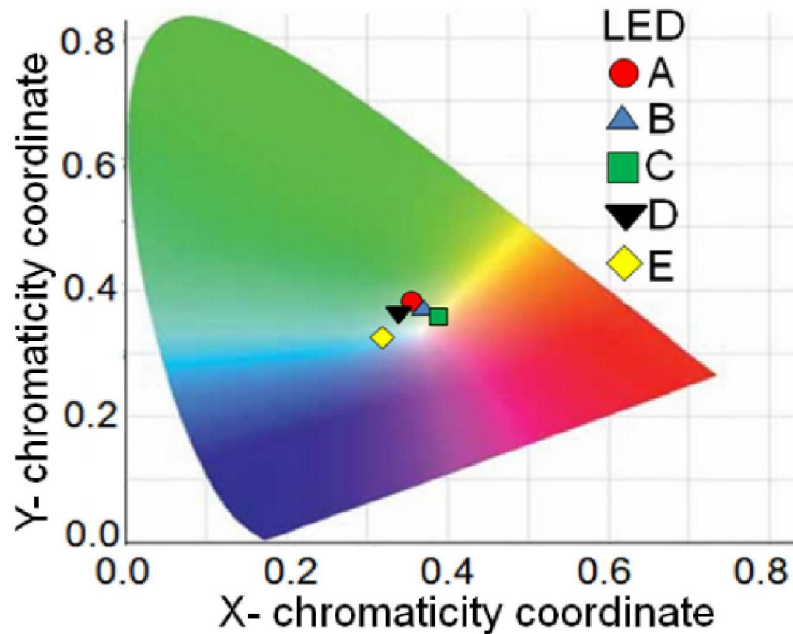

Figure 5.15 Chromaticity coordinates of white emission for different wavelength converter quantum dot white LEDs at a constant injection current density of $45A/cm^2$.

same excitation dot peak emission wavelength of 450nm, but the converter dot peak emission wavelength increases by 35nm from device A′ to C′. As a result, the CCT for white light emission decreases by 930K, with a value of 4420K for device C′ at a current density of 45 A/cm^2. Using a converter dot peak emission $\lambda > 615$nm will result in further decrease in CCT. The design of device D′ is similar to that of device A′, except that the peak emission wavelength of the exciting dots is decreased to

432nm. As a result, the CCT increases from 5350K in device A to 5790K in device D′. Device E′, which contains four excitation dot layers (λ = 432nm) and four converter dot layers (λ = 580nm), exhibits a bluish white emission with a CCT of 6700K at a current density of 45A/cm^2. As mentioned earlier, the desirable values of CCT for high efficiency cool white and warm (soft) white light are ~ 4500K and ~ 3000K, respectively. These values of CCT would be difficult to achieve with planar QWs converter white LEDs, since long wavelength (λ > 600nm) emission with high radiative efficiency is difficult to achieve with such InGaN/GaN multi QWs. A CCT~ 5683K has been reported for a white light converter LED in which blue-emitting QWs pump green-yellow emitting converter wells [129]. Correlated color temperatures of ~ 5900K and ~5500K have been reported for QW UV LED + blue-green-red phosphors and QW blue LED + yellow phosphor converter LEDs, respectively [131]. It is, therefore, evident that InGaN/GaN quantum dot converter LEDs may prove to be crucial for the realization of cool white and warm white light sources for a variety of applications. By varying the number and emission wavelengths of the dot layers, CCT of white emission from the wavelength converter LEDs has been changed from 4420K to 6700K. The lowest CCT obtained from the nanowire white LEDs, mentioned earlier, was 4210K. For the nanowire device, number and peak wavelengths of the InGaN/GaN disks were changed to examine the tunability.

5.8 Summary

In conclusion, we have demonstrated all-nitride electrically injected tunable

InGaN/GaN disk-in-nanowire white light emitting diodes grown on (001) silicon by plasma assisted molecular beam epitaxy incorporating blue, green and red-emitting InGaN disks in the same GaN nanowire. Significantly smaller shift in correlated color temperature of white emission was observed with variation of injection current density and this is attributed to the reduced polarization field in the InGaN disks — a direct consequence of their large surface-to-volume ratio and radial strain relaxation during their epitaxy. To investigate the tunability of white emission from the nanowire LEDs, the number of blue and red-emitting InGaN disks and the peak emission wavelengths of blue-, green- and red-emitting InGaN disks have been varied as tuning parameters for the chromaticity coordinates and correlated color temperature (CCT) of the emitted white light. By increasing the emission wavelengths of the InGaN/GaN disks, the CCT for white light emission was reduced by 1190K at an injection current density of 50 A/cm^2 keeping the same number of disks. Blue disks with emission wavelengths λ= 430nm and 460nm, green disks with λ= 525nm and 550nm, and red disks with λ= 610nm and 650nm have been used in the experiment. By varying the number of InGaN disks in the heterostructures while keeping the same emission wavelengths for the InGaN disks, CCT has been changed by 820K at an injection level of $50A/cm^2$.

We have also reported the characteristics of phosphor-free self-organized InGaN/GaN quantum dot wavelength converter white LEDs grown by plasma assisted molecular beam epitaxy (PA-MBE) on c-plane GaN-on-sapphire templates. The exciting quantum dots, in which electrically injected carriers recombine, are blue-emitting and the converter dots are red-emitting. We have studied the effect of

tuning the number of exciting and converter quantum dot layers and the peak emission wavelengths of the exciting and converter dots on the nature of the emitted white light, in terms of the chromaticity coordinates and correlated color temperatures (CCT). As exciting dots, two different blue-emitting dots, with emission wavelengths of 432 and 450nm, were used whereas three different red-emitting dots with emission wavelengths of 580, 600 and 615nm were grown as converter dots. For most of the devices, five red converter dots were used along with three blue-emitting pump dots—which were found to be the optimum combination of dots to obtain true white light. One device had four blue pump dots along with four red-emitting converter dots, which was emitting bluish white light with relatively higher CCT. Depending on the values of these wavelengths, color temperatures in the range of 4420-6700K have been derived at a current density of 45A/cm^2 across multiple devices, with the lower value resulting from a device with excitation and converter dots having peak emissions at 450nm and 615nm, respectively. The variation of the color temperature with the change in injection current is found to be very small due to the significantly smaller polarization field in the dots resulting from the strain relaxation during self-assembled quantum dot formation. After further optimization of the growth and processing of the device heterostructures, both these device schemes, mentioned above, could be used as alternatives for conventional phosphor-converted white LEDs.

Chapter VI

Electrically Injected Monolithic InGaN/GaN Disk-in-Nanowire Array Edge-Emitting Lasers on (001) Silicon

6.1 Introduction

A monolithic, electrically pumped laser on silicon has long been of significant scientific and technological interest for a host of applications. Due to the indirect bandgap of silicon, realization of a suitable silicon-based laser remains one of the biggest technological challenges to be overcome for the success of silicon photonics [145-148]. A monolithic laser on silicon emitting in the visible spectrum with a low threshold would also provide an alternative for the present nitride-based laser epitaxy on expensive free-standing GaN substrates. In this chapter, the first edge-emitting laser with a III-nitride nanowire heterostructure grown on (001) Si by plasma-assisted molecular beam epitaxy (PA-MBE) is demonstrated. The p-i-n nanowires have multiple InGaN/GaN disks inserted in the waveguide region, which serve as the gain media. We have made green (λ=533 nm) and red-emitting (λ=610 nm) nanowire array lasers by varying the indium composition in the InGaN disks and modifying the cladding layers in the laser heterostructure for the confinement of long wavelength emission. Extensive steady-state and dynamic characterization of the green- and red-emitting lasers have been performed and the values of threshold current, temperature coefficient (T_0), device efficiency,

differential gain, and small-signal modulation bandwidth have been derived. In particular, the green laser exhibits a threshold current density which is significantly lower than those reported for planar green-emitting InGaN/GaN quantum well (QW) lasers [44, 59, 143, 149-152]. The nanowire waveguide loss has also been investigated. Long-term reliability measurements under cw biasing indicate a lifetime of ~7000 hrs for the green-emitting laser. Small signal modulation bandwidth, extremely low values of chirp and linewidth enhancement factor (α) near the peak emission wavelength have been measured for the red-emitting lasers. By varying the indium composition in the InGaN/GaN disks, near-infrared (near-IR) emission from the nanowire laser on (001) Si should be possible, which will be beneficial for silicon photonics applications.

6.2 Different Schemes for Electrically Injected Lasers on (001) Silicon

The prospects of a monolithic nanowire electrically pumped laser on (001) silicon are two-fold. First of all, an electrically injected IR laser on (001) Si is compatible with existing silicon CMOS technology and will be important for silicon photonics applications. This is achievable with nanowire laser by increasing the In composition in the InGaN disks and designing the laser heterostructures properly for the optical mode confinement of the near IR emission wavelengths. Second, a Ga(In)N nanowire laser with low threshold on less expensive silicon substrate will be a promising alternative for the present planar InGaN QW lasers grown on overly expensive free standing GaN substrates and in most cases, with a high threshold. Before moving on to nanowire lasers, a short review on electrically injected lasers on (001) silicon, tried so far, will be presented

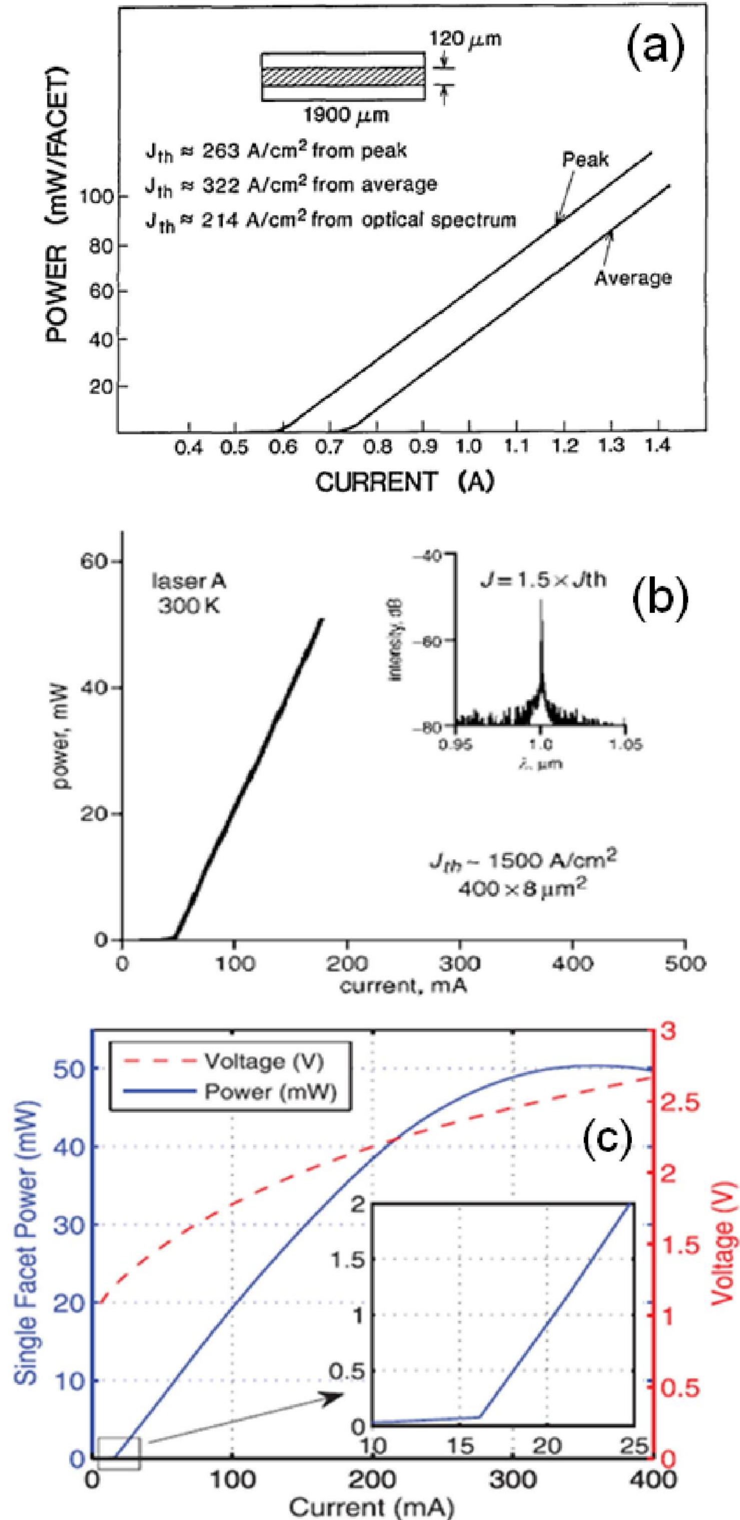

Figure 6.1 (a) Room temperature light-current characteristics of GaAs/AlGaAs lasers [153] on silicon, (b) L-I characteristics of $In_{0.5}Ga_{0.5}As$ QD laser at 300K along with the emission spectrum above threshold [154], (c) room temperature light output from high performance InAs QD laser (λ=1.3μm) grown on misoriented (001) silicon [155].

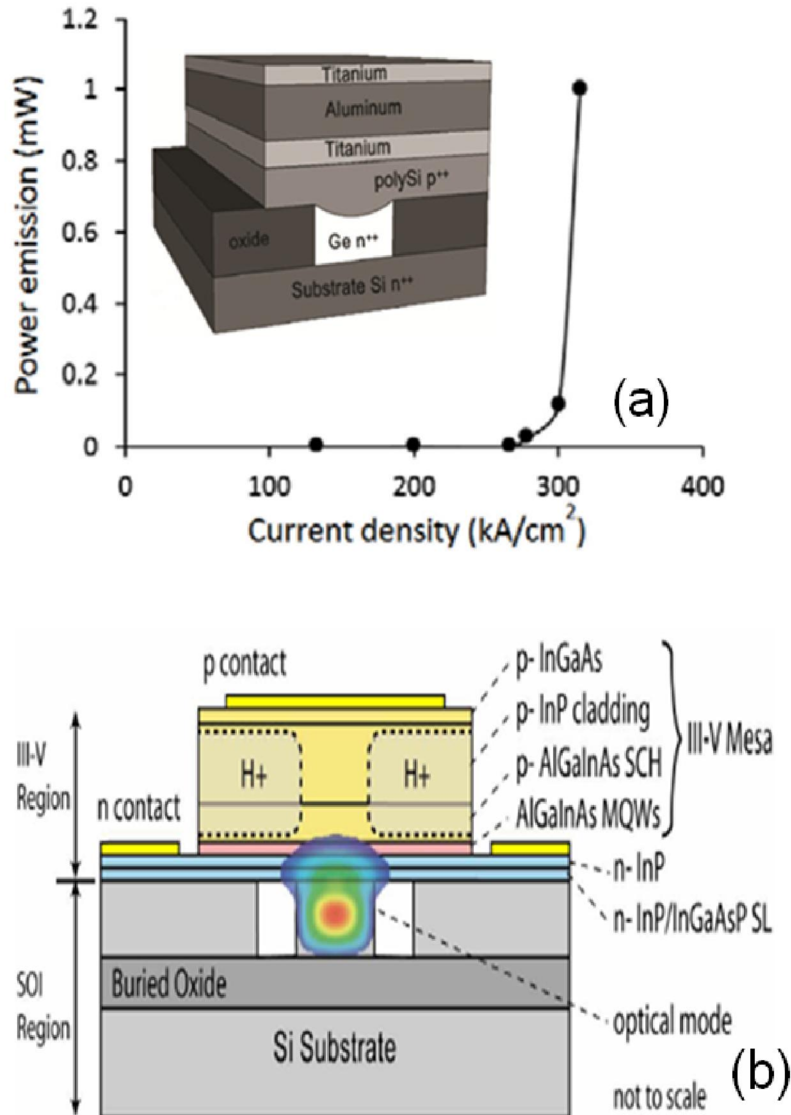

Figure 6.2 (a) Schematic illustration of Ge-on-Si p-n-n laser heterostructure along with the L-I characteristics [158], (b) schematic representation of III-V heterostructure bonded on (001) silicon, where optical mode is guided by the silicon waveguide via evanescent mode coupling [159].

in this section. Three routes for the integration of reliable and high-performance electrically pumped lasers with (001) silicon technology are being explored. The first involves the direct epitaxy of III-V heterostructures on silicon. However, the large lattice mismatch leads to a high density of threading dislocations propagating into the active

region. Furthermore, the formation of antiphase boundaries due to the polar/non-polar nature of the epitaxy necessitates the use of misoriented substrates; generally (001) Si offcut 4° towards the [111] or [110] planes is used [153-155]. This is the greatest drawback of this method since Si CMOS technology on misoriented substrates is not favored. Nonetheless, Morkoc *et al.* [153] have shown the first room temperature GaAs/AlGaAs graded-refractive index separate-confinement lasers grown on misoriented (001) Si substrates. Threshold current densities of 214 A/cm^2 (Fig. 6.1(a)), maximum slope efficiencies of ~0.8 W/A, and optical power above 270 mW/facet were reported under pulsed conditions. Our group has demonstrated the first room-temperature operation [154] of $In_{0.5}Ga_{0.5}As$ quantum dot lasers grown directly on misoriented (001) Si substrates with a thin (~2 mm) GaAs buffer layer. The devices are characterized by J_{th}~1500A/cm^2 (Fig. 6.1(b)), output power above 50 mW, large T_0 of 244 K and output slope efficiency above 0.3 W/A. Recently, Bowers *et al.* [155] have reported high-performance InAs/GaAs quantum dot lasers on offcut (001) silicon with emission wavelengths between 1.1 and 1.3 μm. Room temperature continuous-wave threshold was as low as 16 mA in the ridge waveguide lasers, output power was above 176 mW (Fig. 6.1(c)), and lasing was observed up to a temperature of 119°C. In their device, P-modulation doping of the active region yields large T_0 of 100–200K while maintaining low thresholds and high output power. Various buffer layers are also being investigated for use in this approach [147, 156, 157]. As a second approach, an electrically pumped Ge-on-Si p-n-n heterojunction diode laser, with built-in tensile strain and heavy doping in the Ge layer, which allow direct radiative transitions in indirect bandgap Ge, has been demonstrated recently [158] (Fig. 6.2(a)). The Ge on silicon laser has an impractically

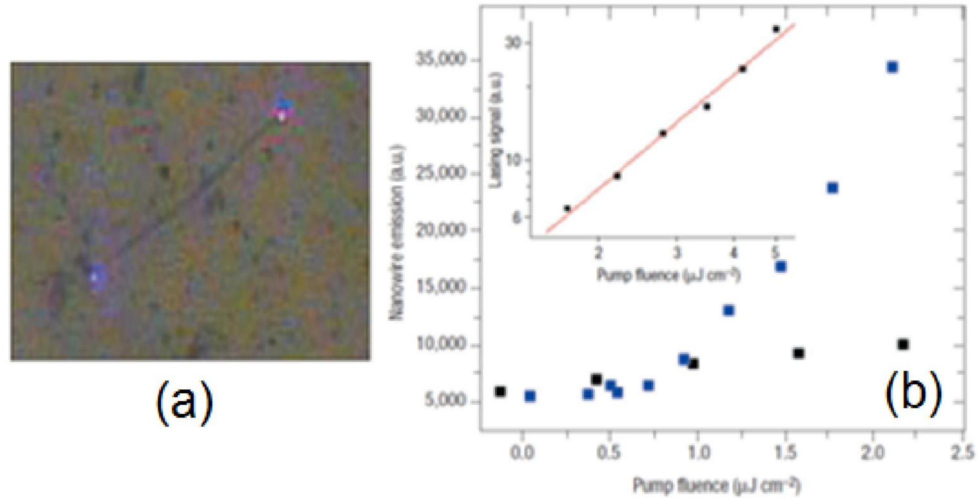

Figure 6.3 (a) SEM image of single GaN nanowire laser dispersed on sapphire substrate. The color indicates laser emission at the two ends of the nanowire, (b) power dependence of the lasing near threshold (blue) and that of the photoluminescence emission from a non-lasing region (black) [165].

large threshold current density (~280 kA/cm^2) and limited output power (~1 mW). The temperature dependence (T_0) and long-term reliability of this device have not been reported. The third and, perhaps the most common technique has been to wafer bond the III-V laser heterostructure on a (001) Si wafer [159-163] (Fig. 6.2(b)). Variations within this approach include guiding in the III-V heterostructures or in silicon via evanescent mode coupling. In this approach, multiple lasers can be operated simultaneously, but there could be a significant loss of light output when the optical mode is guided by the silicon waveguide via evanescent field coupling. However, III-V substrates such as GaAs and InP, on the other hand, are available only in smaller diameters that limit the maximum bonding area. Microdisk lasers bonded on Si have also been reported [164].

6.3 Previous Reports of Ga(In)N Nanowire Lasers

An optically pumped single GaN nanowire laser has been demonstrated by

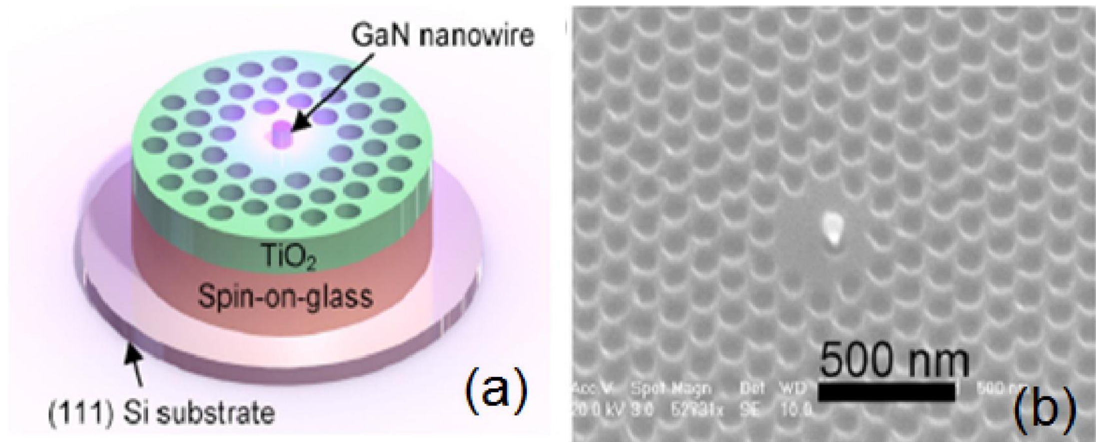

Figure 6.4 (a) Schematic representation of the fabricated nanowire laser consisting of a single GaN nanowire and a 2D photonic crystal microcavity, (b) an oblique view SEM image of the fabricated device, (c) variation of peak output intensity with pump power (the L-L curve). The change in slope of the L-L curve near threshold ~120 kW/cm^2 is clearly observed [166].

Johnson *et al.* [165], which is shown in Fig. 6.3. A single GaN nanowire was dispersed on sapphire substrates, and the nanowire itself acts as a Fabry-Perot laser cavity along the c-axis. By growing GaN nanowires with different lengths, the length of the laser cavity can be varied. The GaN nanowire laser was optically excited with $3\mu Jcm^{-2}$ excitation. In Fig. 6.3(a), the color indicates laser emission at the two ends of the single nanowire.

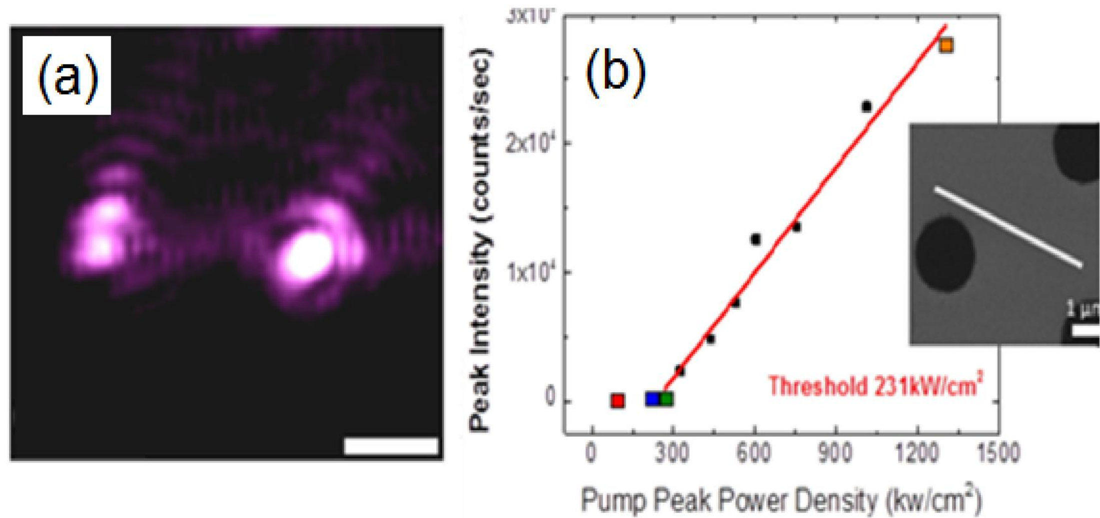

Figure 6.5 (a) CCD image of a single-mode GaN nanowire laser optically pumped above lasing threshold, The nanowire laser emits a highly divergent beam from the facets, some of which is collected by the objective lens. The objective lens also collects radiation emitted from the facets that is scattered by the SiN substrate surface, as well as spontaneous emission exiting perpendicular to the nanowire axis. Scale bars are 2 µm, (b) nanowire laser intensity versus pump laser intensity with cavity length of 4.7 µm. In set shows SEM image of a single GaN nanowire dispersed on SiN substrate [167].

Figure 6.3(b) shows power dependence of the lasing near threshold (blue) and that of the photoluminescence emission from a non-lasing region (black) for comparison. Heo *et al.* has shown monolithic single GaN nanowire laser with photonic crystal microcavity on silicon (Fig.6.4) [166]. Room temperature optically excited lasing from a silicon based monolithic single GaN nanowire with two-dimensional photonic crystal microcavity is demonstrated. Single GaN nanowire laser fabricated on Si is characterized by a linewidth of 0.55 nm. The threshold was observed at a pump power density of ~120 kW/cm^2. Li *et al.* reported single mode optically pumped single GaN nanowire lasers (Fig. 6.5) [167]. The laser structure is a linear, double-facet GaN nanowire acting as gain medium and optical resonator. This is fabricated by a top-down technique that uses a tunable dry etch and anisotropic wet etch for precise control of the nanowire dimensions and high material

gain. A single-mode linewidth of ~0.12 nm and >18dB side-mode suppression ratio are measured. It is found from the simulation that single-mode lasing results from strong mode competition and narrow gain bandwidth. So far, only optically pumped lasers have been realized with III-nitride nanowires. An electrically injected monolithic nanowire array laser on (001) silicon with reasonably low threshold is promising for silicon photonics applications. It can also be an alternative candidate for making visible laser on less expensive Si substrates in comparison to planar InGaN QW lasers on expensive bulk GaN substrates. We have demonstrated, for the first time, electrically pumped monolithic nanowire array laser on (001) silicon with a smaller threshold compared to that reported for planar nitride lasers.

6.4 Design and Growth of Green (λ=533 nm) and Red (λ=610 nm) Edge-Emitting Nanowire Laser Heterostructures on (001) Silicon

Edge-emitting green (λ=533 nm) nanowire array lasers, as shown schematically in Fig. 6.6 (a), were monolithically grown on (001) silicon substrates by Veeco Gen 930 plasma assisted molecular beam epitaxy (PA-MBE) machine. The ensemble of as-grown nanowires has an average diameter of ~ 60 nm and an optimized areal density of ~$2\text{x}10^{10}$ cm^{-2}. For a small nanowire density, the volume of the gain material is reduced, and the formation and fabrication of the top (p-type) ohmic contact of the laser are rendered more difficult. On the other hand, too large a nanowire density leads to coalescing of the nanowires and the formation of extended defects and stacking faults which ultimately reduce the radiative efficiency, as discussed in chapter IV. As-grown nanowire sample placed on a 45° angle mount was introduced into Hitachi SU8000 to capture the SEM

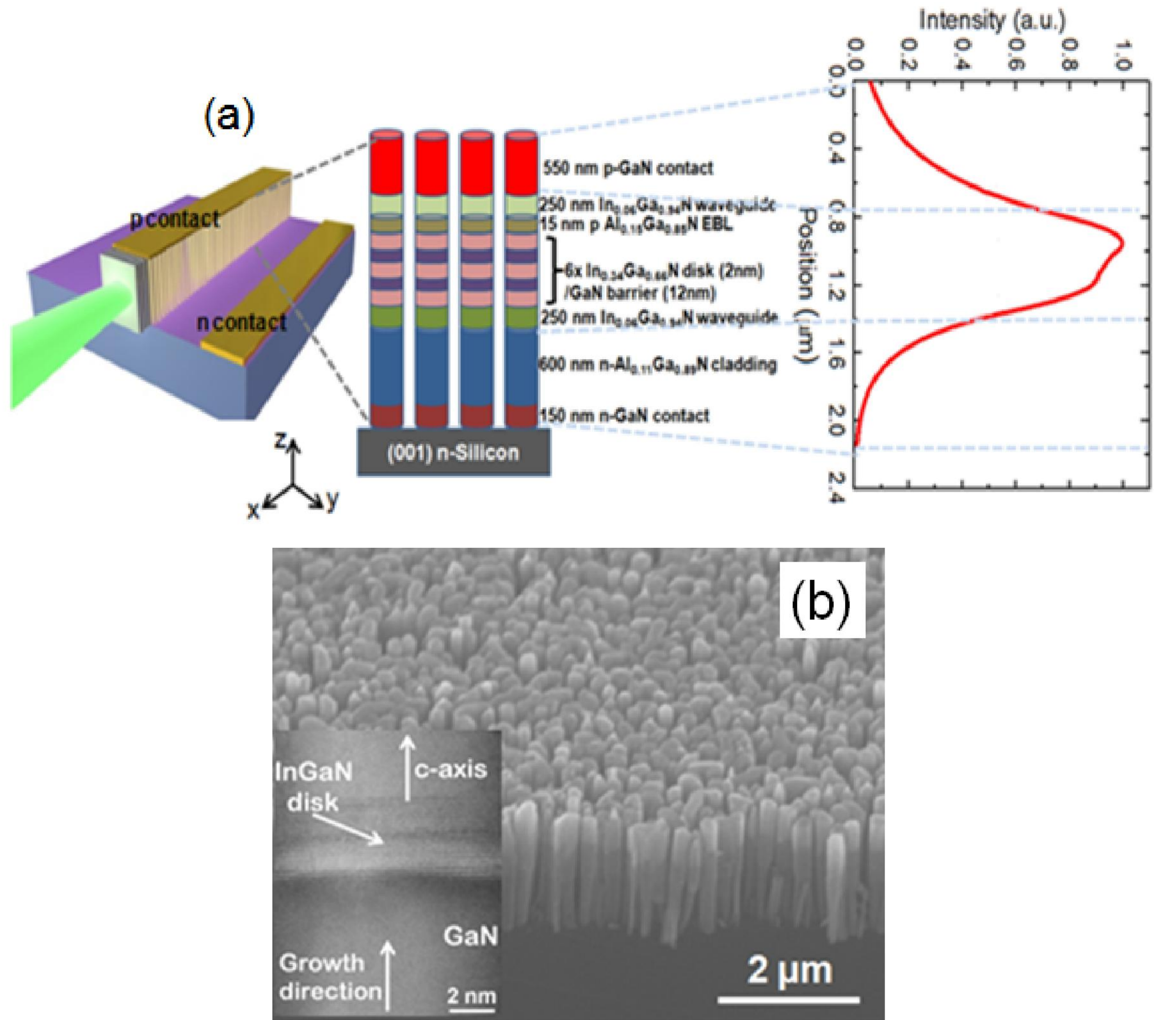

Figure 6.6 (a) Schematic representation of the green-emitting (λ = 533 nm) nanowire array laser heterostructure showing the active region, $In_{0.6}Ga_{0.94}N$ waveguide and asymmetric $Al_{0.11}Ga_{0.89}N$ cladding. The calculated mode profile is shown alongside, assuming that the space between the nanowires is filled with parylene; (b) 45° tilted scanning electron microscope (SEM) image of green-emitting (λ = 533 nm) $In_{0.34}Ga_{0.66}N$/GaN disk-in-nanowire array laser heterostructures grown by molecular beam epitaxy on (001) silicon substrate. Inset shows the high resolution transmission electron microscope (HRTEM) image of a ~2 nm thick $In_{0.34}Ga_{0.66}N$ disk in a single GaN nanowire.

image of the heterostructure at an accelerated voltage 10kV and emission current of 7μA. Figure 6.6 (b) shows 45° tilted scanning electron microscope (SEM) image of green-emitting (λ = 533 nm) $In_{0.34}Ga_{0.66}N$/GaN disk-in-nanowire array laser heterostructures on

(001) Si and inset to Fig. 6.6(b) depicts the high resolution transmission electron microscope (HRTEM) image of a ~2 nm thick $In_{0.34}Ga_{0.66}N$ disk in a single GaN nanowire. As-grown nanowires were removed mechanically from the Si substrate and ultrasonicated in isopropyl alcohol (IPA) for 20 minutes. Few drops of the nanowire-IPA solution were then put on a carbon-coated TEM grid. After evaporation of the liquid, the nanowires on the grid were imaged using a JEOL 3011 high resolution transmission electron microscope. To remove the surface oxide, the substrate was cleaned with hydrofluoric acid solution and then heated inside the MBE chamber at 900°C for 60 min before growth. GaN nanowires were grown on Si at a substrate temperature of 800°C without any initial self-catalysis step. The growth was carried out in a nitrogen rich environment maintaining a constant N_2 flux of 1.0 sccm and the Ga flux was kept at $1.62x10^{-7}$ Torr. 150 nm of Si doped n^+ GaN layer ($n{\sim}6{\times}10^{18}$ cm^{-3}) was first grown, followed by n-$Al_{0.11}Ga_{0.89}N$ cladding layer, $In_{0.06}Ga_{0.94}N$ waveguide in the center of which is placed 6 InGaN disks (2 nm)/GaN barrier (12 nm), 15 nm p-$Al_{0.15}Ga_{0.85}N$ electron blocking layer (EBL) and 550 nm p^+GaN layer. The optimum number of disks and well thickness are dependent on several factors. The first is a growth constraint. The strain accumulated by growing the active region should not generate dislocations in the nanowire that would reduce the radiative efficiency of the disks. Beyond the growth considerations, the number of disks must be chosen as a tradeoff between the lower threshold and higher power. The number of $In_{0.34}Ga_{0.66}N$ disks incorporated in the nanowire heterostructure will affect modal gain of the laser. However, increasing the number of disks will increase the threshold current and will cause a non-uniform injection of holes six amongst the disk layers due to the heterostructure band line-up. We have

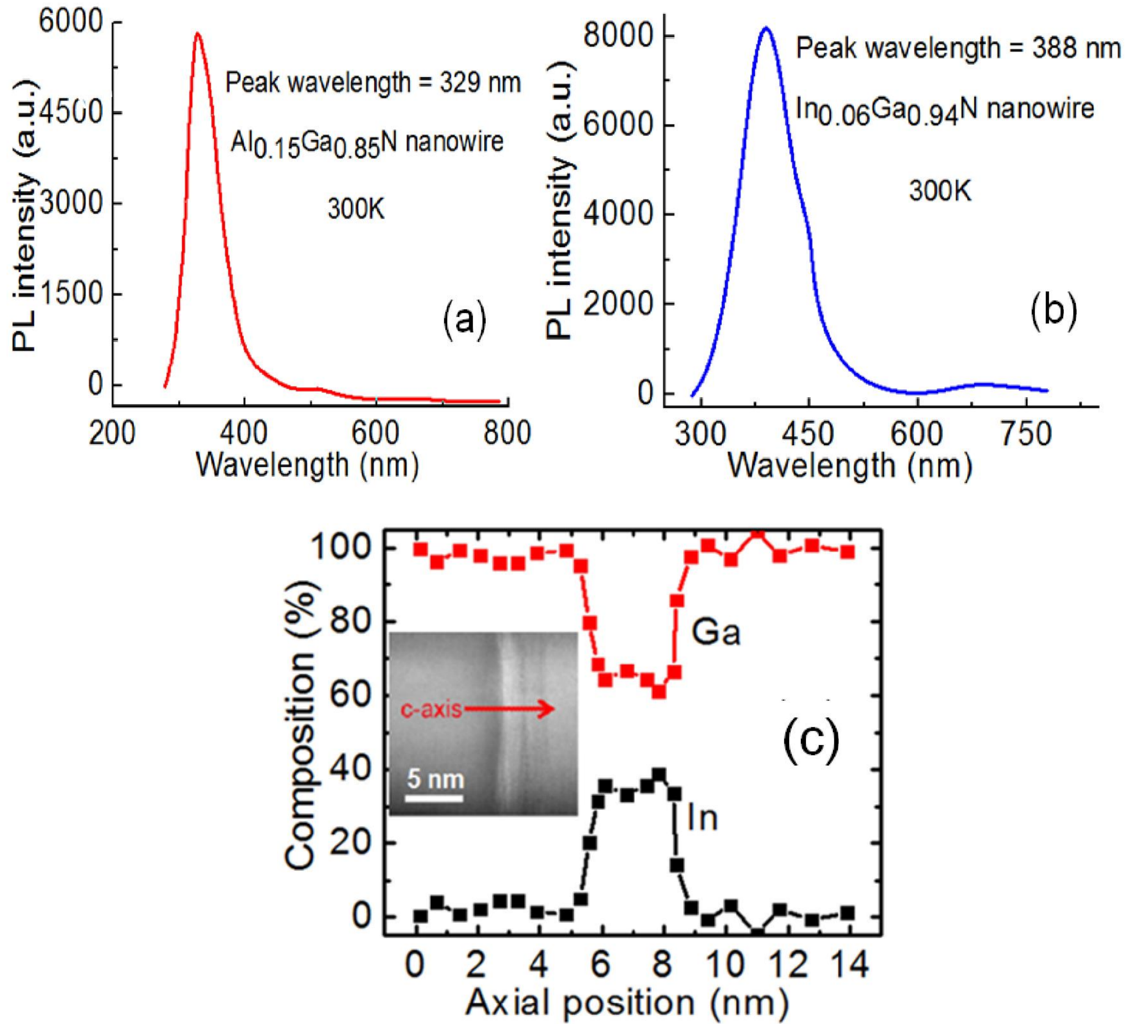

Figure 6.7 Room temperature photoluminescence of (a) $Al_{0.15}Ga_{0.85}N$ nanowire and (b) $In_{0.06}Ga_{0.94}N$ nanowire, which were used as p-doped electron blocking layer (EBL) and waveguide layer, respectively, for both the green and red-emitting nanowire lasers, (c) Energy-dispersive X-ray (EDX) measurement of the elemental composition along the c-axis of an InGaN disk used in the green-emitting (λ=533nm) nanowire laser heterostructure, which yields a maximum In composition of 34% in the disk. Inset shows EDX scan direction across a single InGaN disk.

included disk layers in our heterostructures based on optimization of the photoluminescence intensity. The thickness of the disks affects the electron hole wavefunction overlap and hence the emitted light intensity. We have used the optimum value of 2 nm. During the growth of the green emitting (λ = 533nm) quantum disks, the

substrate temperature was lowered to 590°C and In and Ga fluxes of 6.5×10^{-8} Torr and $1.48\text{x}10^{-7}$ Torr, respectively, were used. Mg-doped p^{+}GaN layer ($p\sim7.5\times10^{17}$ cm^{-3}) was grown at 700°C. The Mg flux was increased during the growth of the final 20 nm of p^{+}GaN to achieve a better ohmic contact. Calculated mode profile for the green-emitting laser, obtained from transfer matrix method, is shown in Fig. 6.6(b) alongside the laser heterostructure. By using asymmetric $Al_{0.11}Ga_{0.89}N$ cladding in the laser heterostructure growing thick p-GaN on top, we reduced the series resistance of the laser to a great extent. P-doped $Al_{0.11}Ga_{0.89}N$ cladding grown on the top side of the initial laser heterostructures was highly resistive. Figures 6.7 (a) and (b) demonstrate the room temperature photoluminescence (PL) of $Al_{0.15}Ga_{0.85}N$ EBL and $In_{0.06}Ga_{0.94}N$ waveguide layer, respectively with the optimized alloy compositions according to the laser design. Indium composition in the green-emitting (λ = 533 nm) disks was estimated to be 34% from energy dispersive x-ray (EDX) measurements as depicted in Fig. 6.7(c). EDX measurements were performed on a single nanowire in a JEOL 2100F TEM facility at an accelerating voltage of 200 kV. Before imaging and spectroscopy, the nanowires were dispersed on a holey carbon grid. A Hitachi SU8000 SEM with EDX capability was used to calibrate the Indium composition in InGaN nanowires, grown under identical conditions. The radiative efficiency of InGaN disks is also reduced by surface states of the nanowire as discussed in chapter II. We have investigated the effect of passivation with various compounds on the radiative efficiency and their compatibility with the nanowire laser fabrication process. Figure 6.8(a) shows the enhancement in room temperature PL of passivated green-emitting $In_{0.34}Ga_{0.66}N$/GaN disks-in-nanowires. Upon parylene passivation, the radiative efficiency of the disks has been improved by ~12%

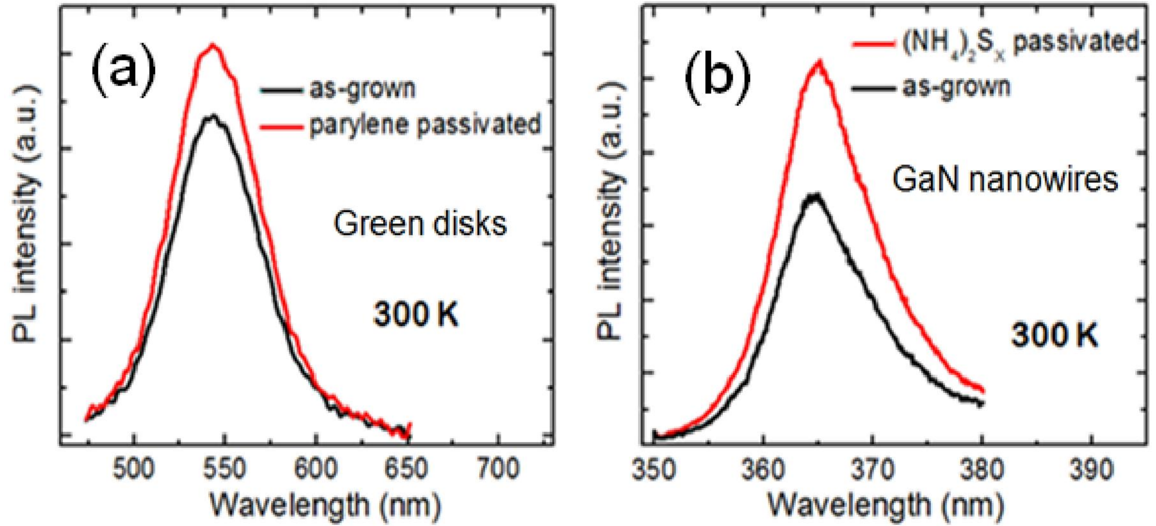

Figure 6.8 (a) Enhancement in 300K photoluminescence of the green-emitting disk-in-nanowire sample by surface passivation with parylene, (b) Photoluminescence of GaN nanowires at 300K, before and after treatment with ammonium sulfide $(NH_4)_2S_x$.

and became as high as 55%. Figure 6.8(b) illustrates the change in luminescence from GaN nanowires upon passivation with ammonium sulfide $(NH_4)_2S_x$. While there is only a minimum increase in the luminescence intensity with the $(NH_4)_2S_x$ treatment, we have determined that the p-contact resistance is reduced upon such treatment. Though we mentioned the heterostructure and epitaxial growth of a green-emitting nanowire laser above, laser emission near infrared (IR) is also possible by increasing the indium composition in the InGaN disks and redesigning the laser heterostructure for the confinement of long wavelengths. With that vision in mind, we first proceeded to realize a red-emitting nanowire laser with higher indium composition in the disks and modified cladding layers in the structure. In order to make monolithic red-emitting (λ = 610 nm) nanowire laser on (001) silicon, we have increased the In composition in the disks to 51% as estimated from the EDS measurements and shown in Fig. 6.9. Red-emitting $In_{0.51}Ga_{0.49}N$ disks were grown at a substrate temperature of 550°C and with In and Ga

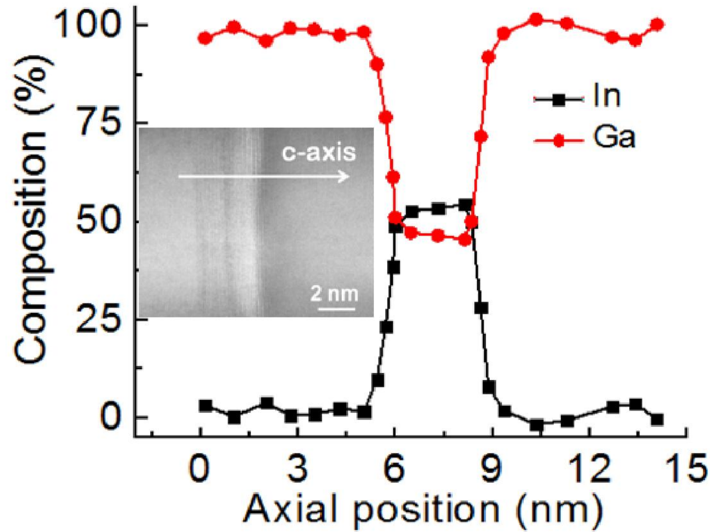

Figure 6.9 Energy-dispersive X-ray (EDX) measurement along the c-axis of an InGaN disk used in the red-emitting (λ=610nm) nanowire laser heterostructure, which yields a maximum In composition of 51% in the disk. Inset shows EDX scan direction across a single InGaN disk.

fluxes of 1.2×10^{-7} Torr and 1.45×10^{-7} Torr, respectively. From temperature dependent PL, radiative efficiency of the passivated red-emitting disks was measured to be ~54%. $Al_{0.11}Ga_{0.89}N$ cladding, used in the green laser structure, was replaced by $In_{0.18}Al_{0.82}N$ cladding grown at 500°C and lattice-matched to GaN as shown by the XRD data in Fig. 6.10(a). Figure 6.10(b) shows the HRTEM image of $In_{0.18}Al_{0.82}N$ nanowire along with the selective area diffraction (SAD) pattern in the inset. Defects have not been observed along the growth direction (c-axis) of the $In_{0.18}Al_{0.82}N$ nanowires. SAD pattern on the $In_{0.18}Al_{0.82}N$ nanowire demonstrates a lattice constant of 5.16 Å, which shows excellent lattice matching to GaN. $In_{0.18}Al_{0.82}N$ provides better optical mode confinement since it has a higher refractive index difference with $In_{0.6}Ga_{0.94}N$ waveguide as compared to the previous $Al_{0.11}Ga_{0.89}N$ cladding. All the nanowire array lasers on Si mentioned in this chapter were planarized and passivated with parylene. The refractive indices of

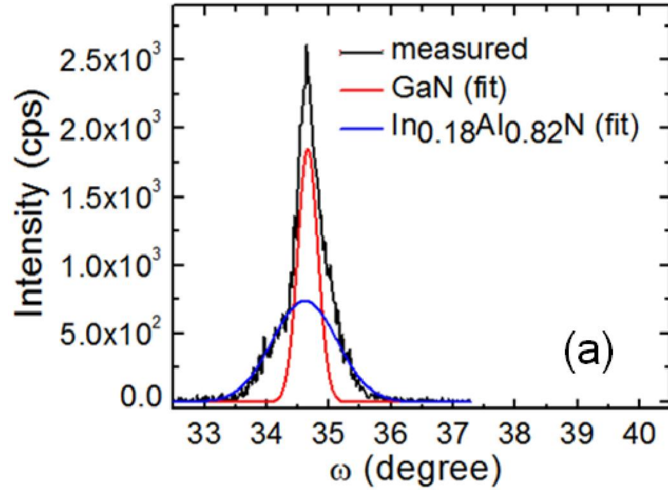

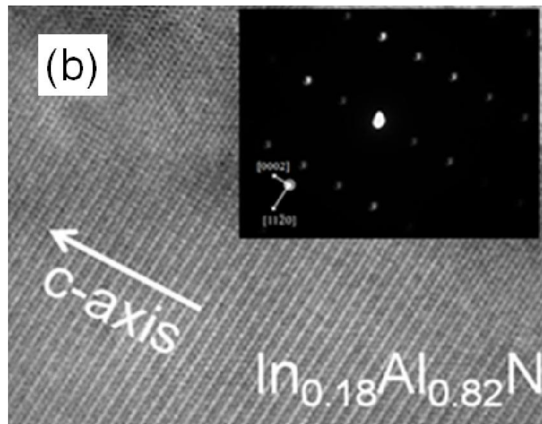

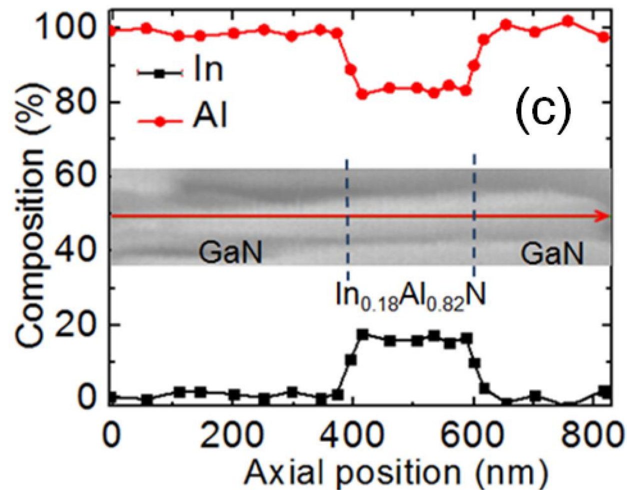

Figure 6.10 (a) XRD data of $In_{0.18}Al_{0.82}N$ nanowire grown on GaN. This $In_{0.18}Ga_{0.82}N$ nanowire lattice matched to GaN was used as cladding layer in red-emitting nanowire laser, (b) High resolution transmission electron microscope image (HRTEM) of $In_{0.18}Al_{0.82}N$ nanowire showing defect-free crystal structure along the growth direction. Inset shows the selective area diffraction (SAD) pattern of the nanowire, (c) Energy-dispersive X-ray (EDX) measurement of the elemental composition along the c-axis of $In_{0.18}Al_{0.82}N$ nanowire.

$In_{0.6}Ga_{0.94}N$ waveguide-parylene composite, $Al_{0.11}Ga_{0.89}N$ cladding-parylene composite and $In_{0.18}Al_{0.82}N$ cladding-parylene composite are 2.32, 2.27 and 1.99, respectively for red emission wavelength. In and Al compositions in InAlN nanowire, grown lattice matched to GaN, were also estimated from EDX measurements as depicted by Fig. 6.10(c).

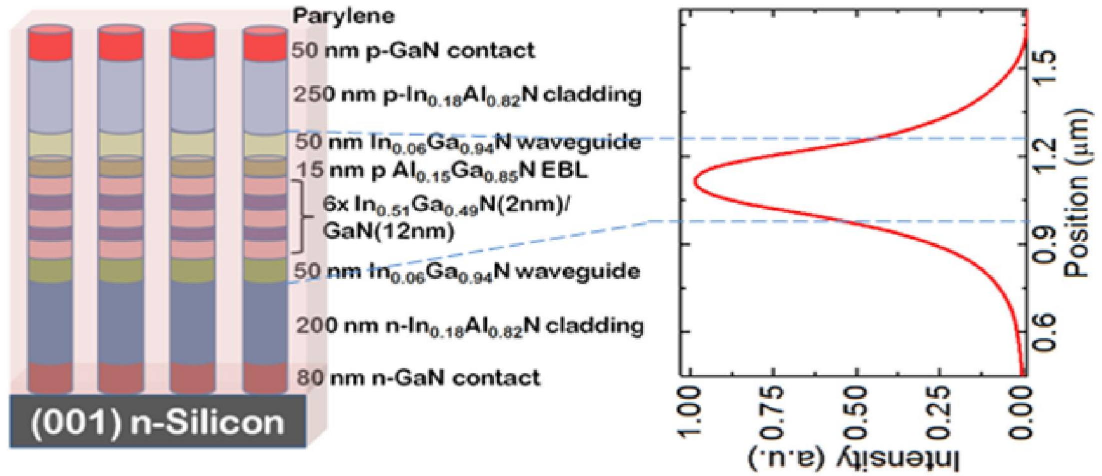

Figure 6.11 Schematic illustration of the red-emitting (λ=610nm) nanowire array laser heterostructure showing the active region, $In_{0.6}Ga_{0.94}N$waveguide and $In_{0.18}Al_{0.82}N$ cladding. The calculated mode profile is shown alongside, assuming that the space between the nanowires is filled with parylene.

Schematic representation of a red-emitting nanowire laser heterostructure on (001) Si is demonstrated in Fig. 6.11 along with the calculated mode profile. Better mode confinement using $In_{0.18}Al_{0.82}N$ cladding also leads to thinner cladding region on both sides that plays an important role on the overall low device series resistance.

6.5 Fabrication of Ridge Waveguide InGaN/GaN Disk-in-Nanowire Lasers

6.5.1 Processing of Ridge Geometry Waveguide Laser Heterostructures

Edge-emitting lasers were fabricated with a two-step mesa in a ridge geometry,

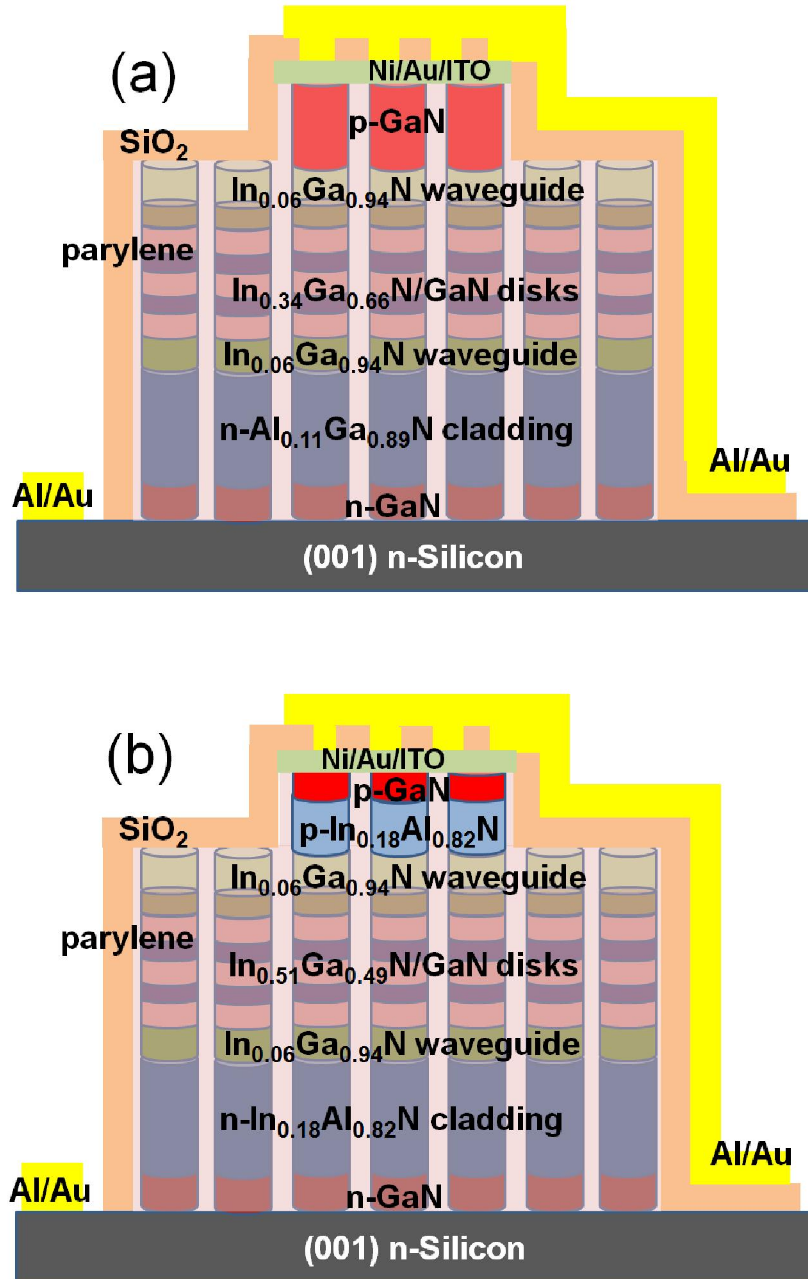

Figure 6.12 Schematic representation of the fabricated ridge waveguide InGaN/GaN disk-in-nanowire array (a) green and (b) red laser heterostructures on (001) silicon.

patterned with a stepper and optical photolithography. Schematic illustrations of fabricated ridge-waveguide green- and red-emitting nanowire lasers are shown in Fig. 6.12. The mesas were etched using reactive ion etching with the first mesa (ridge) etched

to the cladding/waveguide heterointerface and the second (wider) mesa etched all the way to the n-silicon substrate. The ridges were patterned with widths in the range of 4μm to 50 μm with the wider mesa 20μm wider than the respective ridge width and with cavity lengths varying from 0.4 to 2 mm. Parylene was deposited by thermal vapor deposition to planarize the device and passivate the nanowire surface. Excess parylene was etched to expose the nanowire tips to make the p-contact. The p-side of the nanowires were treated with ammonium sulfide ($(NH_4)_2S_x$) to reduce the p-contact resistance. The p-GaN contacts were formed with semitransparent Ni/Au ohmic contacts (5nm/5nm) deposited by electron beam evaporation and ITO (250nm) current spreading layer deposited by sputtering. Ni/Au contact was annealed at 550°C for 2 min in N_2:O_2=4:1 gas mixture and ITO was annealed at 500°C for 1 min in Ar ambient. The n-GaN contacts were formed with Al/Au (100nm/300nm) by e-beam evaporation. SiO_2 passivation was deposited by plasma enhanced chemical vapor deposition. Via holes for the contacts were etched using a solution of HF:H_20 (10:1).

6.5.2 Highly Reflective Facets for Edge-Emitting Nanowire Lasers

The laser heterostructures were cleaved along the direction perpendicular to the laser cavity and then focused ion beam (FIB) etching is used to form the optically flat laser facets. To enhance the facet reflectivity, dielectric distributed Bragg reflectors (DBRs) (SiO_2/TiO_2) were deposited on the facets of the edge-emitting lasers by e-beam evaporation. For the green-emitting laser the facet reflectivities were ~0.72 and ~0.95, respectively. For the red-emitting laser, less number of DBR pairs was deposited on the low reflectivity facet to increase the laser output power and the facet reflectivities were

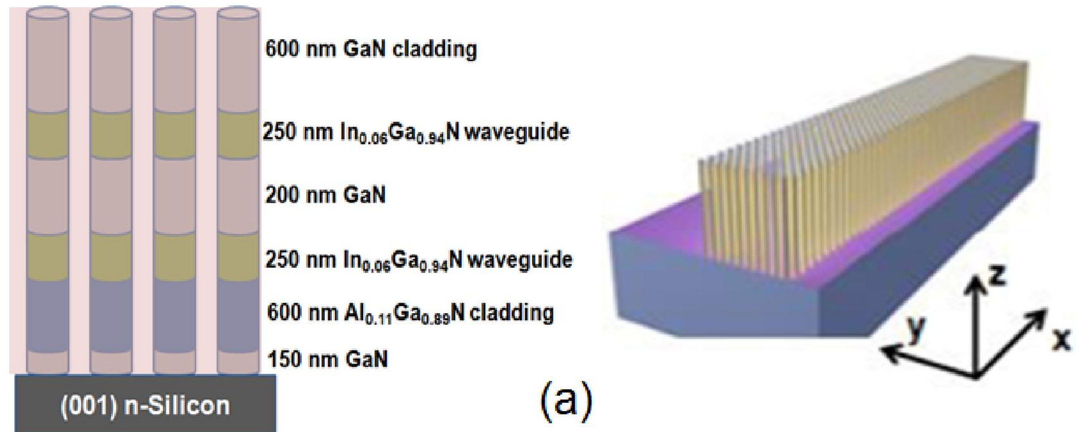

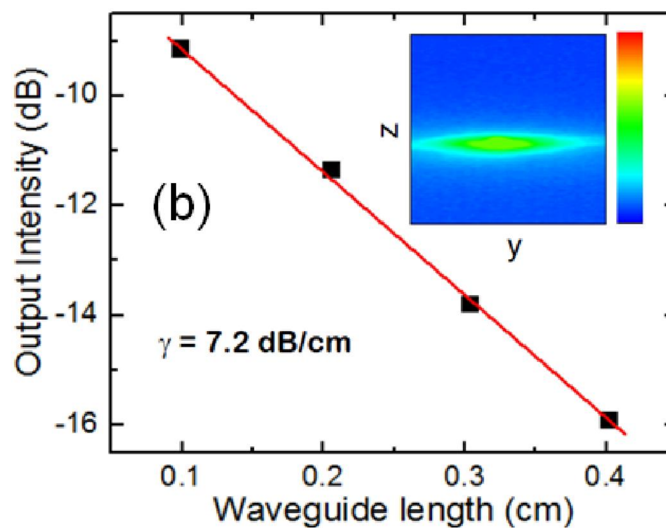

Figure 6.13 (a) Schematic representation of nanowire array waveguide heterostructures similar to green-emitting nanowire laser heterostructures except the disks and without Si and Mg doping used in transmission measurements. x is the direction of the nanowire waveguide/cavity made up of nanowire-parylene composite and z is the nanowire growth direction, (b) output intensity from the nanowire-array ridge waveguides of (a), measured with a CCD detector, as a function of waveguide length. The input excitation was focused light from a 532 nm laser. The propagation loss was obtained for ridge nanowire waveguides of different length and having a fixed width of 10µm. The inset shows a CCD image from the output facet of the nanowire waveguide.

~0.35 and ~0.95, respectively.

6.6 Light Propagation in Nanowire Waveguide

Prior to measuring the fabricated waveguides, 3D finite-difference time-domain

(FDTD) electromagnetic simulation was performed on the nanowire waveguides in order to understand how the lasing mode will propagate through the nanowire-parylene composite cavity. Nanowire spacing and density will affect mode distribution and scattering, and consequently affect macroscopic cavity optical properties of interest to laser operation. Nanowire waveguides were fabricated by mesa etching the nanowire laser heterostructure, grown without Si and Mg doping and the InGaN/GaN disks, in the same way as the edge-emitting lasers. As-grown nanowire heterostructures were passivated and planarized with parylene. Figure 6.13(a) shows the schematic representation of the parylene-planarized nanowire waveguides along with the direction of the cavity. Before proceeding with the transmission measurements on the nanowire waveguides with different lengths, the optical field distribution in the nanowire waveguide was determined by the three-dimensional (3D) finite difference time domain (FDTD) simulation. The waveguide was modeled as a hexagonal close-packed (HCP) nanowire array with 60 nm nanowire diameter, an average period of 67 nm, and parylene filling the gaps between nanowires as in the fabricated devices. An $Al_{0.11}Ga_{0.89}N$ cladding refractive index of 2.3887, $In_{0.06}Ga_{0.94}N$ waveguide refractive index of 2.4369, and a GaN refractive index of 2.4169 were used for the respective nanowire layers in the simulation for the green emission wavelength. To avoid the possible formation of a photonic crystal and associated effects, the nanowires were randomly positioned with a maximum offset of 2 nm from the periodic positions in the simulation. The used 2nm maximum offset represents a random offset of up to 28.5% from the nominal 7nm spacing between the nanowires in the array. It is important to note that the purpose of the random offset it not to accurately simulate the random nanowire growth but rather to suppress photonic

crystal effects that could arise. Also, the region between the nanowires is assumed to be filled with parylene, as in the fabricated devices. Figures 6.14(a) and (b) show the cavity fields in the x-y and x-z planes, respectively (with reference to the schematic in

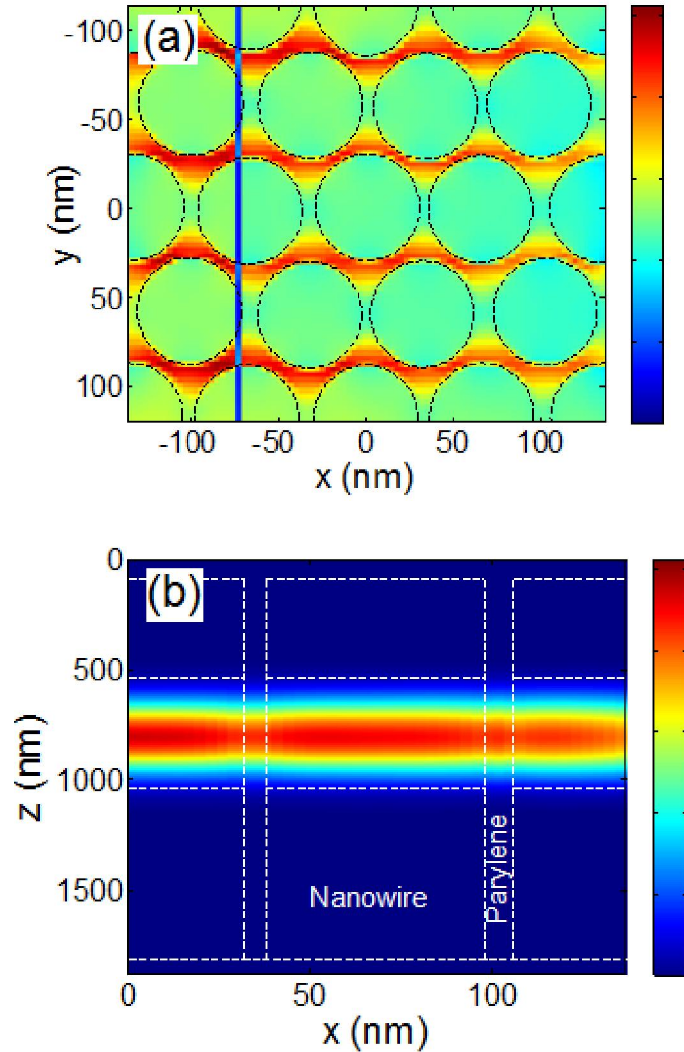

Figure 6.14 Optical field distribution in the (a) x-y and (b) x-z planes, respectively of the nanowire waveguide, used for the green-emitting laser, (with reference to the schematic in Fig. 6.13(a) in response to a y-polarized plane wave modulated by a Gaussian distribution approximating the calculated mode in Fig. 6.6(b). Light can propagate freely in the in-plane direction as the field is continuous over the nanowires.

Fig. 6.13(a)), in response to a y-polarized plane wave modulated by a Gaussian

distribution approximating the calculated guided-mode profile for the green-emitting laser heterostructure shown in Fig. 6.6(a). The field is continuous over the nanowires showing no confinement along the cavity length (x-axis), indicating that light can freely propagate in the in-plane direction. Hence, the nanowire waveguide region can be treated as a nanowire-parylene 3D composite with a lower average refractive index of $n_r \sim 2.1$. The localization of a part of the cavity field between the nanowires results from the mutual enhancement of two evanescent fields in proximity, also observed in slotted waveguides [168, 169]. The discontinuity of the field observed in the y-direction is an artifact of the y-polarized source used in the simulation.

The propagation loss, including the scattering loss and substrate leakage, in nanowire waveguides, used for green-emitting laser, was obtained from transmission measurements on ridge waveguides of different length and having a fixed width of 10µm. This measurement was to confirm that the nanowires act as a waveguide (confining light) and that there is not substantial substrate leakage or scattering loss. Ridge-shaped waveguides were fabricated by mesa etching the nanowire laser heterostructure, grown without Si and Mg doping and the $In_{0.34}Ga_{0.66}N$/GaN disks, in the same way as the edge-emitting lasers. The waveguides were end-fired with light from a 532 nm laser focused to a 10 μm^2 spot. It may be noted that the sub-bandgap (2.33 eV) excitation will be freely transmitted in the nanowire waveguide wherein the smallest bandgap material is the $In_{0.06}Ga_{0.94}N$ waveguide (E_g=3.12 eV). The output intensity was measured with a charged coupled device (CCD) detector. The measured output intensity as a function of guide length is plotted in Fig. 6.13(b), from which a loss of γ=7.2 dB/cm is derived. This value is of the same order as those of bulk III-nitride semiconductor waveguides [144, 170].

The inset to Fig. 6.13(b) shows a CCD image from the output facet of the nanowire waveguide.

6.7 DC Characteristics of Electrically Injected Monolithic Green-Emitting (λ=533nm) InGaN/GaN Disk-in-Nanowire Lasers on (001) Silicon

6.7.1 Light-Current and Spectral Characteristics

Measurements were made on the green-emitting nanowire lasers at room temperature with continuous wave (cw) bias. The electrical characteristics of the lasers were measured with a Keithley 2611 sourcemeter under cw and pulsed (500μs pulse, 1% duty cycle) current bias. The green-emitting laser diodes have a turn on voltage around 8.6V and a series resistance of 32Ω. The light-output characteristics were measured with a power meter and a calibrated silicon photodetector. The laser temperature was kept fixed with an adequately heat sinked thermoelectric cooler during the measurements. The spectral characteristics of the laser were measured using a high resolution (0.03nm) monochromator and detected using a photomultiplier tube. The output power versus current, or light-current (L-I) characteristics, of a broad area device are shown in Fig. 6.15(a). The output is measured from the low reflectivity facet. The threshold current density is J_{th}= 1.76 kA/cm^2 and the maximum measured output power from a single facet is 6.5mW under cw operation. The slope efficiency of the output is 1.15% (0.03 W/A). Pulsed bias measurements have been made on the same device, and the measured L-I characteristics are also shown in Fig. 6.15(a). The threshold current density, maximum measured power and slope efficiency from these data are 1.72 kA/cm^2, 8 mW and 1.3%, respectively. The values of J_{th} at room temperature mentioned above are significantly smaller than those reported for planar InGaN quantum well devices [44, 59, 143, 149-

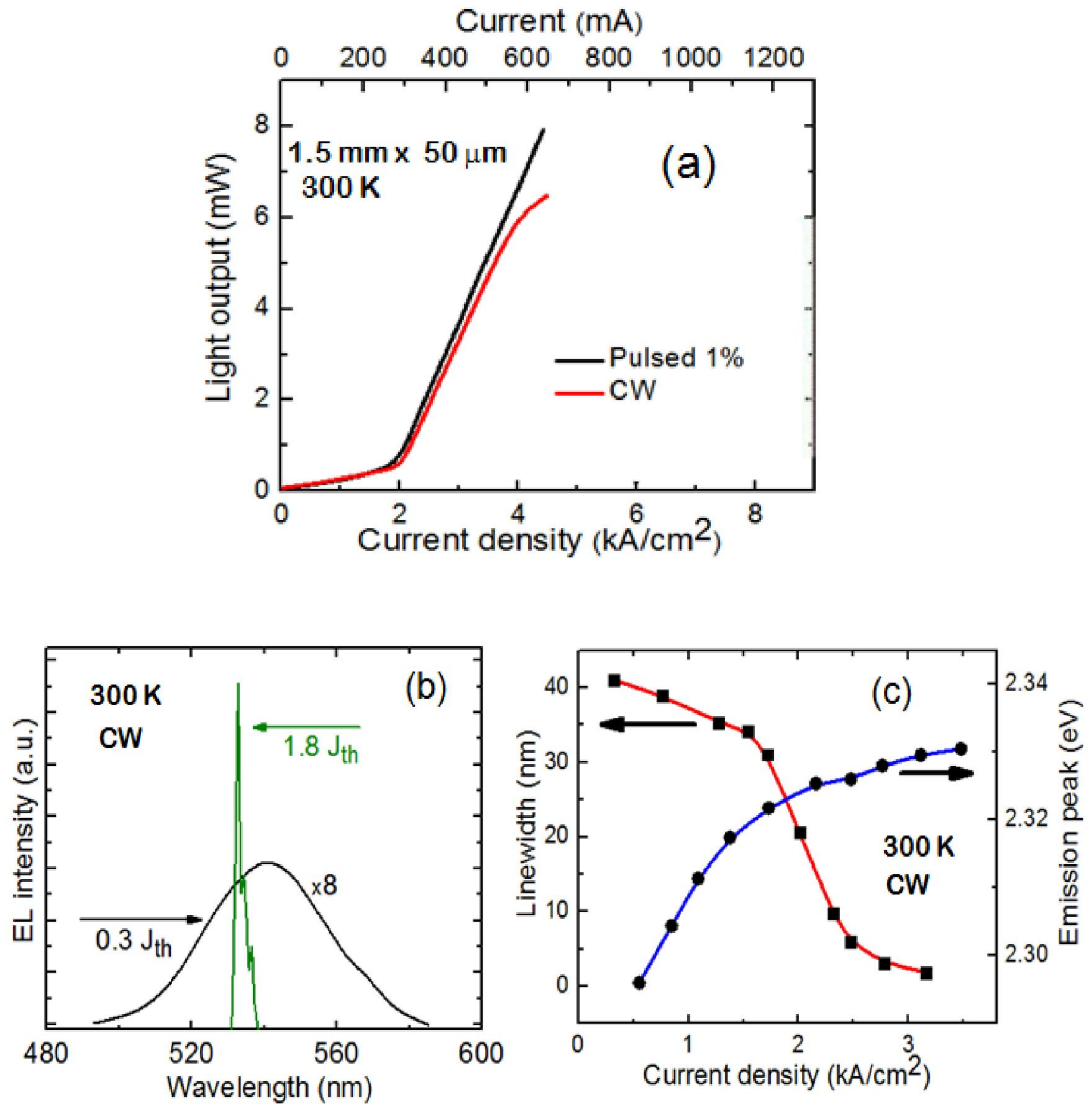

Figure 6.15 (a) Light-current (L-I) characteristics of a broad area (1 mm x 50 µm) green nanowire laser at 300K. The threshold current density, J_{th} is 1.76 kA/cm^2 and 1.72 kA/cm^2, respectively, under continuous wave and pulsed biasing; (b) the electroluminescence (EL) spectrum of the 1.5 mm x 10 µm ridge waveguide laser biased cw above and below threshold. The smallest recorded linewidth is 8Å, (c) the variation of the emission linewidth and the blueshift of the peak emission with increasing injection current density for the ridge waveguide laser.

152] and are comparable to that measured in a green-emitting InGaN/GaN self-organized quantum dot laser [37, 171]. The electroluminescence (EL) spectrum of a ridge waveguide laser biased above threshold is shown in Fig. 6.15(b). The EL spectrum

measured in the same device below threshold is also shown alongside. The variation of the emission linewidth and the blueshift of the peak emission with increasing injection current are plotted in Fig. 6.15(c). The multiple longitudinal mode emission is evident in the lasing electroluminescence spectra. The spectra above threshold are fit by a sum of Gaussian functions, and the smallest linewidth of the dominant longitudinal mode is

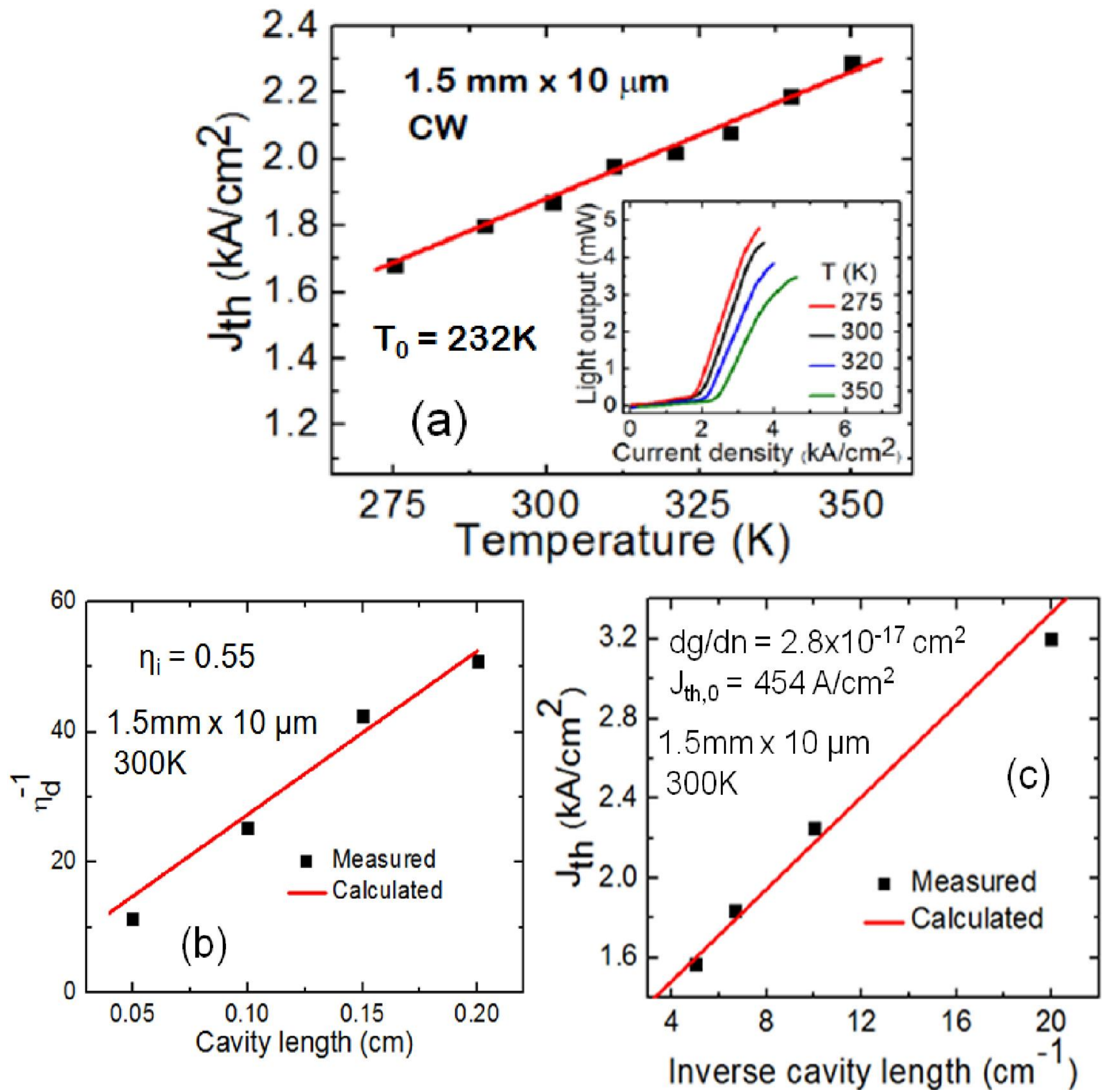

Figure 6.16 (a) Temperature dependence of the threshold current density in a ridge waveguide green nanowire laser under cw biasing. The inset shows the measured L-I characteristics at different temperatures; (b) the variation of the inverse differential quantum efficiency with cavity length for ridge waveguide lasers with 10µm width. (c) the variation of threshold current density, J_{th} with inverse cavity length.

found to be 8Å at $1.8I_{th}$. The corresponding polarization field is calculated to be 618 kV/cm, which is significantly lower than that reported for comparable planar InGaN quantum wells [104]. The lower polarization field in the InGaN disk is a result of the strain relaxation during epitaxy of the nanowires.

The temperature dependence of the threshold current of a 10 μm ridge waveguide laser is shown in Fig. 6.16(a). The corresponding L-I characteristics are shown in the inset. A value of the temperature coefficient T_0 = 232K, in accordance with the relation: $J_{th}(T) = J_{th}(0)\exp(T/T_0)$, is derived, which shows weak temperature dependence of the threshold current. An almost identical value of T_0 was measured for green-emitting self-organized quantum dot lasers [37]. The large value of T_0 reflects small carrier leakage and a negligible rate of Auger recombination in the active region. Steady-state L-I measurements have also been made on ridge waveguide lasers of varying length. Figure 6.16(b) shows the variation of the inverse differential quantum efficiency, corresponding to the slope above threshold, with cavity length. These data can be analyzed using Eq. 6.1 to yield the internal quantum efficiency from its intercept on the η_d^{-1}axis. A value of η_i= 0.55 is derived, which is in very close to what we have measured earlier from temperature dependent PL.

$$\frac{1}{\eta_d} = \alpha_i L \, ln \frac{1}{\sqrt{R_1 R_2}} + \frac{1}{\eta_i} \qquad (6.1)$$

Figure 6.16(c) shows the variation of J_{th} with inverse cavity length. Knowing the values of total carrier lifetime τ (395ps) in the disks measured from time-resolved PL and γ in the nanowire waveguides, a value of differential gain dg/dn = $2.8\text{x}10^{-17}$ cm^2 is derived from the slope of this data. A transparency current density of 454 A/cm^2 is calculated

from the intercept of this plot on the J_{th} axis. The differential gain is calculated by fitting the threshold current density as a function of inverse cavity length according to the relation:

$$J_{th} = J_{th}^{0} + \frac{qd}{\eta_{inj}\Gamma\tau\frac{dg}{dn}}\left[\gamma + \frac{1}{2L}ln\left(\frac{1}{R_1R_2}\right)\right] \tag{6.2}$$

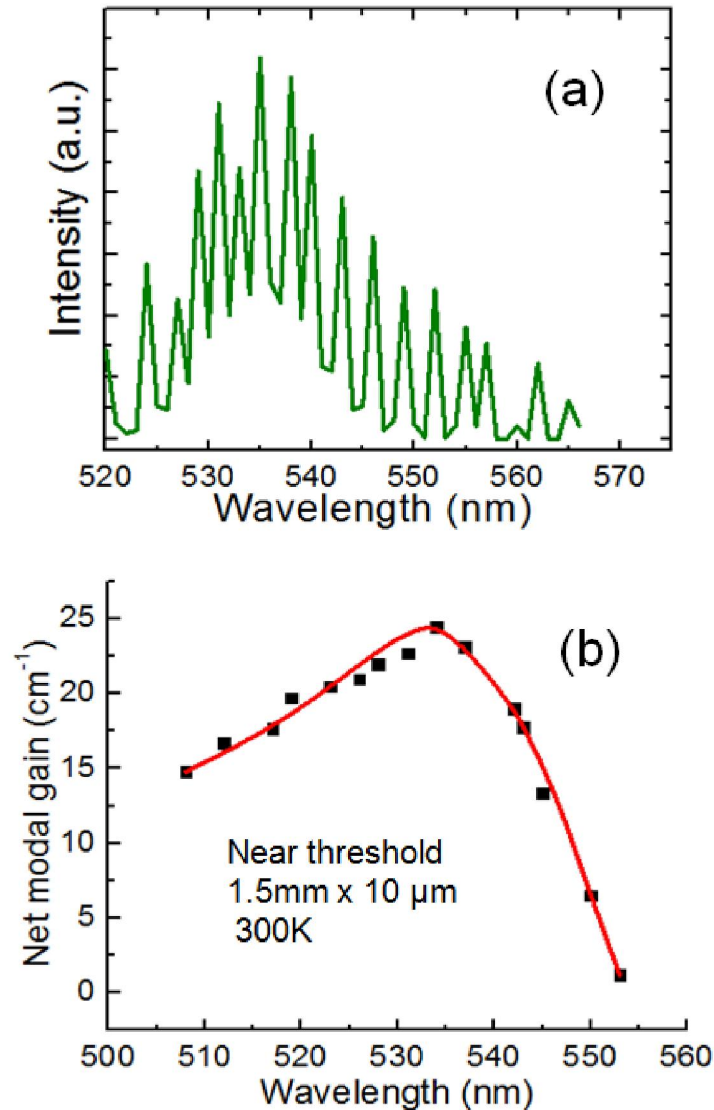

Figure 6.17 (a) Emission spectra of green-emitting nanowire laser near threshold, characterized by a succession of peaks and valleys, (b) modal gain spectrum at threshold obtained from Hakki-Paoli measurement. The peak net modal gain at threshold is $24 cm^{-1}$.

where d is the active region thickness calculated as the number of disk layers times the disk height (2 nm), Γ is the optical confinement factor including the fill factor (0.018) simulated by transfer matrix method, τ is the measured carrier lifetime (395ps), γ is waveguide loss (5.7 cm^{-1} or 7.6 dB/cm), L is the cavity length, R_1 and R_2 are the facet reflectivities (0.72 and 0.95) and injection efficiency (η_{inj}) is assumed to be unity. J_{th}^0 and dg/dn are fitting parameters. The fill factor is the fraction of the silicon substrate surface on which the nanowires have grown and is estimated from SEM images of the grown nanowire heterostructure.

6.7.2 Measurement of Modal Gain

The threshold current of a semiconductor laser and the dynamic characteristics including the small-signal modulation bandwidth, chirp and linewidth enhancement factor are ultimately determined by the gain in the active region. The gain of the nanowire lasing medium near threshold for a 10μm ridge waveguide green-emitting laser was measured by the Hakki-Paoli technique using the formula:

$$\Gamma g_i = \frac{1}{L}\ln\left(\frac{r_i^{\frac{1}{2}}+1}{r_i^{\frac{1}{2}}-1}\right) + \frac{1}{L}\ln(R) \tag{6.3}$$

Here Γ is the optical confinement factor, L is the cavity length, R is the facet reflectivity, and $r_i = (I_p+I_{p+1})/2I_v$, where I_p and I_{p+1} are adjacent peak intensities in the electroluminescence spectrum separated by the valley intensity, I_v. The emission spectra for increasing injection current are recorded (with a spectral resolution of 0.03 nm), till threshold is reached. The spectra is then characterized by a succession of peaks and valleys corresponding to the longitudinal modes, as shown in Fig. 6.17(a). The spectral

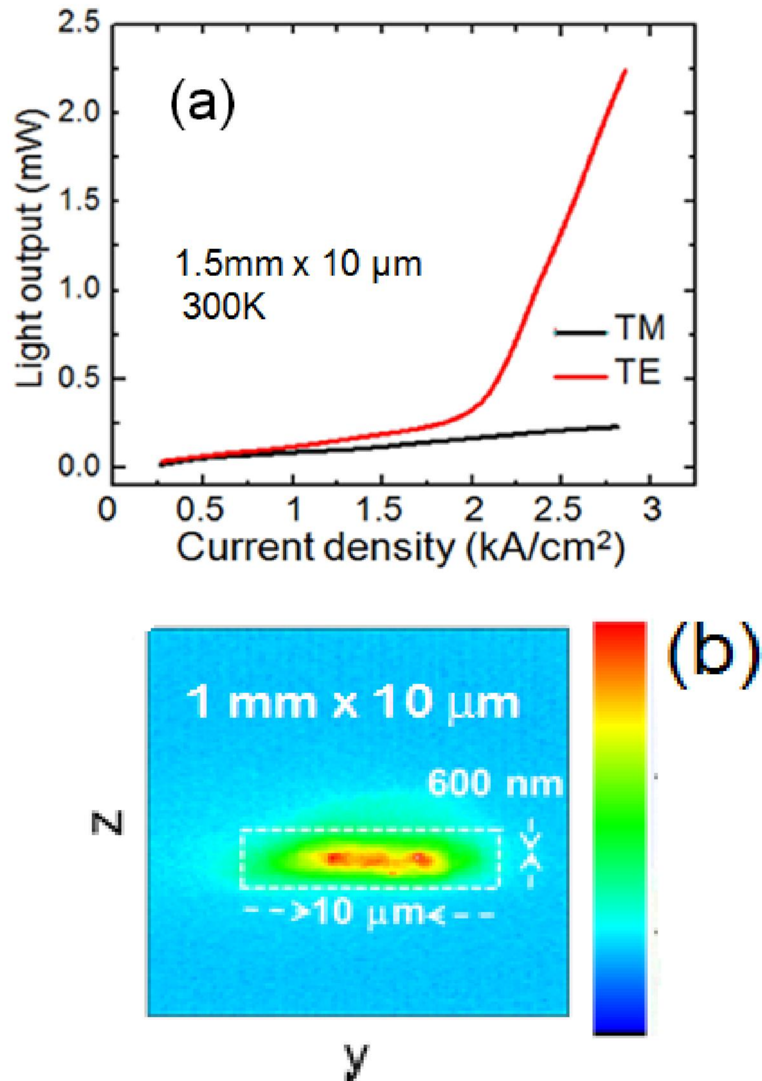

Figure 6.18 (a) Polarization dependent output from single facet of green nanowire array laser, which shows that TE polarized component increases significantly with a threshold of 1.82 kA/cm^2, (b) near field mode intensity profiles from the low reflectivity facet along the growth (transverse) and lateral directions of the green nanowire laser cavity.

gain is derived by analyzing these data. The modal gain Γg is plotted as a function of photon energy in Fig. 6.17(b). The peak modal gain at threshold is 24 cm^{-1}. This value compares well with those of calculated gain spectra for $In_{0.27}Ga_{0.73}N$ self-organized quantum dots of base width and height equal to 50 nm and 3 nm, respectively, in a green emitting laser [101].

6.7.3 Output Polarization and Near-Field Characteristics

An electrically pumped laser with an array of nanowires, surface- or edge-emitting, has never been reported. It was therefore of interest to investigate the nature of the light output of the edge-emitting devices. The polarization of the laser output was measured as a function of injection current by placing a linear polarizer between the laser facet and the silicon photodetector which is used to measure the output power. The L-I characteristics with the linear polarizer aligned along the TE and TM axes are shown in Fig. 6.18(a). The laser output is TE-polarized in the in-plane. While the TM-polarized light output remains low throughout the injection range, the TE-polarized light output increases sharply above ~2 kA/cm^2. This is due to the higher confinement and gain of the TE mode than that of the TM mode. It should be noted that even beyond the TE threshold the TM output intensity does not saturate. This is likely due to the nearly degenerate valence band energy levels, and band mixing effects.

We have measured the near-field pattern from the low reflectivity facet of the ridge-waveguide laser. Measurements were made on a 1 mm x 10 μm ridge waveguide laser under cw bias. The near-field image at the low reflectivity facet, shown in Fig. 6.18(b), indicates good mode confinement in the transverse (growth) direction and multi-mode behavior in the lateral direction, as expected. With smaller ridge widths, it should be possible to realize single mode devices for a specified application.

6.7.4 Far-Field Pattern and Long-Term Reliability Measurements

The measured far-field pattern from the low-reflectivity facet of the 1 mm x 10 μm ridge waveguide green-emitting laser is illustrated in Fig. 6.19(a). The pattern is

characterized by a divergence angle of 22° in the transverse growth direction and 3° in the lateral direction, yielding an aspect ratio of 7.3. This ratio can be improved by re-designing the nanowire heterostructures.

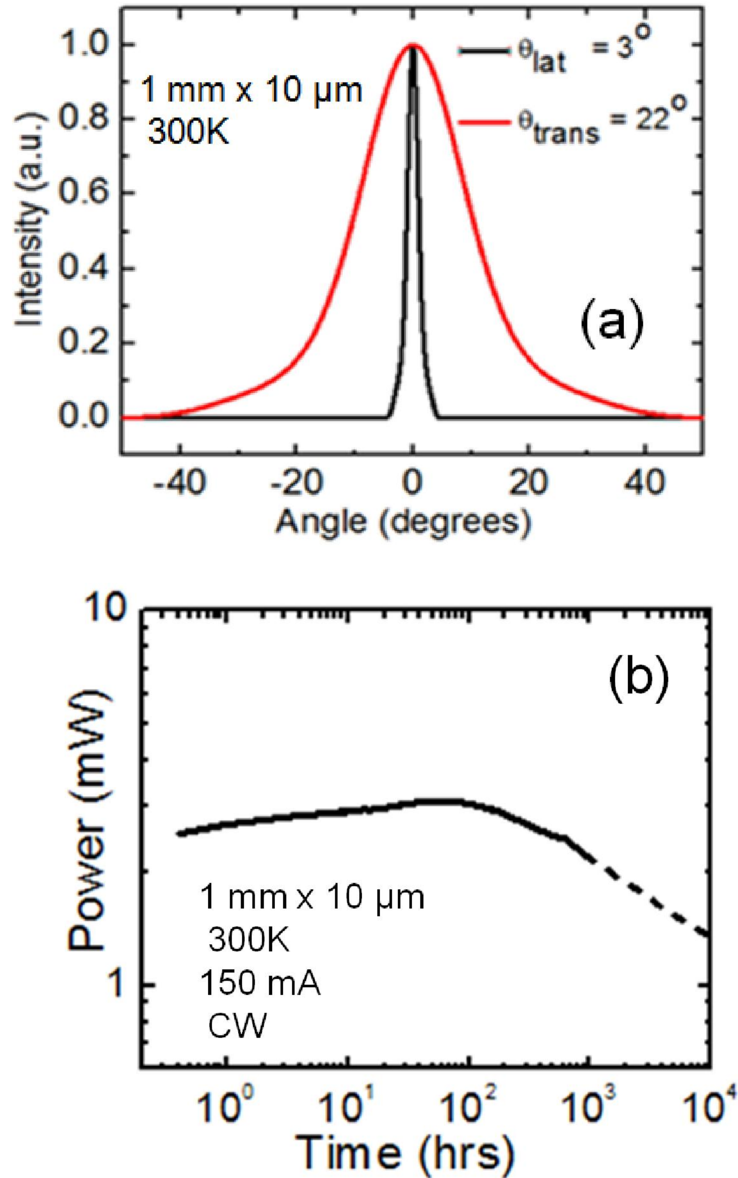

Figure 6.19 (a) Far field pattern from the low reflectivity facet of a ridge waveguide green-emitting nanowire array laser, (b) the output power from the green nanowire laser versus time with an extrapolated lifetime for the output power to be reduced to half the maximum value of 7000hrs.

A preliminary investigation of the long-term reliability of the nanowire lasers was made by observing the change in output power of a 1 mm x 10 μm ridge waveguide laser under a constant injection current of 150 mA at room temperature under cw biasing. The result is shown in Fig. 6.19(b). An extrapolated lifetime of ~7000 hours, at which the output power is expected to be reduced to the half of its initial value (3 mW) at time t =0, is derived. To the best of our knowledge, such reliability data has not been reported for any other laser on silicon. When the laser is biased with constant injection current over a long time, both dopant activation and defect generation occur simultaneously in the structure and compete with each other. Initially, dopant activation [172] in the structure probably dominates the defect generation which leads to an increase in laser output as observed in Fig. 6.19(b). Eventually, defect generation with time takes over and laser output decreases.

6.8 Dynamic Characteristics of Green-Emitting (λ=533nm) InGaN/GaN Disk-in-Nanowire Lasers on (001) Silicon

Measurement of the dynamic characteristics of a laser by direct bias modulation can provide a host of important information. For example, the lasers described here could be directly modulated on a CMOS chip for on-chip communication, without the need for an external modulator. Small-signal modulation experiments provide information regarding the differential gain, gain compression, and other hot-carrier related effects. Measurements were made on 4 μm ridge waveguide $In_{0.34}Ga_{0.66}N$ disk-in-nanowire lasers of 400μm length at room temperature using a 40 GHz high speed detector and spectrum analyzer. The measured response was calibrated for the losses due to cable, connectors,

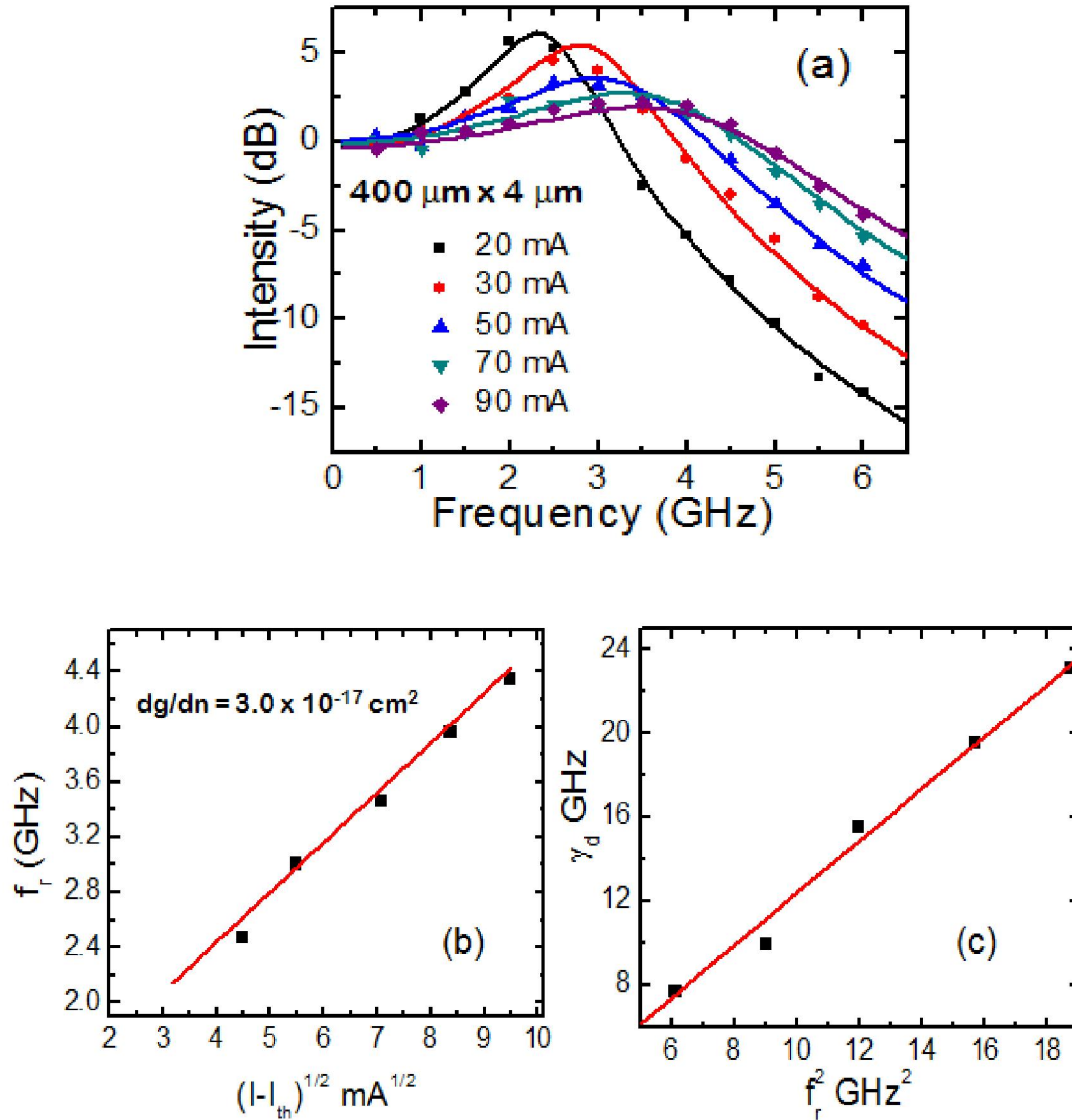

Figure 6.20 (a) Measured small-signal modulation response of a 400µm x 4µm ridge waveguide green nanowire laser at 300K for varying dc injection current values. The data is analyzed to derive the response frequency f_r and damping factor γ_d, (b) plot of f_r versus square root of injection current. The differential gain is derived from the slope of this plot, (c) Plot of γ_d versus square of resonance frequency. The gain compression factor ϵ is derived from the slope of this plot.

bias network and dc-blocking capacitor. The modulation response as a function of dc bias current is shown in Fig. 6.20(a). The sharp peaking at the resonance frequency for small values of current is an indication of small damping of the response and efficient

thermalization and stimulated emission of injected carriers. The measured data have been analyzed with the small-signal response:

$$|R(f)|^2 \propto \frac{1}{(f-f_r^2)+\left(\frac{\gamma_d}{2\pi}\right)^2 f^2} \tag{6.4}$$

where f_r is the resonance frequency and γ_d is the damping factor. A -3dB modulation bandwidth, f_{-3dB}= 5.8GHz was measured for the highest current bias of 90 mA at room temperature. This -3dB bandwidth corresponds to bit rate of ~9 Gb/s for a bit error rate of less than 10^{-11}. Figure 6.20(b) shows a plot of f_r versus $(I-I_{th})^{1/2}$. The differential gain can be derived from the slope of this plot in accordance with the relation:

$$f_r = \frac{1}{2\pi}\left[\frac{v_g\Gamma(I-I_{th})\frac{dg}{dn}\eta_i}{V_{act}q}\right]^{\frac{1}{2}} \tag{6.5}$$

where v_g is the photon group velocity and V_{act} is the active volume of the gain medium. The value of dg/dn = $3x10^{-17}$ cm^2, derived from the plot of Fig. 6.20(b), is in excellent agreement with the value derived earlier from the length dependent L-I measurements. Under gain compression limited modulation conditions γ_d is related to f_r by the approximate relation $\gamma_d = Kf_r^2$, where K is a measure of the damping related bandwidth and is given by:

$$K \cong 4\pi^2\left(\frac{\epsilon}{v_g\frac{dg}{dn}} + \tau_P\right) \tag{6.6}$$

where ϵ is the gain compression factor and τ_p is the cavity photon lifetime. The plot of γ_d versus f_r^2 is illustrated in the Fig. 6.20(c). The value of K derived from the slope is 1.24 ns from which a value of ϵ=1.22 x $10^{-17}cm^3$ is derived. This value is relatively small, confirming that hot carrier effects do not play any significant role in the operation of the

nanowire lasers [173].

6.9 Dynamic Characteristics of Electrically Injected Monolithic Red-Emitting (λ=610nm) InGaN / GaN Disk-in-Nanowire Lasers on (001) Silicon

As mentioned in section 6.4, we have increased the indium composition in the disks to make edge-emitting red nanowire laser on (001) silicon, and have replaced $Al_{0.11}Ga_{0.89}N$ cladding with $In_{0.18}Al_{0.82}N$ cladding, grown lattice matched to GaN. Wehave also measured the characteristics of the fabricated red-emitting laser. The red-emitting laser diodes have a turn on voltage of ~ 8.2V and a series resistance of 26.5 Ω. A threshold current density, J_{th} of 2.85 kA/cm^2 was measured under pulsed biasing (1% duty cycle), and a J_{th} of 2.92 kA/cm^2 was obtained under cw operation. For conventional InAlGaP based red-emitting lasers, the reported J_{th} was 6.4 kA/cm^2, much higher than what we measured in our red-emitting lasers [174, 175]. Maximum light outputs of 14.8 mW and 12.5 mW were measured from the low reflectivity facet of the laser under pulsed and CW mode, respectively as shown in Fig. 6.21(a). The slope efficiency of the laser is η_d= 0.1 W/A (4.4%) with a Wall-plug efficiency of 0.57%. Figure 6.21(c) shows the variation of emission linewidth and peak emission wavelength with increasing injection current density. Figure 6.21(b) shows the electroluminescence of the laser below (0.6J_{th}) and above threshold (1.4J_{th}). The smallest recorded linewidth for the dominant longitudinal mode is 9Å, illustrated and total blueshift of peak emission is 14.8 nm, which corresponds to a polarization field of 1098kV/cm. For a green-emitting (λ=525nm) planar InGaN QW laser with high radiative efficiency, the reported total blueshift of the peak emission was 2MV/cm [104]. From Hakki-Paoli measurements, a peak modal gain

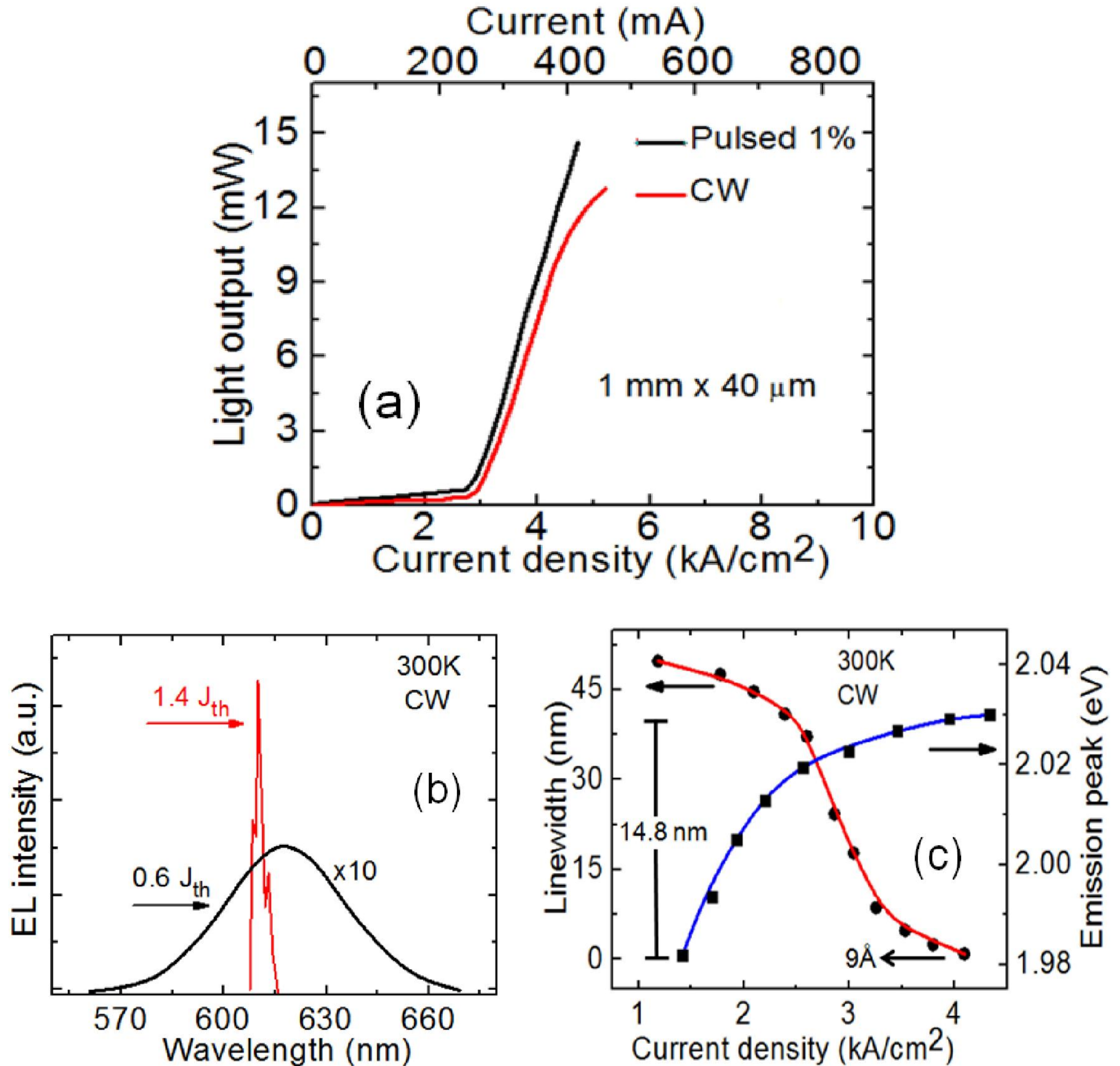

Figure 6.21 (a) Light-current (L-I) characteristics of a ridge waveguide nanowire red nanowire laser at 300K. The threshold current density, J_{th} is 2.88 kA/cm^2 under continuous wave operation; (b) the electroluminescence (EL) spectrum of the 1.5 mm x 10 μm ridge waveguide laser biased cw above and below threshold. The smallest recorded linewidth is 9Å, (c) the variation of the emission linewidth and the blueshift of the peak emission with increasing injection current density for the ridge waveguide laser. The total blueshift of the peak emission is 14.8 nm which corresponds to a polarization field of 1098 kV/cm.

of 27 cm^{-1} was obtained at threshold. Figure 6.22(a) demonstrates the variation of modal gain as a function of wavelength near threshold derived from the emission spectra having succession of peaks and valleys, where the peaks correspond to the different longitudinal

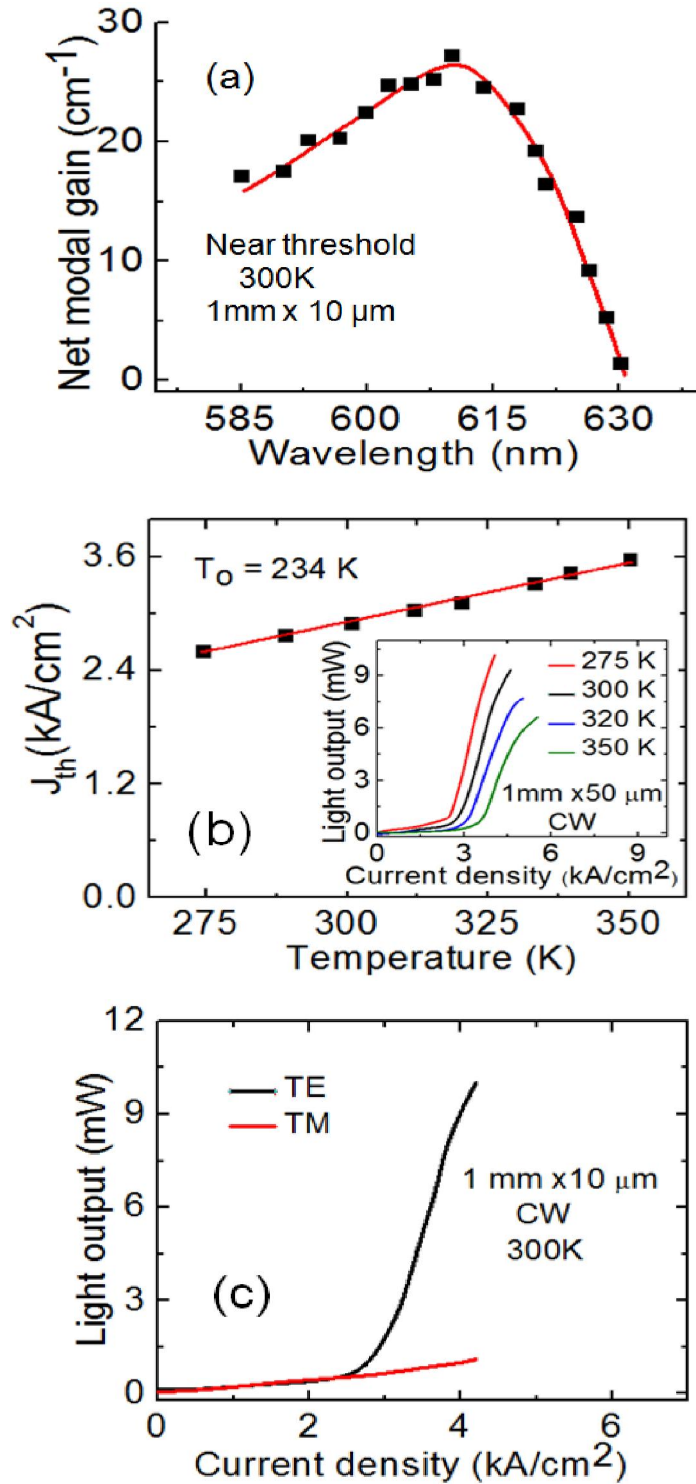

Figure 6.22 (a) Modal gain spectrum at threshold obtained from Hakki-Paoli measurement. The peak net modal gain at threshold is 27cm^{-1}, (b) Temperature dependence of the threshold current density in a ridge waveguide red nanowire laser under cw biasing. The inset shows the measured L-I characteristics at different temperatures, (c) Polarization dependent output from the single facet of red nanowire array laser.

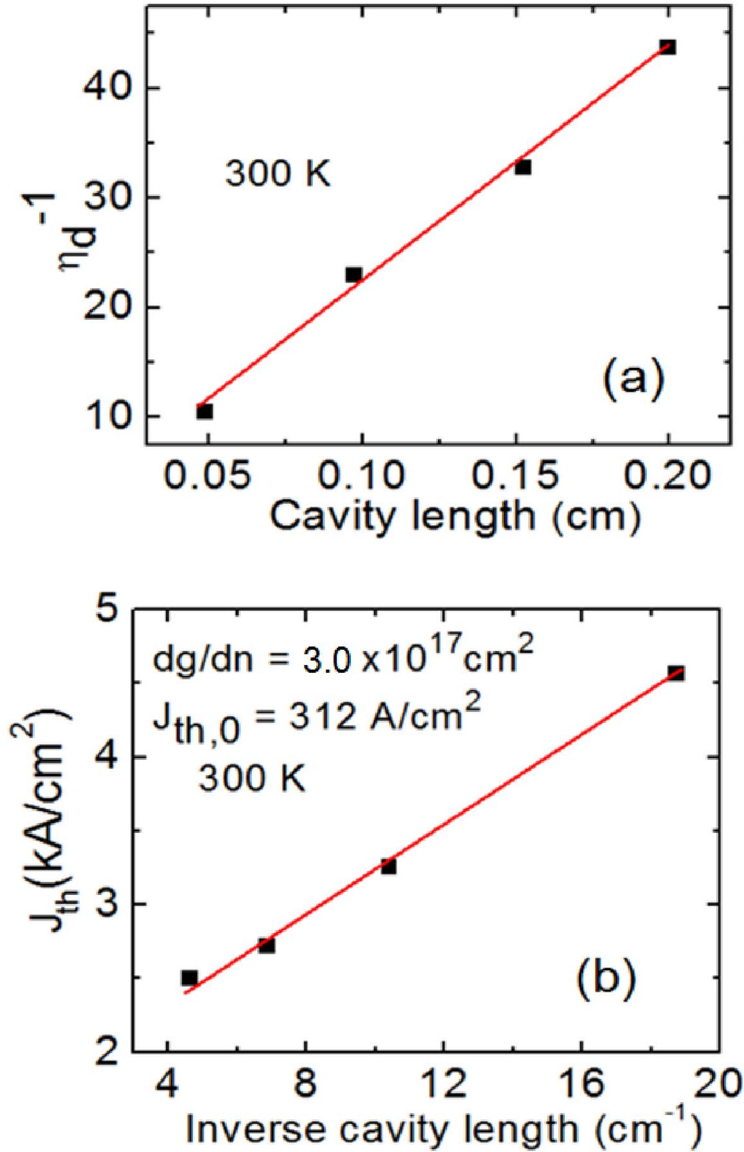

Figure 6.23 (a) The variation of the inverse differential quantum efficiency with cavity length for ridge waveguide lasers with 10µm width. From the analysis of these data, an internal quantum efficiency of η_i= 0.54 was derived, (b) the variation of threshold current density, J_{th} with inverse cavity length. A value of differential gain dg/dn = 3x10^{-17} cm^2 and a transparency current density of 312 A/cm^2 are derived from this plot using a total carrier lifetime τ of ~482 ps.

modes. The modal gain per disk layer is 4.5 cm^{-1}. Taking the mode confinement factor and the nanowire fill factor of 0.3 into account, the peak value of the material gain in the active region is ~ 1.5 x 10^3 cm^{-1}. From the temperature dependence of threshold current

density, a large value of T_0=234K was derived which is significantly higher than that reported for InAlGaP based red-emitting laser (T_0 ~40-60K) in literature [174, 175]. Figure 6.22(b) depicts threshold current density as a function of temperature along with the temperature dependent L-I curves on inset. From the measurement on output polarization, shown in Fig. 6.22(c), it is found that the emitted light is TE-polarized, which increases sharply above threshold. TM-polarized light output remains significantly low throughout the injection range. Figure 6.23(a) shows the variation of inverse differential quantum efficiency with cavity length. Knowing the propagation loss (~7.2 dB/cm) in the nanowire waveguides, we derived a radiative efficiency of 0.54 from the intercept of this data on η_d^{-1}-axis. This value is in good agreement to that we measured from temperature dependent PL. Figure 6.23(b) shows the variation of J_{th} as a function of inverse cavity length. Knowing the transmission loss in the waveguide and the total carrier lifetime (τ~ 482 ps) in the red-emitting InGaN disks, we derived a differential gain, dg/dn of $3x10^{-17}$ cm^2 from the slope of this plot. We also calculated a transparency current density of 312 A/cm^2 from the intercept of this data on y-axis.

Small signal modulation measurements were performed on red-emitting laser at room temperature, and a modulation bandwidth of ~3GHz is derived for the highest injection current of 80mA at room temperature, as depicted in Fig. 6.24(a). The differential gain is derived from a plot of the resonance frequency f_r versus $(I-I_{th})^{1/2}$, with values of η_r and confinement factor Γ equal to 0.52 and 0.018, respectively, to be $3.1x10^{17}$ cm^2. This value compares favorably with the differential gain of red-emitting self-organized quantum dot lasers [139]. Under small-signal modulation, changes in refractive index in the active region in a laser can cause frequency chirping resulted from

the generation of hot carriers and subsequent gain suppression. We have measured chirp in the nanowire lasers during small-signal modulation by measuring the broadening of a single longitudinal mode using an optical spectrum analyzer. The sinusoidal modulation

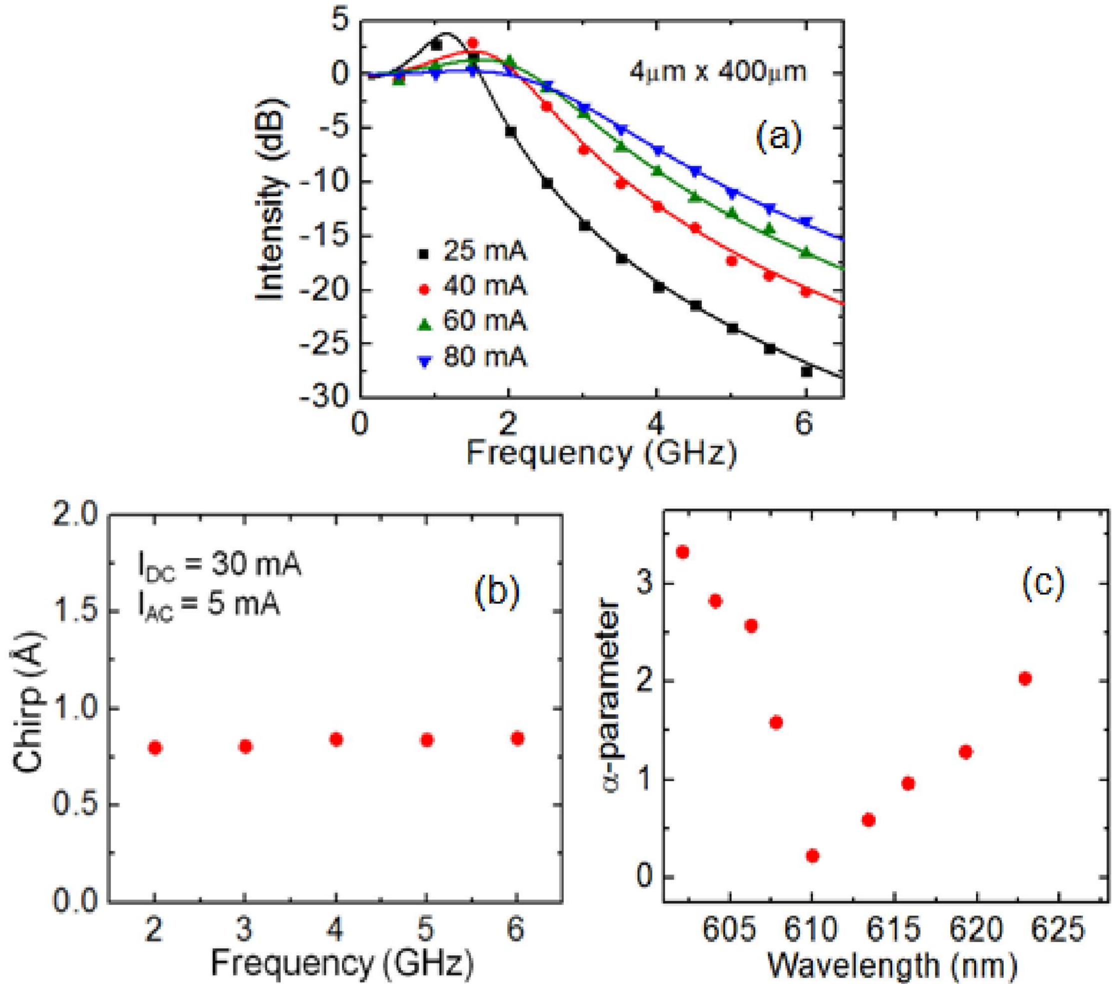

Figure 6.24 (a) Measured small-signal modulation response of a 400μm x 4μm ridge waveguide red nanowire laser at 300K for varying dc injection current values; (b) measured chirp of nanowire laser as a function of small-signal modulation frequency; (c) measured α-parameter as a function of emission wavelength.

current was superimposed on the pulsed dc bias current above threshold. The measurements were done as a function of the frequency of the modulating current. A dc current of 24mA was used while measuring the chirp in a 4 μm x 400 μm red laser with a

peak-to-peak modulation current of 5 mA. The envelope of the dynamic shift in the wavelength was recorded as a function of frequency. The difference between the half-width of the observed envelopes with and without modulation is plotted as the evaluated chirp at room temperature in Fig. 6.24(b). The measured chirp in the device is 0.8Å at a modulation frequency of 6 MHz. Dense and ultra-dense wavelength division multiplexing schemes require narrow emission linewidth with a low dynamic chirp of the emission wavelength [176]. The conventional 1.55 μm light source has been the InGaAsP double heterostructure or multi-quantum well (MQW) laser which has large values of chirp (≥ 2 Å) [177, 178]. Another important parameter related to the effects of the change of refractive index in the gain medium with injection current on the dynamic characteristics of the laser is the linewidth enhancement factor or α-parameter. The α-parameter is expressed as: $\alpha = -\frac{4\pi}{\lambda}(\frac{dn_r/dn}{dg/dn})$ and is derived from Hakki-Paoli measurements using the relation:

$$\alpha = \frac{2}{\delta\lambda}\frac{d\lambda_j}{d\{\ln\left[\frac{\sqrt{r_j}-1}{\sqrt{r_j}+1}\right]\}} \tag{6.7}$$

where λ_j is the peak wavelength of the jth mode in the near-threshold spectrum, r_j is the peak-to-valley ratio in the spectrum and δλ is the mode spacing between adjacent longitudinal modes in the emission spectrum recorded at threshold. The measured α-parameters as a function of emission wavelengths are plotted in Fig. 6.24(c). α is ~0 near the peak emission wavelength (λ=610nm), and increases to above 2 at both shorter and longer wavelengths. From theoretical calculation, it has been shown that the minimum value of α occurs approximately at the emission wavelength at which the peak gain is

derived in quantum dot and quantum wire lasers [179]. Low values of chirp and α-factor measured in these nanowire devices are favorable dynamic characteristics of a semiconductor laser.

6.10 Summary

In conclusion, we have demonstrated the first monolithic electrically injected nanowire array laser on (001) silicon. Both green (λ=533nm) and red (λ=610nm) edge-emitting nanowire lasers were grown on silicon by molecular beam epitaxy. From FDTD simulation, it is found that the optical field is continuous over all the nanowires with parylene filling the gaps between them, and the nanowire waveguide can be treated as nanowire-parylene composite. Edge-emitting electrically pumped green-emitting nanowire lasers on silicon have demonstrated potential for superior performances in terms of threshold current density (1.76 kA/cm^2), differential gain ($2.8 \times 10^{-17} cm^2$), temperature coefficient (232K) and small signal modulation bandwidth (5.8GHz). In particular, the threshold current density is significantly lower than that reported for green-emitting planar InGaN quantum well lasers.

We have also fabricated edge-emitting red nanowire lasers with different cavity lengths and ridge widths. For the red-emitting nanowire laser heterostructure, we have grown $In_{0.18}Al_{0.82}N$ nanowire cladding layer lattice matched to GaN, which provided much better optical mode confinement keeping the overall device series resistance low. Upon a detail characterization of the red nanowire lasers, a threshold current density of 2.85 kA/cm^2, a large T_0 of 234K and a differential gain of $3.1 \times 10^{-17} cm^2$ were measured from these devices. Small signal modulation bandwidth of 3GHz at 300K was measured

for the red-emitting laser. A chirp of less than 1Å for a modulation frequency of 6GHz and a near-zero α-parameter at the peak emission wavelength (λ~610nm) have been extracted from the dynamic measurements on the red lasers. These are favorable characteristics of a semiconductor laser and encouraging for optical communication in plastic fibers. The nanowire array red-emitting lasers demonstrated here have better performances than those of the conventional planar InAlGaP based red-emitting lasers in terms of threshold current density and temperature coefficient. In particular, the temperature coefficient measured from the red nanowire laser is significantly larger than those obtained for conventional InAlGaP based red lasers (T_o~40-60K). Increasing the radiative efficiency of the green- and red-emitting InGaN/GaN disks further in the active region by varying the growth conditions in MBE system, modifying the cladding layers in the laser heterostructure to provide even better optical mode confinement, lowering the overall device series resistance by optimizing p-doping using metal modulation epitaxy, and using anti-reflective coating on the light-extracting facet of the edge-emitting laser, threshold current density, slope efficiency and Wall-plug efficiency of these devices can be improved.

The monolithic green and red-emitting nanowire lasers described in this chapter are epitaxially grown on (001) Si substrates and are, therefore, compatible with mainstream Si CMOS technology. While we have demonstrated a visible laser here, emission into the near infrared should be possible and will be explored by changing the alloy composition in the InGaN disks. Of course, the longer emission wavelengths will present laser heterostructure design challenges in terms of mode confinement, but these are not unsurmountable. Currently, visible lasers are grown on extremely expensive GaN

substrates. We presented extensive data here showing that the nanowire lasers on substantially less expensive silicon substrates have performance characteristics comparable to or surpassing those of devices grown on GaN. This is due to the extremely low density of extended defects and a small polarization field in the nanowires. In the context of silicon photonics, the electrically pumped near-IR nanowire lasers can be monolithically integrated with Si-based passive waveguides and front-end photoreceivers (Ge or SiGe detector integrated with amplifier) [180] to form an optical communication link.

Chapter VII

Conclusion and Suggestion for Future Work

7.1 Summary of Present Work

The present work concentrated on the self-assembled growth and optimization of the radiative efficiency of InGaN/GaN disks-in-nanowires (DNWs) on (001) silicon substrates. Through extensive structural and optical characterization, importance of surface passivation of nanowires and optimum nanowire densities was studied. The findings obtained from this research helped in making nanowire LEDs exhibiting small injection-dependent peak shift and reduced efficiency drop at high injection currents and electrically injected monolithic lasers on silicon with substantially reduced threshold current density.

Growth of self-assembled blue (λ=430nm), green (λ=540nm) and red-emitting (λ=650 nm) InGaN/GaN disks-in-nanowires on (001) silicon by molecular beam epitaxy (MBE) was discussed in chapter II. Detailed structural characterizations including SEM, HRTEM and EDX measurements were performed on InGaN nanowires and InGaN/GaN DNWs to study the crystal quality of the as-grown nanowires and to calibrate the elemental compositions of the disks. Growth conditions inside MBE were varied and nanowire surfaces have been passivated with Si_3N_4 and parylene to maximize the radiative efficiency of the InGaN disks as high as

possible. Internal quantum efficiency (IQE) of as-grown blue, green and red DNW samples were measured from temperature dependent PL (TDPL) and were found to be as high as 48% 43% and 41%, respectively. Upon parylene passivation, maximum IQEs of 54%, 52% and 51% for the passivated blue, green and red disks, respectively were obtained. Parylene provided better surface passivation (~ 10-12% for all emission wavelengths) in comparison to Si_3N_4. Total carrier lifetimes in the as-grown and surface passivated InGaN disks were measured from time-resolved PL (TRPL). Using the data obtained from both TDPL and TRPL measurements, radiative and non-radiative carrier lifetimes in the disks were estimated. The change in the values of lifetimes was consistent with the improved radiative efficiency of the InGaN disks after parylene passivation.

Chapter III outlined the growth, fabrication and characteristics of the self-assembled nanowire blue (λ=430nm), green (λ=540nm) and red-emitting (λ=610nm) LEDs on (001) silicon. The diodes were characterized by a turn-on voltage in the range of ~6-7.5 V and a series resistance in the range of ~17-28Ω. Measured external quantum efficiency (EQE) at 300K has attained a peak value at an injection current density of ~ 18-38 A/cm^2, which is low and undergoes an efficiency drop of ~ 10-15% at $120A/cm^2$ compared to the peak efficiency of the corresponding LED. From the analysis of the EQE curves, Auger coefficients in the InGaN/GaN disks were derived to be ~ 10^{-34}-10^{-33} cm^6 s^{-1} for all emission wavelengths, which are low and consistent with theoretical calculations. The values of efficiency droop at high injection currents in the nanowire LEDs are smaller than those in planar InGaN quantum well (QW) LEDs due to the low Auger coefficients in the disks and the

presence of an electron blocking layer after the active region. Polarization fields of ~396kV/cm, 605kV/cm and 1260 kV/cm, were estimated for the blue, green and red-emitting LEDs on silicon, respectively measuring the blue-shifts in the electroluminescence (EL) peak with injection currents. Due to the radial strain relaxation of the nanowire heterostructure during epitaxy, these values of polarization fields in the disks are significantly smaller than those obtained for equivalent planar green-emitting InGaN quantum wells (~2 MV/cm) grown on c-plane sapphire substrate. Since silicon substrate, on which the LEDs are grown, absorbs light emitting from the disks, nanowire LEDs were transferred from silicon substrate to Ag reflector to increase the light output from the device. Characteristics of the flip-chip nanowire LED on metal reflector were discussed.

In the self-assembled growth of nanowires, optimum areal density plays a crucial role on their optical properties and therefore, on the device performance. We have examined the effect of nanowire coalescence in chapter IV that occurs when the areal density is increased above a certain limit. Detailed structural characterization of the nanowires using high resolution transmission electron microscopy (HRTEM) imaging reveals that coalescing can lead to threading dislocations and stacking faults near the coalesced nanowire boundaries. It was observed that the radiative efficiency of the InGaN/GaN DNWs, used as the gain media in nanowire LEDs and lasers, change significantly with areal density. The radiative efficiency was the lowest for the highest density disks-in-nanowires sample. To investigate the effect of areal density on the device performance, red-emitting nanowire LEDs, with different areal densities, were fabricated. The ones with the lowest optimum density have exhibited

the highest peak efficiency. Near-field images of the electroluminescence from the LEDs demonstrated that only a small percentage of the device area (~3%) was lighting up for the highest areal density (~ $2x10^{11}cm^{-2}$) sample. We have characterized and compared deep level electron and hole traps in GaN nanowires and bulk GaN by performing transient capacitance measurements on planar GaN and GaN nanowire $n^{+}p$ diodes, respectively. The activation energies for the electron and hole traps in them are similar, which indicates that the origin of these trap levels is similar in these structures. It is found that the density of these traps, which act as non-radiative recombination centers for carriers, increases by orders of magnitude with increase of nanowire density i.e. the degree of nanowire coalescence. Our analysis revealed that the absence of the traps in the red LEDs would result in a peak internal quantum efficiency (IQE) of ~60%. Nanowire LEDs have demonstrated their best performance in terms of peak efficiency with an optimized areal density of ~$2x10^{10}$ cm^{-2}.

To overcome the disadvantages of phosphor-converted white LEDs, all-nitride tunable InGaN/GaN disk-in-nanowire white LEDs on silicon, based on direct electrical injection, incorporating different color-emitting InGaN disks in the active region, have been described in Chapter V. A smaller shift in correlated color temperature (CCT) of white emission with injection current density was observed due to the reduced polarization field in the InGaN disks because of the radial strain relaxation during their epitaxy. To investigate the tunability of white emission from the nanowire LEDs, the number and emission wavelengths of the disks were varied which yielded CCTs in the range of 4210-6130K at an injection current density of 50

A/cm^2. The characteristics of phosphor-free self-organized InGaN/GaN quantum dot wavelength converter white LEDs have also been reported for comparison. Carriers were electrically injected in the blue-emitting exciting dots and the red-emitting dots were the wavelength converters. Stable CCTs with injection currents were observed for the wavelength converter LEDs, since self-assembled dots are formed by strain relaxation and therefore, they have significantly smaller polarization field. Color temperatures in the range of 4420-6700K at 45A/cm^2 were derived from these LEDs by changing the number and emission wavelength of the exciting and converter dot layers.

Chapter VI described the first ever demonstration of monolithic electrically injected edge-emitting nanowire array lasers (both green (λ=533nm) and red (λ=610nm)) on (001) silicon. Finite difference time domain (FDTD) simulation reveals that the optical field is continuous in the nanowire waveguide. Green nanowire lasers, grown with $In_{0.6}Ga_{0.94}N$ waveguides and $Al_{0.11}Ga_{0.89}N$ cladding, have demonstrated superior performances in terms of low threshold current density (1.76 kA/cm^2), relatively high differential gain (2.8x10^{-17}cm^2), large temperature coefficient (232K) and small signal modulation bandwidth (5.8GHz). Threshold current density is significantly smaller than that reported for equivalent planar green InGaN quantum well lasers. Red-emitting nanowire lasers were made by increasing the In composition in the disks further and using $In_{0.18}Al_{0.82}N$ cladding grown lattice matched to GaN. The red lasers were characterized with a threshold current density of 2.85 kA/cm^2, a large T_0 of 234K, a differential gain of 3.1x10^{-17}cm^2 and a small signal modulation bandwidth of 3 GHz at 80mA. A chirp of less than 1Å for a

modulation frequency of 6 GHz and a near-zero α-parameter near the peak emission wavelength have been derived from the dynamic measurements. These nanowire lasers have better performances than those of conventional InAlGaP based red lasers in terms of threshold current density and temperature coefficient.

7.2 Suggestions for Future Work

7.2.1 Selective Area Growth of Ga(In)N Nanowires by MBE for Monolithic Tunable White LEDs

As described in Chapters II and III, in self-assembled growth, nanowires grow in random positions on the silicon substrate and a variation of diameter of nanowires is usually observed across the sample. With the same V/III flux ratio for a

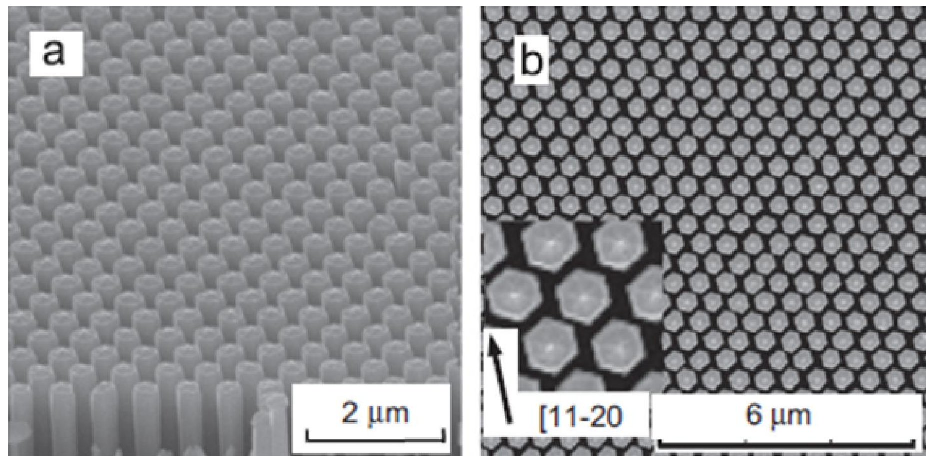

Figure 7.1 Scanning electron microscopy (SEM) imaging of (a) 45° tilted and (b) top surface views for selective area growth (SAG) of GaN nanocolumn array [181].

disk-in-nanowire (DNW) LED designed for a particular emission color, In composition in the InGaN disks varies to some extent between nanowires due to the difference in the nanowire diameter. Consequently, it is seen in the near-field image

of the electroluminescence that some of the nanowires are emitting light at different wavelengths other than the desired one. Selective area growth (SAG) of GaN nanowires using nanomask patterns can contribute to the homogeneity of the nanowire diameter and hence the alloy composition of InGaN nanowires and disks-in-nanowires. This will result in a truly uniform color emission across the sample and subsequently a visible emission with smaller luminescence linewidth. Additionally, by selectively growing different regions of nanowires with different diameters using appropriate growth masks, monolithic integration of blue, green and red-emitting InGaN LEDs can be possible for the same III/V flux ratio on the same silicon substrate. Moreover, if each color region on the silicon substrate has its individual contacts and can be biased independently, then white light source with unparalleled tunability can be obtained. Unlike the white LEDs, mentioned in Chapter V, number of disks/dots and emission wavelength need not be changed to tune the white light. Figure 7.1 demonstrates the SEM imaging of the patterned nanowires obtained by selective area growth. SiO_2 [182, 183] and W metal [184] are used as growth masks for the SAG of GaN by HVPE and metal-organic vapor phase epitaxy (MOVPE) [185] techniques. SAG by metal-organic molecular beam epitaxy (MO-MBE) using triethyl-gallium and gas-source MBE using an ammonia source [186] have been demonstrated. In this approach, gas-phase ingredients are found to facilitate the selective area growth of nanowires. SAG of nanowires by MBE have been demonstrated on nitrided Al nanodot patterns [187]. The problem with this technique is that the Al patterns get deformed before nitridation and hence the shape of the nanowires is not well controlled. SAG technique of GaN nanowires using Ti-mask

has also been reported [188, 189]. Ti nanomask helps in the growth of patterned nanowires with well-controlled diameter and height. Moreover, it has been demonstrated that emission color (from blue to red) can be controlled in SAG simply by tuning nanowire diameter without changing the III/V flux ratio on the same substrate [189].

7.2.2 High Power Near-Infrared Electrically Injected Monolithic Nanowire Lasers on (001) Silicon

In Chapter VI, I have described an electrically injected nanowire array laser on (001) silicon with emission wavelengths in the green (λ=533nm) and red (λ=610nm). I have also mentioned that an electrically injected monolithic near-

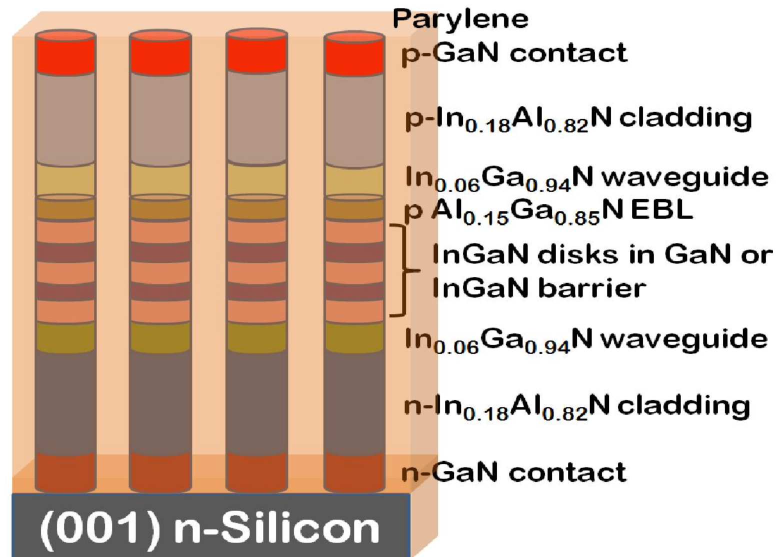

Figure 7.2 Schematic illustration of the proposed edge-emitting near-IR monolithic InGaN/GaN disk-in-nanowire laser heterostructure on (001) silicon.

infrared (near-IR) laser on (001) silicon is compatible with existing Si CMOS

technology and essential for the success of silicon photonics. By increasing indium composition in the InGaN disks, near-IR emission from InGaN/GaN DNWs should be possible without having significant defects and strain induced polarization field due to the large surface to volume ratio of the nanowires and radial strain relaxation during their epitaxy. The electrically pumped IR nanowire lasers can then be monolithically integrated with Si-based passive waveguides and front-end photoreceivers [180] for optical communication. We propose a near-IR (~ 1-1.2 μm) edge-emitting monolithic nanowire laser heterostructure on (001) silicon similar to

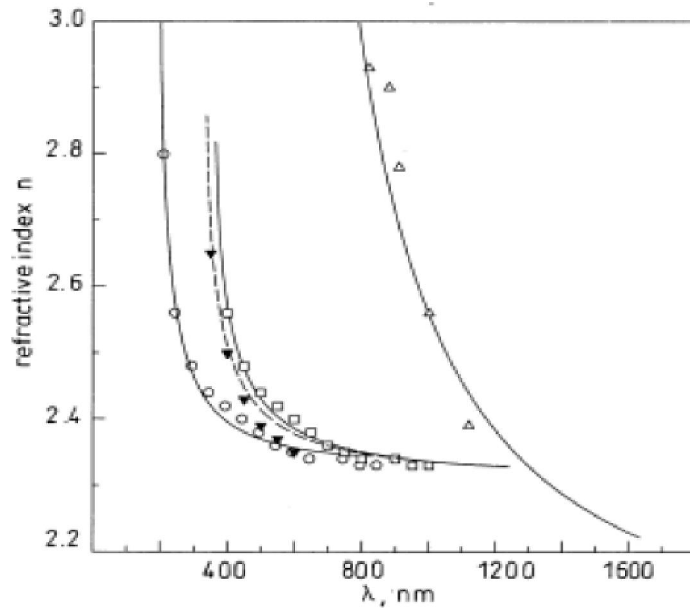

Figure 7.3 Refractive indices of wurtzite GaN (square), InN (empty triangle), AlN (circle) and $Al_{0.1}Ga_{0.9}N$ (solid triangle) [190].

that used for red nanowire laser as shown schematically in Fig. 7.2, with InGaN/GaN disks or InGaN/InGaN disks in the active region where InGaN barrier has the lower indium composition, $In_{0.06}Ga_{0.94}N$ waveguide, and $In_{0.18}Al_{0.82}N$ cladding, grown lattice matched to GaN. However, near infrared emission wavelengths, a cross-over

of refractive indices of InN, GaN and AlN have been reported by Piprek *et al.* [190], as shown in Fig. 7.3. Therefore, laser heterostructure needs to be designed with appropriate cladding layers having optimum thickness and InGaN disks with high indium composition have to be optimized for near-IR emission. From the green and red-emitting nanowire lasers, mentioned in Chapter VI, we obtained a maximum light output of 8mW and 15mW, respectively under pulsed biased operation and the slope efficiency of the lasers was low. In order to make a high power near-IR laser on silicon with higher slope efficiency and Wall-plug efficiency, the following approaches can be adopted. Radiative efficiency of the InN/InGaN disks-in-nanowires, gain media of the laser, need to be maximized by optimizing the growth conditions in MBE system and surface passivation. Waveguide and cladding layers in the laser heterostructure should be modified by changing the thickness and alloy composition to provide optimum optical mode confinement. Series resistance of the device can be reduced by optimizing the p-doping further using metal modulation epitaxy [43] during p-GaN growth. Also, using anti-reflective coating on the light-extracting facet of the edge-emitting laser, output power can be increased.

7.2.3 Room Temperature Nanowire Visible Spin-Polarized LEDs

Semiconductor spintronics has been the focus of attention for its applicability in high-performance logic, memory, and optoelectronic devices. The wide-band-gap wurtzite GaN has inversion asymmetry and is characterized by a weak spin-orbit coupling (SOC), which results in long spin-relaxation time and makes it attractive for the realization of room temperature spintronic devices [191, 192]. GaN also shows

attractive optoelectronic properties in the visible spectrum range, making it suitable for room temperature spin-polarized visible LEDs. We have investigated spin diffusion in bulk GaN by three-terminal Hanle measurements using MnAs spin injector [193]. We also examined spin dynamics in GaN nanowires by performing magnetoresistance (MR), and four-terminal Hanle measurements on single GaN nanowire spin-valve using FeCo/MgO tunnel contacts [194]. Our results reveal that

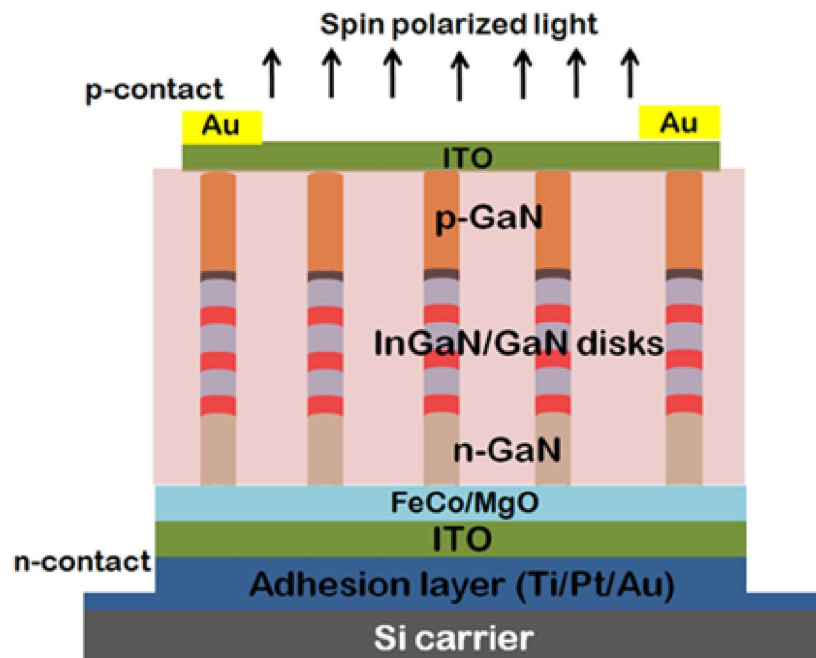

Figure 7.4 Schematic representation of the proposed flip-chip spin-polarized LED heterostructure.

the value of spin diffusion length (L_{sf}) at room temperature is 300 nm (corresponds to a spin lifetime (τ_{sf}) of ~120ps) in GaN nanowires which is almost twice of that derived in bulk GaN (L_{sf} =180nm, τ_{sf} = 44ps at 300K) at similar doping concentrations. Since Ga(In)N nanowires grown on (001) silicon are relatively free of

extended defects compared to bulk GaN, it is evident that defects in bulk GaN systems does play a role in determining the spin relaxation process, which makes GaN nanowire a better candidate for realizing room temperature visible spin-LEDs. Figure 7.4 demonstrates the proposed schematic illustration of the room temperature visible nanowire spin-LEDs with FeCo/MgO tunnel contact. A spurious polarization effect known as "magnetic circular dichroism (MCD)" might arise while designing a surface-emitting spin-LED heterostructure, if the spin-polarized light is collected through the ferromagnetic spin injector. MCD is the differential absorption of right- and left-circularly polarized lights by a ferromagnetic (FM) contact. Therefore, if a light detection scheme is used such that the emitted light will pass through the FM contact, then some degree of circular polarization in the emitted light will be observed even if unpolarized light is emitted from the active region i.e. MCD will change the actual polarization of the emitted light from the InGaN disk active region. To avoid MCD, a LED heterostructure design is proposed here using flip-chip processing of nanowire LEDs (similar to what was described in Chapter III) where the emitted light will be collected vertically from the p-GaN side as it passes through non-magnetic indium-tin-oxide (ITO) contact.

APPENDICES

APPENDIX A

Silicon Substrate Preparation for MBE Growth

Self-assembled Ga(In)N nanowires were grown on ~535 μm n-type (001) silicon substrate. The silicon sample is thoroughly cleaned before introducing it into the intro chamber of the MBE system. The sample is cleaned in hot acetone and isopropanal for 10 minutes each followed by DI water rinse. Native oxide on the silicon sample is removed by wet-etching with diluted HF solution (1:1) for 5 minutes. It is then rinsed in DI water and quickly air-transferred to the intro chamber. Then the sample undergoes a 1 hour intro-chamber baking at 200 ^{o}C for removal of moisture and 1 hour buffer chamber baking at 400 ^{o}C for outgassing of adsorbed gases and surface contaminants. It is then introduced in the growth chamber and is kept at a high temperature (~950°C thermocouple temperature) under high vacuum for 45 minutes to remove the remaining oxide from the sample surface. The substrate temperature is then decreased to the growth temperature, which is typically 800°C.

APPENDIX B

InGaN/GaN Disks-in-nanowire Ridge Waveguide Laser Processing

The processing of ridge waveguide red-emitting nanowire laser with $In_{0.18}Al_{0.82}N$ cladding is discussed in the following:

1. Deposition of alignment mark on the as-grown sample

1.1 Solvent clean:

Acetone: 10 min on hot plate

IPA 10 min

DI water Rinse: 5 min

1.2 Lithography

Dehydrate bake: 2 min, 115 °C hotplate

Resist coating: HMDS, SPR 220-3.0 @ 4.0 krpm, 30 sec

Pre-bake: 90 sec @ 115 °C on hotplate

Exposure: 0.35 sec in projection stepper

Post-bake: 90 sec @ 115 °C

Resist development: AZ 726 MIF 70 sec

DI water rinse 5 min

1.3 Descum

90 sec, 90 W, 250mT, 17% O_2

1.4 Metal Deposition

Ti/Au 100 Å /300 Å

1.5 Metal Lift-off

2 hours in Acetone

2. Defining mesa with ridge geometry

2.1 Solvent clean

Acetone: 10 min on hot plate

IPA 10 min

DI water Rinse: 5 min

2.2 Lithography

Dehydrate bake: 2 min, 115 °C hotplate

Resist coating: HMDS, SPR 220-3.0 @ 4.0 krpm, 30 sec

Pre-bake: 90 sec @ 115 °C on hotplate

Exposure: 0.35 sec in projection stepper

Post-bake: 90 sec @ 115 °C

Resist development: AZ 726 MIF 70 sec;

DI water rinse 5 min

2.3 Plasma Etching

LAM:

Inductively coupled plasma (ICP) etching, etchant gas recipe contains Cl_2 and Ar. Typical etching rate is calibrated to be ~4-4.4 nm/s.

2.4 Resist Removal

Plasma Asher: 300 sec, 200 W, 250mT, O_2 ~17%

Acetone: 30 min on hot plate

IPA: 5 min

DI water rinse: 5 min

2.5 Dektak profilometer: Device mesa height is measured.

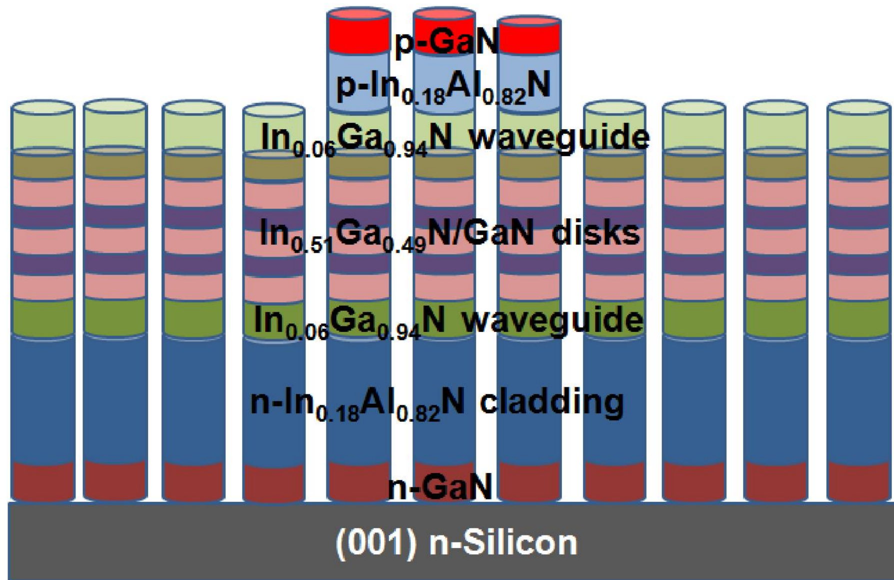

3. Etching the structure till silicon for making n-contact on n-type silicon

3.1 Solvent clean

Acetone: 10 min on hot plate

IPA 10 min

DI water Rinse: 5 min

3.2 Lithography

Dehydrate bake: 2 min, 115 °C hotplate

Resist coating: HMDS, SPR 220-3.0 @ 4.0 krpm, 30 sec

Pre-bake: 90 sec @ 115 °C on hotplate

Exposure: 0.35 sec in projection stepper

Post-bake: 90 sec @ 115 °C

Resist development: AZ 726 MIF 70 sec;

DI water rinse 5 min

3.3 Plasma Etching

LAM

Inductively coupled plasma (ICP) etching, etchant gas recipe contains Cl_2 and Ar. Typical etching rate is calibrated to be ~ 4-4.4 nm/s.

3.4 Resist Removal

Plasma Asher: 300 sec, 200 W, 250mT, O_2 ~17%

Acetone: 30 min on hot plate

IPA: 5 min

DI water rinse: 5 min

3.5 Dektak profilometer: Device mesa height is measured.

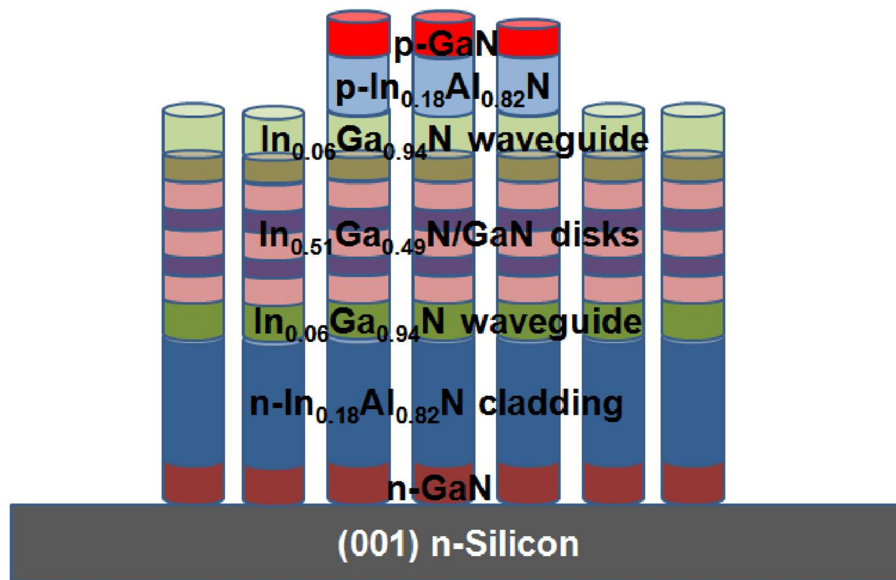

4. **Parylene planarization and passivation of the device**

4.1 Parylene Deposition

Parylene is deposited on the sample by thermal evaporation at 300K.

4.2 Parylene Etching

Parylene is etched in steps by LAM, where etchant gas contains O_2 plasma. Etching steps are calibrated by taking images with SEM.

Parylene is etched up to the silicon substrate surrounding the mesa for making n-contact and up to the p-GaN so that the nanowire tips are exposed for p-metal deposition.

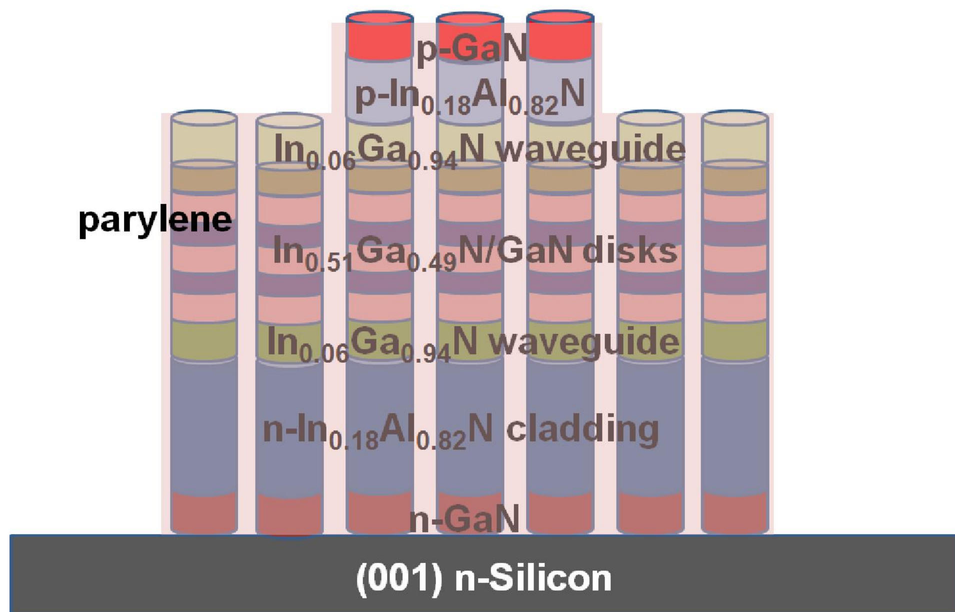

5. **Deposition of Ni/Au semi-transparent p-contact**

5.1 Solvent clean

Acetone: 10 min on hot plate

IPA 10 min

DI water Rinse: 5 min

5.2 Lithography

Dehydrate bake: 2 min, 115 °C hotplate

Resist coating: HMDS, SPR 220-3.0 @ 4.0 krpm, 30 sec

Pre-bake: 90 sec @ 115 °C on hotplate

Exposure: 0.35 sec in projection stepper

Post-bake: 90 sec @ 115 °C

Resist development: AZ 726 MIF 70 sec;

DI water rinse 5 min

5.3 Descum

90 sec, 90 W, 250mT, 17% O_2

5.4 Oxide removal from the top of p-GaN surface:

HCl : DI water = 1:1, 2 min to remove native oxide

DI water rinse: 5 min

5.5 Metal deposition

Ni/Au = 50 Å/50 Å

5.6 Metal lift-off

Overnight in Acetone

IPA: 10 min

DI water: 5 min

6. Annealing of Ni/Au p-contact

Rapid thermal annealing: 550 ^{o}C, 2 min in N_2:O_2 (4:1) environment

7. Deposition of ITO current spreading layer

7.1 Solvent clean

Acetone: 10 min on hot plate

IPA 10 min

DI water Rinse: 5 min

7.2 Lithography

Dehydrate bake: 2 min, 115 °C hotplate

Resist coating: HMDS, SPR 220-3.0 @ 4.0 krpm, 30 sec

Pre-bake: 90 sec @ 115 °C on hotplate

Exposure: 0.35 sec in projection stepper

Post-bake: 90 sec @ 115 °C

Resist development: AZ 726 MIF 70 sec;

DI water rinse 5 min

7.3 Descum

90 sec, 90 W, 250mT, 17% O_2

7.4 Oxide removal from the top of p-GaN surface:

HCl : DI water = 1:1, 2 min to remove native oxide

DI water rinse: 5 min

7.5 Metal deposition

2300 Å ITO is deposited by sputtering.

7.6 Metal lift-off

4 hours in Acetone

IPA: 10 min

DI water: 5 min

8. **Annealing of ITO layer**

Rapid thermal annealing: 450°C, 1 min in Ar environment

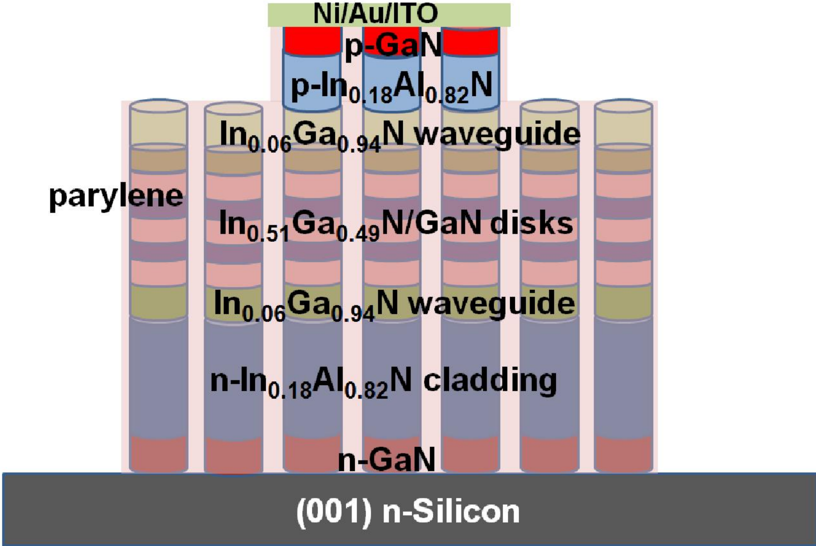

9. **Passivation with SiO_x**

SiO_x deposition: 1000 nm using GSI plasma enhanced chemical vapor deposition (PECVD).

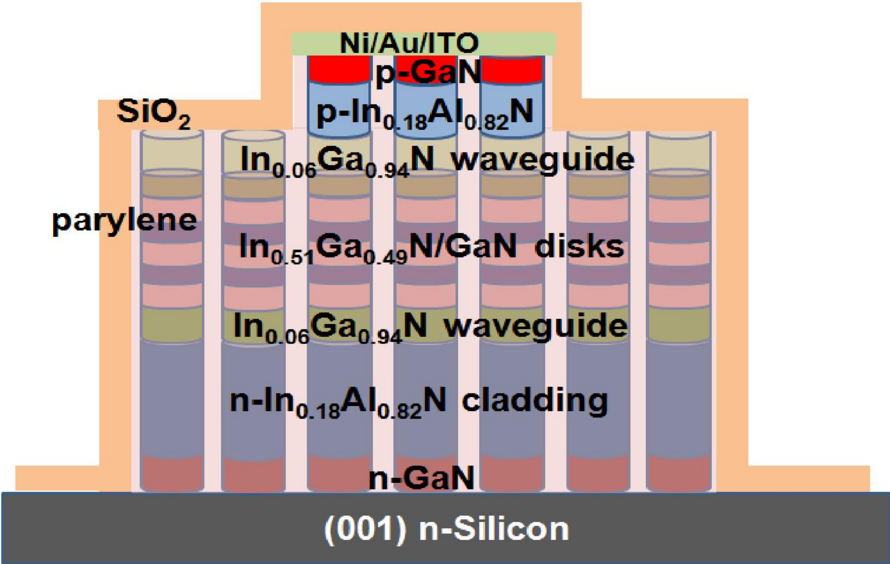

10. **Oxide Etch (Formation of Via holes)**

10.1 Lithography

Dehydrate bake: 2 min, 115 °C hotplate

Resist coating: HMDS, SPR 220-3.0 @ 4.0 krpm, 30 sec

Pre-bake: 90 sec @ 115 °C on hotplate

Exposure: 0.35 sec in projection stepper

Post-bake: 90 sec @ 115 °C

Resist development: AZ 726 MIF 70 sec;

DI water rinse 3 min

10.2 Plasma Etch

LAM

SF_6 : C_4F_8 : Ar = 8 : 50 : 50 sccm, 10 mT, 300 W (rate ~ 184 nm/min)

10.3 Resist Removal

Plasma Asher: 300 sec, 200 W, 250mT, O_2 ~17%

Acetone: 30 min on hot plate

IPA: 5 min

DI water rinse: 5 min

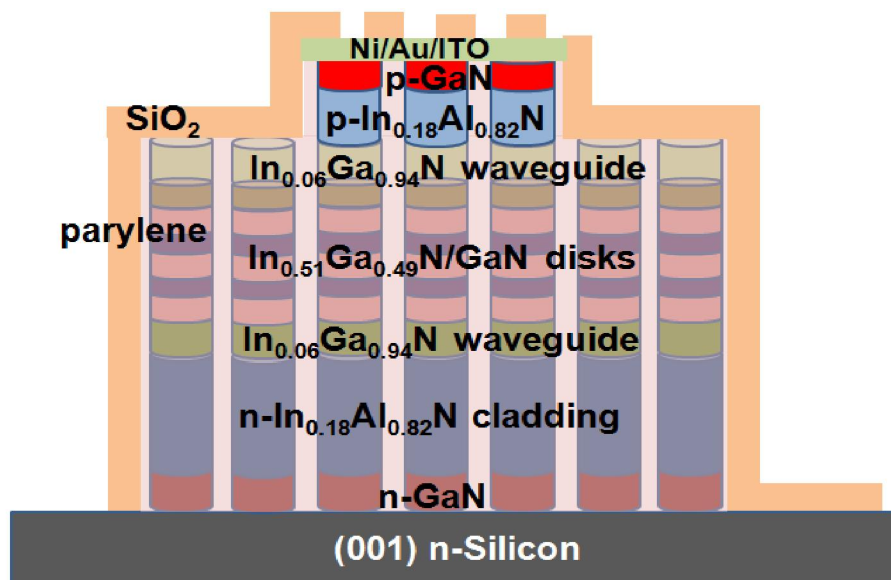

11. Deposition of n-contact and interconnect

11.1 Solvent clean

Acetone: 10 min on hot plate

IPA 10 min

DI water Rinse: 5 min

11.2 Lithography

Dehydrate bake: 2 min, 115 °C hotplate

Resist coating: HMDS, SPR 220-3.0 @ 4.0 krpm, 30 sec

Pre-bake: 90 sec @ 115 °C on hotplate

Exposure: 0.35 sec in projection stepper

Post-bake: 90 sec @ 115 °C

Resist development: AZ 726 MIF 70 sec;

DI water rinse 5 min

11.3 Descum

90 sec, 90 W, 250mT, 17% O_2

11.4 Metal Deposition

Al/Au 1000 Å /1500 Å

11.5 Metal Lift-off

Overnight in Acetone

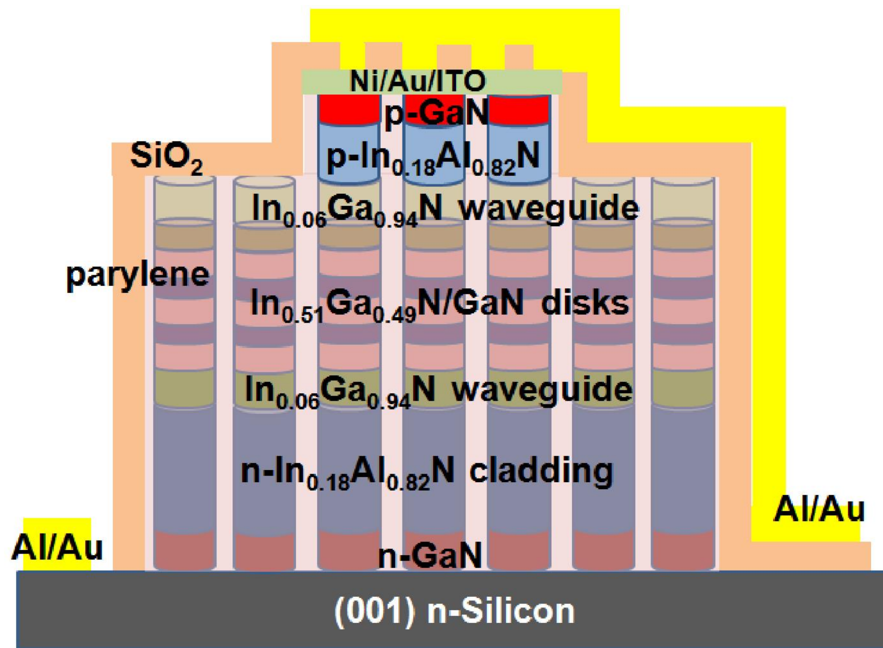

The sample is then cleaved perpendicular to the laser cavity, cleaved surfaces are etched by focused ion beam (FIB) to make them optically flat and TiO_2/SiO_2 dielectric DBR is deposited on the laser facets by physical vapor deposition.

BIBLIOGRAPHY

BIBLIOGRAPHY

[1] J. Y. Tsao, H. D. Saunders, J. R. Creighton, M. E. Coltrin and J. A. Simmons, *J. Phys. D: Appl. Phys.* **43,** 354001 (2010).

[2] E. F. Schubert and J. K. Kim, *Science* **308**, 1274 (2005).

[3] http://www.societyofrobots.com/sensors_color.shtml

[4] www.ssl.energy.gov/tech_reports.html

[5] R. Mueller-Mach, G. O. Mueller, M. R. Krames, T. Trottier, *IEEE J. Sel. Top. Quantum Electron.* **8**, 339 (2002).

[6] Y. J. Lee, P. C. Lin, T. C. Lu, H. C. Kuo, S. C. Wang, *Appl. Phys. Lett.* **90**, 161115 (2007).

[7] H. S. Chen, D. M. Yeh, C. F. Lu, C. F. Huang, W. Y. Shiao, J. J. Huang, C. C.Yang, I. S. Liu, W. F. Su, *IEEE Photonics Technol. Lett.* **18**, 1430 (2006).

[8] C. F. Huang, C. F. Lu, T. Y. Tang, J. J. Huang, C. C. Yang, *Appl. Phys. Lett.* **90**, 151122 (2007).

[9] M. Ueda, T. Kondou, K. Hayashi, M. Funato, Y. Kawakami, Y. Narukawa, T. Mukai, *Appl. Phys. Lett.* **90**, 171907 (2007).

[10] G. Moore, *IEEE IEDM Tech Digest*, p.11 (*1975*).

[11] http://researcher.watson.ibm.com/researcher/view_group.php?id=2757

[12] http://www.cnet.com/news/will-intel-and-usb-make-fiber-optics-mainstream/

[13] N. Holonyak Jr. and S. F. Bevacqua, *Appl. Phys. Lett.* **1**(4), 82 (1962).

[14] H. Amano, N. Sawaki, I. Akasaki, and Y. Toyoda, *Appl. Phys. Lett.* **48**, 353 (1986).

[15] S. Nakamura, *Jpn. J. Appl. Phys.* **30**, L1705 (1991).

[16] H. Amano, M. Kito, K. Hiramatsu, and I. Akasaki, *Jpn. J. Appl. Phys.* **28**, L2112 (1989).

[17] S. Nakamura, T. Mukai, M. Senoh, and N. Iwasa, *Jpn. J. Appl. Phys.* **31**, L139 (1992).

[18] S. Nakamura, M. Senoh, N. Iwasa, and S. Nagahama, *Jpn. J. Appl. Phys.* **34**, L797–L799 (1995).

[19] A. A. Setlur, *Electrochem. Soc. Interface* **18**(4), 32 (2009).

[20] S. Nakamura, T. Mukai, and M. Senoh, *Appl. Phys. Lett.* **64**, 1687 (1994).

[21] S. Nakamura , M. Senoh , S. Nagahama , N. Iwasa , T. Yamada , T. Matsushita , Y. Sugimoto and H. Kiyoku, *Appl. Phys. Lett.* **69**, 4056 (1996).

[22] Y. Enya, Y. Yoshizumi, T. Kyono, K. Akita, M. Ueno, M. Adachi, T. Sumitomo, S. Tokuyama, T. Ikegami, K. Katayama, and T. Nakamura, *Appl. Phys. Exp.* **2**, 082101 (2009).

[23] T. Zhua and R. A. Olivera, *Phys. Chem. Chem. Phys.* **14**, 9558 (2012).

[24] J. Piprek, *Phys. Status Solidi A* **207**, 2217 (2010).

[25] S. Yamada, Y. Zhao, C. C. Pan, R. B. Chung, K. Fujito, J. Sonoda, S. P. DenBaars, and S. Nakamura, *Appl. Phys. Exp.* **2**, 122102 (2010).

[26] Y. Enya, Y. Yoshizumi, K. Akita, M. Ueno, M. Adachi, T. Sumitomo, S. Tokuyama, T. Ikegami, K. Katayama, and T. Nakamura, *Appl. Phys. Exp.* **2**, 082101 (2009).

[27] Y. Yoshizumi, M. Adachi, Y. Enya, T. Kyono, S. Tokuyama, T. Sumitomo, K. Akita, T. Ikegami, M. Ueno, K. Katayama, and T. Nakamura, *Appl. Phys. Exp.* **2**, 092101 (2009).

[28] N. F. Gardner, G. O. Muller, Y. C. Shen, G. Chen, S. Watanabe, W. Gotz, and M. R. Krames, *Appl. Phys. Lett.* **91**, 243506 (2007).

[29] J. Piprek and S. Li, *Optical and Quantum Electronics* **42**(2), 89 (2010).

[30] J. H. Son and J. L. Lee, *Opt. Express* **18**, 5466 (2010).

[31] J. M. Phillips, M. E. Coltrin, M. H. Crawford, A. J. Fischer, M. R. Krames, R. Mueller-Mach, G. O. Mueller, Y. Ohno, L. E. S. Rohwer, J. A. Simmons, and J. Y. Tsao, *Laser and Photon. Rev.* **1**, 307 (2007).

[32] J. Iveland, L. Martinelli, J. Peretti, J. S. Speck, and C. Weisbuch, *Phys. Rev. Lett.* **110**, 177406 (2013).

[33] Y. Yang, X. A. Cao and C. Yan, *IEEE Trans. on Elec. Dev.* **55**, 1771 (2008).

[34] M. H. Kim, M. F. Schubert, Q. Dai, J. K. Kim, E. F. Schubert, J. Piprek, and Y. Park, *Appl. Phys. Lett.* **91**, 183507 (2007).

[35] A. David, M. J. Grundmann, J. F. Kaeding, N. F. Gardner, T.G. Mihopoulos, and M. K. Krames, *Appl. Phys. Lett.* **92**, 053502 (2008).

[36] A. D. Drager, H. Jonen, C. Netzel, U. Rossow, and A. Hangleiter, *8th Intern. Conf. Nitride Semicon.*, Jeju (2009)

[37] M. Zhang, P. Bhattacharya, J. Singh and J. Hinckley, *Appl. Phys. Lett.* **95**, 201108 (2009).

[38] A. E. Yunovich, V. E. Kudryashov, A. N. Turkin, A. Kovalev, and F. Manyakhin, *MRS Int. J. Nitride Semicon. Res.* **3**, 44 (1998).

[39] I. V. Rozhansky and D. A. Zakheim, *Phys. Status Solidi A* **204**, 227 (2007).

[40] A. Laubsch, M. Sabathil, W. Bergbauer, M. Strassburg,H. Lugauer, M. Peter, S. Lutgen, N. Linder, K. Streubel, J. Hader, J. V. Moloney, B. Pasenow, and S. W. Koch, *Phys. Status Solidi C* **6**, S913 (2009).

[41] S. Nakamura, T. Mukai, M. Senoh, and N. Iwasa, *Jpn. J. Appl. Phys.* **31**, L139 (1992).

[42] M. Zhang, P. Bhattacharya, W. Guo, and A. Banerjee, *Appl. Phys. Lett.* **96**, 132103 (2010).

[43] G. Namkoong, E. Trybus, K. K. Lee, M. Moseley, W. A. Doolittle, and D. C. Look, *Appl. Phys. Lett.* **93**, 172112 (2008).

[44] A. Avramescu, T. Lermer, J. Müller, S. Tautz, D. Queren, S. Lutgen, and U. Strauß, *Appl. Phys. Lett.* **95**, 071103 (2009).

[45] M. Rao, D. Kim, and S. Mahajan, *Appl. Phys. Lett.* **85**, 1961 (2004).

[46] N. K. van der Laak, R. A. Oliver, M. J. Kappers, and C. J. Humphreys, *Appl. Phys. Lett.* **90**, 121911 (2007).

[47] S. D. Hersee, A. K. Rishinaramangalam, and M. N. Fairchild, *J. Mater. Res.* **26**, 2293 (2011).

[48] J. R. Cerutti, S. F. Garrido, E. Calleja, A. Trampert, K. H. Ploog, S. Lazic, and J. M. Calleja, *Appl. Phys. Lett.* **88**, 213114 (2006).

[49] P. U. Kuykendall, S. Aloni, and P. Yang, *Nature Mater.* **6**, 951 (2007).

[50] S. F. Garrido, J. Grandal, E. Calleja, M. A. S. Garcia, and D. L. Romero, *J. Appl. Phys.* **106**, 126102 (2009).

[51] Q. L. Armstrong, K. H. A. Bogart, Y. Lin, G. T. Wang, and A. A. Talin, *J. Appl. Phys.* **106**, 053712 (2009).

[52] L. G. Chèze, O. Brandt, W. Weber, H. Riechert, S. Münch, R. Rothemund, S. Reitzenstein, A. Forchel, T. Kehagias, P. Komninou, G. Dimitrakopulos, and T. Karakostas, *Nano Res.* **3**, 528 (2010).

[53] X. Duan, and C. M. Lieber, *J. Am. Chem. Soc.* **122**, 188 (2011).

[54] W. Guo, M. Zhang, P. Bhattacharya and J. Heo, *Nano Lett.* **11**, 1434 (2011).

[55] W. Guo, A. Banerjee, M. Zhang and P. Bhattacharya, *Appl. Phys. Lett.* **98**, 183116 (2011).

[56] Y. H. Cho, G. H. Gainer, A. J. Fischer, J. J. Song, S. Keller, U. K. Mishra and S. P. DenBaars, *Appl. Phys. Lett.* **73**, 1370 (1998).

[57] F. B. Naranjo, M. A. S. García, F. Calle, E. Calleja, B. Jenichen and K. H. Ploog, *Appl. Phys. Lett.* **80**, 231 (2002).

[58] C. F. Huang, C. F. Lu, T. Y. Tang, J. J. Huang and C. C. Yang, *Appl. Phys. Lett.* **90**, 151122 (2007).

[59] C. Y. Huang, M. T. Hardy, K. Fujito, D. F. Feezell, J. S. Speck, S. P. DenBaars and S. Nakamura, *Appl. Phys. Lett.* **99**, 241115 (2011)……..

[60] A. Kikuchi, M. Kawai, M. Tada and K. Kishino, *Jpn. J. Appl. Phys.* **43**, L1524 (2004).

[61] W. Guo, A. Banerjee, P. Bhattacharya and B. S. Ooi, *Appl. Phys. Lett.* **98**, 193102 (2011).

[62] H. P. T. Nguyen, K. Cui, S. Zhang, S. Fathololoumi and Z. Mi, *Nanotech.* **22**, 445202 (2011).

[63] F. Glas, *Phys. Rev. B* **74**, 121302(R) (2006).

[64] C. Koelper, M. Sabathil, M. Mandl, M. Strassburg and B. Witzigmann, *J. of Lightwave Tech.* **30**, 2853 (2012).

[65] W. Guo, M. Zhang, A. Banerjee, and P. Bhattacharya, *Nano Lett.* **10**, 3355 (2010).

[66] H Y. Narukawa, I. Niki, K, Izuno, M. Yamada, Y. Murazaki and T. Mukai, *Jpn. J. Appl. Phys.* **41**, L371 (2002).

[67] J. K. Park, C. H. Kim, S. H. Park, H. D. Park and S. Y. Choi, *Appl. Phys. Lett.* **84**, 1647 (2004).

[68] S. C. Allen and A. J. Steckl, *Appl. Phys. Lett.* **92**, 143309 (2008).

[69] S. Ye, F. Xiao, Y. X. Pan, Y. Y. Ma and Q. Y. Zhang, *Mat. Science and Eng. R* **71**, 1 (2010).

[70] D. A. Steigerwald, J. C. Bhat, D. Collins, R. M. Fletcher, M. O. Holcomb, M. J. Ludowise, P. S. Martin, and S. L. Rudaz, *IEEE J. of Sel. Topics in Quant. Elec.* **8**, 310 (2002).

[71] J. Baur, F. Baumann, M. Peter, K. Engl, U. Zehnder, J. Off, V. Kuemmler, M. Kirsch, J. Strauss, R. Wirth, K. Streubel and B. Hahn, *Phys. Status Solidi C* **6**, S905 (2009).

[72] I. H. Cho, G. Anoop, D. W. Suh, S. J. Lee, and J. S. Yoo, *Optical Mat. Exp.* **2**, 1292 (2012).

[73] K. Kishino, A. Kikuchi, H. Sekiguchi, and S. Ishizawa, *Proc. of SPIE* **6473**, 64730T (2007).

[74] H. P. T. Nguyen, K. Cui, S. Zhang, S. Fathololoumi, and Z. Mi, *Nanotech.* **22**, 445202 (2011).

[75] J. B. Schlager, K. A. Bertness, P. T. Blanchard, L. H. Robins, A. Roshko, and N. A. Sanford, *J. Appl. Phys.* **103**, 124309 (2008).

[76] R. Calarco, M. Marso, T. Richter, A. I. Aykanat, R. Meijers, A. D. Hart, T. Stoica, and H. Luth, *Nano Lett.* **5**, 981 (2005).

[77] H. P. T. Nguyen, M. Djavid, K. Cui, and Z. Mi, *Nanotech.* **23**, 194012 (2012).

[78] W. Guo, M. Zhang, P. Bhattacharya and J. Heo, *Nano Lett.* **11**, 1434 (2011).

[79] F. Furtmayr, M. Vielemeyer, M. Stutzmann, J. Arbiol, S. Estrade, F. Peiro, J. R. Morante, M. Eickhoff, *J. Appl. Phys.* **104**, 034309 (2008).

[80] T. Stoica, E. Sutter, R. J. Meijers, R. K. Debnath, R. Calarco, H. Luth, D. Grutzmacher, *Small* **4**, 751 (2008).

[81] K.A. Grossklaus, A. Banerjee, S. Jahangir, P. Bhattacharya, and J. M. Millunchick, *J. of Crys. Growth* **371**, 142 (2013).

[82] K. A. Bertness, A. Roshko, L. M. Mansfield, T. E. Harvey, N. A. Sanford, *J. of Crystal Growth* **310**, 3154 (2008).

[83] K. A. Bertness, N. A. Sanford and A. V. Davydov, *IEEE J. of Sel. topics in Quant. Elec.* **17**, 847 (2011).

[84] T. Stoica, E. Sutter, and R. Calarco, *Trends in Nanophysics, Engineering Materials*, pp. 73 (2010).

[85] E. Calleja, J. Ristić, S. Fernández-Garrido, L. Cerutti, M. A. Sánchez-García, J. Grandal, A. Trampert, U. Jahn, G. Sánchez, A. Griol, and B. Sánchez, *Phys. Stat. Sol. (b)* **244**, 2816 (2007).

[86] S. D. Hersee, X. Sun, and X. Wang, *Nanolett.* **6**, 1808 (2006).

[87] K. Kishino, K. Nagashima, and K. Yamano, *Appl. Phys. Exp*. **6**, 012101 (2013).

[88] H. Y. Chen, H. W. Lin, C. H. Shen, and S. Gwo, *Appl. Phys. Lett.* **89**, 243105 (2006).

[89] V. Consonni, M. Knelangen, U. Jahn, A. Trampert, L. Geelhaar, and H. Riechert, *Appl. Phys. Lett.* **95**, 241910 (2009).

[90] P. Lefebvre, S. F. Garrido, J. Grandal, J. Ristic , M. A. S. Garcıa, and E. Calleja, *Appl. Phys. Lett.* **98**, 083104 (2011).

[91] Y. P. Varshni, *Physica* **39**, 149 (1967).

[92] Y. H. Cho, G. H. Gainer, A. J. Fischer, J. J. Song, S. Keller, U. K. Mishra, and S. P. DenBaars, *Appl. Phys. Lett.* **73**, 1370 (1998).

[93] F. B. Naranjo, M. A. S. García, F. Calle, E. Calleja, B. Jenichen, and K. H. Ploog, *Appl. Phys. Lett.* **80**, 231 (2002).

[94] S. Chevtchenko, X. Ni, Q. Fan, A. A. Baski, and H. Morkoc, *Appl. Phys. Lett.* **88**, 122104 (2006).

[95] N. A. Sanford, P. T. Blanchard, K. A. Bertness, L. Mansfield, J. B. Schlager, A. W. Sanders, A. Roshko, B. B. Burton, and S. M. George, *J. Appl. Phys.* **107**, 034318 (2010).

[96] C.Y. Chen, Y. C. Lu, D. M. Yeh, C. C. Yang, *Appl. Phys. Lett.* **90**, 183114 (2007).

[97] Y.R. Wu, Y.Y. Lin, H.H. Huang, and J. Singh, *J. Appl. Phys.* **105**, 013117 (2009).

[98] A. Konar, A. Verma, T. Fang, P. Zhao, R. Jana and D. Jena, *Semicond. Sci. Technol.* **27**, 024018 (2012).

[99] R. Songmuang, O. Landre, and B. Daudin, *Appl. Phys. Lett.* **91**, 251902 (2007).

[100] C. T. Foxon, S. V. Novikov, J. L. Hall, R. P. Campion, D. Cherns, I. Griffiths, and S. Khongphetsak, *J. Cryst. Growth* **311**, 3423 (2009).

[101] M. Zhang, A. Banerjee, C. S. Lee, J. M. Hinckley, and P. Bhattacharya, *Appl. Phys. Lett.* **98**, 221104 (2011).

[102] T. Li, A. M. Fischer, Q. Y. Wei, F. A. Ponce, T. Detchprohm, and C.Wetzel, *Appl. Phys. Lett.* **96**, 031906 (2010).

[103] http://en.wikipedia.org/wiki/Reflectivity

[104] Y. D. Jho, J. S. Yahng, E. Oh, and D. S. Kim, *Phys. Rev. B* **66**, 035334 (2002).

[105] A. Banerjee, PhD thesis dissertation (2014); http://deepblue.lib.umich.edu/

[106] Q. Dai, Q. Shan, J. Wang, S. Chhajed, J. Cho, E. F. Schubert, M. H. Crawford, D. D. Koleske, M. H. Kim, and Y. Park, *Appl. Phys. Lett.* **97**, 133507 (2010).

[107] M. Zhang, P. Bhattacharya, and W. Guo, *Appl. Phys. Lett.* **97**, 011103 (2010).

[108] J. Piprek, *Semiconductor Optoelectronic Devices: Introduction to Physics and Simulation*; Academic Press: San Diego, CA, 2003.

[109] J. Hader, J. V. Moloney, B. Pasenow, S. W. Koch, M. Sabathil, N. Linder, S. Lutgen, *Appl. Phys. Lett.* **92**, 261103 (2008).

[110] R. Meijers, T. Richter, R. Calarco, T. Stoica, H. P. Bochem, M. Marso, H. Luth,

J. Crys. Growth **289**, 381 (2006).

[111] J. Ristic´, E. Calleja, S. Fernandez-Garrido, L. Cerutti, A. Trampert, U. Jahn, K. H. Ploog, *J. Crys. Growth* **310**, 4035 (2008).

[112] R. Calarco, R. J. Meijers, R. K. Debnath, T. Stoica, E. Sutter, H. Luth, *Nano Lett.* **7**, 2248 (2007).

[113] L. Geelhaar, C. Cheze, B. Jenichen, O. Brandt, C. Pfuller, S. Munch, R. Rothemund, S. Reitzenstein, A. Forchel, T. Kehagias, P. Komninou, G. P. Dimitrakopulos, T. Karakostas, L. Lari, P. R. Chalker, M. H. Gass, H. Riechert, *IEEE J. Sel. Topics in Quant. Elec.* **17,** 878 (2011).

[114] V. Consonni, M. Knelangen, A. Trampert, L. Geelhaar, H. Riechert, App. Phys. Lett. **98**, 071913 (2011).

[115] D. V. Lang, *J. Appl. Phys.* **45**, 3023 (1974).

[116] W. Götz, N. M. Johnson, and D. P. Bour, *Appl. Phys. Lett.* **68**, 3470 (1996).

[117] H. Nagai, Q. S. Zhu, Y. Kawaguchi, K. Hiramatsu, and N. Sawaki, *Appl. Phys. Lett.* **73**, 2024 (1998).

[118] P. Hacke, H. Nakayama, T. Detchprohm, K. Hiramatsu, and N. Sawaki, *Appl. Phys. Lett.* **68**, 1362 (1996).

[119] P. Hacke, T. Detchprohm, K. Hiramatsu, N. Sawaki, K. Tadatomo, and K. Miyake, *J. Appl. Phys.* **76**, 304 (1994).

[120] S. A. Chevtchenko, J. Xie, Y. Fu, X. Ni, H. Morkoç, and C. W. Litton, *Proc. SPIE* **6473**, 64730N (2007).

[121] J. Xie, S. A. Chevtchenko, U. Özgür, and H. Morkoç, *Appl. Phys. Lett* **90**, 262112 (2007).

[122] Z. Q. Fang, D. C. Look and L. Polenta, *J. Phys.: Condens. Matter* **14**, 13061 (2002).

[123] J. Elsner, R. Jones, M. I. Heggie, P. K. Sitch, M. Haugk, and Th. Frauenheim, S. Oberg, P. R. Briddon, *Phys. Rev. B* **58**, 12571 (1998).

[124] R. Hu, X.B. Luo, H. Feng and S. Liu, *J. Lumin.* **132**, 1252 (2012).

[125] B. Damilano, N. Grandjean, C. Pernot and J. Massies, *Jpn. J. Appl. Phys.* **40**, 918 (2001).

[126] M. Yamada, Y. Narukawa and T. Mukai, *Jpn. J. Appl. Phys.* **41**, 246 (2002).

[127] I. K. Park, J. Y. Kim, M. K. Kwon, C. Y. Cho, J. H. Lim, and S. J. Park, *Appl. Phys. Lett.* **92**, 091110 (2008).

[128] S. N. Lee, H. S. Paek, H. Kim, T. Jang, and Y. Park, *Appl. Phys. Lett.* **92**, 081107 (2008).

[129] B. Damilano, P. Demolon, J. Brault, T. Huault, F. Natali, and J. Massies, *J. Appl. Phys.* **108**, 073115 (2010).

[130] S. Nakamura and G. Fasol, *The Blue Laser Diode*, Springer-Verlag, Berlin, Germany, pp. 216-219 (1997).

[131] J. K. Sheu, S. J. Chang, C. H. Kuo, Y. K. Su, L. W. Wu, Y. C. Lin, W. C. Lai, J. M. Tsai, G. C. Chi, and R. K. Wu, *Photon. Tech. Lett.* **15**, 18 (2003).

[132] M. Huang and L. Yang, *Photon. Tech. Lett.* **25**, 1317 (2013).

[133] T. Tamura, T. Setomoto, and T. Taguchi, *J. Lumin.* **87**, 1180 (2000).

[134] J. H. Hwang, Y. D. Kim, J. W. Kim, S. J. Jung, H. K. Kwon, and T. H. Oh, *Phys. Status Solidi C* **7**, 2157 (2010).

[135] Q. Zhang, F. Jiao, Z. Chen, L. Xu, A. Wang, and S. Liu, *J. Semicond.* **32**, 012002 (2011).

[136] C. Yuan and X.B. Luo, *Int. J. Heat Mass Transfer* **56**, 206 (2013).

[137] B. Damilano, N. Grandjean, S. Dalmasso, and J. Massies, *Appl. Phys. Lett.* **75**, 3751 (1999).

[138] S. Schulz and E. O'Reilly, *Phys. Rev. B* **82**, 033411 (2010).

[139] T. Frost, A. Banerjee, K. Sun, S. L. Chuang, and P. Bhattacharya, *IEEE J. Quant. Elec.* **49**, 923 (2013).

[140] T. Frost, A. Banerjee, and P. Bhattacharya, *Appl. Phys. Lett.* **103**, 211111 (2013).

[141] T. Frost, A. Banerjee, S. Jahangir, and P. Bhattacharya, *Appl. Phys. Lett.* **104**, 081121 (2014).

[142] Z. Qin, J. Feng, C. Zhaohui, X. Ling, W. Simin, and L. Sheng, *J. Semicond.* **32**, 012002 (2011).

[143] D. Queren, A. Avramescu, G. Bruderl, A. Breidenassel, M. Schillgalies, *App. Phys.Lett.* **94**, 081119 (2009).

[144] A Banerjee, T Frost, E Stark, P Bhattacharya, *Appl.Phys. Lett.* **101**, 041108 (2012).

[145] B. Jalali and S. Fathpour, *J. Lightwave Technol.* **24**, 4600 (2006).

[146] R. Soref, *IEEE J. Selected Topics in Quant. Elec.* **12**, 1678 (2006).

[147] Z. Mi, J. Yang and P. Bhattacharya, G. Qin, Z. Ma, *Proc. the IEEE.* **97**, 1239 (2009).

[148] D. Liang, J. E. Bowers, *Nature Photon.* **4**, 511 (2010).

[149] Y. D. Lin, S. Yamamoto, C. Y. Huang, C. L. Hsiung, F. Wu, K. Fujito, H. Ohta, J. S. Speck, S. P. DenBaars, S. Nakamura, *Appl. Phys. Exprs.* **3**, 082001 (2010).

[150] A. Avramescu, T. Lermer, J. Müller, C. Eichler, G. Bruederl, M. Sabathil, S. Lutgen, U. T. Strauss, *Appl. Phys. Lett.* **3**, 061003 (2010).

[151] J. Müller, U. Strauß, T. Lermer, G. Brüderl, C. Eichler, A. Avramescu, S. Lutgen, *Phys. Status Solidi* **208**, 1590 (2011).

[152] M. Ueno, Y. Yoshizumi, Y. Enya, T. Kyono, M. Adachi, S. Takagi, S. Tokuyama, T. Sumitomo, K. Sumiyoshi, N. Saga, T. Ikegami, K. Katayama, and T. Nakamura, *J. Crys. Growth* **315**, 258 (2011).

[153] H. Z. Chen, A. Ghaffari, H. Wang, H. Morkoç, and A. Yariv, *Opt. Lett.* **12**, 812 (1987).

[154] Z. Mi, P. Bhattacharya, J. Yang and K.P. Pipe, *Elec. Lett.* **41**, 13 (2005).

[155] A. Y. Liu, C. Zhang, J. Norman, A. Snyder, D. Lubyshev, J. M. Fastenau, A. W. K. Liu, A. C. Gossard, and J. E. Bowers, *Appl. Phys. Lett.* **104**, 041104 (2014).

[156] B. Kunert, S. Zinnkann, K. Volz, and W. Stolz, *J. Crys. Growth* **310**, 4776 (2008).

[157] L. Cerutti, J. B. Rodriguez, And E. Tournie, *IEEE Photon. Technol. Lett.* **22**, 553 (2010).

[158] R. E. Camacho-Aguilera, Y. Cai, N. Patel, J. T. Bessette, M. Romagnoli, L. C. Kimerling, and J. Michel, *Opt. Exp.* **20***,* 11316 (2012).

[159] A. W. Fang, H. Park, O. Cohen, R. Jones, M. J. Paniccia, and J. E. Bowers, *Opt. Exp.* **14**, 9203 (2006).

[160] D. Liang, G. Roelkens, R. Baets, and J. E. Bowers, *Materials* **3**, 1782 (2010).

[161] K. Tanabe, K. Watanabe, and Y. Arakawa, *Scientific Reports* **2010**, 2349 (2012).

[162] G. H. Duan, C. Jany, A. L. Liepvre, J. G. Provost, D. Make, F. Lelarge, M. Lamponi, F. Poingt, J. M. Fedeli, S. Messaoudene, D. Bordel, S. Brision, S. Keyvaninia, G. Roelkens, D. V. Thourhout, D. J. Thomson, F. Y. Gardes, and G. T. Reed, *ECOC Technical Digest* (2012).

[163] S. Tanaka, S. H. Jeong, S. Sekiguchi, T. Kurahashi, Y. Tanaka, and K. Morito, *Opt. Exp.* **20**, 28057 (2012).

[164] J. V. Campenhout, P. Rojo-Romeo, P. Regreny, C. Seassal, D. V. Thourhout, S. Verstuyft, L. D. Cioccio, J. M. Fedeli, C. Lagahe, and R. Baets, *Opt. Exp.* **15**, 6744 (2007).

[165] J. C. Johnson, H. J. Choi, K. P. Knutsen, R. D. Schaller, P. Yang and R. J. Saykally, *Nat. Mat. Lett.* **1**, 106 (2002).

[166] J. Heo, W. Guo, and P. Bhattacharya, *Appl. Phys. Lett.* **98**, 021110 (2011).

[167] Q. Li, J. B. Wright, W. W. Chow, T. S. Luk, I. Brener, L. F. Lester, and G. T. Wang, *Opt. Exp.* **20**, 17873 (2012).

[168] T. Baehr-Jones, M. Hochberg, C. Walker, and Scherer, *Appl. Phys. Lett.* **86**, 081101 (2005).

[169] G. Wang, T. Baehr-Jones, M. Hochberg, and Scherer, *Appl. Phys. Lett.* **91**, 143109 (2007).

[170] J. Piprek, and S. Nakamura, *IEE Proc. Optoelectron.* **149**, 145 (2002).

[171] P. Bhattacharya, A. Banerjee, and T. Frost, *Proc. of SPIE* **8640**, 86400J (2013).

[172] X. A. Cao, P. M. Sandvik, S. F. LeBoeuf, S. D. Arthur, *Microelec. Rel.* **43**, 1987 (2003).

[173] B. N. Gomatam and A. P. DeFonzo, *IEEE J. Quant. Electron.* **26**, 1689 (1990).

[174] M. Ikeda, Y. Mori, H. Sato, K. Kaneko, and N. Watanabe, *Appl. Phys. Lett.* **47**, 1027 (1985).

[175] J. Rennie, M. Okajima, M. Watanabe, and G. Hatakoshi, *IEEE J. Quant. Elec.* **29**, 1857 (1993).

[176] *ITU-T G.694.1*, International Telecommunication Union, Geneva, Switzerland, (2002).

[177] P. J. A. Thijs, L. F. Tiemeijer, P. I. Kuindersma, J. J. M. Binsma, and T. van Dongen, *IEEE J. Quant. Elec.* **27**, 1426 (1991).

[178] Y. Suematsu and S. Arai, *IEEE J. Sel. Topics Quantum Electron.* **6**, 1436 (2000).

[179] T. C. Newell, D. J. Bossert, A. Stintz, B. Fuchs, K. J. Malloy, and L. F. Lester, *IEEE Photon. Technol. Lett.* **11**, 1527 (1999).

[180] O. Qasaimeh, M. Zhenqiang, P. Bhattacharya and E. T. Croke, *J. Lightwave Tech.* **18**, 1548 (2000).

[181] K. Kishino, H. Sekiguchi and A. Kikuchi, *J. of Crys. Growth* **311**, 2063 (2009).

[182] A. Usui, H. Sunakawa, A. Sakai and A. Yamaguchi, *Jpn. J. Appl. Phys.* **36**, L899 (1997).

[183] S. Nakamura, M. Senoh, S. Nagahama, N. Iwasa, T. Yamada, T. Matsushita H. Kiyoku, Y. Sugimoto, T. Kozaki, H. Umemoto, M. Sano and K. Chocho, *Jpn. J. Appl. Phys.* **36**, L1568 (1997).

[184] Y. Kawaguchi, S. Nambu, H. Sone, T. Shibata, H. Matsushima, M. Yamaguchi H. Miyake, K. Hiramatsu and N. Sawaki, *Jpn. J. Appl. Phys.* **37**, L845 (1998).

[185] S. D. Hersee, X. Y. Sun and X. Wang, *Nano Lett.* **6**, 1808 (2006).

[186] H. Tang, S. Haffouz and J. A. Bardwell, *Appl. Phys. Lett.* **88**, 172110 (2006).

[187] S. Ishizawa, K. Kishino and A. Kikuchi, *Appl. Phys. Express* **1**, 015006 (2008).

[188] K. Kishino, T. Hoshino, S. Ishizawa and A. Kikuchi, *Electron. Lett.* **44**, 819 (2008).

[189] H. Sekiguchi, K. Kishino, and A. Kikuchi, *Appl. Phys. Lett.* **96**, 231104 (2010).

[190] T. Peng and J. Piprek, *Elec. Lett.* **32**, 24 (1996)

[191] J. H. Buss, J. Rudolph, F. Natali, F. Semond, D. Hagele, *Appl. Phys. Lett.* **95**, 192107 (2009).

[192] A. Banerjee, F. Doğan, J. Heo, A. Manchon, W. Guo, and P. Bhattacharya, *Nano Lett.* **11**, 5396 (2011).

[193] S. Jahangir, F. Doğan, H. Kum, A. Manchon, and P. Bhattacharya, *Phys. Rev. B* **86**, 035315 (2012)

[194] H. Kum, J. Heo, S. Jahangir, A. Banerjee, W. Guo and P. Bhattacharya, *Appl. Phys. Lett.* **100**, 182407 (2012)